Finite Element Simulation of the Human Body in Vehicle Side Impact

by

Dipl.-Ing. Rötger Jost

Thesis submitted to the Department of Mechanical Engineering,
University of Cape Town, in fulfilment of the requirements
for the degree of

Doctor of Philosophy

at the

UNIVERSITY OF CAPE TOWN

September 2000

DIGITISED
10 JUL 2012

To my friend Rolf Lengenfelder (†)

In memory of all the good times we had together

Declaration

I declare that this thesis is my own, unaided work. It is being submitted for the degree of Doctor of Philosophy at the University of Cape Town. It has not been submitted before for any degree or examination at any other university.

Signature of Author ....

Department of Mechanical Engineering

Cape Town, September 2000

Abstract

Accident statistics have shown that automotive side impacts are a major safety problem. The side impact dynamics of an occupant are very complex and difficult to investigate. Industrial research has mainly focused on the impact dynamics of man-made side impact dummies, rather than on the dynamics of real human bodies. Therefore fundamental research of the impact dynamics of real human bodies is rare. The objective of this thesis has been to make a contribution to this research by developing a computer-simulated model of the human body using the finite element technique.

Fundamental research has been conducted in the past to investigate the biomechanical impact responses of the human body subjected to lateral impact. For obvious reasons, tests exceeding injury levels are not performed with living humans and hence human cadavers were used. A pendulum mass is usually used in impactor tests to impact the cadaver at different body regions with varying initial velocities. Sled tests are another test procedure, in which cadavers are impacted against a rigid or padded wall by means of a horizontally accelerated sled.

Since the number of cadaver tests is limited, mathematical models have been developed to further investigate the dynamics of cadavers in impact tests. The simplest type of impact model is the one-dimensional lumped mass model, which typically consists of five or six masses with spring-damper interconnections between each of the lumped masses. More advanced multi-dimensional lumped parameter models are used to describe the three-dimensional motion of linked rigid bodies. These bodies usually have a simplified geometry consisting of planes and ellipsoids. Finite element programs have been used for some time to examine impact problems in many research fields. The impact effects require dynamic capabilities, thereby adding inertial forces to internal stresses in the structure, providing more complex material properties and geometry descriptions, and allowing large deformation and self-contact of surfaces. Such models are expensive in preparation and computational time.

The FE-model of the human body developed by the author consists of all relevant skeletal parts of the human body, which have been modelled in detail using shell elements. The different joints and ligaments, which connect the skeletal bones, display a high geometrical complexity. All major muscles of the back, neck, abdomen and of the complex shoulder are included in the entire FE-model as separate FE-models, and are not lumped together as in previous FE-models developed by other authors. Furthermore, three techniques are used to model the different muscle groups. These three different techniques make use of one-dimensional spring-damper elements, two-dimensional membrane elements and three-dimensional solid elements respectively.

The validation process comprises a visual comparison of the dynamics of the FE-model with cadaver sled tests at two different initial velocities. Despite some minor differences in the observed dynamics of the cadavers, the FE-model shows very similar dynamics compared to these sled test simulations.

A quantitative comparison is conducted, comparing the numerical responses of the FE-model subjected to lateral impactor tests and sled tests with the corresponding responses measured in the experiments. The FE-model shows its high level of biofidelity in the shoulder, thorax, abdomen and pelvis impactor tests and in the sled tests. The experimental results are often defined by a response corridor with an upper and lower limit, due to the fact that the cadaver responses often vary within a wide range. The biofidelity of the FE-model is assessed by comparing the simulated responses to the experimental corridors. The simulated force and deflection responses show good agreement with the corresponding experimental results and generally are within the limits of the response corridors.

The dynamics of the head-neck complex are examined by comparing the FE-model responses to low g-level volunteer sled tests and to high g-level cadaver sled tests. The FE-model performs very well compared to the experimental volunteer tests and fairly well to the high g-level cadaver sled tests.

The FE-model shows that the shoulder, thorax and abdomen impact performance is mainly influenced by the deformation of the rib cage. A high level of biofidelity depends strongly on the compliance of the body. This is shown when comparing the simulated impact responses with the corresponding experimental results of the present side impact dummies, which also demonstrates the deficiency of biofidelity of the existing dummies.

Acknowledgements

I would like most sincerely to thank my supervisor, Professor G.N. Nurick, for his support and guidance throughout the project period. Over the years I have benefited greatly from his expertise and from the help and advice he has given me.

For financial assistance I am grateful to the National Research Foundation (NRF), formerly known as the Foundation for Research Development (FRD), and to my supervisor.

I wish to thank my friend Richard Lord for always lending a helping hand and for the many fruitful discussions we have had on a variety of topics. My thanks go to my grandmother Elisabeth Jost and to my brother Elmar Jost for all their moral support. I also wish to send my sincerest apologies to Dr Marion Funke for being so involved in my thesis work for the last four years and thereby straining our relationship.

Finally I wish to thank Charlotte Funke for proof-reading this thesis, and all the fellow graduates of the Centre for Research in Computational and Applied Mechanics (Cerecam) at UCT for providing an enjoyable and stimulating work environment.

Contents

1. Introduction

2. Review of Research

3. Development of the Finite Element Model of the Human Body

4. The Validation of the Model

5. Discussion and Conclusion

List of Figures

List of Tables

Nomenclature

ABAQUS - Finite Element code
APR - Association Peugeot-Renault
APF - Abdominal Peak Force
ASA - Average Spine Acceleration
AIS - Abbreviated Injury Scale
C - Compression
C1 – C7 - Cervical vertebrae (first - seventh)
CEESAR - European Centre of Safety and Risk Analysis
c.g. - Centre of Gravity
ENSAM - Laboratory of Biomechanics, Paris
EPIDM - External Peripheral Instrument for Deformation Measurement
Eurosid - European Side Impact Dummy for European side impact test
FE-model - Finite Element Model
HIC / HPC - Head Injury Criterion / Head Protection Criterion
HSRI - Highway Safety Research Institute / Michigan
ISO - International Standard Organisation
LPB - Laboratoire d'Accidentologie et de Biomecanique
MADYMO - Mathematic Dynamic Model
MPV - Multi Purpose Vehicles
NBDL - Naval Biodynamic Laboratory
NCSS - American National Crash Severity Study
NHTSA - National Highway Transport and Safety Administration
o.c. - occipital condyles

LTV	- Light Transport Vehicles
L1 – L5	- Lumbar vertebra (first – fifth)
PSPF	- Pubic Symphysis Peak Force
RDC	- Rib Deflection Criterion
Ribn	- lateral peak acceleration of nth rib
S3	- Third sacral vertebra
SID	- Side Impact Dummy for US side impact test
SIC	- Side Impact Cadaver (test at Wayne State University)
SRP	- Seat Reference Point
VC	- Viscous Criterion
T1 – T12	- Thoracic vertebrae (first - twelfth)
Tn_y	- lateral peak acceleration of nth thoracic vertebra
TTI	- Thoracic Trauma Index
WSU	- Wayne State University / Detroit

1. Introduction

1.1 Background

1.1.1 Statistics of automotive side impacts

Automotive side impacts are a major safety problem. Approximately 18% of all injuries and 35% of all serious and fatal injuries have been found to occur in crashes where the principal component of the force on the vehicle is to the side [Lau91, Ott82, Ott90]. Accident investigations have shown the complexity of the event when a car collides laterally with either another car or a rigid object. Therefore it is no surprise that the statistical results vary within a wide range among different accident investigations due to a lack of uniformity of the accident investigation methodology. However, analyses of accident statistics have shown several similar trends in Europe and the USA. The proportion of side collisions among all car accidents ranges from 20% to 40% [Ott90, Ott93, Rou85, Kal86, Mil91]. Figure 1.1.1 a) shows the frequency of side collisions among all vehicle accidents and Figure 1.1.1 b) shows the distribution of the impact angle of all vehicle side impacts.

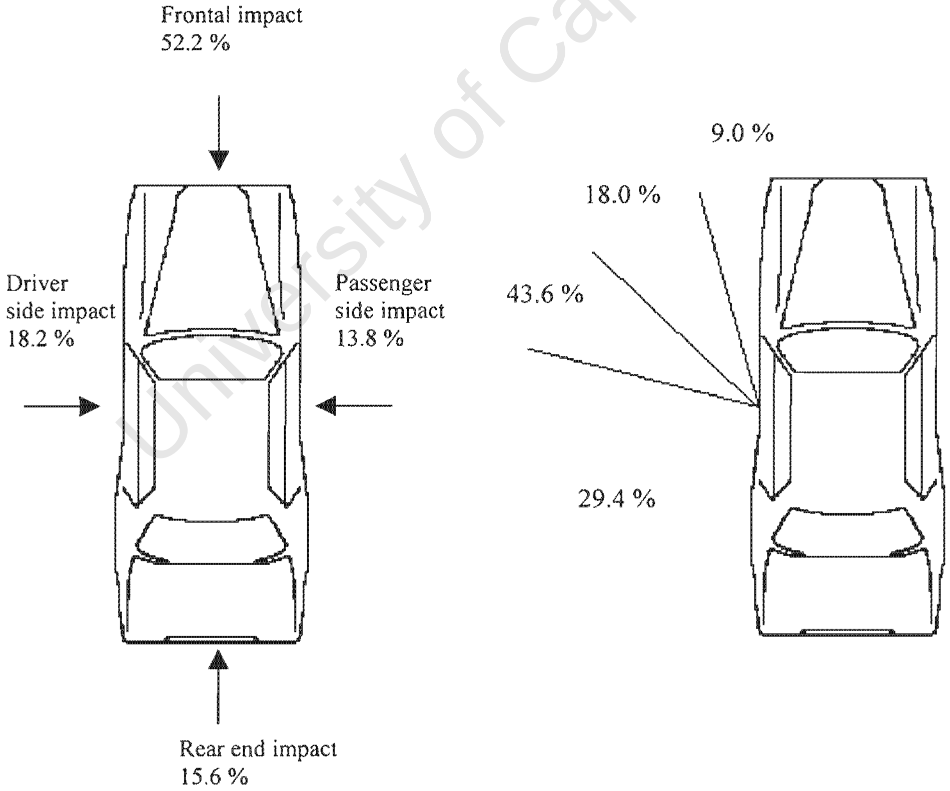

a) Frequency of side collisions *b) Distribution of impact angle*

Figure 1.1.1: Side impact statistics (redrawn from [Ott93])

In 60% of all side impact collisions the passenger compartment is affected [Ott93, Rou85, Mon77]. The oblique frontal impact at angles between 30° and 120° is the most frequent situation [Dan76, Rou85] as shown in Figure 1.1.1 b). The intrusion of the side panel into the passenger compartment is considered to be one of the main causes of serious injuries, so that nearside occupants have a 2 to 4 times higher risk of serious and fatal injury than the farside occupant [Ces76, Tho87, Rou85, Dan76, Ott84].

The severity of injuries is classified into 6 groups by an Abbreviated Injury Scale (AIS). AIS 1 covers minor injuries while AIS 6 is not survivable. Classification criteria have been changed over the past 20 years which makes a comparison between different accident investigation reports even more difficult. Table 1.1.1 shows the results of an analysis of the American National Crash Severity Study (NCSS), illustrating those body regions which are seriously injured in lateral impacts.

AIS	3-6	4-6	5-6	6
Head [%]	12.2	28.7	34.5	32.0
Neck [%]	6.7	0.4	18.1	46.6
Abdomen [%]	15.6	24.2	21.0	0.1
Chest [%]	38.3	24.2	24.5	19.4
Other [%]	27.3	-	-	0.1

Table 1.1.1 Injuries in vehicle side impact [Rou85]

When all serious injuries with AIS between 3 and 6 are considered, chest injuries are most prevalent, whereas head and neck injuries dominate if only immediately fatal injuries (AIS 6) are closer examined more closely.

1.1.2 Side impact tests and regulations

In 1990 regulations for a test procedure, with regard to establishing the protection of occupants in side impacts was issued in the USA by the National Highway Transport and Safety Administration (NHTSA). It applies to passenger cars from the model year of 1997 and Multi Purpose Vehicles (MPV) from the model year of 1999. The test configuration is shown in Figure 1.1.2 a).

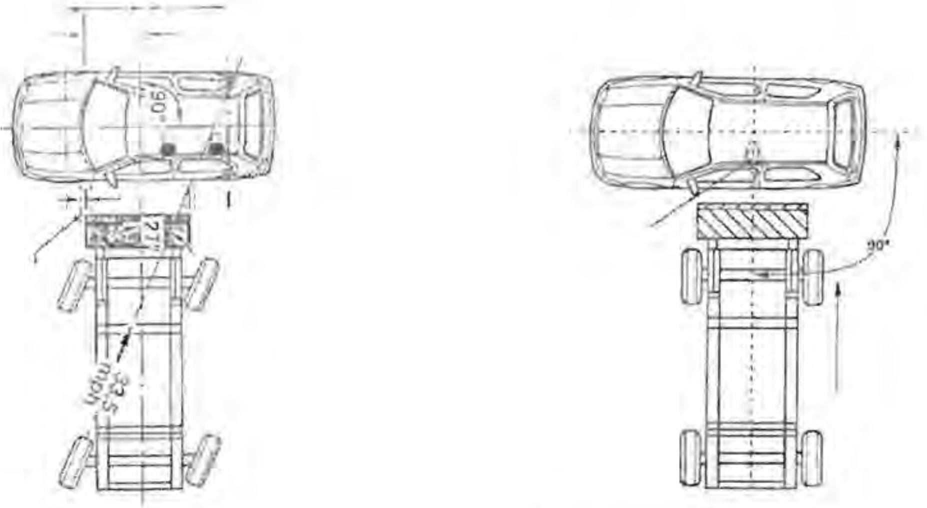

a) US test *b) European test*

Figure 1.1.2 Side impact test configurations

In this test procedure a barrier is propelled into a precisely defined point of impact on the driver's side of a stationary car. The barrier travels in a crab-like manner at an angle of 27° and a speed of 33.5 mph (~54 km/h). The impact line of the barrier is located 37 inches (940mm) in front of the centre of the wheelbase and an additional 2 inches (50mm) behind the centre of the front wheel. This test requirement has a considerable effect on the introduction of force into the side structure of the vehicle. In medium-sized vehicles, the A-pillar is usually also struck. The 27° inclined barrier motion is intended to take into consideration the fact that in real-world accidents both vehicles are moving and that the impacted vehicle is struck at an angle. The US test configuration simulates a lateral velocity for the striking vehicle of 30 mph (~48 km/h) and a velocity of 15 mph (~25 km/h) for the struck vehicle. The mass (1368 kg) and dimensions of the deformable moving barrier correlate with the vehicle data for typical US vehicles. The test body on the front of the barrier consists of an aluminium honeycomb structure with defined front structural stiffness including the bumper profile of a comparison vehicle. The test vehicle is equipped with two SID test dummies (Side Impact Dummy), one on the driver's seat and one on the rear seat. Test weight, seat adjustment, dummy positioning and other test parameters, including photographic and measurement equipment, are described in detail in the test regulations. These parameters must be rigorously observed to ensure the reproducibility of the test procedure.

The European side impact test differs substantially from the US procedure with respect to test configuration as shown in Figure 1.1.2 b). The deformable barrier is propelled perpendicularly against the driver's side of the stationary vehicle at a speed of 50 km/h. The point of impact of the centre of the moving barrier is located at the seat reference point (SR point) of the driver, as specified by the vehicle manufacturer. The total mass of the barrier is 950 kg. The deformable test device mounted on the front of the barrier consists of six deformation elements of differing stiffness which are intended to represent the front-end structural stiffness of a typical European vehicle. The vehicle is equipped with only one Eurosid dummy on the driver's seat. The European test parameters generally contemplate greater structural loading of the vehicle, because of the smaller impact area of the barrier, which usually does not impact with the A-pillar. The extremely stiff centre portion of the test device generates substantial loading and deformation in the door area. This effect is further amplified by the higher position of the European barrier. The result is an impact with a high door intrusion which accords with accident statistics that indicate a great risk of injury when the door intrusion is high [Ott93].

1.1.3 Dummies and injury criteria

With regard to both American and European regulations, successful test performance is further determined by dummy injury criteria. These criteria were derived by cadaver tests that are described in detail in section 2.1.1. However, the two regulations differ in both the test dummy and the injury criteria. Figure 1.1.3 shows the two side impact dummies; the Eurosid-1 in Figure 1.1.3 a) used in the European side impact test, and the SID in the American test in Figure 1.1.3 b).

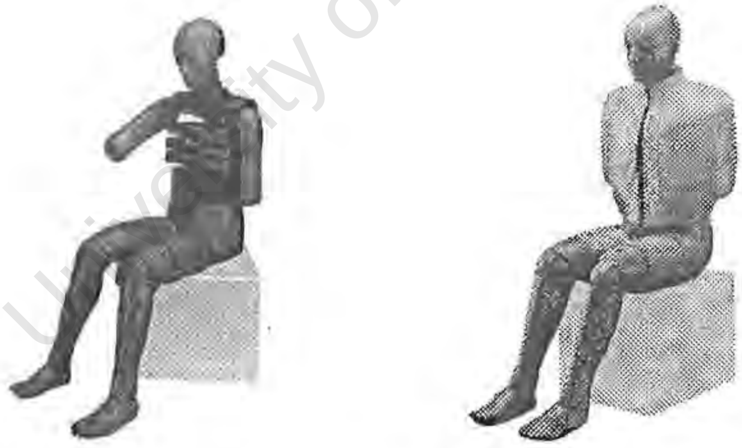

a) Eurosid-1 *b) SID*

Figure 1.1.3 Side impact dummies

Although both dummies ideally represent a 50th percentile side impact anthropomorphic device, they are based on different designs and have different measurement capabilities. In particular, the Eurosid-1 has an articulating half-arm, while in the case of the SID, the response of the arm is moulded into the design of the thorax. The relevant injury criteria, as set out in Table 1.1.2, relate to the measurement capabilities of the respective dummy used. These injury criteria are described in more detail in Section 2.2.

	Eurosid-1	SID
Head	Head injury criterion Head protection criterion HIC / HPC - 1000	-
Thorax	Rib deflection – 42 mm Viscous Criterion - 1.0 m/s	Thoracic Trauma Index TTI – 85 g front TTI – 90 g rear
Abdomen	Abdominal force – 2.5 kN	-
Pelvis	Pubic symphysis force – 6 kN	Pelvic acceleration – 130 g

Table 1.1.2 Test dummy injury criteria

As illustrated in Table 1.1.2 the SID injury criteria are acceleration based, while the Eurosid-1 also incorporates force and deflection criteria. SID was designed to measure only the acceleration of the ribs, spine and pelvis to compute thoracic and pelvic injury criteria [Epp84]. The rib and spine accelerations are combined into a single injury criterion called the Thoracic Trauma Index (TTI(d) - (d for dummy)), which has an 85 g limit for 4-door passenger cars and all Light Transport Vehicles (LTV). The TTI(d) limit for 2-door passenger cars is 90 g. The pelvic acceleration (PelvicG) has a 130 g limit.

EUROSID-1 has additional measurement capabilities, including force and displacement, as well as acceleration-based readings. The EU regulations allow for a limit of five dummy criteria to determine the vehicle safety in side impact. The head protection criterion (HPC) specified is that which is generally used for frontal impact protection and is derived from head acceleration over a head contact time duration and must remain below 1000. A rib deflection criterion (RDC) permits a maximum of 42 mm of deflection in the thorax. A soft tissue viscous criterion (VC), computed from combined rib deflection and velocity, is given a proposed limit of 1 m/s. The abdominal peak force (APF) is limited to 2.5 kN. Finally, the pubic symphysis peak force (PSPF), which is in the pelvic region, must be less than 6 kN.

Experimental tests [Lau89] have shown that it cannot be concluded that vehicles designed to meet the EU regulations will also automatically meet the U.S. regulations. The performance of the SID cannot be compared directly with the Eurosid, because they have different measurement capabilities. In impactor-, drop- and sled-tests [Via95, Ben91] the performances of the present dummies have been examined in comparison to the corresponding cadaver tests. The results showed some lack of biofidelity for both the SID and the Eurosid. The international safety community has for a long time recognised the need for international harmonisation of side impact requirements and the potential of added safety benefits that would result from this. Car-manufacturers have also stated that the existing differences lead in fact to different vehicle designs, thus posing financial burdens in terms of dual development, testing and manufacturing of vehicles in various markets. Car-manufacturers have also stated that the existing differences lead in fact to different vehicle designs, thus posing financial burdens in terms of dual development, testing and manufacturing of vehicles in various markets. Therefore the Worldsid project, initiated under the auspices of the International Organization for Standardization (ISO), is supported by automotive manufacturers, suppliers and governmental organizations around the world. A major part of the work of the EC funded program SID-2000 is being contributed to WorldSID and constant coordination with the International Harmonized Research Activity (IHRA) ensures that the dummy developed will be suitable for use in future worldwide regulatory test procedures as well as in advanced research and development work. Target date for completion of the total WorldSID Development Program is early 2004. A fundamental understanding of the occupant dynamics and injury mechanisms is essential for the development of a new, more biofidelic, side impact dummy.

1.2 Thesis Objectives

Accident statistics, which were shown in the previous section, have demonstrated the importance of continued research in the field of vehicle side impacts. Existing side impact test procedures, which include the side impact dummies, have been used extensively by car manufacturers in their research in the area of side impact testing. These test procedures are necessary, because production cars need to fulfil the existing safety requirements.

Industrial research has mainly focussed on the dynamics of man-made dummies rather than on the dynamics of real human bodies. Therefore fundamental research of the impact dynamics of human bodies in vehicle side impact is rare. This is unfortunate, because the impact dynamics of real human bodies differ significantly from the impact dynamics of dummies, mainly because the dummies do not possess the required biofidelity.

The objective of this thesis is to make a contribution to this research by means of computer simulations. More specifically, the objective is to build an advanced FE-model of the human body in order to investigate the dynamics of the human body in lateral impact scenarios. This FE-model should be accurate enough to model the biofidelity of the human body. The degree of accuracy is measured by comparing the simulated side impact dynamics with those obtained from cadaver tests. In a recursive manner, the cadaver test results are used to validate and modify the FE-model. The validation results are critically discussed and the different cadaver test procedures examined.

A further objective of this thesis is to summarise the current state of knowledge regarding the human body in side impacts, by describing the most important experimental tests that have been conducted in the field of cadaver impactor tests. The limited number of tests that have been conducted further verifies the importance of increasing the research done with computer simulations. A summary of the existing FE-models shows the potential for improvement and the requirement for further development.

1.3 Thesis Development

The second chapter reviews the experimental tests that have been conducted to examine the biomechanical responses of the human body, when subjected to lateral impact. For obvious reasons, tests exceeding injury levels are not performed with living humans and hence human cadavers were used. These experimental impactor and sled tests are described in detail. From these cadaver tests injury criteria have been derived that are subsequently reviewed. As the number of cadaver tests are limited, mathematical models have been developed to further investigate the dynamics of cadavers in impact tests. The four different types of mathematical models are summarised and critically reviewed.

The third chapter presents the development of the FE-model of the human body. The material properties are summarised and the modelling techniques illustrated. A detailed description of the development of the FE-model is presented according to the main body regions. The first region to be described is the back, including the spinal column and the different muscle groups of the back. Following this, the FE-model of the thorax is shown, including the rib cage and the visceral contents that represent the internal organs of the thorax. The abdominal and pelvic region are subsequently described, including the abdominal visceral contents, the abdominal and pelvic muscles as well as the skeletal parts of the pelvis and the lumbar spinal column. The FE-model of the head-neck complex including the cervical spine is described together with the different muscles and ligaments of the neck. The body parts of the upper limb are described including the skeletal parts of the shoulder and arm and the different muscle groups of these regions. Finally the remaining body region of the lower limbs is presented, including the skeletal and muscle parts of the legs.

The fourth chapter covers the validation of the FE-model by comparing the simulation results with the corresponding data of the experimental cadaver tests that are described in chapter 2. The validation process comprises a visual comparison of the dynamics of the FE-model and a numerical comparison of the simulated and measured responses. The visual comparison of a simulated cadaver sled test and the corresponding experiment is presented in the form of a picture series of the impact event and as animation files on the accompanying CD. Additionally the validation results of the shoulder impactor and sled tests are quantitatively presented by comparing the simulated responses with the corresponding experimental results. Subsequently the validation results of the head-neck region are illustrated, followed by the validation results of the thoracic, the abdominal and the pelvic region.

In the fifth chapter the validation results are critically discussed and compared with the measured responses of the existing side impact dummies. Conclusions drawn from these comparison and recommendation for future work complete this chapter.

1.4 Statement of Originality

The entire development and validation of the FE-model of the human body is the author's own work. A highly novel aspect of this work is the high complexity of the FE-model. Never before has a FE-model of the human body been developed with such a high level of refinement, in order to be used in vehicle impact simulations.

The FE-model developed by the author distinguishes itself from other models in following aspects:

- All relevant skeletal parts of the human body are modelled with shell elements in greater detail than in other models
- The different joints and ligaments of the human body are represented by FE-models, which display a higher geometrical complexity than those in previous models.
- Most importantly, this work introduces the combination of three modelling techniques for the different muscles groups of the human body. These three different techniques are one-dimensional spring-damper elements, two dimensional membrane elements and three-dimensional solid elements respectively.
- Different muscle groups are modelled separately, whereas other, previous FE-models have lumped different muscle groups together. Thus all major muscles of the back, the neck, the abdomen and of the complex shoulder are included in the entire FE-model of the author as separate FE-models.

Extensive work has been conducted by the author to validate the FE-model by comparing it to relevant lateral cadaver impactor tests and sled tests. This work has verified that a highly complex FE-model is necessary to achieve the required biofidelity, which is essential for a high quality of the simulation results. This important aspect has also been verified by comparing the FE-model with the present side impact dummies, which have been shown to back the required biofidelity.

Despite its complexity, the FE-model developed by the author operates numerically stable, even under severe impact conditions.

2. Review of Research

The investigation of accident statistics provides important information about the injuries suffered by an occupant in a car crash. Although some progress has been made in terms of accident reconstruction, the exact circumstances of complex accidents can only be examined to a certain extent. There are too many unknowns; for instance, it may only be able to estimate the initial impact velocity and the resultant occupant dynamics. In vehicle crash tests, on the other hand, the mechanical input, as well as the output in the form of dummy dynamics, can be measured accurately. In order to be able to use such human surrogates, it is essential that these substitutes behave exactly like the original: this is called biofidelity. Further, in order to examine the biofidelity of such human substitutes, one has to know precisely how the human body does in fact behave under impact conditions in terms of kinematic behaviour and injuries. The final aim of this biomechanical research is to establish the relationship between a mechanical input to the human body and the resulting dynamics and injury thresholds. For obvious reasons biomechanical tests exceeding injury levels cannot be conducted on living human beings. Therefore, with respect to human-like behaviour, human cadavers are the best test subjects. On the other hand, the fact that the results of cadaver tests are so inconsistent with each other, leads one to the conclusion that there is no such thing as a "typical" human response. Such wide-ranging results are caused by a whole range of factors, each of which significantly affects the test subject's condition, for instance age, mass, height, bone condition and other parameters. In order to reduce the influences of different sizes and masses among the cadavers, Merz [Mer84] developed a method of normalisation, which has been used for most of the following described tests. An example of this normalisation procedure is illustrated in Appendix B.

2.1 Experimental Tests

This chapter reviews the experimental tests that have been conducted to examine the biomechanical behaviour of cadavers under impact. In the first group of impactor tests it is usually the case that a free-flying mass with a predefined initial velocity hits a relatively small area of a resting body. The most important responses of these tests are reaction forces and deformations. The advantage of this type of test is that the body region, which is being impacted, is closely associated with the specific input loading, which thereby minimises any interaction between other body regions. The linear impactor makes a localised thoracic impact and can give a more direct biomechanical response to the impact, in contrast to the sled test, which simultaneously loads several body regions (shoulder, thorax, abdomen and pelvis), depending on impacted wall topologies [Chu98]. In the sled test the cadaver is placed on a seat which in turn is placed on a moveable sled. The sled is accelerated to a predefined velocity and stopped abruptly, so that the cadaver impacts a wall as it continues travelling off the decelerated sled seat. The impact force, as well the acceleration and deformation responses of the body are measured and define the reference range of response of a particular test procedure.

The International Standard ISO TR 9790 [ISO89] defines technical aspects of experiments dealing with human and surrogate human testing, and procedures for collecting and reporting biomechanical data. Recommended practices regarding measurements, instrumentation and reporting of results are outlined. Parts 1 to 6 of the ISO standards describe the biomechanical response requirements, which are needed to assess the biofidelity of the dummy (or the mathematical model) with regard to lateral impacts to head, neck, thorax, shoulder, abdomen and pelvis. These requirements are the result of a critical evaluation of data selected from past experiments. Results of these experiments are reviewed and summarised by means of the ISO-requirements. Furthermore, the results of additional cadaver sled and impactor tests that are not included in the ISO standard supplement the biomechanical response database used for the validation of models. The responses and injuries, which resulted from these impactor tests will be reported in chapter 3 together with the corresponding validation results of the FE-model.

2.1.1 Cadaver impactor tests

Shoulder impactor test – ISO-requirements

ISO TR 9790 part 4 describes the requirements for a shoulder impactor test based on impact tests conducted by the Association Peugeot-Renault [APR]. The cadaver was seated on a horizontal hardwood surface with a vertical backrest, as depicted schematically in Figure 2.1.1.

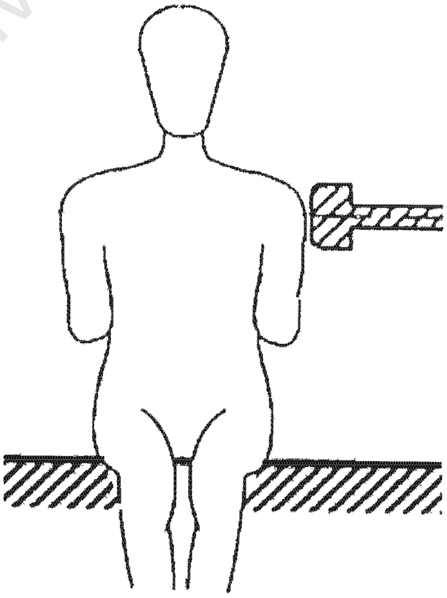

Figure 2.1.1: ISO shoulder impactor set up

The cadaver's hands were placed on its lap, and the arm on the side to be impacted was suspended as if supported by an armrest. The impact was delivered laterally by a 23 kg impactor with a flat surface 150 mm in diameter at impact velocities between 4.4 and 4.6 m/s. The resulting forces recorded during the impacts of different cadavers define a response corridor for the shoulder impactor test. The maximum shoulder deflection relative to the thoracic spine showed an average value of 37.5 mm. Allowing approximately 10% deviation from this value gives a proposed range of 34 to 41 mm for a maximum shoulder deflection.

Thorax impactor test – ISO-requirements

ISO TR 9790 part 3 describes requirements for thoracic impactor tests, based on a test series conducted by the Highway Safety Research Institute (HSRI)/ Michigan [Epp78]. The impactor was aimed at the lateral aspect of the chest and centred on the rib structure, while the cadavers were seated in an upright position with one arm raised. The impact was delivered at 4.3 m/s by a 23.4 kg (51 pounds) flat rigid pendulum mass with a diameter of 150 mm (6 inches). The acceleration of the impactor was measured during the impact. The response of the human thorax was measured by an array of accelerometers developed by Robbins et al. [Rob76] shown in Figure 2.1.2 b).

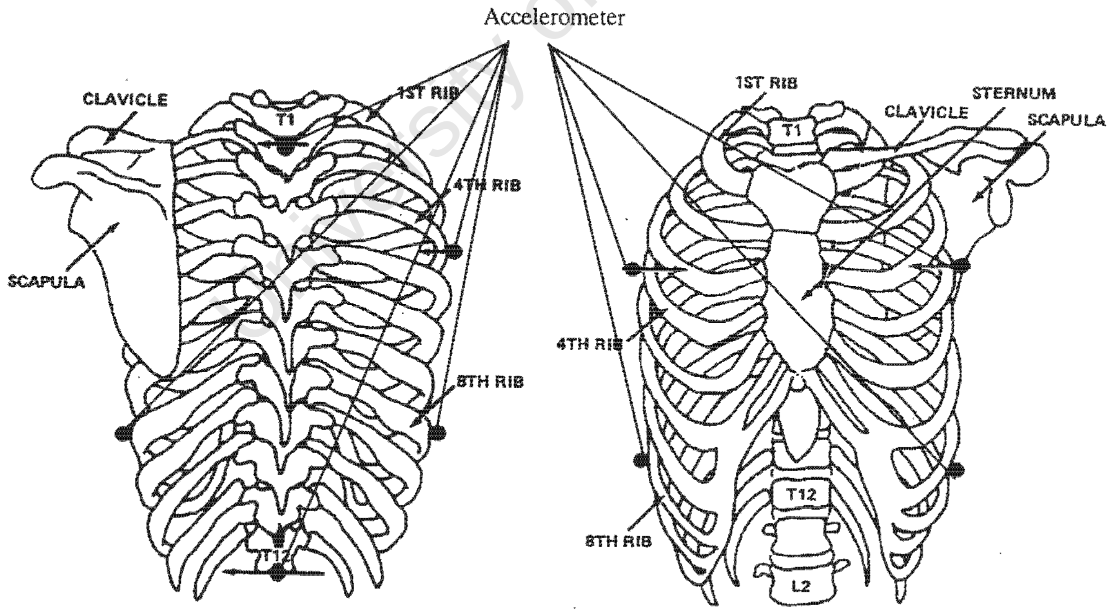

a) Front view

b) Rear view

Figure 2.1.2: Locations of thoracic accelerometers in the HSRI impactor tests

The ISO TR-9790 lateral impact requirements include the acceleration response of the impactor and the first thoracic vertebra. The measured cadaver responses differ within a response corridor that defines the upper and lower limit of acceleration values. The acceleration-time histories of some of the other measurement points shown in Figure 2.1.2 b) can be found in [Epp78], but are not included in the ISO-requirements.

Pelvis impactor test – ISO-requirements

ISO TR 9790 part 6 defines impactor response requirements to the pelvis that are based on cadaver tests conducted by Onser [Ces80, Ces82]. Figure 2.1.3 shows the test set up.

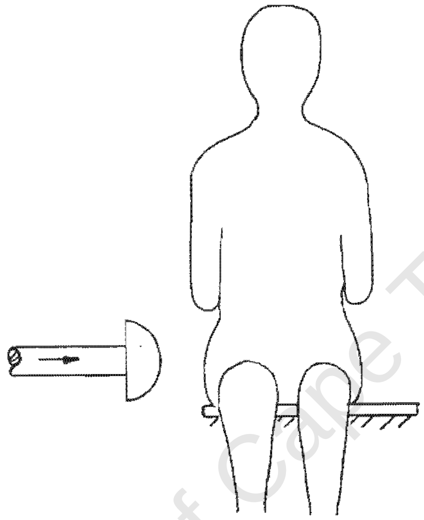

Figure 2.1.3 Pelvis impact test set up

A 17.3 kg impactor was used to strike the pelvic region at the greater trochanter level with initial velocities between 6 m/s and 10 m/s. The unbelted cadavers were seated without lateral support as shown in Figure 2.1.3. The impactor had a rigid spherical segment face with a radius of 175 mm. Accelerometers were placed at the sacrum of the cadaver pelvis to monitor the acceleration response during the impact. The impact force was determined from the impactor acceleration multiplied by the impactor mass. A scatter plot of the impact velocity versus normalised peak forces shows an almost linear relationship between impact force and velocity. The ISO requirements define a response corridor of peak impact forces vs. impact velocity. These results will be shown in section 4.6.1 in comparison with the FE-model responses.

Viano pendulum tests

Viano [Via86, Via89] conducted a test series in which cadavers were subjected to blunt impacts at the thorax, abdomen and pelvis. The pendulum impactor was freely suspended by guide wires and accelerated to impact speeds of 4.5, 6.7 and 9.5 m/s respectively by a pneumatically charged cylinder with a thrust piston. The cadaver was suspended in an upright position, with the hands and arms overhead. The specimen was rotated 30° so that the point of impact on the thorax and abdomen was slightly oblique. This protocol was used to assure that principally lateral thoracic and abdominal impact occurred with the axis of force through the centre of gravity of the torso. This impact configuration resulted in controlled compression of the torso without coincident rotation of the body about the spine axis. The centre of the pendulum impact on the thorax was aligned 75 mm below midsternum, whereas abdominal impact was aligned 150 mm below midsternum. Pelvic impacts were conducted at 90° lateral with the impactor centred on the greater trochanter. The pendulum interface was a smooth, flat, 150 mm diameter disc with rounded edges. The test configuration is shown in Figure 2.1.4.

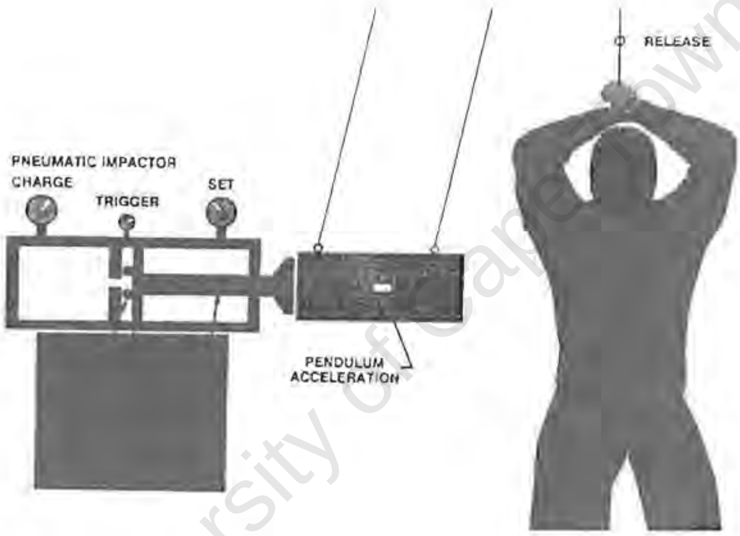

Figure 2.1.4 Viano impactor test set up [Via89]

A uniaxial accelerometer was attached to the pendulum and its response was multiplied by the pendulum mass to calculate the force of impact. A suspension system released the arm at the impact, with the intention of approximating a free torso response to impact. Multiple tests were conducted on a specimen to increase biomechanical response data. These tests could include a low-severity abdominal impact, a high-severity thoracic impact and a lateral pelvic impact. The normalised force-deflection and force-time data for the nine test conditions were used to define corridors within which the response data could be found. In several cases an individual test was excluded from the corridor definition because it was markedly different from others which clustered around a typical response.

WSU impactor test with limited stroke

The previously described cadaver impactor tests all used pendulum impactors, which have an initial kinetic energy that is dissipated into the human body during the impact. Depending on the compliance of the impacted body area, the impactor caused a certain deformation. The objectives of the cadaver impactor tests conducted by Chung [Chu98] were to investigate the injury mechanisms in thoracic impactor tests with a limited stroke and having a high-energy lateral velocity pulse. Theimpactor was pneumatically driven to ensure that the velocity did not decrease too much during the impact stroke, which itself was limited to 305 mm. These impactor dynamics were intended to replicate the door intrusion dynamics in a "real-world" side impact. The front of the impactor had a flat, circular wooden disc with a diameter of 152 mm and rounded edges. For the padded tests, a circular 152 mm diameter, 102 mm thick pad was affixed to the face. Figure 2.1.5 shows this test set up.

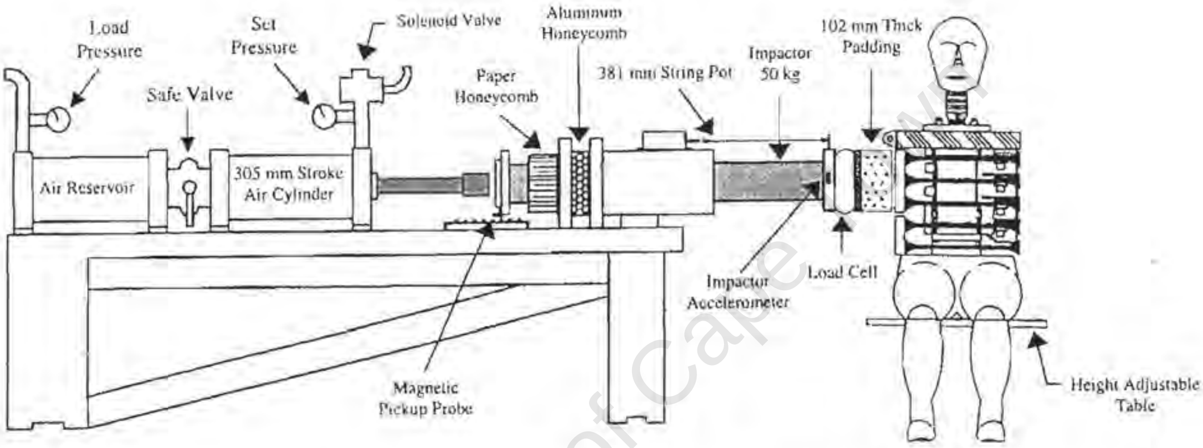

Figure 2.1.5: Test set up of WSU limited stroke impactor tests [Chu98]

The first 152 mm of the 305 mm stroke were used to accelerate the impactor, the next 102 mm to traverse the space occupied by the padding material or air space, and the final 51 mm to traverse the space occupied by the struck side of the test subject. A load cell mounted on the front end of the impactor measured the contact force. The impactor stroke was measured by a position transducer. A chestband unit (EPIDM) [Epp89] was used to measure chest deformation at the edge of the sixth rib, which was the centre of impact. Accelerometers were mounted to ribs 4, 6 and 8 on the impacted side and ribs 4 and 8 on the non-impacted side, to measure the lateral acceleration. Tri-axial accelerometers were mounted at T1, T6, T12 and midsternum. The twelve accelerometer thoracic array developed by Robbins et al. [Rob76] and Nusholtz et al. [Nus79], as previously shown in Figure 2.1.2 b), was used to instrument the ribs, sternum and thoracic vertebrae.

The cadaver impactor tests of the thorax provide the comprehensive data base of experimental impact responses that will be used for the validation of the FE-model of the thorax in section 4.4. Table 2.1.1 summarises these biomechanical responses of the lateral thoracic impactor tests described above.

		Test Conditions	Biomechanical Response Data
Shoulder	ISO / APR	23 kg; 4.5 m/s 90°-lateral	impact force - time history shoulder deflection: 34 to 41 mm
Thorax	ISO / HSRI	23.4 kg; 4.3 m/s 90°-lateral	impact force – time history T1 – acceleration - time history
	Viano	23.4 kg; 4.4; 6.5; 9.5 m/s 60°-lateral	impact force - time history force – deflection, VC, vertebrae acceleration
	Chung / WSU	4.3 m/s; 90°-lateral, limited stroke	impact force - time history force – deflection, Rib + vertebrae acceleration, VC, TTI
Abdomen	Viano	23.4 kg; 4.8; 6.8; 9.4 m/s 60°-lateral	impact force - time history force – deflection, VC, vertebrae acceleration
Pelvis	ISO / Onser	17.3 kg; 6 – 10 m/s 90°-lateral	peak force – impact velocity
	Viano	23.4 kg; 4.3; 6.5; 9.8 m/s 90°-lateral	impact force - time history, force –deflection compression, vertebrae acceleration

Table 2.1.1 Lateral impactor test data used for the FE-model validation

2.1.2 Low and High g-Level Lateral Sled Tests

Head-neck sled test – ISO-requirements

In order to assess the biofidelity to lateral neck impacts, the ISO requirements include both low and high g-level lateral sled tests. The low g-level tests are based on the volunteer sled tests conducted by Ewing et al. [Ewi76, Ewi77] at NBDL, whereas the high g-level tests are based on the cadaver sled tests conducted by Bendjellal et al. [Ben87] at LPB/APR. These tests focus on the dynamic behaviour of the head-neck complex, subjected to lateral acceleration without impact to the head.

Volunteer Tests

In the volunteer tests the subjects were seated in an upright position on a pneumatically driven accelerator sled. The test set up is shown in Figure 2.1.6 a). The subject was restrained by shoulder straps, a lap belt and an inverted pelvis strap tied to the lap belt. To limit the upper torso motion, the subject was positioned against a lightly padded wooden board. The thrust vector of the sled was nominally directed from the right to the left shoulder. The sled was accelerated using a defined acceleration-time profile, as illustrated in Figure 2.1.6 b), with a maximum acceleration of 7g to a maximum velocity of 6 m/s. Figure 2.1.6 b) also depicts the acceleration time history of the first thoracic vertebra that is used as the input acceleration function for the head-neck validation of the FE-model described in section 4.3.

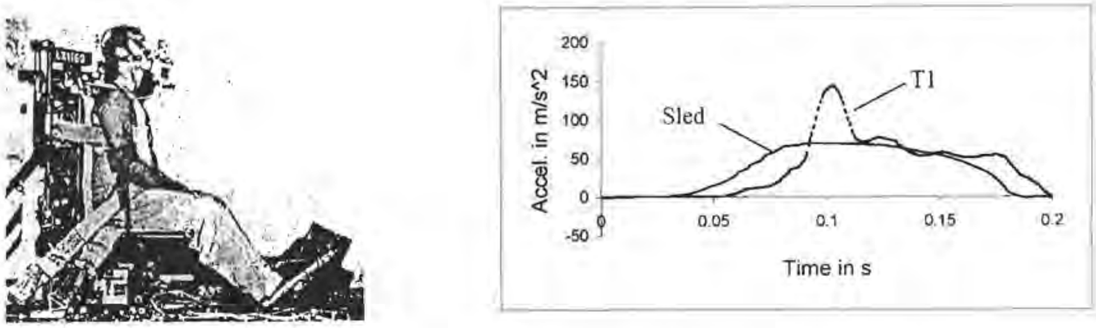

a) Volunteer sled test set up *b) Sled and T1acceleration time history*

Figure 2.1.6 Volunteer test set up [Ewi76]

Cadaver Tests

The cadaver tests conducted by Bendjellal et al. [Ben87] used a similar test configuration as is shown in Figure 2.1.7 b). The acceleration time histories of the cadaver sled and the first thoracic vertebra is shown in Figure 2.1.5 a). Just as the volunteer subjects were restrained to the seat, the cadavers were belted around the chest and pelvis. A wooden sideboard was attached vertically to the seat to prevent upper torso motion. In contrast to the volunteer sled, the cadaver sled was first brought up to a velocity of between 6 and 8.6 m/s and then decelerated at levels between 12.2 and 14.7g..

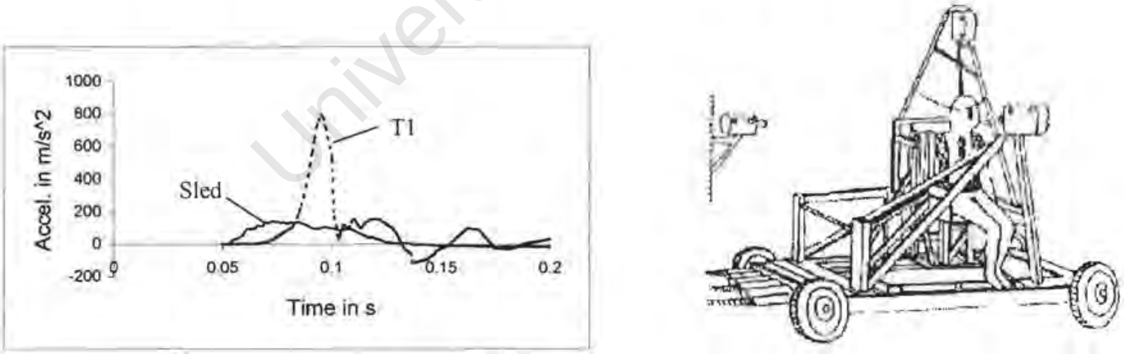

a) Sled and T1 acceleration time history *b) Cadaver sled test set up*

Figure 2.1.7 Cadaver test set up [Ben87]

The relative motion of the head and neck with respect to the thorax is therefore the same in the volunteer and the cadaver tests. The array of instrumentation developed by the NBDL for the volunteer tests was also used in the cadaver tests. Two T-shaped plates, each equipped with 6 monoaxial accelerometers, were fitted to the chin and at the level of the first thoracic vertebra of the subject. In addition, two accelerometers, which were fixed to the seat and sled, were used to measure the sled acceleration and deceleration respectively. The measured responses that define the biofidelity of the neck are head acceleration- and rotation-time histories of the centre of gravity of the head with respect to the first thoracic vertebra. The acceleration and displacement of the first thoracic vertebra with respect to the sled may indicate indirectly the biofidelity of the shoulder, although one has to consider that the thorax and shoulder was belted to the seat. Table 2.1.2 summarises the experimental data of the low g-level volunteer and high g-level cadaver sled test that will be used for the validation of the FE-model of the head and the neck.

Low g-level volunteer test	High g-level cadaver test
Translational acceleration in x, y and z direction Rotation around the x and z direction Rotational acceleration around the x and z direction	Translational acceleration in y and z direction Rotation around the x and z direction Rotational acceleration around the x and z direction
Trajectories of occipital points and centre of gravity Neck length - time	Trajectories of centre of gravity Neck length - time

Table 2.1.2 Sled test data for the validation of the FE-model of the head and neck

Heidelberg Sled Tests

A series of cadaver sled tests, sponsored by the National Highway Traffic Safety Administration [NHTSA], were conducted at the University of Heidelberg [Kal81, Mar83] and have become well known as the "Heidelberg tests". Figure 2.1.8 shows the set up of the test procedure.

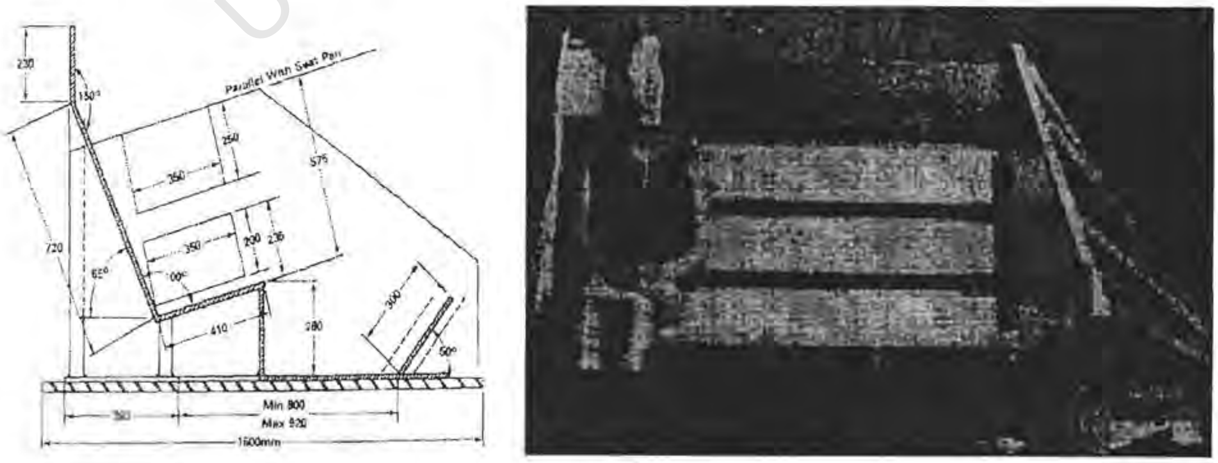

a) Schematical test set up *b) Frontal view of cadaver positioned on sled seat*

Figure 2.1.8 Heidelberg sled test configuration for side impact tests [Mar83]

The test subject is initially placed parallel to and approximately 600 to 900 mm from the impacting wall, which is at 90° to the direction of travel of the sled. The sled is gradually accelerated to the test speed, while the offset distance between the cadaver and the wall is maintained. The sled is then rapidly decelerated to zero velocity. The test subjects continue to move over the low-friction ground in the seated position, at the speed of the sled prior to deceleration, towards the wall, which is now stationary. The test conditions are determined by the speed of the sled before deceleration, and by the compliance and geometric characteristics of the impacted wall, which is either padded or rigid. The tests were conducted under four different conditions, 6.7 m/s (15 mph) into a rigid wall, 8.9 m/s (20 mph) into a rigid wall, and 8.9 m/s (20 mph) into two different types of padding materials. The cadavers were instrumented with nine accelerometers mounted to the head, the twelve thoracic accelerometer array as described previously in Figure 2.1.2 b) [Epp78], and a triaxial accelerometer unit attached to the pelvis. In a later test series [Mar83], the test configuration was upgraded by load cells that were placed in the wall fixture. These load cells measured the force response of the plate for the thorax and the pelvis separately. The Heidelberg tests are included in the ISO requirements, which define a thoracic reaction force-time response corridor. The pelvic response requirement describes acceleration peak values for the pelvic reaction force.

Wayne State Sled Tests

Cavanaugh et al. [Cav90a, Cav90b, Cav93, Cav96] conducted a series of cadaver sled tests at Wayne State University using a Heidelberg-type seat fixture in a slightly modified form, as shown in Figure 2.1.9.

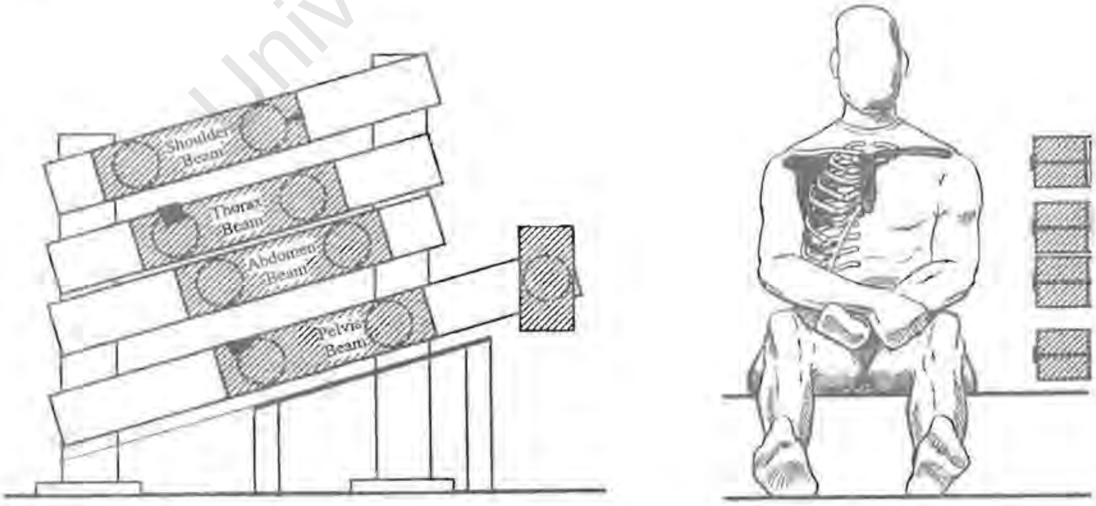

a) Impacted wall with pressure transducers *b) Front view of cadaver in WSU-test*

Figure 2.1.9 WSU sled test set up [Cav90a]

The cadavers were positioned on a seat, which in turn was mounted to a horizontally accelerated sled. The sled was accelerated to velocities between 6.7 and 10.5 m/s and then rapidly decelerated, so that the cadavers would continue to translate laterally on a Teflon seat into the wall of the seat fixture. The impacted side wall was instrumented with nine load cells to record impact forces. The shoulder beam incorporates the upper ribs of a typical test subject, the thoracic beam the middle ribs and the abdominal beam the lower ribs. The shoulder and thoracic beam together incorporate the same area as the thoracic force plate of the Heidelberg tests. The cadavers were instrumented by a 12 accelerometer thoracic array [Epp89] as was previously shown in Figure 2.1.2 b) to measure the acceleration response of the ribs, the sternum and the thoracic vertebrae. The sacrum was instrumented with a triaxial accelerometer. Phototargets were mounted at the upper and lower sternum, first, fifth and twelfth thoracic vertebra, right iliac crest, right fourth rib, right eighth rib, right shoulder joint, left clavicle and left scapula. This array of targets can be used to measure trunk deformation, rib cage rotation and the trajectory of the shoulder during impact. The force-time histories at each of the four anatomical levels, namely the shoulder, thorax, abdomen and pelvis, are computed by summing the load cell responses of the two load cells at that level. In some of the tests, the impacted wall was covered with padding material. The response data of these tests are not used for the model validation, because the crushing characteristic of the soft padding material may only be estimated and therefore implements even more unknown parameters. For the validation of the FE-model of the human body the results of two test groups at 6.7m/s and 8.9 m/s initial impact velocity are used. Table 2.1.3 summarises the sled test data of the Heidelberg and WSU cadaver tests that will be used for the FE-model validation.

	6.7 m/s - Heidelberg	**8.9 m/s - Heidelberg**
Thorax + Shoulder	Impact force-time Vertebrae + rib acceleration-time	Impact force-time Vertebrae + rib acceleration-time
Pelvis	Impact force-time Pelvis acceleration-time	Impact force-time Pelvis acceleration-time
	6.7 m/s - WSU	**8.9 m/s - WSU**
Shoulder	Impact force-time Acromion displacement-time	Impact force-time history Acromion displacement-time history
Thorax	Impact force-time history Chest compression, VC	Impact force-time history Chest compression, VC
Abdomen	Impact force-time Peak acceleration of rib8 + T12	Impact force-time Peak acceleration of rib8 + T12
Pelvis	Impact force-time Pelvis compression	Impact force-time Pelvis compression

Table 2.1.3 WSU and Heidelberg – cadaver sled test data used for model validation

2.2 Injury Criteria

It is obvious that mechanical loads to the human body cause injuries if they exceed injury limits. However the actual severity of the injury is influenced by many different factors. The magnitude, direction, location and time-history of the load are all important aspects. The kind and severity of injuries depend strongly on the individual injury thresholds of the human body. These thresholds are influenced by material properties of the impacted organs and tissue, the mass of the impacted body parts and their interaction. The body mass and size, fat volume and the size and shape of body parts, such as the rib cage for example, all influence the body's biomechanical response to impact. Furthermore the mechanical properties of biological tissue can also be influenced by age or illness. This complexity shows that one cannot expect to find a simple relationship between mechanical load and the severity of injuries: the same load may not necessarily cause the same injury to different bodies. Injury criteria are intended to predict the severity of an injury by means of measured biomechanical response values. A classification of injuries into an injury scale assists in finding such a relation, although not without problems. The internationally recognised AIS (Abbreviated Injury Scale) classifies injuries in following categories:

Scale	Description
0	none
1	minor
2	moderate
3	serious
4	severe (life threatening – survival probable)
5	critical (survival uncertain)
6	not survivable (currently untreatable)

Table 2.2.1 Classification of the AIS (Abbreviated Injury Scale)

These classifications, as is evidenced by the numerous revisions (AIS 1976, 1980, 1985, 1990), are not as clearly defined as it appears. The limits of a quantitative classification of injuries into a scale that can be used to find a correlation to mechanical load are also illustrated by the following example. If the neck of an impacted occupant hits the shattering glass of the side windows, the injuries suffered can be either relatively harmless, when for example only the neck musculature is affected, or they can be severe, if for example the aorta, which is located only a few centimetres away, is injured. In both cases, the mechanical load might be almost identical but the AIS ranking would differ significantly. Therefore it is unlikely to find a simple injury criterion that would be suited for all regions of the body.

A number of tolerance criteria have been derived, based on four injury mechanisms, viz. acceleration-, force-, compression- and viscous injuries.

Acceleration criteria

Acceleration-based criteria have a long history in automotive safety development. The simplest acceleration injury criterion is given by the maximum limit, which defines an injury threshold. The American side impact standard defines a maximum pelvic acceleration of 130 g. Another widely used acceleration criterion is the HIC (Head Injury Criterion) which is intended to express human tolerance to injury in terms of head acceleration.

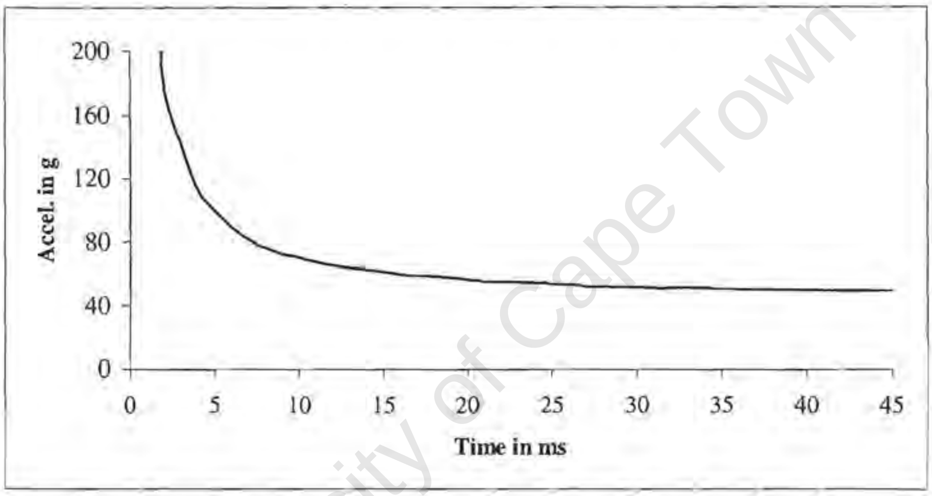

Figure 2.2.1 Wayne State tolerance curve for head injuries [Pa63]

The HIC is based on the Wayne State tolerance curve shows in Figure 2.2.1, which illustrates that the head can withstand higher accelerations for shorter durations but that any exposure above the curve leads to brain injuries [Pat63]. A severe but not life-threatening injury is expected if the HIC reaches or exceeds 1000, calculated by:

$$\mathrm{HIC} = (t_1 - t_2) \cdot \left[\frac{1}{(t_1 - t_2)} \int_{t_1}^{t_2} a(t)\,dt \right]^{2.5}$$

The HIC is a current criterion for the European side impact safety standard and is called HPC (Head Protection Criterion) for lateral impacts.

Eppinger et al. [Epp84] and Morgan et al. [Mor86] proposed the TTI (Thoracic Trauma Index), based on their analysis of cadaver impactor and sled tests. In these tests thoracic cage injuries correlated best with the peak lateral acceleration of the struck side of the rib cage, the lower thoracic spine and the subject's age and mass. For human cadavers the TTI is calculated by:

$$TTI = 1.4\ age + \tfrac{1}{2}\left(T12_y + Rib_y\right)\left(\frac{Mass(kg)}{75}\right)$$

Rib_y is the maximum acceleration of either the fourth or eighth rib of the struck side and T12y is the peak acceleration of the twelfth thoracic vertebrae in the lateral direction. Because age is not a relevant factor for a dummy and the mass of the dummy is ~75 kg, the dummy TTI is calculated in a simplified form:

$$TTI = \tfrac{1}{2}\left(T12_y + Rib_y\right)$$

The American side impact standard defines the limit for the TTI as 85 g for four-door cars and 90 g for two-door cars. These limits are based on a 50th percentile 45-year-old male. Assuming that the peak accelerations of the struck ribs in a lateral impact is 155 g and that of T12 is 12 g, then the TTI value is 83.5 g.

Another acceleration-based criterion for the chest is "Average Spine Acceleration" (ASA), as developed by Cavanaugh et al. [Cav93] which performed well in a series of cadaver sled tests. ASA is obtained by integrating the acceleration-time response of the twelfth thoracic vertebra to calculate the spine velocity pulse. ASA is defined as the slope of the spine velocity between specified ranges of a minimum and maximum spine velocity. This is demonstrated in Figure 2.2.2.

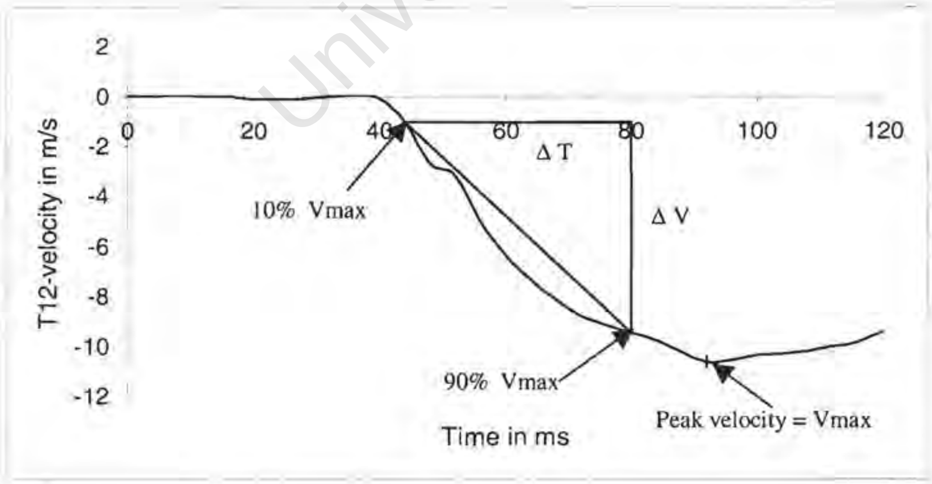

Figure 2.2.2 Definition of ASA – Velocity of twelfth thoracic vertebra

Figure 2.2.2 shows the velocity response of the twelfth thoracic vertebra, which is obtained by integration of the measured spine acceleration. ASA10 is taken between 10% and 90% of the peak spine velocity and ASA15 between 15% and 85%. It is calculated by:

$$ASA = \frac{\Delta V}{\Delta T}$$

ASA considers the rate of change of the spine velocity over time and appears to reflect the rate of change of energy or momentum transfer into the body [Cav93].

Force criteria

Force criteria generally define force limits and injuries are caused when these are exceeded. Force criteria are used in the European side impact standard, in which abdominal and pelvic forces are measured using the Eurosid dummy. The limit for the abdominal force is 2.5 kN and the pubic symphysis force for the pelvis is 6 kN. A thoracic force criterion, proposed by Tarriere et al. [Tar79], defines a maximum normalised thoracic force of 7.40 kN for AIS 0 and 10.20 kN for AIS 3.

Compression criteria

The wide range of cadaver responses is illustrated again by the different injury thresholds in terms of body compression found in different cadaver tests. Stalnaker et al. [Sta79] examined the thoracic force-deflection response in cadaver drop tests from heights of 1 to 3 m onto padded and unpadded force plates. Based on these tests a criterion of 35% chest compression relative to the half chest width was proposed, while Tarriere et al. [Tar79] suggested a criterion that limits the chest compression to 30% relative to the whole chest width. In Viano's [Via89] pendulum impactor tests compression was found to be a good predictor of thoracic injuries. A compression of 38.4% of the whole chest width and 44% compression of the whole abdomen width was determined as a tolerance level for a 25% probability of serious injuries.

The European side impact standard defines a maximum chest deflection of 42 mm as a thoracic injury criterion, which translates to a 24% compression of the 50^{th} percentile male thorax.

The compression criterion for the pelvis defines 27% compression for the 25% probability of pubic ramus fractures.

Viscous criterion

Viano and Lau [Via86, Lau86] proposed this criterion to assess viscous injuries of soft biological tissue. The viscous criterion (VC) is defined as the product of the time-dependant compression C(t) or deformation D(t) and the rate of this deformation as illustrated in Figure 2.2.3 and Figure 2.2.4.

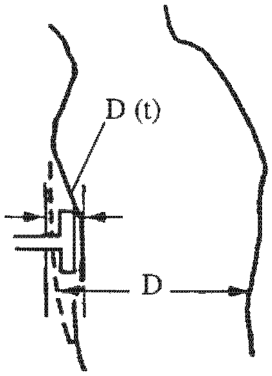

Figure 2.2.3 Body Deformation under impact [Lau86]

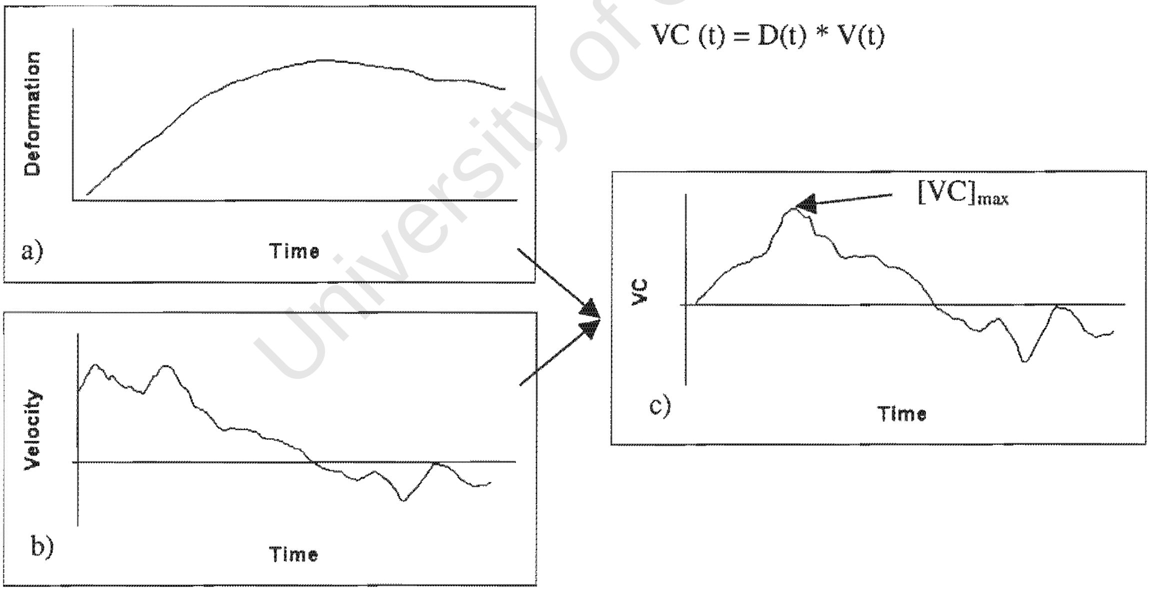

Figure 2.2.4 Definition of the Viscous Criterion [Lau86]

Subsequent tests [Lau89] verified that serious injury occurred at the time of peak VC, which is earlier than the peak compression which can be seen in Figures 2.2.4 a) and c).

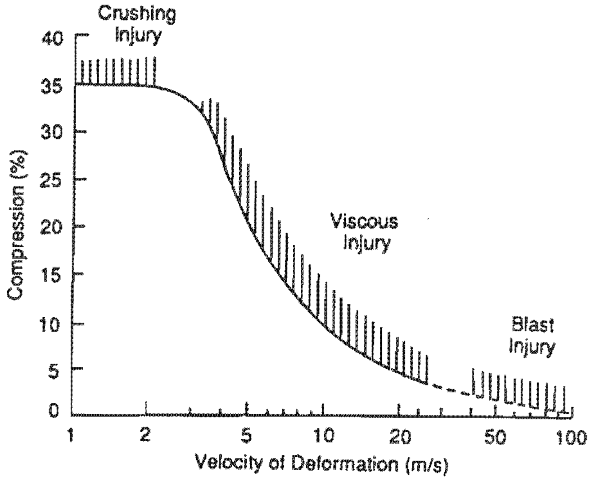

Figure 2.2.5 Torso injury mechanisms [Pra96]

Figure 2.2.5 summarises torso injury mechanisms associated with impact deformation. For low speeds of deformation, the limiting factor is the risk of crush injury from high compression of the body. For deformation speeds above 3 m/s, a similar level of injury risk is determined by the peak viscous response. Both mechanisms can occur during impact. At extreme rates of loading, injury occurs with less than 10-15% compression by a high-energy transfer to the body. A tolerance level of 25% probability of serious injury was determined with VC_{max} of 1.5 m/s for the chest and 2.0 m/s for the abdomen.

2.3 Mathematical Models of the Human Body in Lateral Impact

Mathematical modelling has long been a tool to investigate problems in the field of vehicle safety. Among the most important advantages of computer simulation is the detailed investigation of crash dynamics, many details of which are difficult to examine experimentally. Once a model has been set up and validated against experimental results, parameter studies can be conducted to improve the understanding of the crash process. This information may lead to more effective testing procedures and it contributes to cost reduction. Therefore different model techniques have been used to investigate the side impact dynamics of the human body, which have been experimentally examined in various cadaver and volunteer tests as described in the previous sections. Modelling techniques can be divided into four different groups:

1. **Analytical models**
2. **Lumped mass models**
3. **Multi-dimensional rigid body models**
4. **Finite element models**

In the following section these four groups are described, which of the FE-models are discussed in more detail.

2.3.1 Analytical models

Lau et al. [Lau91] presented an analytical model that is helpful in explaining some important differences between the frontal and side impact occupant dynamics. Since the occupant dynamics of a real impact scenario are very complex, this analytical model inevitably simplifies many of the aspects that are involved in both crash processes.

A frontal crash event involves two impact scenarios. The first impact occurs when the vehicle strikes the barrier or another vehicle, which in turn causes the front end to crush. The kinetic energy of the vehicle is partially absorbed by deforming the vehicle's structure. The occupant continues to move forward as a free-flying mass and strikes the vehicle's interior, causing the second impact after loading the restraint system. Some of the kinetic energy of the occupant is expended in deforming the vehicles' interior or the restraint system and deforming the occupant's torso. The remaining kinetic energy is dissipated as the occupant decelerates with the vehicle. Without describing the injury pattern in detail, injury occurs while the occupant is loading the interior or the restraint system. If there is a large differential velocity between the occupant and the interior, then much of the kinetic energy must be dissipated during the impact with the interior. If this second impact is of short duration, then the resulting forces on the occupant can exceed human tolerance levels. Improvements in front impact safety are achieved by using energy absorbing materials (belts, airbags, etc.) that provide two important benefits. Firstly, they enhance the "ride down" and secondly, they absorb some of the energy of the second impact. These absorbing materials can be designed to crush at forces below human tolerance levels, thereby absorbing energy as they are crushed. Because of this crush, the occupant's differential velocity with respect to the interior is reduced over a longer period of time.

According to Lau et al. [Lau91] a side impact is more appropriately characterised by a single event, in which the moving barrier or vehicle strikes the side of the car. The struck door intrudes into the occupant compartment and strikes the stationary occupant directly. Thereafter, barrier momentum is transferred to the centre of gravity (CG) of the struck car away from the door, and the door decelerates to the car's CG velocity. Typical velocity-time histories of the door, the striking car, the struck car and the driver's spine are shown in Figure 2.3.1.

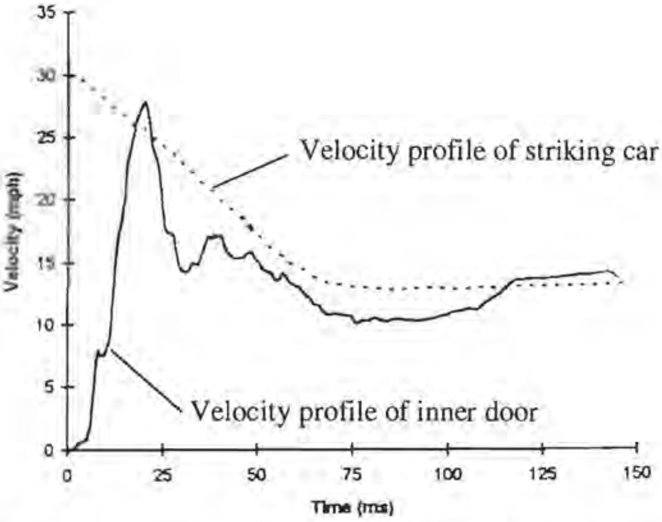

Figure 2.3.1 Velocity-time history of inner door and striking car - redrawn from [Kin96]

Following Lau's theory, the barrier strikes the door of the struck car with a large amount of momentum, so that the door behaves like a "power source" or a "punch" to the occupant. This punch can be characterised by the velocity-time history of the door, which, according to Lau, marginally affects the presence of the occupant. Figure 2.3.1 shows the velocity-time history of the intruding door, which is considered as a programmed punch and is not affected by loads along this path. The shape of this velocity profile is an important part of the analytical model. This model illustrates the influence of padding material between the occupant and the inner door on the dynamics of the occupant using a point mass analogy.

Figure 2.3.2 a) shows the simplified kinematics of a point mass in the unpadded case in comparison to the padded case depicted in Figure 2.3.2 b).

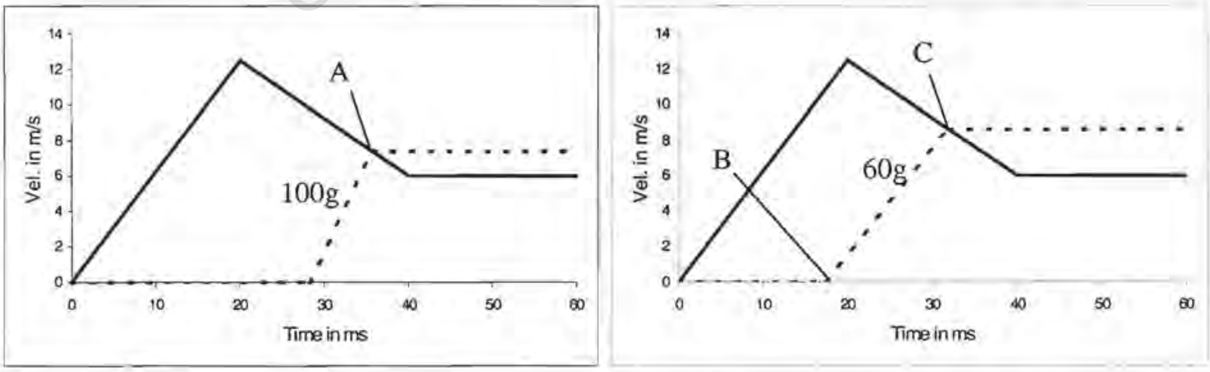

a) Unpadded case *b) Padded case*

Figure 2.3.2 Analytical model using a point mass analogy to describe the kinematics of an occupant

In the baseline (unpadded) case, the point mass is initially spaced 0.2 m from the struck door, which then crushes to fill this distance. The door has a finite compliance and it crushes as the point mass accelerates for example at 100g. The point mass quickly acquires the velocity of the door (~6 m/s), and then continues to travel at that velocity, as can be seen at point A in Figure 2.3.2 a).

In the padded case, the addition of a pad leaves only 0.1m of space between the point mass and the pad. This space is quickly filled due to the crushing door, thereby advancing the moment of contact to point B as illustrated in Figure 2.3.2 b). The door has a higher velocity at point B than at point A for the baseline case, and is accelerating instead of decelerating. In this example the pad limits the acceleration of the point mass to 60g. This results in the point mass reaching the door velocity of ~7.4 m/s at point C. Despite the energy absorption, the pad allows more energy to be transferred to the point mass than in the baseline case, due to the reduced initial space between occupant and door. This point mass analogy is based on a specific door velocity-time history and its specific acceleration-deceleration shape.

The effect of the popular side airbag solution can also be included into the point mass analogy as illustrated in Figure 2.3.3. If an airbag can be designed to be blown up right from the beginning of the door intrusion, the occupant could be accelerated with 15 g depending on the airbag's stiffness, which is an important parameter that needs to be determined.

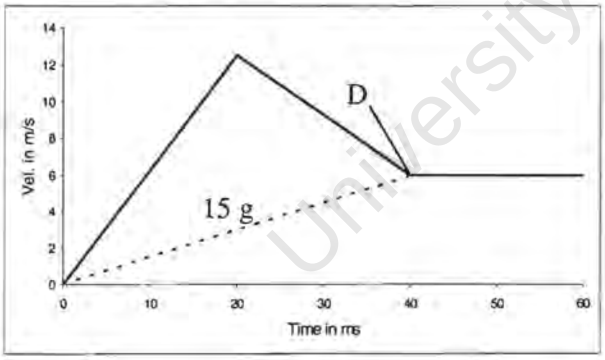

Figure 2.3.3 Point mass analogy for side airbag solution

This low average acceleration would lead the occupant to be accelerated to point D at which the door is reached at the slowest point and therefore a minimum of energy is transformed. It is important to mention that this analytical model considers average velocities only and not peak values as the common injury criteria.

2.3.2 Lumped mass model

The simplest type of numerical model is the one-dimensional lumped mass model. The phrase "one dimensional" implies that the motion is confined to a single direction and that rotation is not considered, which in turn reduces the complexity of the motion. Typically, such a whole body model would have five lumped masses representing the main body parts, which are the pelvis, abdomen, thorax, shoulder and head. These lumped masses are connected by spring-damper systems that define the deformation characteristics of the model. When it is feasible, the spring-damper characteristics are obtained by experimental quasi-static testing, otherwise a "guess first – validate later" method is used. After supplying a set of initial conditions, the system of equations is solved by numerical methods, thereby obtaining values for the displacement, velocity and acceleration of the lumped mass. Force-time histories can also be obtained, as well as the dissipated and kinetic energy of the system.

Viano [Via87a] presented a modified one-dimensional lumped mass model for side impact investigations that was initially developed by Lobdell [Lob73] for frontal impact simulations of the thorax. Chen et al. [Che88] presented a similar one-dimensional lumped mass model of the thorax, which was used to investigate the influence of padding material in a lateral thorax impactor test. This model is also based on the Lobdell model. Figure 2.3.4 a) shows Chen's model, where M1 is the mass of the impactor, M2 is the effective interior mass which includes the arms, and M3 is "the remaining mass". K12 is the stiffness of the skin and the muscle between the impactor and the ribcage, and K23 is the stiffness of the ribcage. C23 includes all inner-thoracic damping. The results of impact simulations that were obtained with this model have shown that the response of the model, subjected to an impactor load, showed decreasing thorax deflection and acceleration with increasing padding thickness.

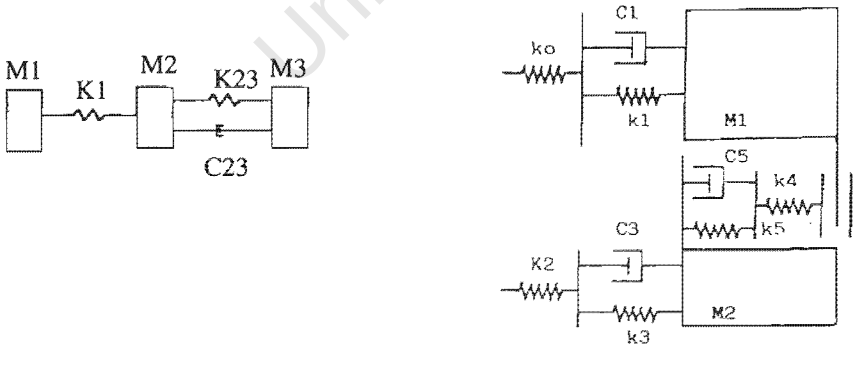

a) Chen's thorax model *b) Mack's Thorax-Pelvis model*

Figure 2.3.4 One-dimensional models of Thorax and Thorax + Pelvis

A similar approach was chosen by Mack et al. [Mac89], who added a pelvis model to the thorax model shown in Figure 2.3.4 b). This model was validated against thoracic and pelvic impactor tests and showed a satisfactory agreement when comparing thoracic force-deflection curves, deflection and compression-time histories and the thoracic viscous criterion. The difficulties involved in determining the moving masses of the thorax limits the capabilities of this model, since the rib acceleration cannot be obtained. The peak rib acceleration is part of the TTI, and therefore it would be important that this value can be calculated when using such a model.

Several lumped mass models have been developed to model the kinematics of the human head subjected to frontal and lateral acceleration. Examples were presented by Bowman et al. [Bow84], Bosio et al. [Bos86] and Wismans [Wis86]. These models basically consist of two masses, which represent the mass of the spine and of the head, and are connected by spherical joints with defined rotational spring characteristics. In more complex models, the spinal vertebrae were represented by lumped masses interconnected by spring-damper systems that represented the properties of intervertebral discs, facet joints, muscles and ligaments. Examples of such models used for lateral loading were presented by Merill et al. [Mer84], Tien et al. [Tie87] and Deng et al. [Den87]. These models were validated and compared against experimental volunteer sled test data, as described in section 2.1.2. Simulation results generally compared fairly well with the experimental results.

King et al. [Kin91] presented a one-dimensional lumped mass model of the entire human body consisting of 5 rigid masses connected by a system of spring-damper elements and is shown in Figure 2.3.5. This model was aimed to simulate the Wayne State University cadaver sled tests and to investigate the influence of padding materials in sled tests and in door intrusion simulations.

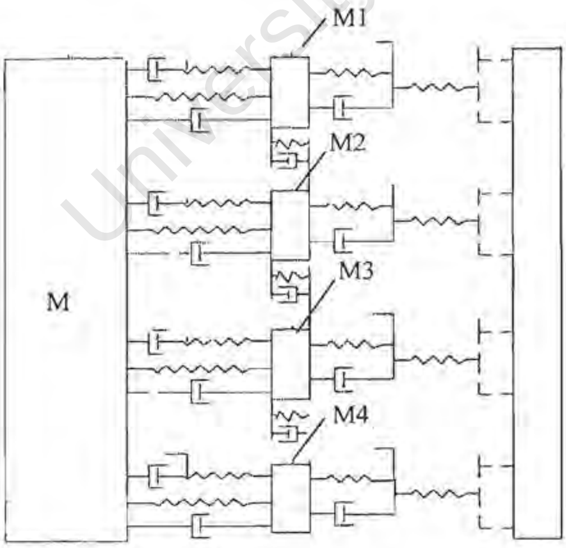

Figure 2.3.5 King's model of the entire body

This model contains four smaller masses representing the shoulder (M1), the rib cage (M2), the abdominal casing (M3) and the lateral aspect of the pelvis (M4). A three-element spring-damper combination was used to simulate the soft tissue covering for these masses, which in turn are also connected to the main torso mass by springs and dashpots. The validation results in the form of force-time histories at different body levels and thorax compressions showed good agreement with the experimental counterparts for rigid and padded wall tests. This model was then used to examine the influence of padding material and therefore the loss of airspace between the occupant and the intruding door. The velocity-time history of the entire door, relative to the occupant, was computed from car-to-car test data, and then integrated and used as input for the model. The simulation results showed that padding material that takes up all the free space between the side door and the occupant, needs to be extremely soft before it can be effective in reducing thoracic force and deformation. Baudrit et al. [Bau96] extended King's model to simulate Viano's cadaver pendulum impact tests [Via89a, Via89b] and Heidelberg-type sled tests, in order to compare deflection and viscous criterion. Since the Viano pendulum test does not include the arms, King's model configuration was modified accordingly.

The main advantage of one-dimensional lumped mass models is the structural simplicity, which leads to short modelling and processing times and therefore low costs. King's model demonstrated the ability to examine the influence of padding material and the loss of air-space in combination with door velocity profiles obtained from car-to-car crash data. The results of this model support the results of the analytical model by Lau [Lau91]. However, the one-dimensional model concept has its limitations, because it cannot reproduce complex 3-dimensional motion, nor can it examine local effects accurately. Rather than to introduce further complications to the basic model, it may be better to use a more sophisticated multi-dimensional model.

2.3.3 Multi-dimensional rigid body model

Multi-dimensional rigid body models use the equations of rigid body motion to simulate the dynamics of an occupant under impact. The main body parts are generally modelled by sub-systems with defined mass and inertial properties. These sub-systems are connected by joints, having defined properties, to build up a two- or three-dimensional system of rigid bodies. The system of equations is solved numerically with a fixed or variable time step. Initial conditions, for example velocity or acceleration, define the impact situation. The geometry of a vehicle occupant (dummy or human body) can be modelled in a simplified form by using planes and ellipsoids. By defining stiffness properties of the surfaces and ellipsoids, the contact behaviour is described when different rigid body systems interact. An interaction algorithm calculates the direction of the penetration force that influences the motion of both interacting rigid bodies.

Mack et al. [Mac89] presented a two-dimensional model of the human body for side impact simulations using the rigid body system Prakimod. The geometry, mass and inertial data was obtained from scanned images of a 50th percentile human.

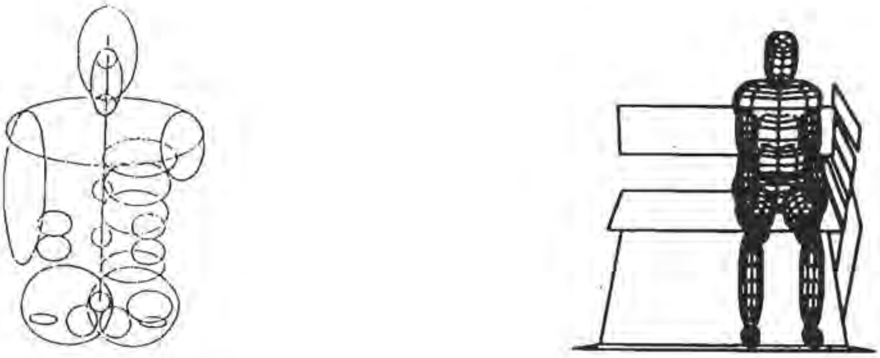

a) 2-D Mack model *b) 3-D Huang model*

Figure 2.3.6 Multi-dimensional rigid body model

As shown in Figure 2.3.6, contact ellipses were defined for the shoulder, arm, hard upper, middle and lower thorax, soft thorax, upper and lower abdomen, pelvis, iliac wing and ischium. The model was validated with Viano's pendulum impact data [Via98a, Via98b] for the thorax, abdomen and pelvis. In terms of deflection and Viscous Criterion, the model showed satisfactory agreement with the experimental data, while the predicted impactor-force response differed more from the experimental results. This model was further used to simulate the dynamics of an occupant in a vehicle side impact. The transverse acceleration and car door deformation obtained from structural simulations were used as input data to the model. The deformation levels of the thorax, abdomen and pelvis seemed to be too high in this simulation.

Among the different software packages that are based on rigid body dynamics, the MADYMO package developed by TNO is widely known. Several MADYMO-models of occupants have been developed and validated with experiments using side impact dummies. Huang et al. [Hua94b] used the MADYMO system to develop and validate a model of the human body for side impact investigations. This model is shown in Figure 2.3.6 b). The inertial properties used for each of the 18 body segments were based on a 50th percentile male with a body mass of 75 kg. Human stiffness characteristics were defined and validated against cadaver experimental data for the four torso-segments; shoulder, thorax, abdomen and pelvis. In order to simulate the soft tissue covering the rib cage, a visco-elastic mini-model was inserted into each ellipsoid, consisting of two small masses and three pairs of spring-dampers and a bilinear spring in series with the entire subsystem. The model was validated against cadaver pendulum and sled tests with satisfactory agreement with the corresponding experimental force and deflection time histories. The simulated force-time history for the padded wall showed a better agreement than the rigid wall simulation. In parametric studies the model was additionally used to investigate the influence of different door intrusion impulses, the effect of air space and padding material, and the effect of shoulder engagement. One of the major findings was the realisation that padding, which takes up all the free air space between door and occupant, needs to be very soft before it can be effective in reducing thoracic force and deformation levels.

De Jager et al. [dJa96] presented the development of a head-neck model based on the rigid body model using the program system MADYMO. Among other material properties an active muscle behaviour was included. This model is shown in Figure 2.3.7.

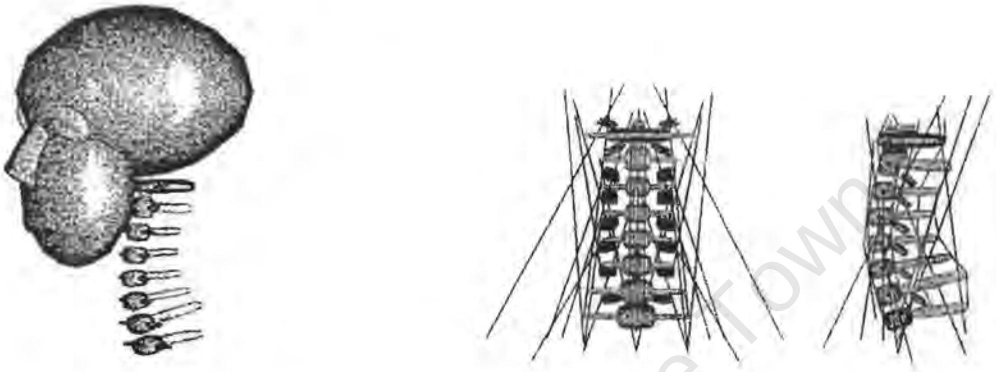

a) de Jager model b) Spring-damper neck muscles

Figure 2.3.7 Madymo-model of the human neck [dJa96]

An improved version of de Jager's model was presented by Horst et al. [vdH97] and may be considered as one of the most advanced models created within the MADYMO system. The properties of the connecting spring-damper elements are either derived from experimental force-deflection curves, or by validation of the entire model against experimental results. The important influence of muscle activity for volunteer response simulations was confirmed by very similar rigid body head-neck models by Astori et al. [Ast98] and Hayamizu et al. [Hay99].

The rigid body modelling technique has important advantages over the one-dimensional modelling approach, because three-dimensional dynamics are simulated. The three-dimensional movement of for example the head, arm and legs cannot be simulated with a one-dimensional model. Rigid body systems do not require as much preparation and calculation time as finite element models might require. On the other hand, such a model cannot be used to examine geometry changes, e.g. the deformation of the door at different levels, or the damage within the human body, because the geometry is only represented by the contact planes and ellipsoids. The contact interaction between rigid bodies is defined by stiffness and damping functions, which make general assumptions about the material behaviour and the geometry of the structure. Therefore material effects can only be considered indirectly and stress analyses cannot be conducted in rigid body systems.

2.3.4. Finite element models

Finite element programs have been used for some time to examine impact problems in many research fields. In order to study impact effects thoroughly, a model is required which includes dynamic capabilities, which can add inertial forces to internal stresses in the structure, which can provide more complex material properties, and which is able to describe the geometry by allowing for large deformation and self-contact of surfaces. Given the requirement of having an adequate number of elements, FE-models describe complex geometries accurately. Such models are, however, expensive in preparation and computational time. Since only a few FE-models of the human body have been published which were specifically designed for side impact investigations, the following FE-models that have been developed for other impact situations are also reviewed.

Finite Element thorax models

Plank et al. [Pla89, Pla94] presented the development of a FE-model of the thorax of a 50th percentile male depicted in Figure 2.3.8. This model was used for frontal impact simulations and is represented by a segmented spinal column consisting of twelve thoracic and five lumbar vertebrae, as well as the associated intervertebral disks, twelve ribs, back, abdominal and intercostal muscles, homogeneous viscera and concentrated masses representing head, arms and lower torso. The model uses symmetry in the mid-sagittal plane for frontal impacts to reduce the required number of elements. The mesh consists of 23248 nodes and 20758 8-node solid elements and is fine enough not to get distorted under impact situations. Head, neck, arms and lower body masses are represented by high-density parts attached to the 12-rib basic thorax model.

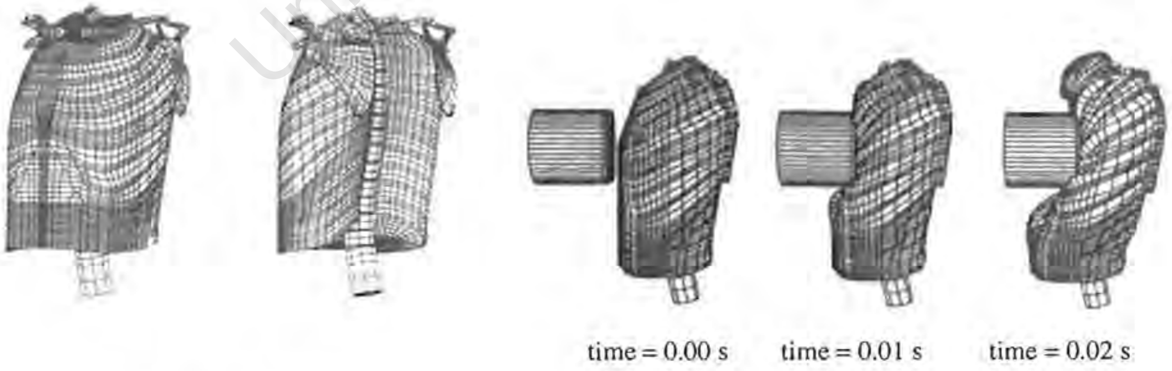

a) Thorax FE-model

b) Frontal impactor simulation

Figure 2.3.8 FE-model of the thorax for frontal impact investigation [Pla89]

The properties (elastic modulus, bulk modulus and Poisson's ratio) of these high-density elements is chosen to match that of the adjacent elements in order to avoid large mismatches in material characteristics. The bone, cartilage and ligaments have been represented by linear elastic materials, while the interior thoracic volume and some of the muscle elements have been represented by visco-elastic properties. This model proved that it is feasible to simulate the interaction with a rigid impactor as shown in Figure 2.3.8 b). Additional to the force and deflection responses, the FE-model provides information about the stress distribution of within the thorax over the entire simulation period. This capability of FE-models is one of the most important advantages compared to any other simulation technique. A stress analysis of a rib cage under impact is experimentally difficult to measure.

Finite element pelvis models

Renaudin et al. [Ren93] presented a three-dimensional finite element model of the pelvis designed for side impact simulations. Most design requirements were derived from fracture patterns of the pelvis observed in accident investigations. Figure 2.3.9 a) illustrates the symbolic pelvis model, including the deformable bony FE-pelvis, which in turn is shown in Figure 2.3.9 b).

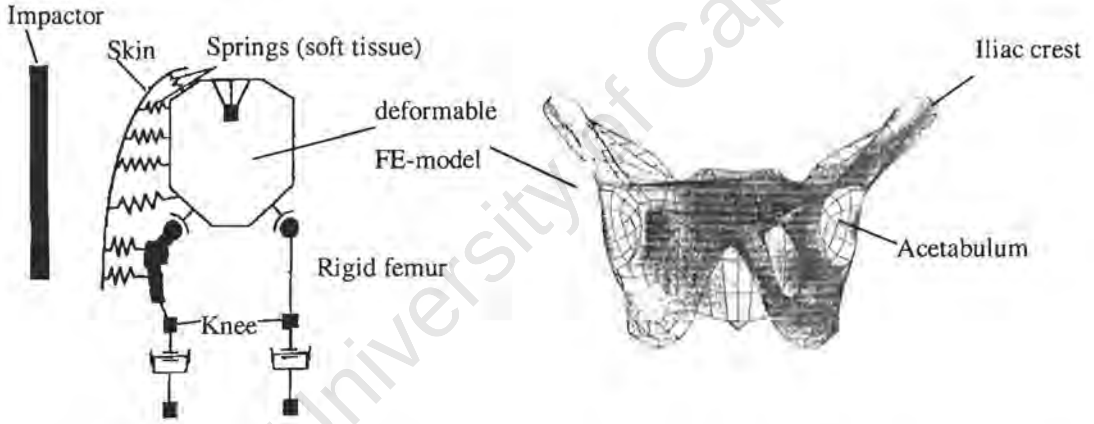

a) Symbolic model of the FE-Pelvis *b) FE-model of the bony pelvis using shell elements*

Figure 2.3.9 FE-model of the pelvis [Ren93]

The pelvis may be loaded either directly on the iliac crest or indirectly through the greater trochanter and femoral head by the acetabulum. Regarding these lateral collisions, impact energy is transformed into kinetic energy of the whole pelvis and into deformation energy of the soft tissue structure. Therefore the design requirements for the model were to reproduce the global inertia of the segment, as well as to reproduce the stiffness of the most mechanically resistive component, namely the bones. The size of the model was based on a 50th percentile male. Fat and muscles were represented using springs that connect the skin to the bone structure. Rigid bodies were used to represent the inertia of the legs. The upper segments of the body (torso, neck, head and arms) were not included in the model. The bony pelvis is modelled by 4-noded shell elements that only represent the cortical bone.

Furthermore, the pubic symphysis and the sacro-iliac joints have no relative movement, therefore the pelvic bone was represented as a continuous structure. Shell elements outline the pelvis shape of the skin, which defines a contact area. A global approach was chosen to represent all muscles and ligaments of the hip joint. At each hip joint, two springs were used with non-linear stiffnesses for the three rotational degrees of freedom. The rigid bodies representing mass and inertial properties for abdomen and torso were tied together to the upper sacrum by a 3D spring joint. The complete model, including pelvis, soft tissues, skin and legs, has 1816 shell elements, 144 springs and 9 rigid bodies.

Plummer et al. [Plu96] presented a side impact study on an isolated hemi-pelvis using the finite element method, as shown in Figure 2.3.10.

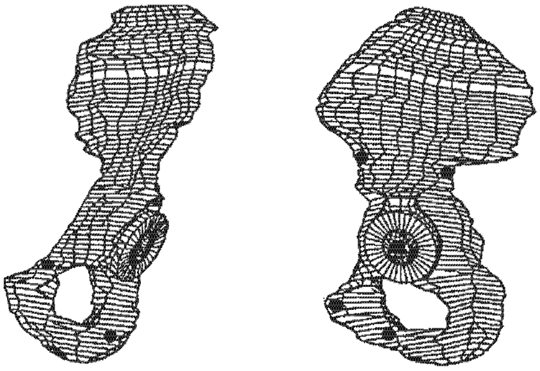

Figure 2.3.10 FE-model of the bony pelvis using solid elements [Plu96]

In contrast to Renaudin's model, solid elements were used for the cortical and trabecular bone. Depending on the density of the different sections, 524 Hookean-based material properties were chosen, but no visco-elasticity considered. Failure criteria were defined differently for tension and compression of cortical and trabecular bone. The model consisted of 2199 elements and 3161 nodes and was loaded by applying a uniform pressure across the surface of the femoral head elements. It was concluded from the parametric study that the loading rate influences pelvis fracture prediction.

Besnault et al [Bes98] presented a study that described the development of a refined parametric FE-model of the human pelvis. The geometrical data was obtained from statistical studies to develop a parameterised model of a 5th, 50th and 95th percentile human pelvis. An interpolation technique was used to distort a reference mesh and adapt its geometry to different sizes. The mechanical validation of the model was carried out by comparing numerical and experimental results. The pelvis was modelled by shell elements that represent the cortical bone with a thickness ranging from 0.45 to 1.8 mm. An elastic-plastic isotropic material behaviour was assumed, including a maximum stress damage criterion. The predicted results of a drop test simulation showed that the maximum displacement values exhibit quite large differences, namely 15% between the 5th and 95th percentile pelvis. The maximum force difference is 6 %. This gives a quantitative assessment of the influence of the geometry alone on the behaviour of the pelvis. The main aim of this study was to simulate the experimentally investigated injury mechanisms of different pelvises under lateral impacts. Although the simulated results did not appear to be satisfactory for some of the tested pelvises, this study demonstrated the important factors in biomechanical modelling, such as the bandwidth of the experimental test results and the influence of the variety of material and geometrical properties.

Finite element head-neck models

Williams and Belytschko [Wil83] presented a model of the head-neck complex using a hybrid technique that modelled the head, neck and spine by using a combination of rigid bodies and deformable elements. The model concept is shown in Figure 2.3.11.

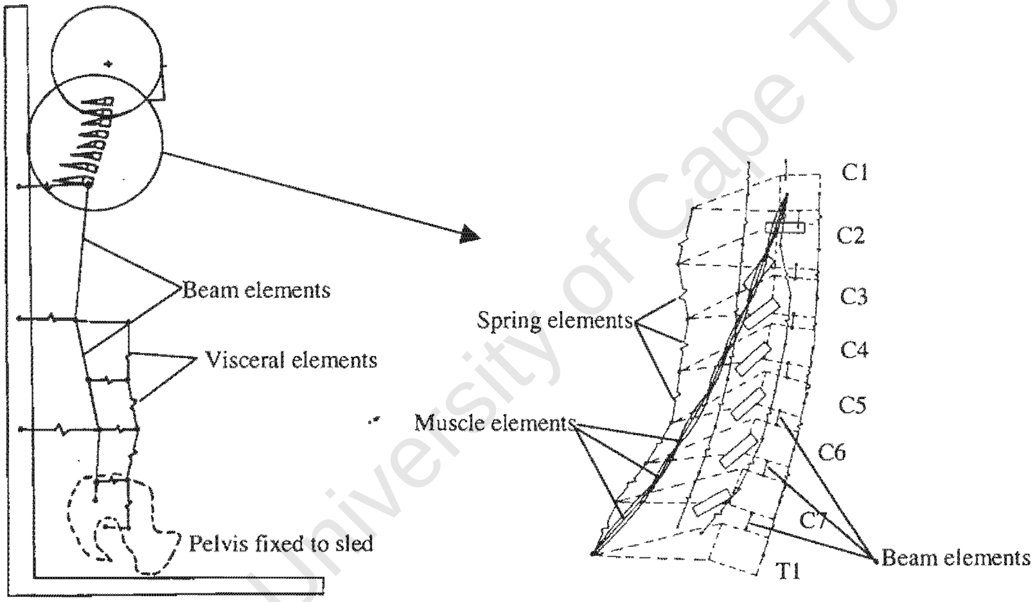

a) Hybrid model of the human body *b) FE-model of the human neck*

Figure 2.3.11 Rigid body – FE-Hybrid Model of the human head and neck [Wil83]

The model was built to simulate the dynamic response of the human head subjected to low g-level frontal and lateral acceleration. The vertebrae T1 through C1 were modelled using rigid bodies interconnected with deformable beam elements and several spring elements. The beam elements represented the intervertebral discs and had torsional and bending stiffness. The joint between articular facets was modelled by solid elements. The model's response in the form of head acceleration, velocity and deformation showed a fairly good agreement with the corresponding experimental results.

Kleinberger [Kle93] presented a finite element model of the cervical spine and head. Although no simulation results were shown for lateral loading directions, it is worthwhile to mention this model here, as it was one of the first complex finite element models of the human head-neck system. The model shown in Figure 2.3.12 includes a rigid head, vertebrae, intervertebral discs and all relevant ligaments.

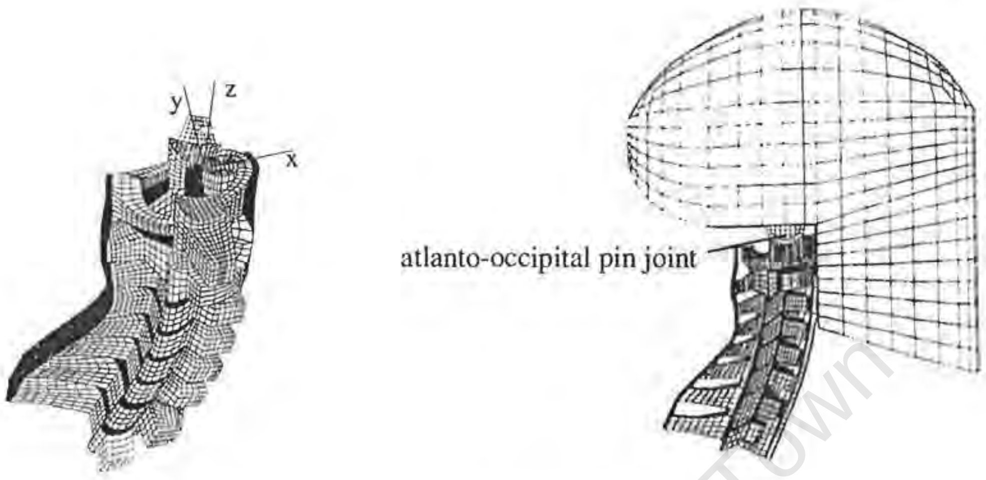

a) FE-model of the human neck *b) Side view of Kleinberger FE-model*

Figure 2.3.12 Kleinberger-FE-model of the human Neck [Kle93]

The atlanto-occipital articulation is represented by a simplified pin joint, which allows rotation about the y-axis and also maintains atlas-skull contact in both compression and tension. This configuration probably limits the lateral flexion, so that it might need to be modified for side impact simulations. At the first stage of the model development, the skull and all vertebrae were treated as rigid bodies to save computational time. All material properties were defined as being linear-elastic. A simulated frontal flexion response of the model showed fairly good agreement with the corresponding experimental result. Proposed enhancements included substituting the solid elements for the ligament with shells, improving the atlanto-occipital region of the model, and using more complex material models that show a visco-elastic behaviour.

Dauvilliers et al. [Dau94] presented a finite element model of the head-neck complex that was validated with experimental volunteer sled test data in frontal and lateral direction. This model, shown in Figure 2.3.13, was intended to be used as part of a model of the entire human body for vehicle occupant impact situations. In order to achieve a short computational time, the number of elements was limited. The vertebrae and the head were defined as rigid bodies, because their deformation was considered as negligible compared with the deformation of the neck tissue. The intervertebral discs were modelled with 8 solid elements with linear elastic material properties. Additionally, 32 crossed spring-dampers placed on the circumference of the disc simulated the action and slants of the disc fibres. The most important spinal ligaments were also represented by spring-damper elements. The link between the first and second vertebra and the head was simply modelled with two spherical joints.

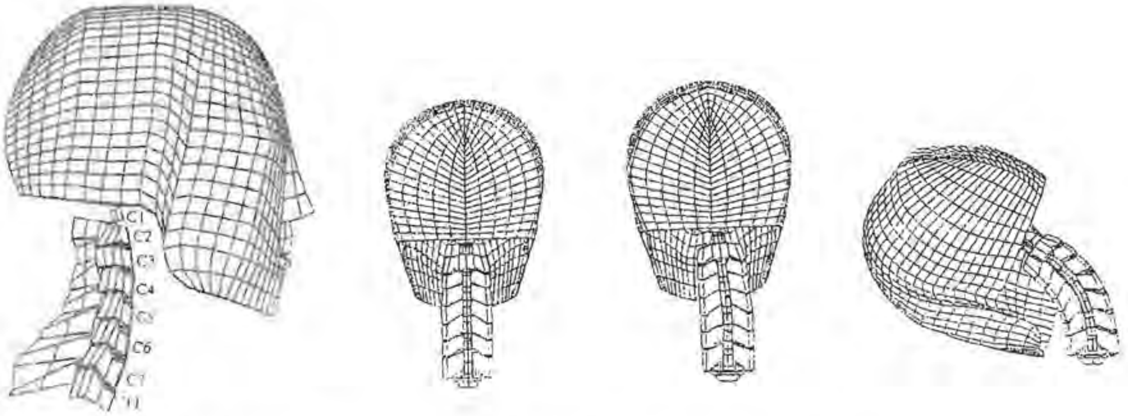

a) Side view of the FE-model *b) Response to lateral loading*

Figure 2.3.13 Dauvillier-FE-model of the human head and neck[Dau94]

The entire model included 150 solid-, 104 shell-, 412 spring-damper elements and 2 spherical joints. The simulated model response, shown in Figure 2.3.13 b), showed good agreement with the corresponding volunteer sled test data. The acceleration pulse of the 12th thoracic vertebra obtained from these volunteer tests at low g-levels was used as the input pulse for the head-neck model. The responses in the form of translational and rotational acceleration, velocity and displacement agreed well with the corresponding experimental results.

An extremely detailed head-neck model was presented by Yang et al [Yan98], including all bony structures, articular surfaces, relevant ligaments and intervertebral discs. This model is shown in Figure 2.3.14. The model was validated in a global sense against data obtained from drop and rear-end impact tests, and was applied to the study of neck loads while impacting an airbag.

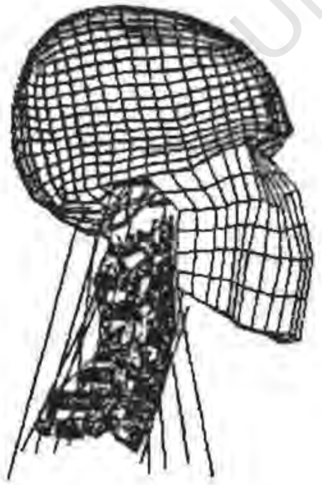

Figure 2.3.14 Yang-FE-model of the human head and neck [Yan98]

The head model has a layer of scalp, an outer layer of cortical bone, a layer of spongy bone and an inner layer of cortical bone, all encasing the brain. The head model has a total of 7351 elements, while the neck model consists of 11498 solids, 3071 shell/membrane elements and 108 spring/bar elements. All seven cervical vertebrae and the first thoracic vertebra are represented by solid elements. In addition, the nucleus pulposus and annulus fibrosus of each intervertebral disc are also represented by solid elements. All relevant ligaments are modelled by tension-only membranes and bar elements. Sixty tension-only spring elements are used to represent passive muscles. Contact interfaces are defined so that free sliding motion is allowed between the bony surfaces of the atlanto-occipital joint, the dens and C1, and all articular facet joints. The validation process of such an advanced model is limited by the computational time needed, however this problem will be overcome by future hardware developments.

Finite element models of the entire human body

Huang et al. [Hua94] presented a FE model of the entire human body that was designed to simulate the gross motion of cadavers in side impact sled tests. To keep computational time low, the model consists of a relative coarse mesh with 9308 8-node solid elements, 2384 shell elements and 514 dashpot elements. Since most cadaver data is scaled to that of a 50th percentile male with a body mass of 75 kg, the model's mass and size was chosen accordingly. The model and its sub-systems are shown in Figure 2.3.15.

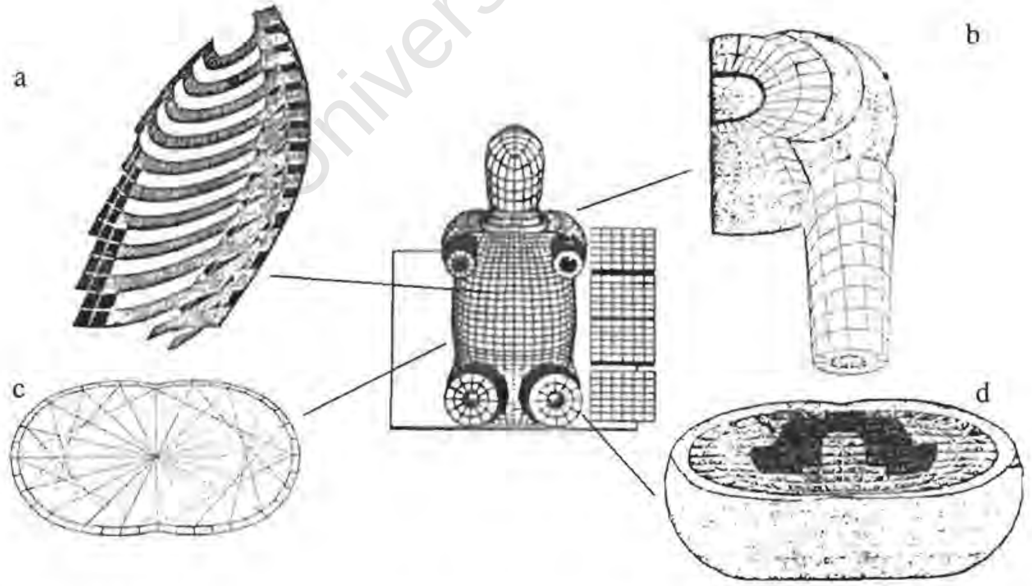

Figure 2.3.15 FE-model of the entire human body [Hua94]

The rib cage, shown in Figure 2.3.15 a), consists of 12 ribs modelled with 20 shell elements per rib. The vertebral column serves as a support for the rib cage and undergoes much less strain than the ribs and internal organs. Therefore every vertebra and intervertebral disc was modelled with only 8 elements. The rib cage was filled with a visceral content and modelled with 8-node solid elements composed of a soft viscous isotropic and homogeneous material to represent the internal organs. An array of discrete damper elements, illustrated in Figure 2.3.15 c), strategically placed within the rib cage, simulates the visco-elastic behaviour of the internal contents. The muscles and ligaments were simply modelled by a single layer of membrane elements, whereas solid elements were used for the skin model. In the interests of simplicity, the shoulder was represented by a group of isotropic elastic elements as shown in Figure 2.3.15 b). The skin and muscles of the arm were modelled by a layer of solid elements, and the long bone was simulated by shell elements which were assumed to be rigid. The shoulder joint was defined as a spherical joint, and a contact surface was used between the arm and the torso to prevent the arm from penetrating the torso. The pelvis depicted in Figure 2.3.15 d) is simply modelled by a stiff part to represent the lumbar spine and pelvic ring and a soft part to represent the muscles. The thigh is modelled in a similar manner to the arm, with rigid elements for the long bone and solid elements for the skin and muscles. A spherical joint simulates the hip joint. The head and neck are modelled by a coarse mesh, as the head/neck responses are not considered in this model. In order to preserve a proper global motion, the head is modelled by shell elements and defined as a rigid body. The neck is represented by solid elements and has nodal connectivity to the shoulder. The head and neck are connected by a rigid link. The response of this model was compared to experimental cadaver pendulum and sled tests and showed good agreement with the exception of the shoulder force. The main problem was that the shoulder was simply compressed, and there was no inward rotation as observed in the experiments. Although the model results of the padded sled test simulations do not always follow the test data precisely, the model is still acceptable considering the difficulty of modelling a very soft paper honeycomb padding material.

Another advanced model of the human body for the use of vehicle impact situations has been developed by LAB (Laboratoire d'Accidentologie et de Biomecanique) in partnership with CEESAR and ENSAM over several years and was presented by Lizee et al. [Liz98]. The geometry of the model, shown in Figure 2.3.16 is based on a 50th percentile male adult. The number of elements used to represent the anatomy is limited to 10 000, as the model was intended to fit into vehicle models without penalising their time steps. The model presented by Dauvilliers [Dau94] that was described earlier is used for the neck. A similar modelling technique continued for the model of the thoracic and lumbar spine. The geometry of each vertebra is reduced to that of its vertebral body, which is assumed to be rigid. The joint between two vertebrae is represented only by a stiff intervertebral disk modelled by 4 brick elements. The soft tissues filling the rib cage, the abdomen and the pelvic cavity are represented by a uniform mesh of brick elements. In order to take into account the different stiffness of the internal organs, this volume was divided into three parts as can be seen in Figure 2.3.16 b).

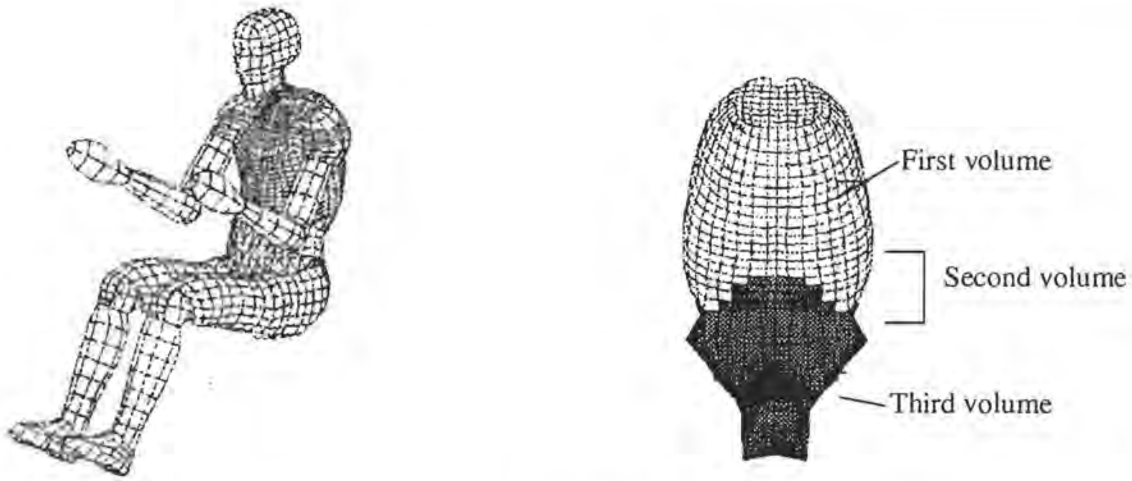

a) Lizee FE-model *b) internal thoracic and abdominal organs*

Figure 2.3.16 Lizee FE-model of the entire human body

The first one is roughly constituted by the lungs and the heart, the second one by the spleen and the stomach and the third one by the abdominal organs. The muscles and the adipose tissue, which covers the rib cage and the abdominal organs, are represented by a layer of brick elements. Several layers of brick elements were also used for the shoulder and the pelvic muscles because of their complex geometry. The bony parts of the shoulder and pelvis are shown in Figure 2.3.17 together with the entire skeletal model.

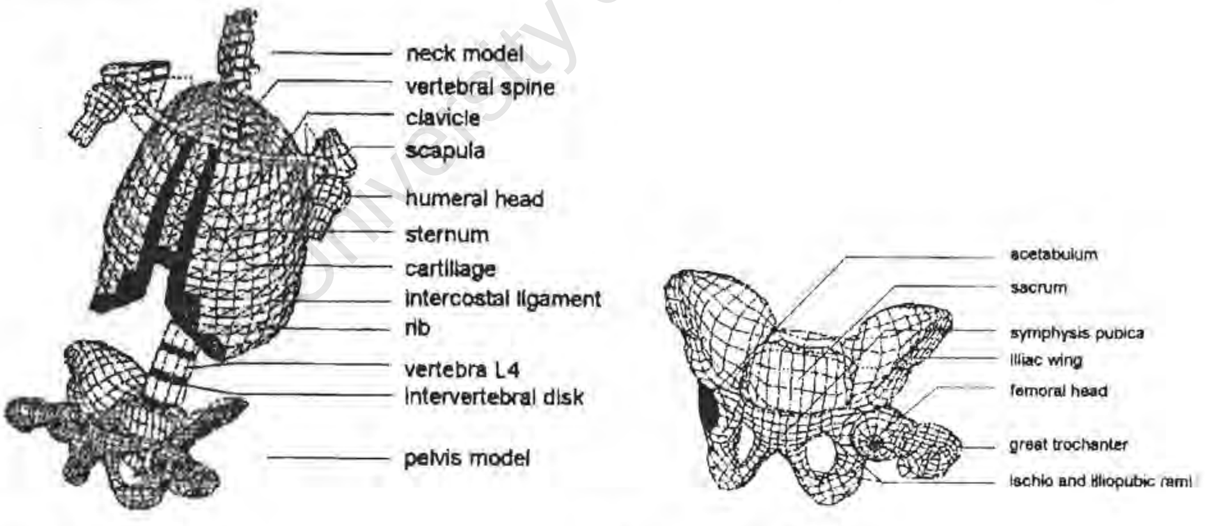

a) Skeletal FE-model *b) Pelvis FE-model*

Figure 2.3.17 Skeletal part of Lizee FE-Model

The shoulder complex consists of the clavicle, the head of the humerus and the scapula. A square-sectioned deformable cylinder, described by quadrangular shells, represents the clavicle. The two extremities of this cylinder, the head of humerus and the scapula, are assumed to be rigid. Three couples of 3-D springs model the joints between the sternum, the clavicle and the humerus. The rib cage is made up of ribs, intercostal ligaments, sternum and costal cartilage represented by shell elements. The first generation of the global model of the pelvis was presented by Renaudin [Ren93], as described earlier. The pelvic joints were taken into account and were considered to be practically rigid. The complete surface of the pelvic bone was meshed using shell elements representing the cortical bone, and using seven thickness to describe the various parts of these bones. The femoral head and the acetabulum are represented by rigid bodies, their surfaces meshed using shell elements. The hip joints are represented globally by 3-D springs and contact interfaces are defined between the acetabulum and the femoral head. The skin of the thorax, the shoulder, the abdomen and the pelvis is meshed with quadrangular and triangular membrane elements directly covering the muscle bricks. The head, upper and lower extremities are modelled as articulated rigid bodies with defined force-displacement formulation for contact interfaces if necessary. The total number of nodes of the entire model is 8490 and the number of elements is as follows: 225 springs, 1308 triangular shells or membranes, 5000 rectangular shells or membranes and 3638 bricks. The CPU time on a Cray J-90 for a 150 ms calculation is 20 hours, which is still reasonable. The model was validated with cadaver impactor and sled tests, which proved the high level of biofidelity of this FE-model of the human body.

The FE-model presented by Lizee et al. [Liz98] has shown that an essential requirement for future FE-models to be used for side impact research, is a complex geometry of the entire human body. In contrast to FE-models of body parts, only whole body FE-models are able to simulate the complexity of the interactions between the numerous body parts within lateral impact. A FE-model of a higher level of refinement than the existing models is needed to analyse injury mechanisms and tolerance limits in the future.

3. Development of the Finite Element Model of the Human Body

In this chapter the development of the FE-model of the human body, shown in Figure 3.1, is described, parts of which have been published in [Jos99, Jos00a, Jos00b]. The first section provides information about the material properties of biological tissue that are used in the model. These mechanical properties cannot be considered separately from the modelling techniques used to build this model. The following sections cover the development of the FE-model of the different body regions. The first region to be described is the back, including the spinal column and the different muscle groups of the back. Thereafter the FE-model of the thorax is depicted, including the rib cage and the visceral contents that represents the internal organs of the thorax. The abdominal and pelvic region are subsequently described including the abdominal visceral contents, the abdominal and pelvic muscles as well as the skeletal parts of the pelvis and the lumbar spinal column. Subsequently the FE-model of the head-neck complex including the cervical spine is described together with the different muscles and ligaments of the neck. The body parts of the upper limb are described including the skeletal parts of shoulder and arm, as well as the different muscle groups of these regions. The development of the FE-model of the lower limb completes this chapter.

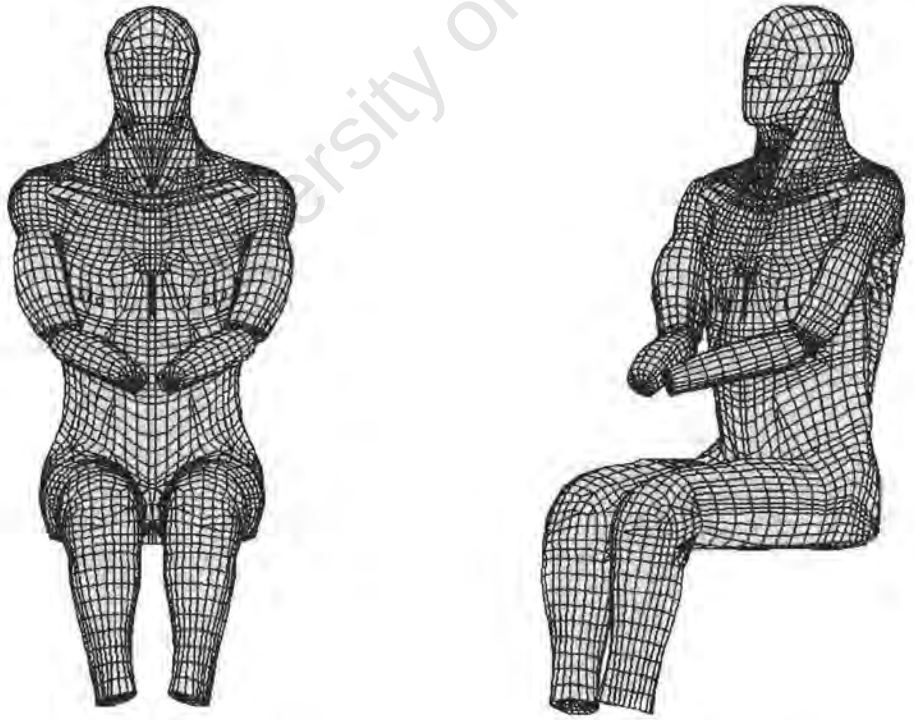

a) Front view *b) Oblique front view*

Figure 3.1 ABAQUS FE-model of the human body

3.1 Material Properties and Modelling Techniques

The model of the human body described herein is intended to be used for vehicle side impact simulations. It is therefore not considered necessary to include the micro-structure of the human body for example blood vessels, nerves, etc. A model that comprises such a high level of sophistication cannot be built at this stage, as it would exceed present computational resources and preparation time. Furthermore, it is questionable whether it is in fact possible to create a valid micro-structure model due to the large number of variables and the uncertainties of the material properties of the material properties under impact conditions. The aim of the model described herein is to simulate the impact behaviour of the human body on a "macroscopic" level using a geometrically very advanced model. The biomechanical responses of this model are to investigate in terms of forces, acceleration, deformation of body parts in more detail than it is possible to investigate experimentally but not on a microscopic level, as this would exceed existing computing resources.

Figure 3.1 shows the entire FE-model of the human body in a seated position. The geometry was obtained from atlas of human anatomy [Hal90] and the visible human project [Vispr], which is based on scanned anatomical data of a human body. The Patran based Finite Element preprocessor Abapre was used to generate the FE mesh, which was implemented into the FE-code ABAQUS Explicit.

3.1.1 Bones

The bones of the body perform a number of functions, of which the most obvious is to serve as rigid levers in the motion of the body. Bones also support the soft tissue of the body and give it a permanent shape. The bones of the skull, vertebral column and the thorax protect underlying organs that are vitally important. The assessment of the severity of an injury is strongly influenced by damage caused to the skeletal system of the body. The number of rib fractures, for example, is a value that can simply be counted and the number used for statistical injury analysis.

Bone is a hard, mineralised tissue consisting of a fibrous, organic matrix of collagen bound together by inorganic salts [Via86, Dum75]. The resulting network of interconnected fibres of collagen forms sheets or thin layers of bone called lamella. The plane of lamella winds around a central opening called the haversian canal, which is the main blood vessel of the tissue [Dum75]. The system of concentric lamella surrounding a canal which contains blood vessels and nerves is called the haversian system or osteon. The interconnected osteons of bone, aligned parallel to the long axis of a bone, form the basic components of cortical bone. Bone consists of two mechanically different sections; the external "hard" cortical shell and the internal "soft" cancellous bone. A sectional cut through a femur bone shows these two sections in Figure 3.1.1.

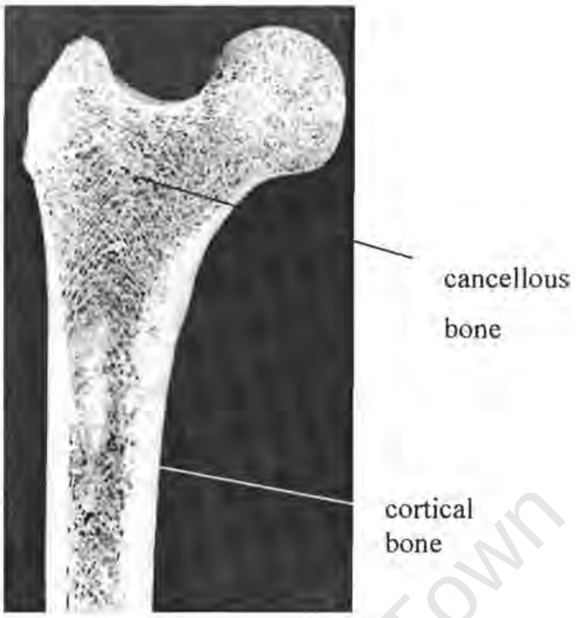

Figure 3.1.1 Cortical and cancellous bone of the femur [Hei62]

The classification of bone as cortical and cancellous bone is based on the porosity of the material. Cortical bone has a porosity of 5-30% whereas cancellous bone has a porosity in the range of 30-90%. The tensile strength of bone is mainly due to the collagen fibres which are held together tightly by mineral salts, preventing shear between adjacent fibres. These mineral salts also resist compression loads and determine the compression strength of bone material. The complex structure, which can be compared to a composite material, indicates a complex mechanical behaviour of bone material. However, the complex material properties can be approached in a simplified manner by the behaviour of an elastic or elastic-plastic material. Table 3.1.1 lists the mechanical properties of cortical bone, found in the literature that have been used either in previous FE-models or represent results of material testing. The material properties that were used in published biomechanical FE-models vary within a wide range from 1000 MPa up to 18900 MPa for the Young's modulus. The ultimate stress value varies from 15 MPa to 1400 MPa.

The last line of Table 3.1.1 depicts the range of bone material parameters used for the presented FE-model of the human body. The values of these parameters have been determined during the validation process described in detail in chapter 4 and Appendices C 2. While Table 3.1.1 shows the material parameter range used for the presented FE-model in comparison to the values found in literature, Table 3.8.1 (page 89) presents the specific values used for all bony parts of the body.

	Young's modulus (MPa)	**Yield stress** (MPa)	**Ultimate stress** (MPa)	**Poisson's ratio**	**Density** (g/cm^3)
[Bes98] Pelvis model cortical bone	1000	135 – 800	157 - 1000	0.3	12.2
[Bea97] Ankle model	15000 – 18900	linear elastic	-	0.29	2
[Tan96] Ankle model	19 000	linear elastic	-	0.3	1.8
[Yam70] Material testing	17265 – 18540	linear elastic	121 - 149	-	-
[Liz98] Pelvis / rib	9000 6100 - 11500	linear elastic		0.3	-
[Hua94a] Skeleton	9000	-	-	0.3	-
[Pla89] Rib cage	12000	-	-	-	4.788
[Ber93] Leg	17900	1200	1400	0.326	1.9
[Yan98] Head - neck	1500 - 4500	15	15	0.25 – 0.3	1.41
FE-model	**2500 - 12000**	**9 - 150**	**10 - 180**	**0.3**	**2.0 – 2.5**

Table 3.1.1: Material properties of cortical bone

The material properties of bones do not only depend on various factors that affect the condition of the bones, as for example the influence of the mineral contents, but also on the rate at which the material is deformed. Figure 3.1.2 a) shows the influence of the mineral content on the ultimate strength of cortical bone. This ultimate strength may differ between 75 MPa to 240 MPa, which makes up a fairly wide range.

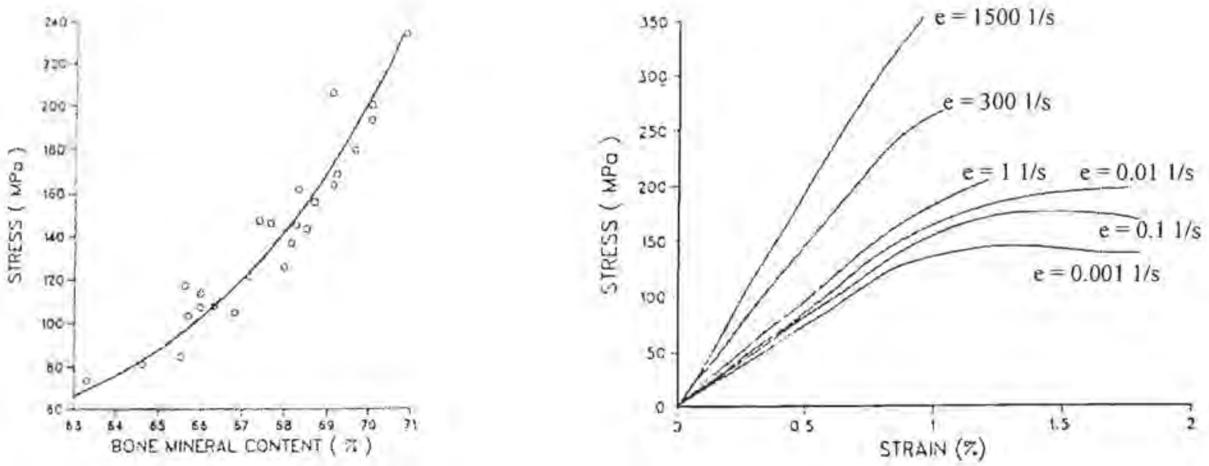

a) Influence of mineral content *b) Influence of strain rates*

Figure 3.1.2 Influencing parameters on the material properties of cortical bone [Via86]

Figure 3.1.2 b) shows the strain rate sensitivity of cortical bone, which also has a significant influence on the mechanical properties. The problematic nature of defining the appropriate material properties for cortical bone is shown by the wide range of experimental results of material tests found in the literature. A complex material model that considers the parameter influences, which are described above, is only superior to a simpler model if there is experimental data available to validate the material model. Furthermore the computational resources limit the complexity of the material model that can be used for such a complex FE-model of the human body. Another criterion for the material model is numerical stability, which is important especially for impact and contact simulations as they occur in the FE-model of the human body subjected to impact loading. The relatively simple elastic-plastic material behaviour, which is easy to define in the FE-code ABAQUS, is considered to fulfil the requirements for the material model. The Young's modulus and yield stress are the determining parameters of this material model and vary within a range in the FE-model as depicted in Table 3.1.1. The elastic-plastic material model does not consider material failure, because simulation tests using a maximum stress failure criterion in ABAQUS proved to be inapplicable, due to numerical instabilities with the existing mesh under severe impact conditions. Material failure may only be assumed indirectly if large strain values occur during the simulation.

Modelling of bones can be approached in at least two different ways. The first approach for a FE-model of human bone is the use of solid elements to represent the entire bone. The material properties of these solid elements must change, depending on whether cortical or cancellous bone is modelled. Even more accurate results could be obtained if a property function, depending on the density of the region modelled, was taken into account. Examples of solid element modelling techniques are limited to specific skeletal parts as, for example, pelvic bones [Plu96] or vertebrae [Kle93].

An approach that is less time intensive with regard to computation time, is the use of shell elements, which only represent the cortical shell of the bone. Such simplification is based on the assumption that the outer cortical shell contributes most to the stiffness of a bone [Ren93] because cortical bone is about 100 times stiffer than cancellous bone. This modelling technique has found multiple uses in the existing FE-models of human body parts [Ren93, Pla94, Bes98, Yan98, Liz98]

3.1.2 Joints

The bones of the body are joined together at articulations or joints. Joints vary considerably in both structure and function, but fundamentally provide for the stability and movement of the skeleton. The articulating bone surfaces and the type and arrangement of the connecting tissue determine the amount of movement of a joint. The anatomical designation "joint" does not always imply movement, as evidenced by, for example, the fibrous joints of the adult skull bones. The variations that exist in the form and function of the various joints of the body may be grouped into three different classifications, namely fibrous, cartilaginous and synovial joints.

In fibrous joints, bones are connected to each other by fibrous tissue, which allows for minimal movement. For reasons of simplification, the fibrous joints are not modelled but are considered to be a rigid connection between adjacent bones.

In cartilaginous joints, the bones are united by cartilage material, which allows for a limited range of movement. The joints between bodies of the vertebrae, and the joint between the two pubic bones (pelvis) are typical examples of cartilaginous joints. They are modelled by solid elements, which have the material properties of cartilage and are described in more detail below.

Synovial joints permit free movement around a limited axis. Therefore, the majority of the permanent joints of the limbs consist of synovial joints. The articular ends of the bones in a synovial joint are usually enlarged and covered by a thin lamina of articular cartilage. The bones are connected to each other by a tubular ligament called the articular capsule, which encloses the joint cavity. The outer layer of the articular capsule is formed of dense fibrous tissue and is called a fibrous capsule. This fibrous capsule provides an articular cavity containing a synovial fluid that is used for joint lubrication. Figure 3.1.3 shows the structure of a synovial joint in the human body alongside its FE-model counterpart. A detailed FE-model of a synovial joint including solid elements for the articular cartlige and for the synovial fluid would require too many elements. Such an advanced model could be used for stress analysis of the articular cartilage which in turn is not required for the presented FE-model. Therefore simplied modells are used that fulfill the dynamic functions of synovial joints, shown in Figure 3.1.3 b). While the first important function is to provide the same degrees of freedom of the joints, the second is to incorporate the damping effects of synovial joints.

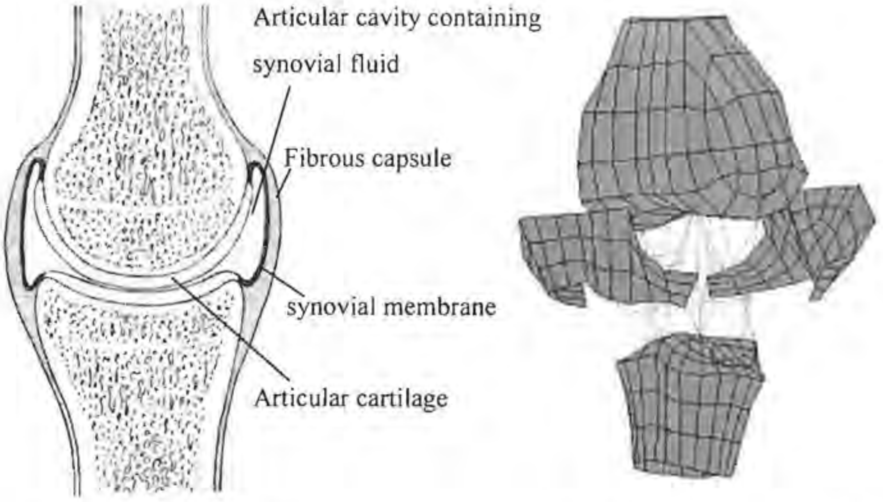

a) Synovial joint [Hei62] *b) FE-model of synovial joint*

Figure 3.1.3 Structure of synovial joints

These damping effects are caused by the visco-elastic behaviour of the articular cartilage, the synovial capsule, ligaments and the synovial fluid, shown in Figure 3.1.3 a). A system of spring-damper elements, shown in Figure 3.1.3 b), is used to consider these damping effects and to provide the required stiffness of the synovial joints. The estimated linear characteristics of these spring-damper elements used for the different synovial joints is listed in detail in Table 3.8.3.

The function of tendons and ligaments is primarily to resist tensile loading either due to muscular contraction or loads tending to displace the joint. The ligaments that hold together the synovial joint are modelled by tensile membrane elements using linear elastic material behaviour.

3.1.3 Cartilage

Cartilage material principally consists of a network of collagen fibres embedded in an amorphous intracellular substance. The second major component is proteoglycan gel, which includes long molecules of hyaluronic acid and forms large molecules that interact with collagen [Via86]. The interaction between collagen, proteoglycans and water is important to the function of the tissue. Proteoglycans retain water and endow cartilage with an internal swelling pressure that determines the rigidity and compliance of the cartilage material. An important factor that influences the mechanical properties under loading is the fluid flow through the collagen network, which dissipates energy and operates like a damper. This material behaviour can be described by visco-elastic properties. An approach to modelling cartilage material that is less intensive with regard to computation time is the use of solid elements, which have an elastic material behaviour, in combination with additional spring-damper elements as reported by Dauvilliers [Dau94]. This latter method has been adopted for the FE-model as schematically shown in Figure 3.1.4.

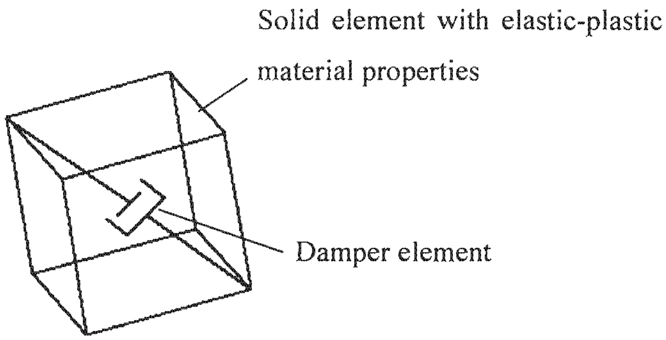

Figure 3.1.4 Solid elements with additional spring-damper system

The number and characteristics of the damper elements are estimated and adapted during the validation process. These cartilage material models are used for the intervertebral discs, pubis symphysis and for the costal cartilage of the ribs. The ranges of material properties of cartilage found in the literature and used for FE-models are listed in Table 3.1.2. Table 3.8.2 and Table 3.8.3 present the specific values used for all cartilage parts of the body.

	Young's modulus (MPa)	**Yield stress** (MPa)	**Ultimate stress** (MPa)	**Poisson's ratio**	**Density** (g/cm^3)	**Damper element** (Ns/mm)
[Via86]	7.1 – 12.0	(elastic)	(elastic)	0.42	-	
[Dau94] Intervertebral disc	200	(elastic)	(elastic)	0.29	1.1	
[Hua94a]		(elastic)	(elastic)			
Costal cartilage	3000			0.42	2.768	
Intervertebral disc	10.3			0.2	2.768	
[Pla94]		(elastic)	(elastic)			
Costal cartilage	20.68					
Intervertebral disc	10.3			0.2	2.768	
[Yam70]	3.82 – 24.5	-	-	-	-	
[Liz98] Intervertebral disc	10	(elastic)	(elastic)	-	-	
[Kle93] Intervertebral disc	3.4	(elastic)	(elastic)	0.49	-	
[Yan98] – Neck Intervertebral disc	98	visco-elastic		0.45	1.3	
FE-model						
Costal cartilage	**2500**	**10**	**13**	**0.3**	**2.5**	-
Intervertebral disc	**500 - 700**	**1.0 – 1.2**	**1.2 - 1.4**	**0.3**	**2.0**	**0.05**

Table 3.1.2: Material properties of cartilage

3.1.4 Tendons and Ligaments

Tendons and ligaments are soft connective tissues, which are formed from groups of collagen fibres, called fascicles, which in turn are enclosed in a tough connective tissue sheath. The alignment and arrangement of the fibres within the fascicles differs from one tissue in the body to the next, and there is a range of different mechanical responses for various tendons and ligaments, as shown in Table 3.1.3.

	Young's modulus (MPa)	**Yield stress** (MPa)	**Ultimate stress** (MPa)	**Poisson's ratio**	**Density** (g/cm^3)
[Yan98]	4.56 – 22.8			0.4	1.1
[Ber93]	15 - 35			0.3	1.0
[Kle93]	1.5 - 30			0.49	-
[Yog89]	1.5 - 30			-	-
FE-model	**1.5 - 10**	**0.2**	**0.4**	**0.3**	**1.0**

Table 3.1.3: Material properties of ligaments

Unlike cartilage, the function of tendons and ligaments is primarily to resist tensile loading either due to muscular contraction or loads tending to displace the joint. Therefore tensile membrane elements are well suited for ligament models using a linear elastic-plastic material behaviour. Table 3.8.3 (page 91) presents the specific values for all ligaments of the FE-model

3.1.5 Muscles

Almost all movements are produced by muscle systems, which consist of muscle fibres that are bundled together by connective tissue to produce a wide variety of shapes and sizes. Muscles are attached to the skeleton by tendons, and the points at which the tendons join the bone are known as the origin and insertion of a muscle. They contribute significantly to the body mass and define the shape of the body by covering the skeletal system. The outer surfaces of some muscles serve as contact surfaces and distribute the impact load. Although muscle activity plays a certain role in low g impact, as illustrated by e.g. Astori [Ast98] and van der Horst et al. [vdH97], the presented FE-model of the human body does not include active muscle elements, because it has been developed to simulate cadaver tests, in which muscle activity does not exist. Muscles are modelled in three different ways, of which the simplest is a system of spring-damper-elements placed between the origin and insertion of the muscle, as illustrated in Figure 3.1.5. These spring-damper-elements are not to be confused with the spring-damper systems that are defined within a synovial joint model.

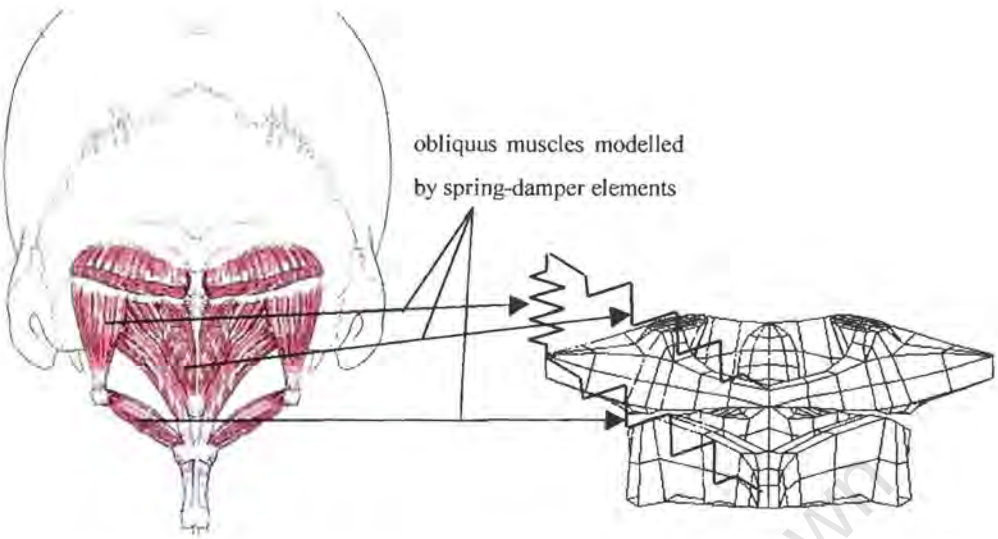

Figure 3.1.5 Spring-damper muscle model for short muscles [Hei62]

This method takes into account the force generated by the muscle but not its inertial properties. The material properties of this spring-damper system have been taken from the literature [dJa98].

A more advanced modelling method is the use of membrane elements that more accurately take into account the mechanical properties of muscles. The shapes of rather thin muscles are modelled by using layers of membrane elements, which also serve as contact surfaces with other muscle layers or parts of the body.

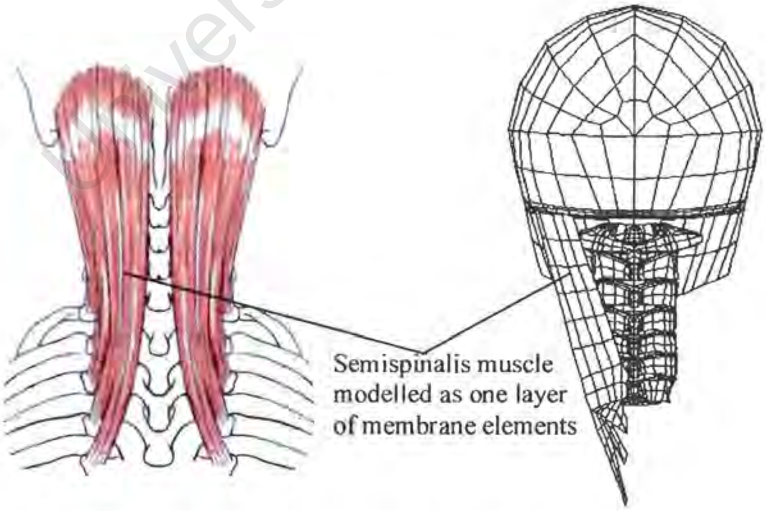

Figure 3.1.6 Layers of membrane elements for long and thin muscles [Hei62]

The third approach is the use of solid elements to model the muscle's geometry as realistically as possible, in order to build a 3-dimensional model, as shown in Figure 3.1.7.

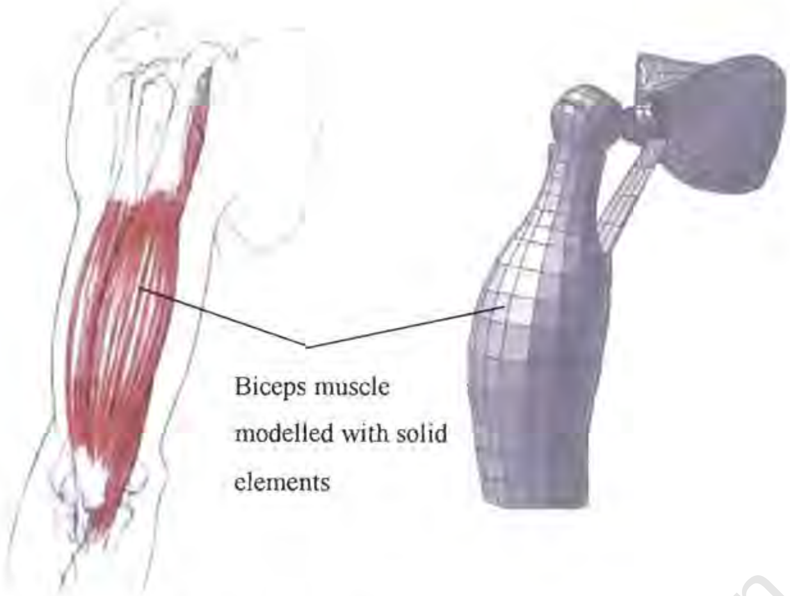

Figure 3.1.7 Solid element muscle model [Hei62]

This technique is expensive both in preparation and computational time, because the shapes of many muscles are very complex and difficult to replicate mechanically. The compression responses of muscles can best be considered using these three-dimensional solid elements. Table 3.1.4 shows the range of material properties of the muscle elements used in the FE-model in comparison to properties found in literature. Table 3.8.2 (page 90) presents the specific value for all muscles of the FE-model.

Muscles	**Young's modulus** (MPa)	**Yield stress** (MPa)	**Ultimate stress** (MPa)	**Poisson's ratio**	**Density** (g/cm^3)
[Liz98]	17 - 20	elastic	elastic	0.4	1.1
[Hua94a]	20	elastic	elastic	0.3	1.0
[Yam70]	20	elastic	elastic	0.3	1.0
FE-model	**20 - 100**	**0.2 –0.8**	**0.4 – 1.0**	**0.3**	**1.0**

Table 3.1.4: Material properties of muscle material

3.2 The BACK

3.2.1 Spinal column

The back or posterior part of the trunk is the main part of the body to which the head, neck and limbs are attached. The spinal column is the skeleton of the back and forms a strong but flexible support for the body and plays an important role in posture, locomotion and protection of the spinal cord. It consists of seven cervical, twelve thoracic and five lumbar vertebrae that are connected by intervertebral discs. The stability of the vertebral column is provided by the shape and strength of the vertebrae, intervertebral discs, surrounding ligaments and the back muscles. Figure 3.2.1 shows the front-, side- and back view of the spinal column and the corresponding FE-model.

a) Front view *b) Side view* *c) Back view*

Figure 3.2.1 Spinal column and FE-model of spinal column [Net89]

The seven cervical vertebrae (C1 to C7) are part of the neck and are described in more detail in section 3.2.5. The twelve thoracic vertebrae are connected with intervertebral discs to form the thoracic part of the spinal column. A typical vertebra is composed of two main parts; a body and a vertebral arch as shown in Figure 3.2.2. The body, which forms the anterior part, has a cylindrical shape. The bodies of the vertebrae increase in size downwards in order to be able to bear greater weight. The vertebral arch is the posterior part of a vertebra and encloses the vertebral foramen. The arch is formed by two pedicles that are attached on each side of the body. These in turn support a pair of laminae, which unite posteriorly to form a spinous process. Four articular and two transverse processes arise from the junction of the pedicles with the lamina. The articular processes bear articular facets that are part of a synovial joint, which unites adjacent vertebral arches. The articular facets allow for some flexion and extension as well as some lateral flexion and rotation of the spinal cord. Some minor simplifications were needed for the vertebra models in order not to exceed the number of 280 shell elements that represent the cortical bone of the vertebrae. The rib-vertebra articulation is represented in simplified form by a rigid connection, which probably does not influence the function significantly.

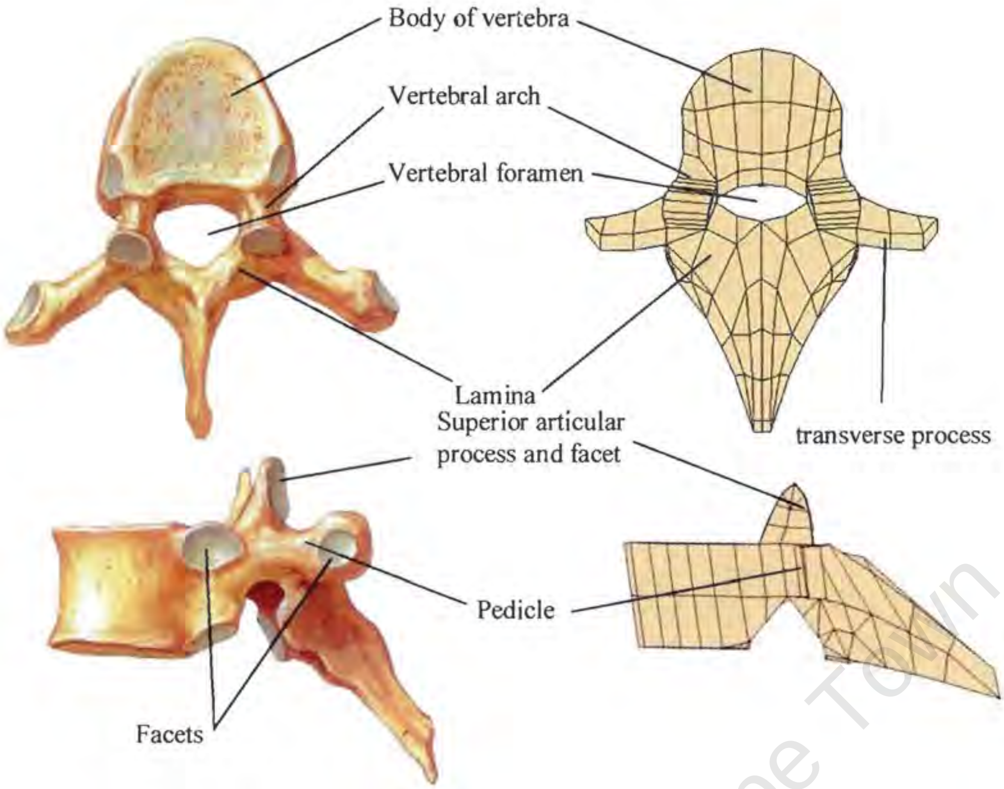

a) Top and side view [Net89] *b) FE-model of thoracic vertebra*

Figure 3.2.2 Thoracic vertebrae

As can be seen in Figure 3.2.2, the thoracic vertebrae bear facets at the upper and lower borders of the body and facets on the transverse processes for articulation with the corresponding ribs. A more sophisticated model of this ligamentous connection would require many additional elements.

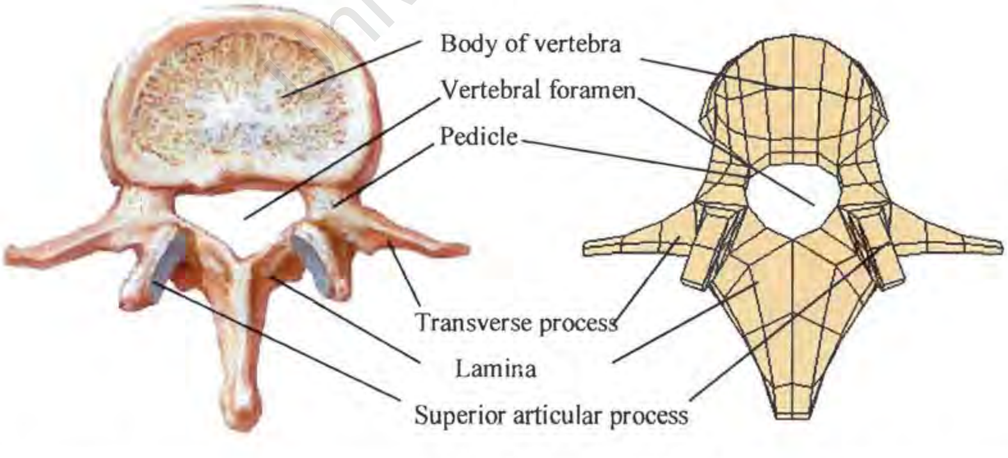

a) Lumbar vertebra – superior view [Net89] *b) FE-model of lumber vertebra*

Figure 3.2.3 Lumbar vertebra

The lumbar vertebrae differ in shape from the thoracic vertebrae as they do not articulate with any ribs. They are distinguished by their large kidney-shaped bodies and stout laminae as shown in

Figure 3.2.3. These vertebrae are bigger because they bear more body weight and articulate with the sacrum at the bottom end. The orientation of the upper and the corresponding lower articular processes face more laterally.

3.2.2 The joints of the vertebral column

The vertebrae articulate with one another at joints both between their bodies and between their articular processes. The intervertebral discs provide the strongest attachment between the bodies of the vertebrae as shown in Figure 3.2.4.

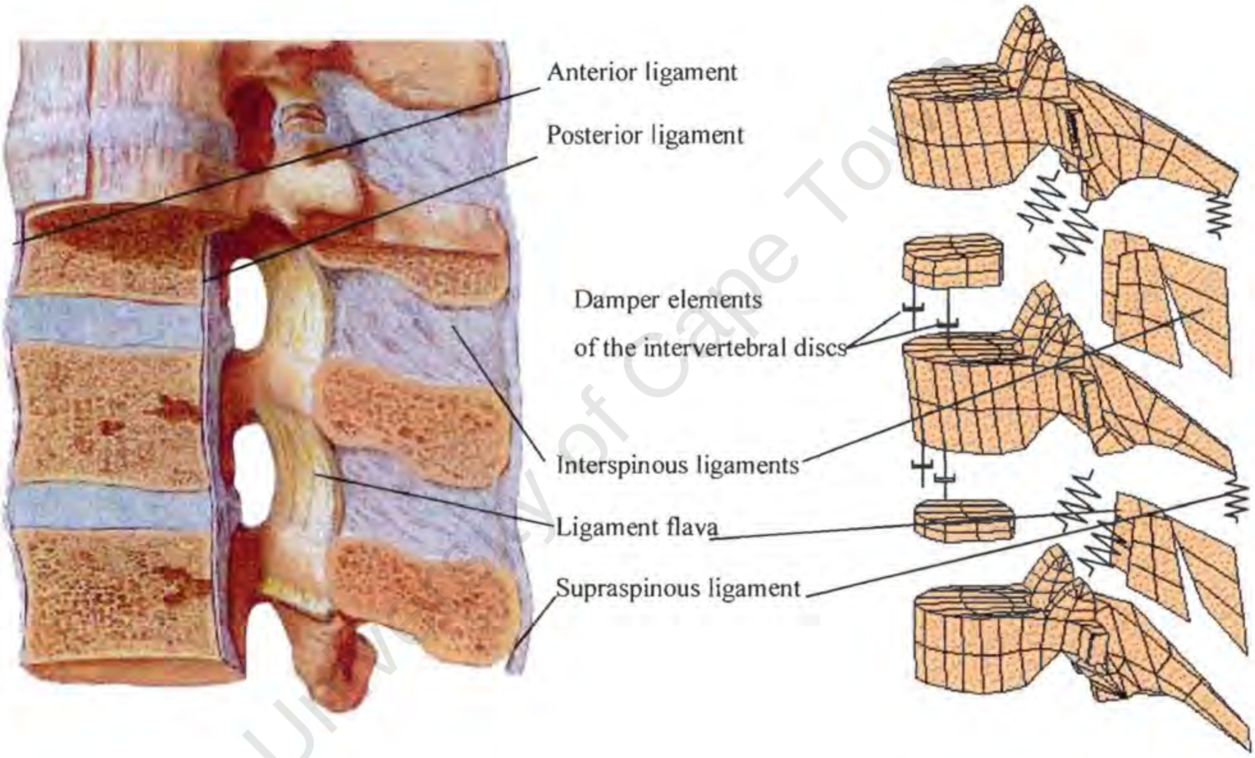

a) Spinal column section [Net89] *b) FE-model of spinal column*

Figure 3.2.4 Intervertebral discs and ligaments of the spinal column

The discs vary in size and thickness in different regions of the vertebral column and are thinnest in the thoracic and thickest in the lumbar region, where they constitute a third of its length. In the cervical and lumbar region the discs are thicker anteriorly, making them wedge-shaped. This structure of the discs is related to the normal curvature of the spine in these regions. Each disc consists of an outer ring composed of concentric layers of fibrous tissue and fibrocartilage called annulus fibrosus, and a soft core, the nucleus pulposus. The design of the intervertebral discs allows them to provide a strong union between the vertebral bodies and to absorb compression forces. The FE-model of an intervertebral disc consists of 16 solid elements with an elastic-plastic material behaviour. The visco-elastic properties of this type of cartilage are taken into account by an additional system of damper elements within the model of the intervertebral disc as shown schematically in Figure 3.2.4. In addition to these discs, the bodies are united by strong anterior and posterior longitudinal ligaments. The anterior ligament (not shown in Figure 3.2.4) is broad and is attached to the anterior surfaces of the bodies and the discs. The posterior ligament is narrower, and is attached to the upper and lower margins of the bodies, but it is not included in the FE-model. The anterior longitudinal ligament is represented by 60 membrane elements, which connects the upper and lower border of adjacent vertebrae. The laminae of adjacent vertebral arches are joined by broad, elastic bands called ligament flava, which extend almost vertically from the lamina above to the lamina below. These ligaments help to preserve the normal curvature of the vertebral column and to straighten the column after it has been flexed. Adjacent spinous processes are joined by weak interspinous ligaments and a strong cord-like supraspinous ligament. The ligament flava and the interspinous ligament are modelled by 80 and 60 membrane elements respectively.

Joints between the articular processes on the vertebral arches are small-plane synovial joints in which one articular facet glides over the other. A thin articular capsule supports these joints. In the FE-model, contact is defined between the articulating surfaces, which form such a synovial joint between adjacent vertebrae. Twelve damper elements with an estimated damping characteristic are included between these contacting surfaces. These damper elements simulate the damping effects within the synovial joint and prevent oscillation between the contact surfaces.

3.2.3 Muscles of the back

The muscles of the back can be divided into the superficial, intermediate and deep layer. The superficial and intermediate groups are concerned with the movements of the limbs and with respiration, whereas the deep layers move and stabilise the spinal column. Behind the spinal column lies a big muscle, the erector spinae, which consists of long muscle fibres spanning many vertebrae. It can be divided into three portions: iliocostalis, longissimus and spinalis. The most lateral portion arises from the sacrum, lumbar vertebral spines and the posterior part of the iliac crest. From this origin, laterally running bundles of fibres extend to the ribs and transverse processes in the thoracic and cervical region as shown in Figure 3.2.5.

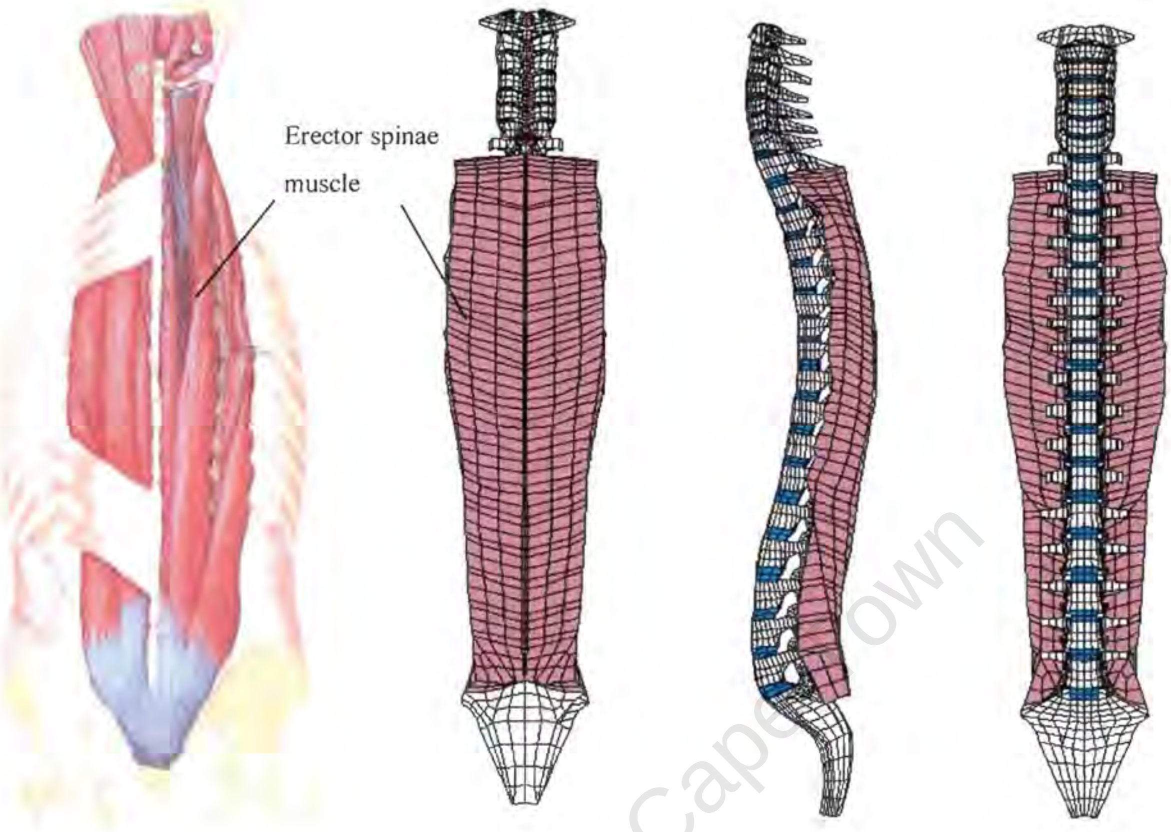

a) Erector Spinae muscle [Net89] b) FE-model - Front view c) Side view d) Back view

Figure 3.2.5 Deep muscle layer of the back

The FE-model of the erector spinae represents the erector spinae as one muscle using 678 solid elements and 128 membrane elements. The muscle starts at the upper surface of the sacrum and is also connected to the inner pelvic wings. Connected at the spinous processes and transverse processes of the lumbar and thoracic vertebrae, the FE-model of erector spinae follows the curvature of the spine up to the first thoracic vertebra. The cervical parts of the erector spinae are modelled in more detail in the form of separate FE-models of the semispinalis and splenius capitus.

The second major muscle of the back is the trapezius muscle, shown in Figure 3.2.6., that covers the upper part of the erector spinae and the thoracic spine. 767 solid elements are used to model this muscle. The upper end of this muscle inserts at the lower part of the back of the skull and forms a major part of the neck musculature. Laterally, the trapezius is connected to the top of the clavicle. The outer surface of the upper part of the trapezius is covered by a layer of membrane elements that represent the skin of the neck. The inner surface is in contact with the deeper muscle layers of the back.

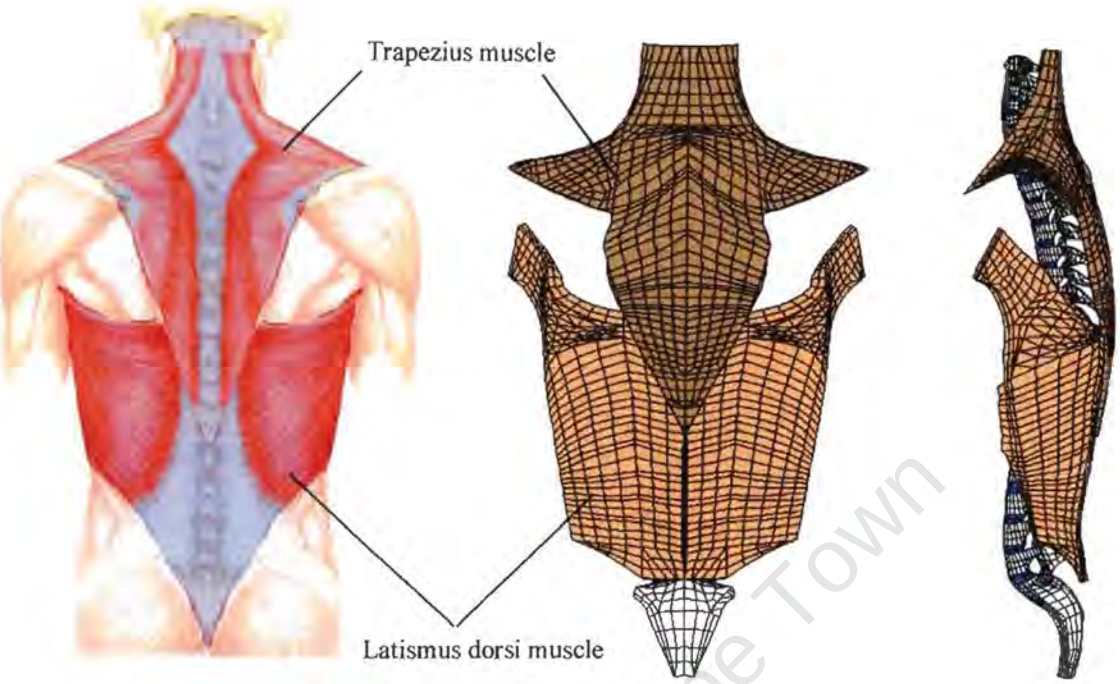

a) Trapezius and Latissimus dorsi [Net89] *b) FE-model - Back view* *c) Side view*

Figure 3.2.6 Superficial muscles of the Back

The latissimus dorsi covers the lower half of the back from the sixth thoracic vertebra down to the iliac crest of the pelvis. This wide, fan-shaped muscle passes between the trunk and the humerus where it inserts. 720 solid elements are used to build the model of the latissimus. The anterior midline of the latissimus model is connected to all the vertebrae from T6 downwards. The upper part of the posterior midline is connected to the lower midline of the trapezius muscle model. Additionally, the upper part of the posterior surface of the latissimus is defined as a connective surface to the lower inner surface of the trapezius muscle. The inner surface of the latissimus serves as a contact surface to the model that represents the internal visceral contents as described in section 3.3. Contact is also defined between the membrane elements of the outer skin of the model and the outer surface of the latissimus muscle.

3.3 The Thorax

3.3.1 The rib cage

The thorax is the upper part of the trunk that lies between the neck and the diaphragm. The cavity of the thorax contains the lungs, the heart, a number of large blood vessels and the respiratory passages. The thoracic cavity is surrounded by the thoracic wall, which also surrounds and protects the upper part of the abdominal cavity. The rib cage, shown in Figure 3.3.1, is the skeletal part of the thoracic wall and is formed by the thoracic vertebral column, twelve pairs of ribs, their costal cartilages and the sternum.

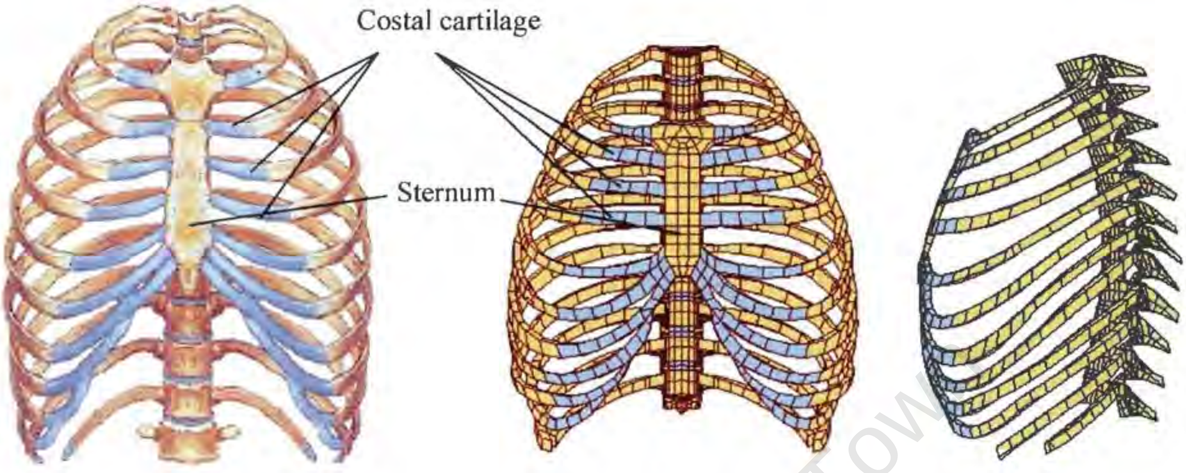

a) Rib cage [Net89] *b) FE-model-front view* *c) Side view*

Figure 3.3.1 Rib cage

A typical rib has a body which is flattened and curved. The body of the rib follows a curve of gradually increasing radius towards the anterior end. The upper seven pairs of ribs articulate through their costal cartilages with the sternum. The eighth, ninth and tenth pairs of ribs articulate with the costal cartilage of the adjacent ribs. The eleventh and twelfth pairs lie free anteriorly and are capped by only a small piece of costal cartilage. These costal cartilages contribute significantly to the flexibility of the rib cage, which is necessary for respiration-related movements. In the FE-model of the costal cartilage, 478 shell elements of 10 mm thickness and with cartilage material properties are used, whereas the ribs are modelled by 1962 shell elements of 2 to 4 mm thickness with a cortical type of bone material.

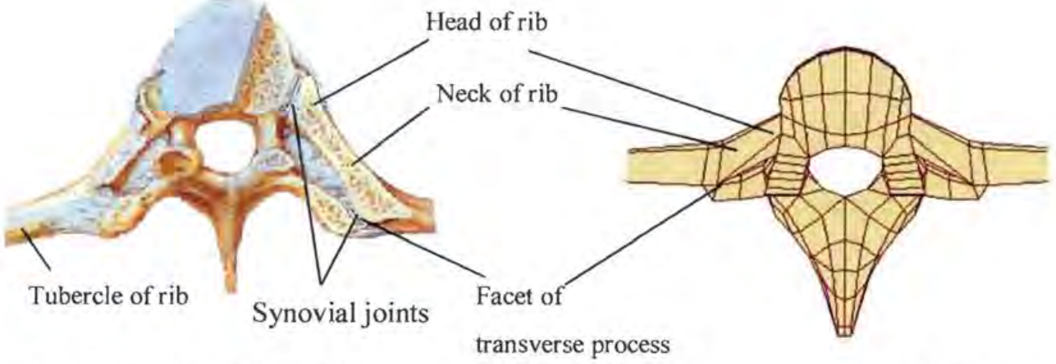

a) Costovertebral joint [Net89] *b) FE-model*

Figure 3.3.2 Superior view of costovertebral joint

The connections of the costal cartilages and the sternum are modelled in simplified form by a direct fusion of the cartilage elements and the shell elements of the sternum. Bone material properties are defined for the 148 shell elements of the sternum. Posteriorly, the body is joined to the head of the rib by a short neck. The head and the tubercle of the rib articulate with the corresponding thoracic vertebrae by synovial joints that unite the ribs with the upper border of the vertebral body and the facets of the transverse processes, as can be seen in Figure 3.3.2 and 3.3.3. By means of a synovial joint the ribs are additionally connected to the lower border of the adjacent vertebrae above.

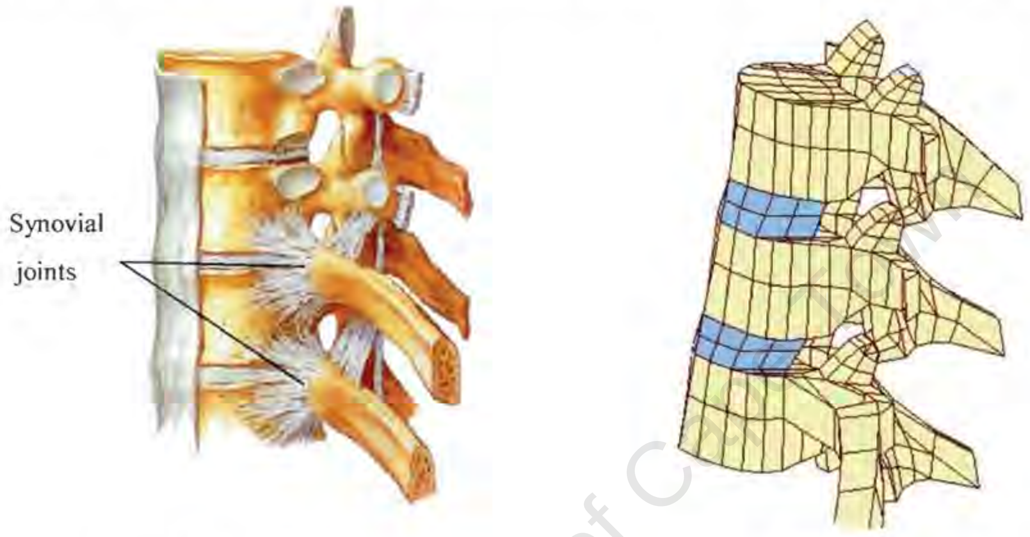

a) Lateral view [Net89] *b) FE-model*

Figure 3.3.3 Lateral view of costovertebral joint

This complex system of synovial joints provides a strong connection between the ribs and the thoracic vertebral column, but is still flexible enough to allow movement of the spinal column. For the FE-model the rib-vertebra connection needs to be simplified without sacrificing either flexibility or stability of the spine. Figures 3.3.2 and 3.3.3 depict the FE-model and the real human costovertebral joints. The heads of the ribs are directly connected to the body of the corresponding vertebra and to its transverse process. The stiffness of the missing link to the adjacent vertebra above is compensated by an increased stiffness of the intervertebral disc.

3.3.2 Muscles of the thoracic region

The intercostal spaces between the ribs are largely filled by external and internal intercostal muscles. The intercostal muscle layers are modelled by an inner and outer layer of 572 membrane elements running from the upper inner and outer border to the corresponding lower border of the adjacent rib above. Figure 3.3.4 depicts the intercostal muscles of the rib cage.

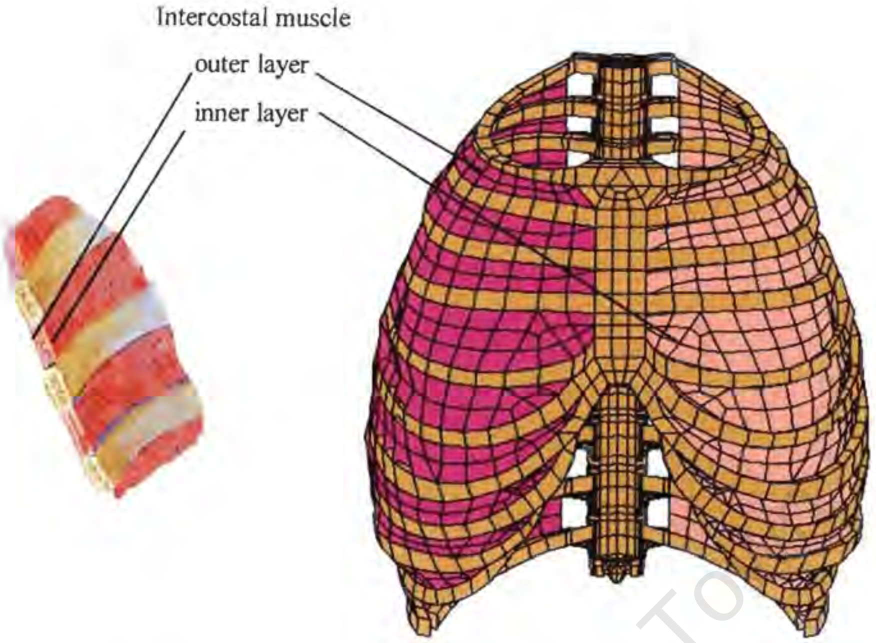

a) Intercostal muscles [Net89] *b) FE-model of rib cage with intercostal muscles*

Figure 3.3.4 Intercostal muscles of the rib cage

The inner intercostal muscle layer together, with the inner surface of the ribcage, forms a contact surface for the contents of the thoracic cavity, while the outer layer forms a contact surface to the muscle and skin elements that surround the rib cage.

3.4 The Abdomen and Pelvis

The abdomen is separated from the thorax by the diaphragm which, because of its domed shape, allows some abdominal organs to lie within the protection of the thoracic cage. The lower part of the abdominal cavity lies within the wings of the pelvis. A thick layer of back muscles and the spinal column protect the abdominal cavity at the back, and some muscle layers at the side and front protect the abdominal cavity at the front. Before describing the muscles of the abdominal wall in more detail, the skeletal part of the pelvis needs to be specified.

3.4.1 The bony pelvis

As illustrated in Figure 3.4.1, the bony pelvis is formed anteriorly and laterally by two hip bones, posteriorly by the sacrum and anteriorly by the two pubic bones at the pubic symphysis. The large, irregularly shaped hip bone is formed by three bones: the ilium, the ischium and the pubis. The ilium forms the upper two-thirds of the hip bone and the upper two-fifths of the cup-shaped acetabulum.

The iliac crest, which is the upper margin of the the ilium, has a thicker posterior superior iliac spine and ends anteriorly in a rounded anterior superior iliac spine.

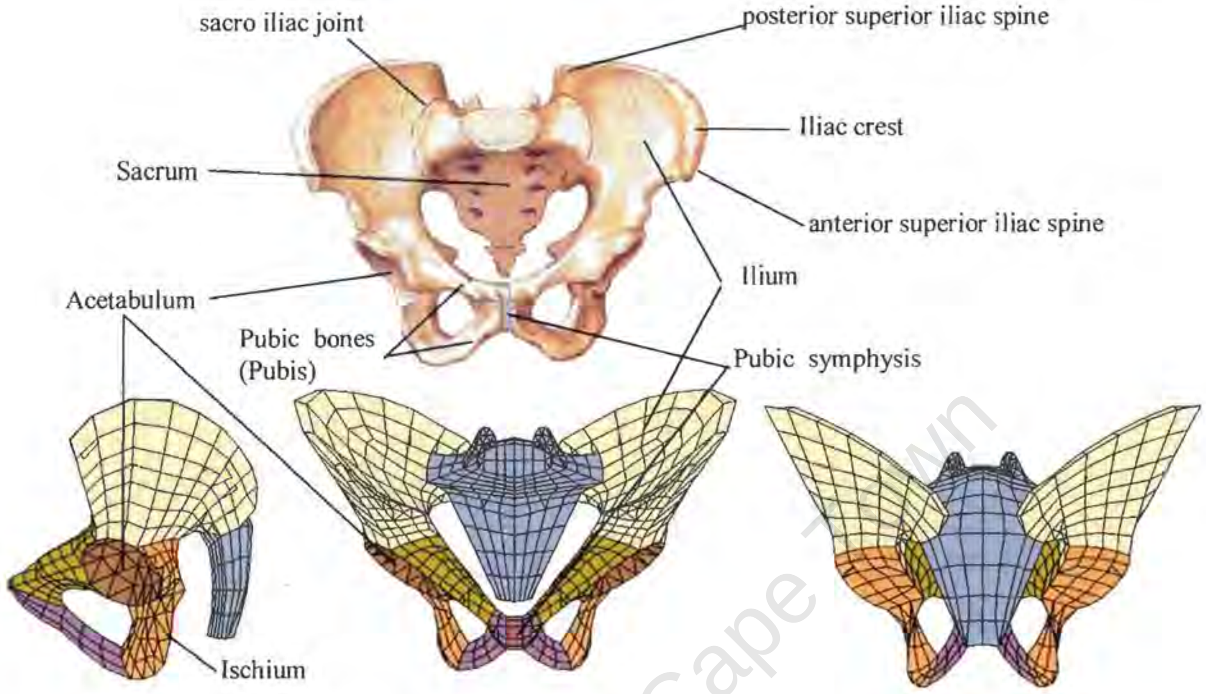

a) Side view *b) Front view* *c) Rear view*

Figure 3.4.1 Bony Pelvis and FE-model [Net89]

The ischium forms the lower rear third of the hip bone and the upper two-fifths of the acetabulum. It is roughly L-shaped and consists of the two parts, the body and the ramus. The superior thick portion of the body is fused with the ilium and the pubic bones at the acetabulum. The ramus of the ischium is an inferior, thinner bar of bone that extends from the body and joins the inferior ramus of the pubis to form the ischiopubic ramus. The L-shaped pubis forms the inner front part of the hip bone and the anteromedial one-fifth of the acetabulum. The pubis consists of three parts, a body and two rami. From the pubic body, an inferior ramus extends posteriorly, inferiorly and laterally to join the ramus of the ischium, forming half of the pubic arch. The superior ramus of the pubis passes superolaterally to the acetabulum, where it is fused with the ilium and ischium. The body of the pubis joins the body of the opposite pubis in the median plane at a fibrocartilaginous joint, called the pubic symphysis. The acetabulum lies at the site of the fusion of the three parts of the hip bone. It is a cup-shaped cavity that is laterally faced and tilts slightly downwards and forwards.

The FE-model of the pelvis consists of 4 sections modelled by 1180 shell elements with a thickness varying between 2 and 5 mm, which represent the cortical bone. To start with, the thickness distribution of the different sections was estimated based on the FE-models by [Bes98] and [Dal95]. The bony pelvis is posteriorly closed by the sacrum at the sacro-iliac joints. This joint is modelled in a simplified way by means of a rigid connection of the pelvic bones. The sacrum is modelled by 320 shell elements. Anteriorly, the pelvis is closed off at the pubic symphysis, which is modelled by 5 solid elements with cartilage material properties.

3.4.2 The abdominal muscles

The musculature of the anterior and lateral walls of the abdomen is made up of a trilaminar sheet on either side of the vertically oriented rectus abdominis muscles, shown in Figure 3.4.2.

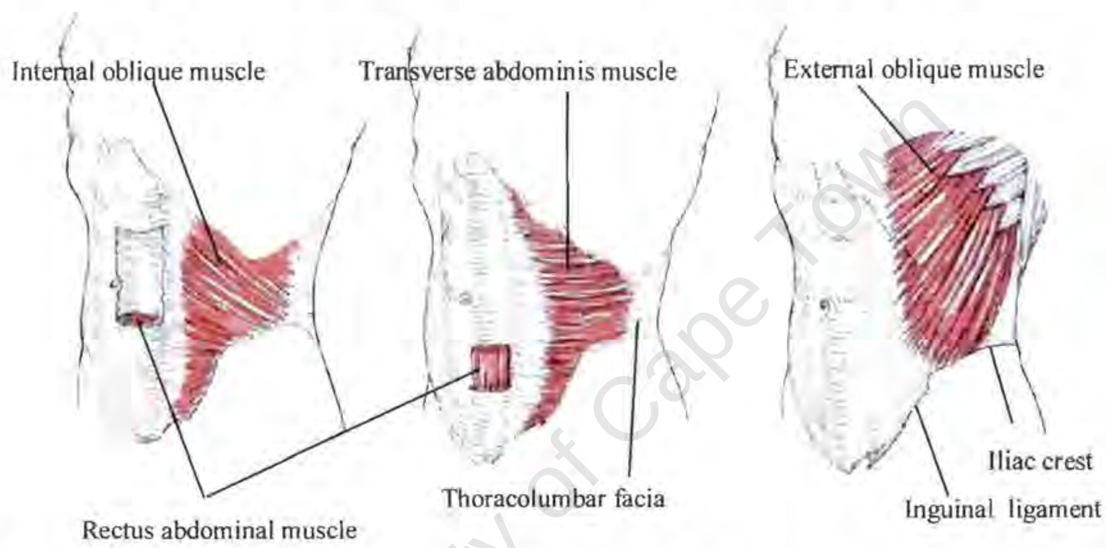

a) Internal oblique muscle *b) Transverse abdominis muscle* *c) External oblique muscle*

Figure 3.4.2 Abdominal muscles [Hei62]

The trilaminar sheet is composed of the external oblique muscle, the internal oblique muscle and the transversus abdominis muscle. The external oblique muscle arises from the outer surfaces of the lower eight ribs and extends downwards and forwards to the iliac crest. Its lower margin extends from the anterior superior iliac spine to the pubic tubercle and is called the inguinal ligament. The internal oblique muscle arises from the thoracolumbar fascia, the anterior two-thirds of the iliac crest deep to the attachment of the external oblique muscle and the inguinal ligament. The fibres fan out from this origin. The uppermost fibres run upward and medially to attach to the lower costal margin. The lowermost fibres are attached by a flattened tendon to the superior pubic ramus. This tendon is fused with a similar attachment of the transversus abdominis muscle. The fibres of the transversus abdominis muscle arise from a long origin which extends from the deep surface of the costal margin, the thoracolumbar fascia, the anterior two-thirds of the medial margin of the iliac crest and the outer half of the inguinal ligament. The two parts of the rectus abdominis are attached to the fifth, sixth and seventh costal cartilages and below to the pubic crest and the pubic symphysis.

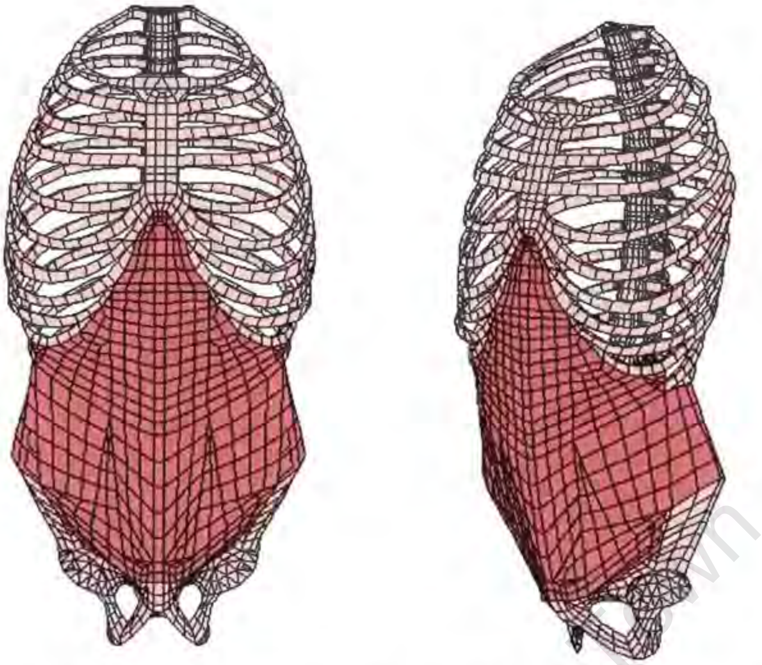

a) front view of abdominal muscle FE-model *b) oblique side view of FE-model*

Figure 3.4.3 FE-model of abdominal muscles

The FE-model of the abdominal muscles, shown in Figure 3.4.3 a) and b), is a simplified representation of these three muscle layers. The rectus abdominis muscle is modelled by 178 solid elements forming one muscle that starts at the pubic symphysis and the upper pubic bones on either side. Its top-end is attached to the lower border of the costal cartilages of the seventh and eight rib and the sternum.

Between the anterior superior spine, the pubic symphysis and the upper pubic bone is a layer of 86 membrane elements, which is intended to represent the function of the inguinal ligament. This layer of membrane elements runs upwards and half-way along the inner border of the iliac wing, ending at the inner borders of the costal cartilage of the seventh to twelfth ribs. This layer serves as a contact surface with the internal visceral contents of the abdomen. Almost parallel to this outer membrane layer lies another layer of membrane elements that runs along the outer border of the pubic symphysis, the upper pubic bone and the iliac crest, and ends at the outer borders of the costal cartilages of the seventh to twelfth ribs.

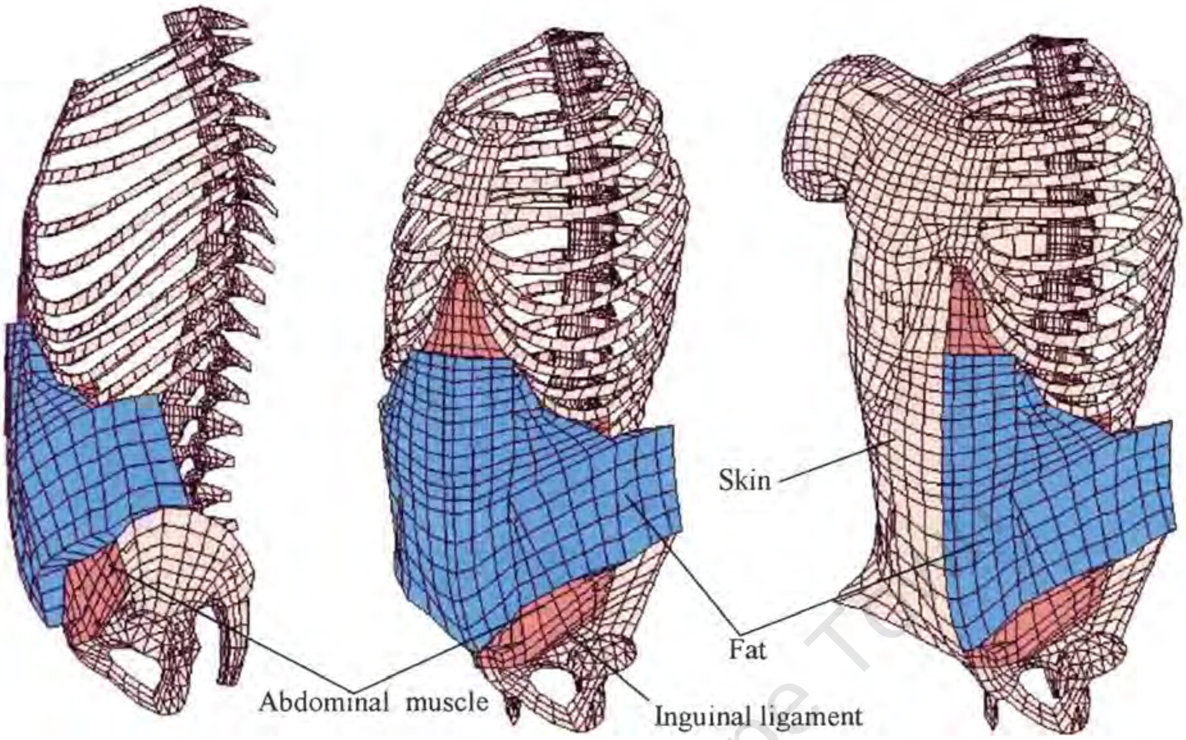

a) Side view *b) oblique side view* *c) oblique side view without skin*

Figure 3.4.4 FE-model: abdominal muscle, skin and fat

The space between these two layers is filled with 768 solid elements. It was initially intended to define different orientations for the membrane layer, with the aim of representing the different orientations of the internal oblique, external oblique and transversus abdominis muscles; however, this turned out to be unnecessary in terms of simulated impact response. Another layer of very compliant 318 solid elements, representing body fat, is wrapped around the abdominal muscles as shown in Figure 3.4.4.

3.4.3 The contents of the pelvic, abdominal and thoracic cavity

The urinary system and the reproductive organs are the main pelvic organs. The internal organs of the abdomen are stomach, liver, spleen, kidneys and the intestines. These abdominal and pelvic contents are modelled by two sections of 442 and 244 solid elements respectively, shaped in such a way that they fill the abdominal and pelvic cavities as depicted in Figure 3.4.5. Contact is defined between the inner abdominal membrane layers, the inner surfaces of the pelvic bones and the visceral contents.

3.5 The Head and Neck

3.5.1 The vertebrae of the cervical spine

The cervical spine consists of seven vertebrae, which connect the skull with the thoracic spine. The cervical spine is not designed to bear heavy weight – other than the head - and therefore a level of stability has been sacrificed in favour of moveability. The cervical spine provides the head with a wide range of motion, which is primarily achieved by the shape of the first two vertebrae. Figure 3.5.1 shows a picture of the head and the neck in comparison to the FE-model counterpart.

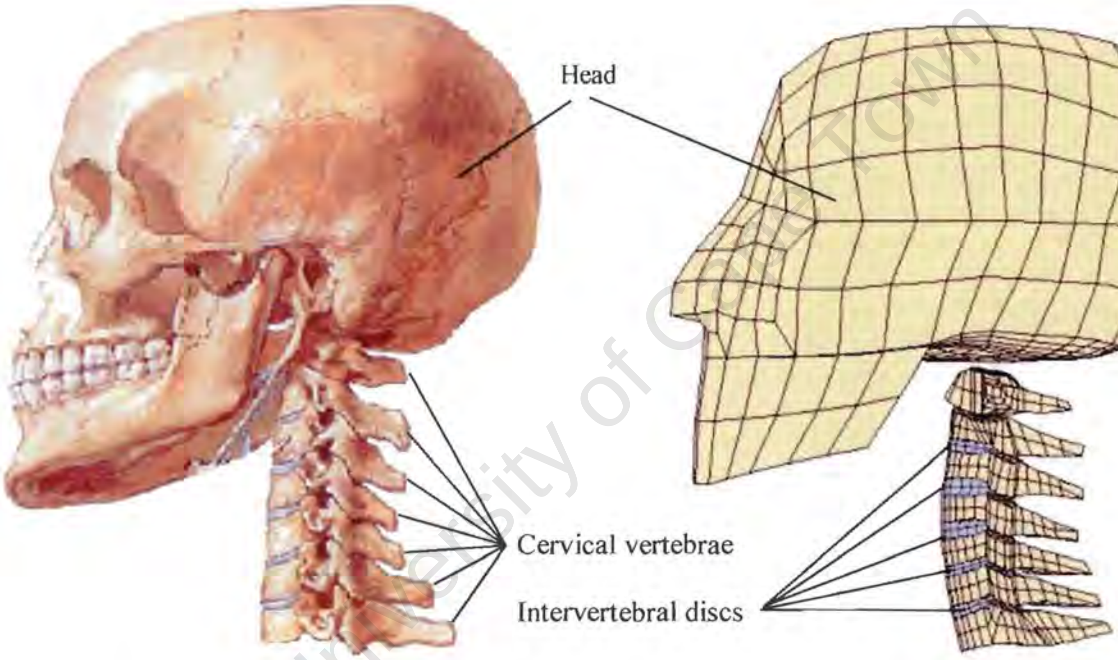

a) Head-Neck [Net89] *b) FE-model - side view*

Figure 3.5.1 Head and Neck

The head model shown in Figure 3.5.1 was built to simulate head-neck dynamics without taking into consideration the requirements needed to predict head injuries. Therefore the head is modified in a simplified manner by means of 520 non deformable elements. The mass and intertial properties of these elements as well as the properties of the cervical vertebrae are defined by data obtained by Wismans [Wis86] as can be seen in Table 3.5.1.

Mass [kg]	I_{xx} [kgm^2]	I_{yy} [kgm^2]	I_{zz} [kgm^2]
4.78	0.0267	0.0293	0.0149

Table 3.5.1 Mass and inertial properties of the head[Wis86]

The cervical verterbrae are connected by intervertebral discs that follow the curvature of the cervical spine. Compared to a thoracic vertebra, the body of a cervical vertebra is smaller and rather quadrangular in shape. The spinous processes are larger and extend further backwards in relation to its overall length. A typical cervical vertebra is modelled by means of 240 shell elements. For reasons of simplification, the oval foramen of the transverse process is not included in the FE-model of the cervical vertbrae.

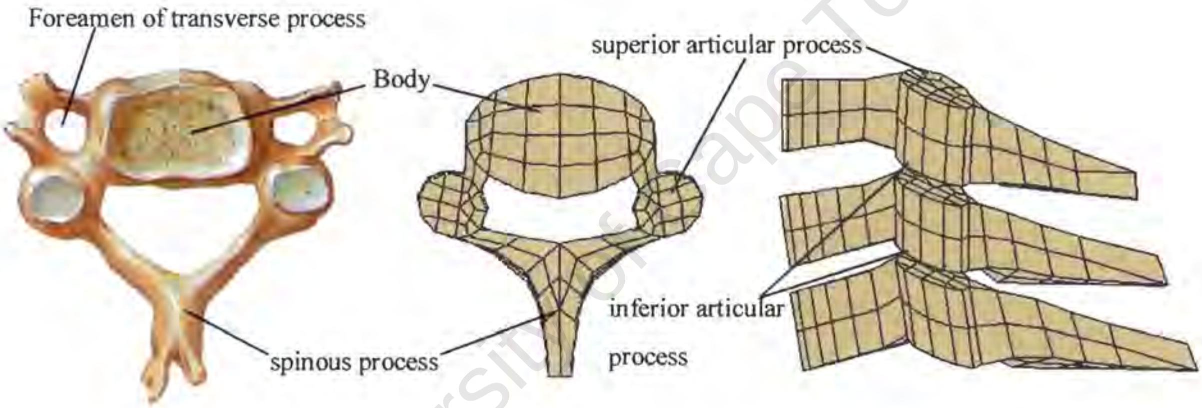

a) Cervical vertebrae [Net89] *b) FE-model* *c) FE-model of C4-C5-C6*

Figure 3.5.2: Cervical vertebra

The superior articular processes face upwards and tilt backwards, and the inferior processes face downwards and tilt forwards. The processes of adjacent vertebrae form synovial joints on both sides of the body. In contrast to the thoracic synovial joint, the articulating surfaces have a round shape. These synovial joints are modelled by the two contacting surfaces and a system of damper elements that simulate the damping effects occurring within the joint.

The upper part of the cervical spine is shown in Figure 3.5.3. The shape of the second cervical vertebra is similar to the typical shape of the remaining cervical vertebrae, with the exception of the dens. The dens is a cylindrically shaped bone that extends vertically upwards from the superior aspect of the vertebral body, forming an axis around which the first cervical vertebrae rotates. The first cervical vertebra consists of two lateral masses connected by an anterior and posterior arch. The upper surface of each lateral mass forms an oval facet for articulation with an occipital condyle of the skull. On the lower surface of each lateral mass are facets for articulation with the superior articular facet of the second cervical vertebra. The posterior wall of the anterior arch of C1 articulates with the anterior aspect of the dens, thereby forming a rotational pivot which is held together by a complex of ligaments. These joints between the skull and C1 (atlas) and between C1 and C2 (atlas and axis) are called the atlanto-occipital and atlanto-axial joints.

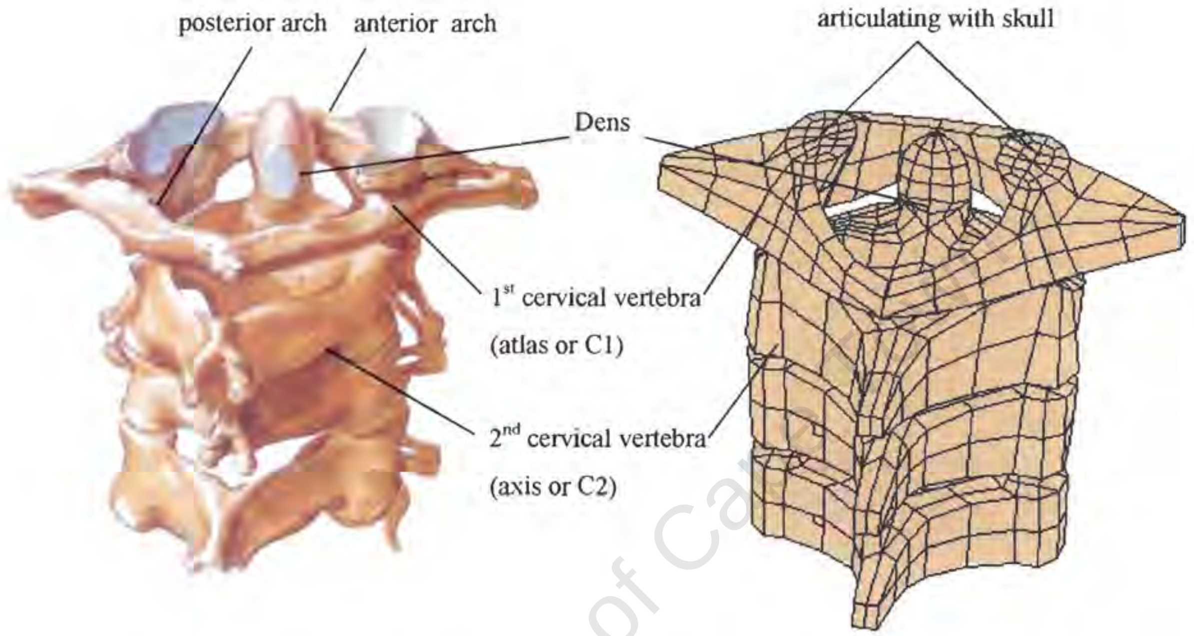

a) Upper cervical spine [Net89] *b) FE-model of upper cervical spine*

Figure 3.5.3 Cervical spine

In contrast to the other joints of the vertebral column, they do not consist of intervertebral discs. The FE-model of these first two cervical vertebrae is shown in Figure 3.5.3 a). 162 shell elements are used to model the first cervical vertebra and 278 shell elements for the second. The facet joints between C1 and the skull and between C1 and C2 consists of two contact surfaces combined with a system of damper elements. The surface of the dens of C2 is in contact with the inner surface of C1 to build a pivot joint that is supported by membrane elements, which represent the ligaments of the suboccipital joints described in the following section.

3.5.2 Ligaments of the cervical spine

Figure 3.5.4 illustrates the ligament of the cervical spine, which connects the first and second cervicle vertebrae to the head at the craniovertebral joints. The transverse ligament of the atlas is a strong band extending between the tubercles on the lateral masses of the C1 vertebra. It holds the dens of C2 against the anterior arch of C1. Vertically oriented superior and inferior bands (not shown in Figure 3.5.4) pass from the transverse ligament to the occipital bone and to the body of C2. Together these ligaments are known as the cruciform ligament. Additionally 18 membrane elements are used to model the ligament flava (not shown) between the first and the second cervical vertebra and the skull.

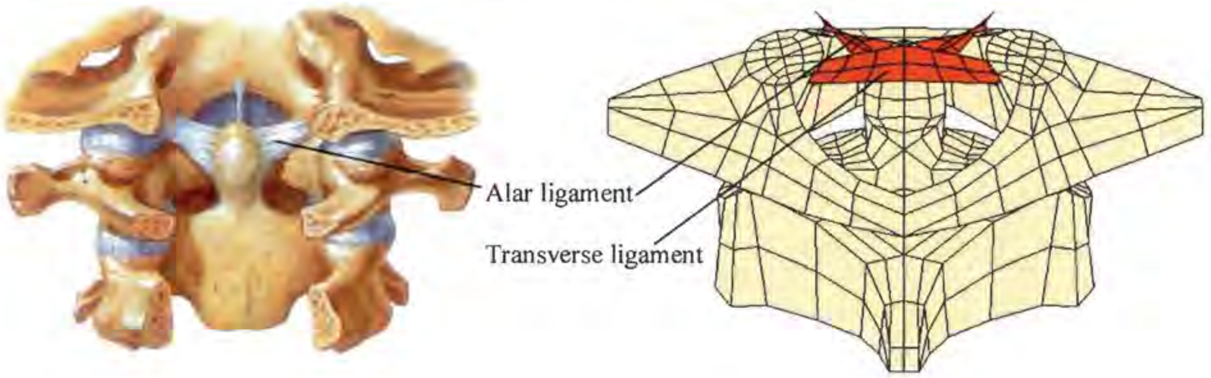

a) Suboccipital joints [Net89] *b) FE-model*

Figure 3.5.4 Suboccipital joints and ligaments of the cervical spine

The corresponding FE-model of the craniovertebral joint is shown in Figure 3.5.4 b). The cruciform ligament is modelled by 12 membrane elements and 4 spring-damper elements, which represent its function. The alar ligaments extend from the sides of the dens to the lateral margins of the foreamen magnum. These short, strong, rounded cords attach the skull to the C2 vertebra. They prevent excessive rotation of the atlanto-axial joints. 18 membrane elements are used to model these ligaments.

3.5.3 Muscles of the Neck

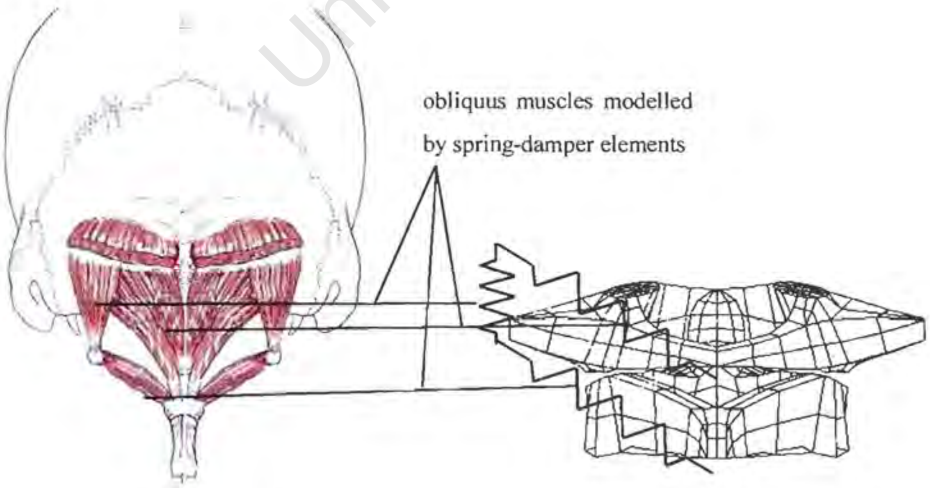

a) Suboccipital triangle muscles [Hei62] *b) Spring-damper system of the FE-model*

Figure 3.5.5 Suboccipital triangle muscles

In addition to the ligaments of the neck, a group of smaller muscles of the suboccipital triangle supports the head-neck complex. These muscles are modelled by a system of spring-damper elements, which connect the first and the second cervical vertebra to the head.

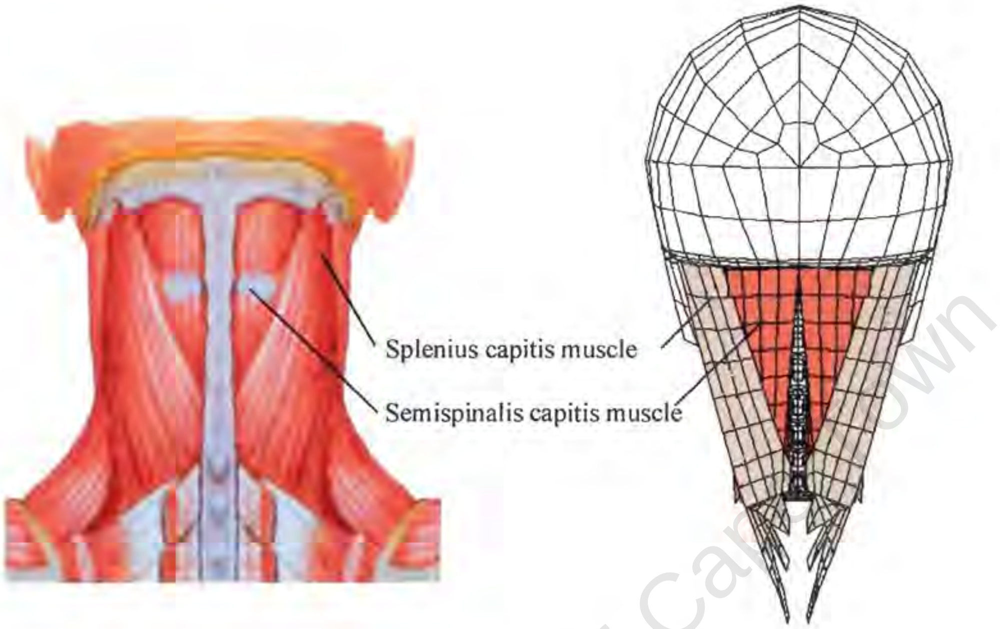

a) Splenius capitis and Semispinalis capitis b) FE-model of Splenius capitis and Semispinalis capitis
Figure 3.5.6 Muscles of the neck [Net89]

The trapezius, which has been described in more detail before, is the biggest muscle of the neck and connects the back and the shoulder to the neck. It inserts at the back of the skull and covers the deeper muscle layer of the neck. The deeper muscle layers that are included in the model are the splenius capitis and the semispinalis capitis muscles. Figure 3.5.6 shows the FE-model and its counterparts. The most bulky of the deep layers of neck muscles is the semispinalis capitis. It arises as thin slips from thoracic and cervical transverse processes and forms a bulky mass, which is attached to the occipital bone of the skull. This muscle is modelled using 648 solid elements. Between the deep and the superficial layer lies a flat sheet of muscle called splenius capitis. This muscle arises from the upper thoracic spines and inserts into the bottom of the skull. Its function is to help rotate the head and laterally flex the neck. This muscle is modelled by 128 membrane elements. For the inner surface of the semispinalis muscle contact is defined with the cervical spine and for the outer surface with splenius capitis and trapezius muscle. No friction is defined for this contact.

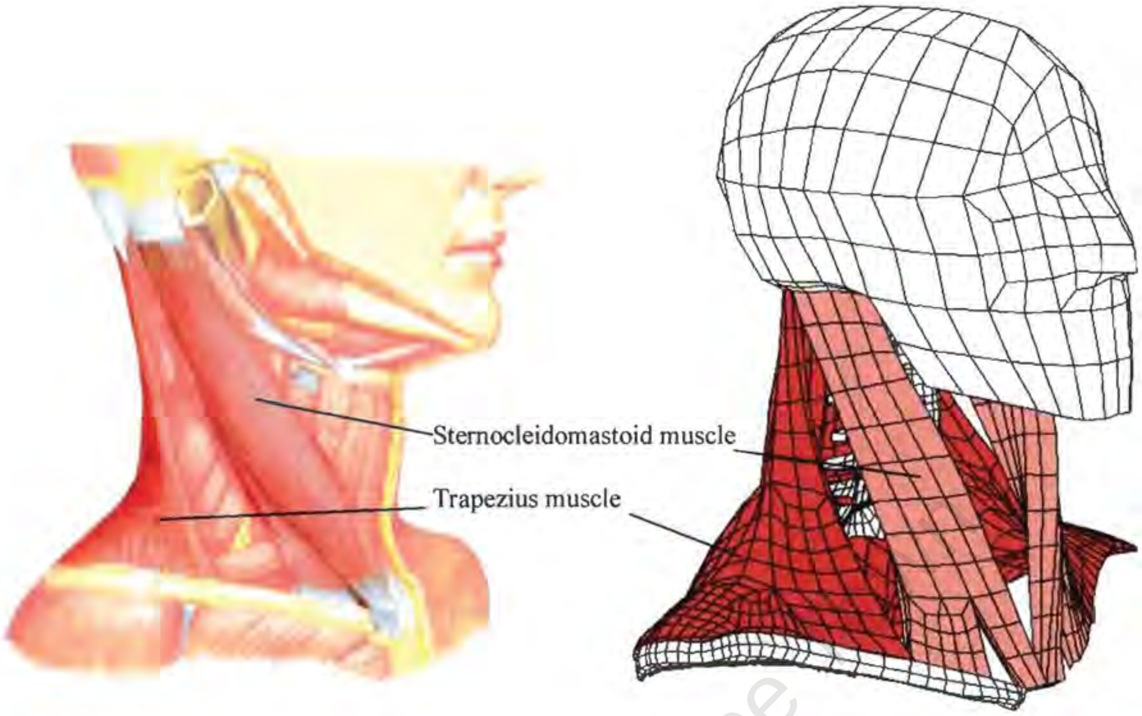

a) sternocleidomastoid muscle [Net89] *b) FE-model of sternocleidomastoid muscle*

Figure 3.5.7 Muscles of the neck

The main frontal and lateral muscle of the neck is the sternocleidomastoid, which runs obliquely across the side of the neck and covers its great vessels. It is attached to the skull at its lateral surface and inferiorly at the clavicle and the sternal head, forming a dual attachment. The action of one muscle is to tilt the head toward the same shoulder while rotating the face to the opposite side. Both parts of the sternocleidomastoid are modelled by 192 solid elements altogether. The FE-model of these muscles is shown in Figure 3.5.7 next to the original muscle.

3.6 The Upper Limb

The upper limb is not usually involved in weight bearing; as a result its stability has been sacrificed to gain greater mobility. Figure 3.6.1 shows how the upper limb is suspended from the bony shoulder girdle, which also links it to the trunk.

3.6.1 Bones to the upper limb

The clavicle articulates with the sternum and the scapula. The humerus, which is the bone of the arm, articulates with the girdle at the shoulder joint, and with the radius and ulna at the elbow joint. The radius articulates with the hand at the wrist joint.

The shoulder girdle is formed anteriorly by the clavicle and posteriorly by the scapula. The clavicle extends laterally and almost horizontally across the root of the neck. It streches from the sternum to the acromion of the scapula.

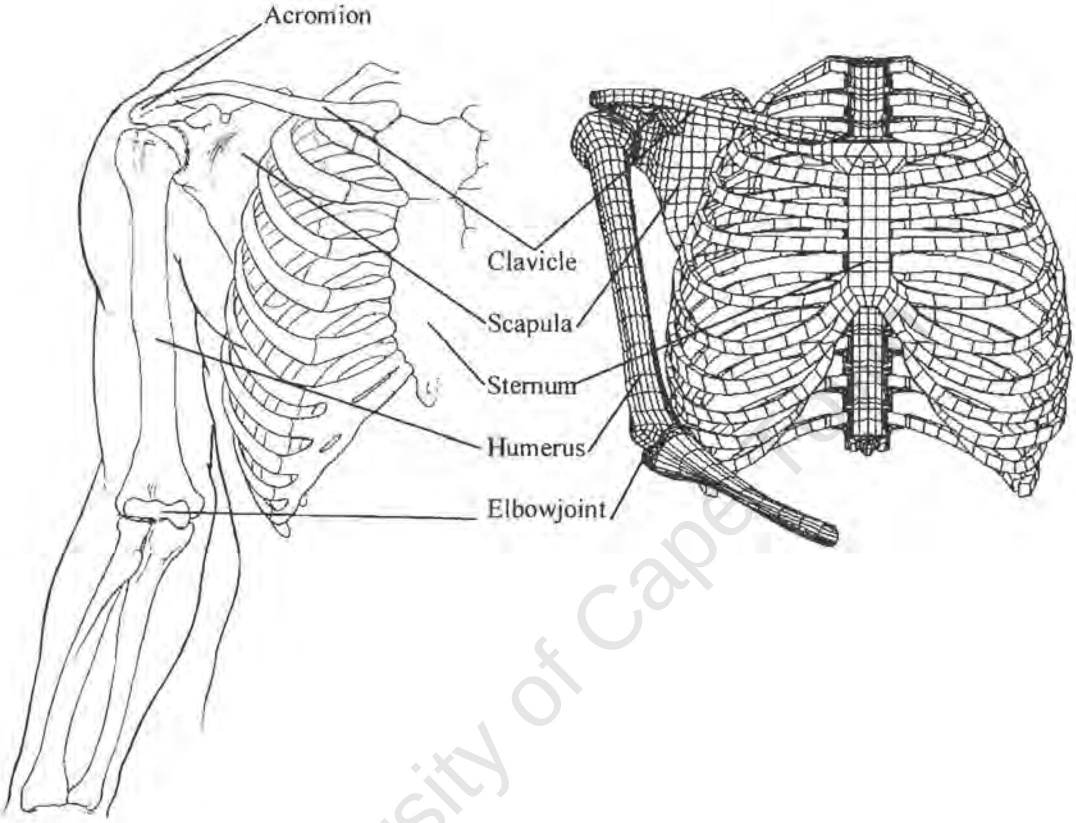

a) Upper limb [Hei62] *b) FE-model of upper limb*

Figure 3.6.1 The upper limb

The clavicle connects the upper limb to the axial skeleton and the trunk. The medial end is slightly expanded and articulates with the sternum and the first costal cartilage at the sternoclavicular joint. The broader lateral end of the clavicle articulates with the acromion of the scapula at the acromioclavicular joint. The FE-model of the clavicle consists of 588 shell elements of 2 to 4 mm in thickness. The first elements next to the junction with the sternum are modelled by 18 membrane elements with cartilage material properties to simulate the flexibility of the sternoclavicular joint. The acromioclavicular joint is a small synovial joint between the flattened lateral end of the clavicle and the medial border of the acromion. The range of movement of this joint is limited by the strong ligaments and a fibrous capsule. The joint at the acromion bears a high injury risk in lateral impacts. For reasons of simplification this joint is modelled by shell elements with cartilage material properties. A more complex model would include a synovial joint model with ligamental support and a capsule for stabilisation, which in turn would have required significantly more elements.

The scapula is a flattened, triangular bone that lies on the posteriolateral aspect of the thorax, covering parts of the 2nd to 7th ribs and connecting the clavicle to the humerus. Its body is thin and has a concave anterior surface and a convex posterior surface from which the spine of the scapula projects.

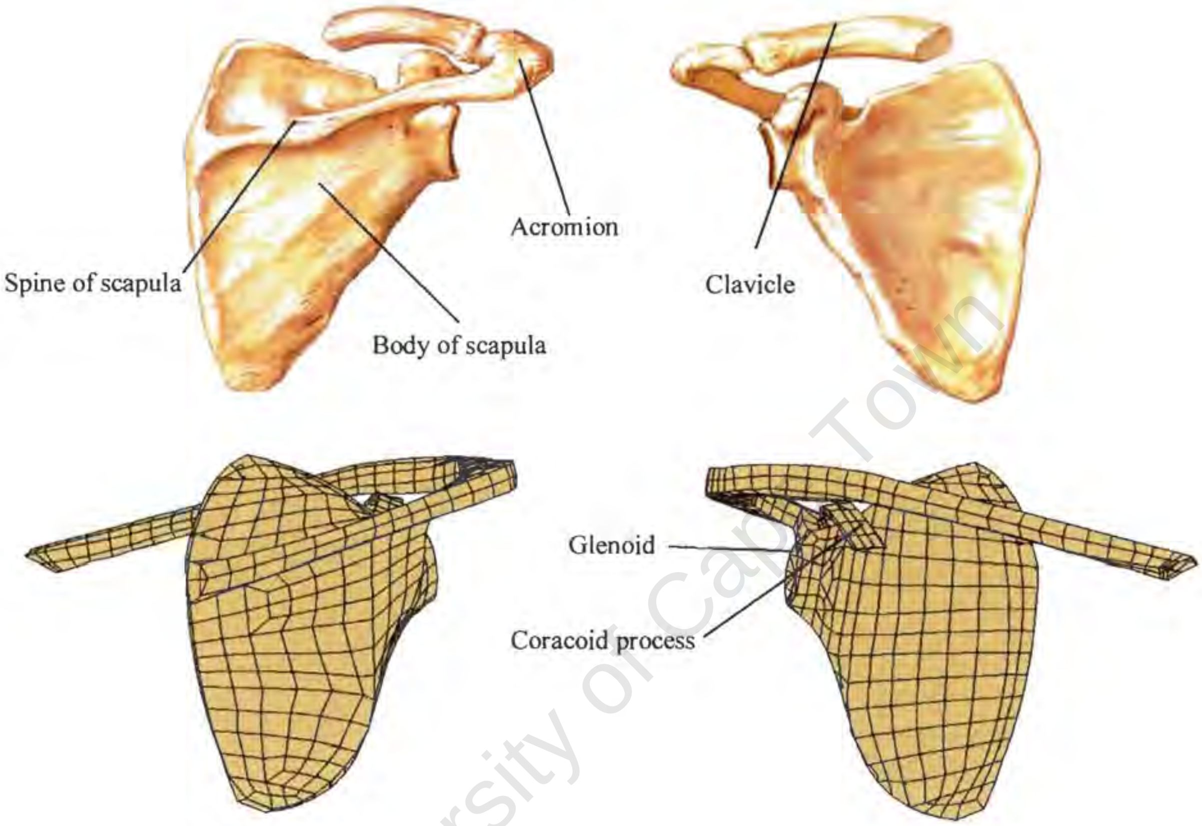

a) Rear view *b) front view*

Figure 3.6.2 Scapula [Net89] and FE-model of scapula

The smaller part, which is superior to the spine, is called the supraspinous fossa, and the larger part, which is inferior, is called infraspinous fossa. The spine continues laterally into a flattened process called the acromion, which projects anteriorly and articulates with the clavicle. Superolaterally, the scapula has a shallow glenoid cavity for the articulation with the head of the humerus. This part is called the head of the scapula from where the coracoid process arises, which in turn the biceps muscle is attached. 596 shell elements are used for the scapula model.

The humerus is the largest bone in the upper limb. Its smooth, ball-like head articulates with the glenoid cavity of the scapula. Close to this head lie the greater and lesser tubercles, which form the insertion point for the muscles that surround and move the shoulder joint The superior half of the body of the humerus is cylindrical. The shoulder joint is supported by a ligament complex, which is simply modelled by a system of 18 spring-damper elements, symbolically shown in Figure 3.6.3.

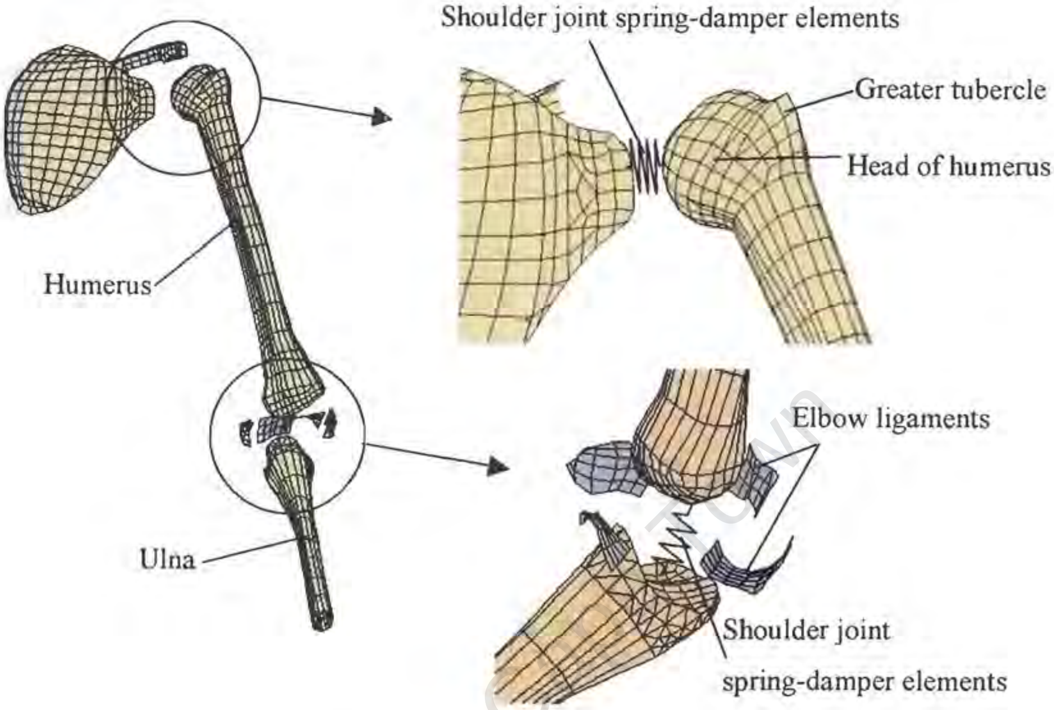

Figure 3.6.3 FE-model of shoulder and elbow joint

The humerus model consists of 504 shell elements. The lower end of the humerus is bigger and is of cylindrical shape. The forearm bones are the radius and the ulna, which is the longer forearm bone and is medially located. Only the ulna is represented by 400 shell elements in the FE-model. The upper end of the ulna is characterized by a hook-like process, which grasps the lower end of the humerus to form the elbow joint. Its movements are almost entirely limited to flexion and extension. The surrounding ligaments, which support the elbow joint are modelled by 76 membrane elements. A system of spring-damper elements between the contact surfaces of ulna and humerus simulates the damping effects within the elbow joint. This model of the elbow joint is a simplification of the real joint but can be justified by the fact that the gross motion of the arm and forearm has been shown to be adequate.

3.6.2. Muscles of the upper limb

Between the ribs and the scapula lie the serratus anterior and the subscapularis muscles, which are very important, as they serve as "buffers" in a lateral impact. Figures 3.6.4 and 3.6.5 show the serratus anterior and subscapularis muscle and the corresponding FE-models.

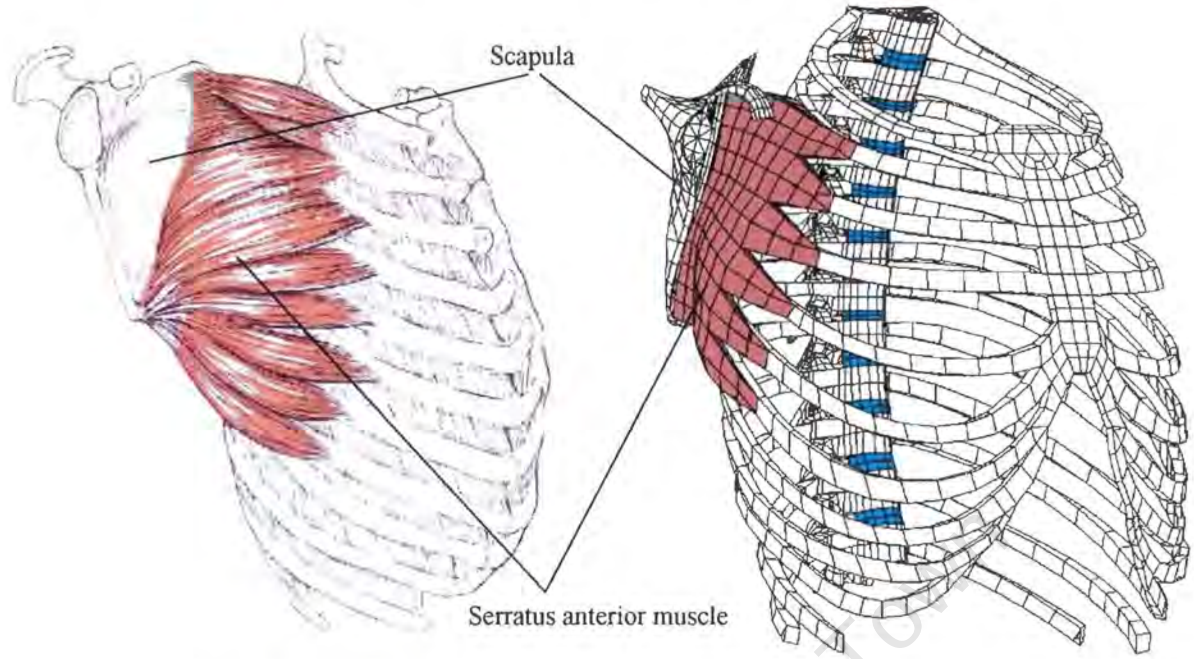

a) Serratus anterior muscle [Hei62] *b) FE-model of serratus anterior*

Figure 3.6.4 Muscles of the upper limb

The serratus anterior is a broad, flat muscle wrapped around the chest wall. It arises by eight fleshy digitations from the anterior extremities of the upper eight ribs, of which the main six have been modelled by 324 solid and 128 membrane elements. The muscle passes backwards around the chest wall and beneath the scapula to be attached to the deep surface of the scapula's medial border.

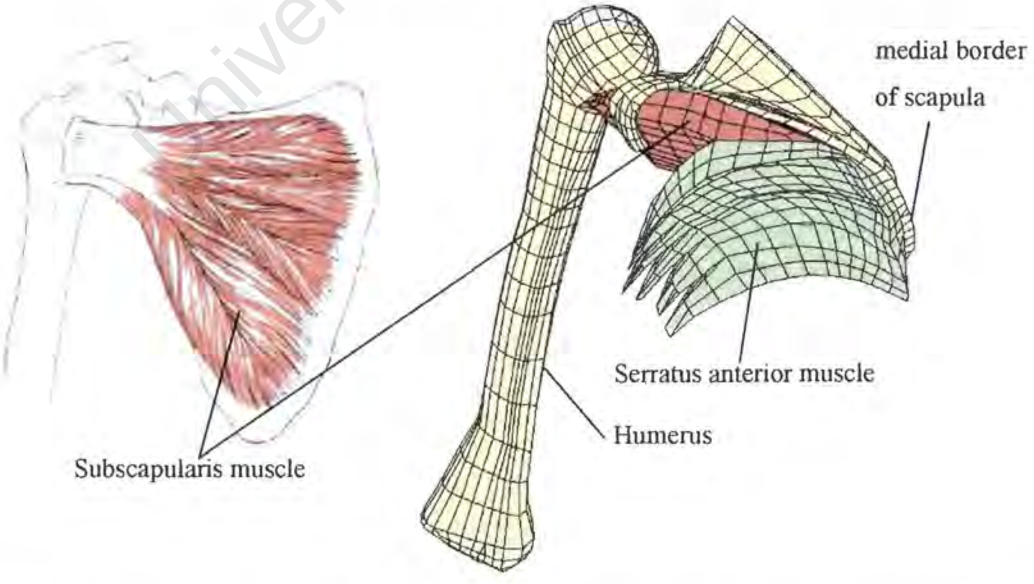

a) Subscapularis muscle [Hei62] *b) FE-model of subscapularis muscle*

Figure 3.6.5 Muscles of the upper limb

The subscapularis is a fanshaped muscle, which arises from the greater part of the subscapular fossa and passes laterally between scapula and serratus anterior to converge on a tendon, which is attached to the lesser tubercle of the humerus. 228 solid and 24 membrane elements are used to model this muscle.

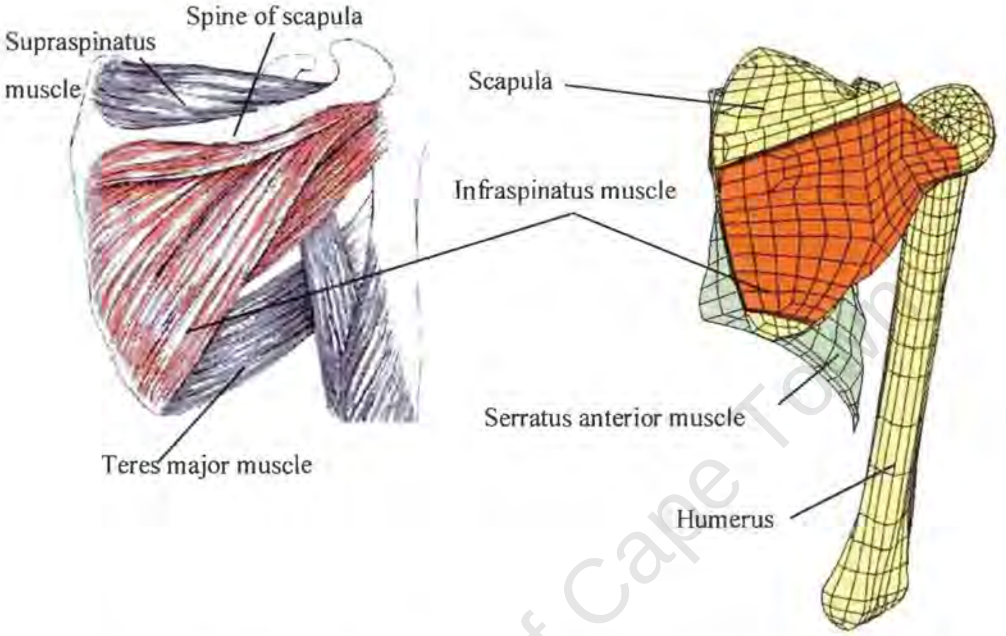

a) Infraspinatus muscle [Hei62] *b) FE-model of infraspinatus muscle*

Figure 3.6.6 Muscles of the upper limb

On the back of the scapula the infraspinatus, shown in Figure 3.6.6, is modelled using 278 solid elements. This muscle arises from the spine of the scapula and is directed towards the shoulder joint and inserts at the greater tubercle of the humerus. The smaller teres major muscle is not included in the model but its function is represented by the FE-model of the infraspinatus muscle.

Figure 3.6.7 show the rear muscles of the upper limb and the corresponding FE-models.

The rhomboid muscle is attached on the medial border of the scapula. It connects the scapula with the upper five thoracic vertebrae and the first cervical vertebrae. It serves as the main stabiliser of the back of the shoulder and is built of 244 membrane elements in the model.

Although the lattissimus dorsi muscle originates at the lower six thoracic, lumbar and sacral spines and the iliac crests of the pelvis, it is a muscle of the upper limb. This muscle covers a large area of the lower back and inserts at the medial side of the humerus.

The trapezius muscle, described earlier, also forms part of the upper limb muscles, as it connects the spine of the scapula and part of the clavicle to the thoracic and cervical spine and the lower back part of the head.

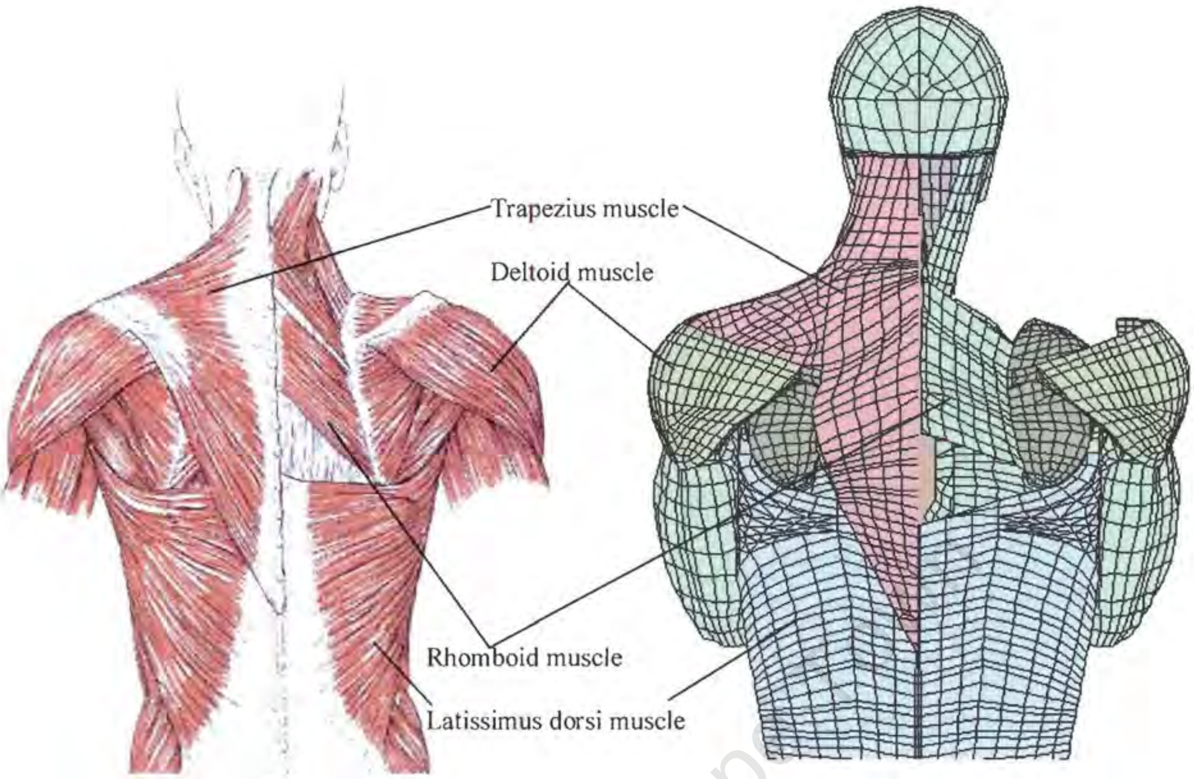

a) Rhomboid and trapezius muscle [Hei62] *b) FE-model of Rhomboid and trapezius muscle*

Figure 3.6.7 Muscles of the upper limb

In Figures 3.6.7 and 3.6.8, the deltoid muscle is shown, which covers the shoulder joint arising from the lateral third of the clavicle, the outer margin of the acromion and the lower lip of the spine of the scapula. It inserts into the humerus about half-way down on the side of the shaft. 648 solid elements and 354 membrane elements are used for the deltoid muscle model.

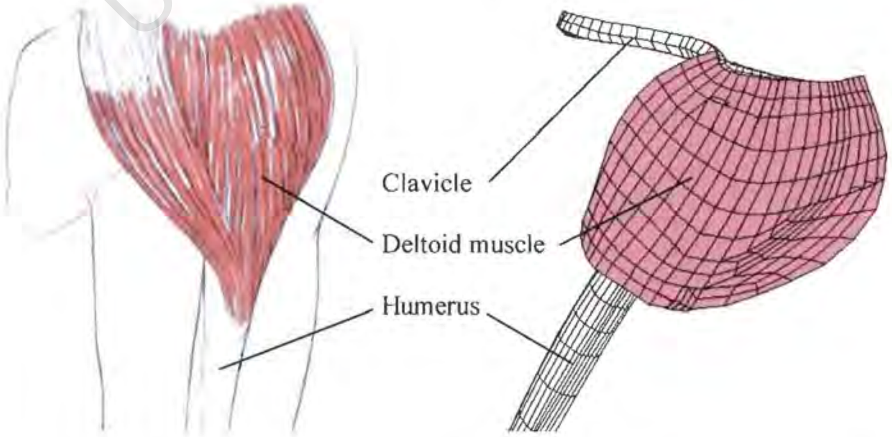

a) Deltoid muscle [Hei62] *b) FE-model of deltoid muscle*

Figure 3.6.8 Muscles of the upper limb

The deltoid muscle is directly impacted in sled test and the shoulder impactor tests. The inner surface of the deltoid covers the head of the humerus. Contact without friction is defined for this surface interaction.

The main muscle of the shoulder and arm on the anterior side of the thorax is the pectoralis shown in Figure 3.6.9.

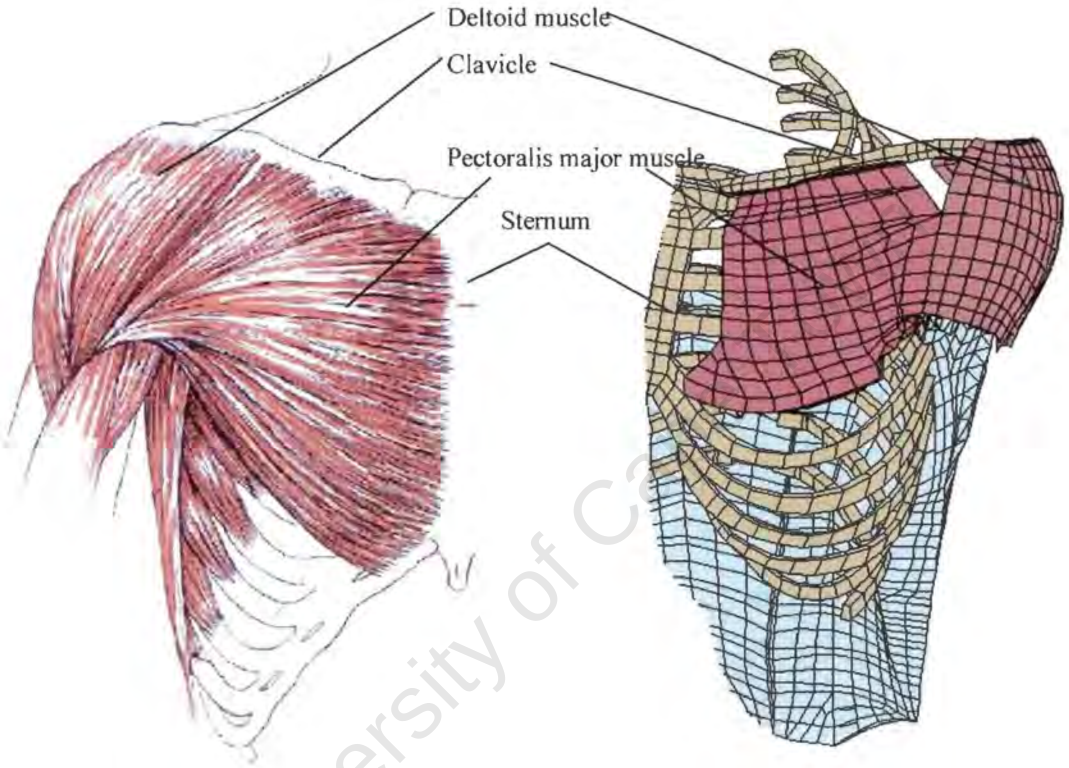

a) Pectoralis major and deltoid muscle[Hei62] *b) FE-model of Pectoralis major and deltoid muscle*
Figure 3.6.9 Muscles of the upper limb

This fan-shaped muscle has its origin on the lower border of the clavicle and the upper six costal cartilages and adjacent sternum. The muscle converges on the arm, where it inserts into the humerus next to the deltoid muscle, shown in Figure 3.6.9. 584 solids and 344 membrane elements are used for the FE-model of the pectoralis muscle.

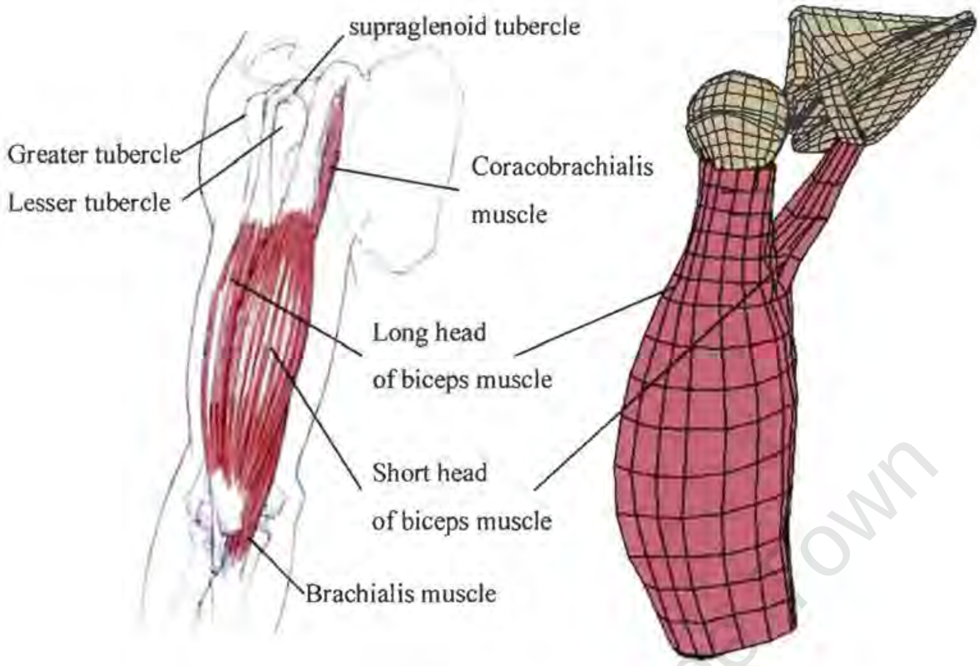

a) Biceps muscles [Hei62] *b) FE-model of biceps muscles*

Figure 3.6.10 Muscles of the arm

The main muscle groups of the arm are the biceps and the triceps muscles. The biceps consist of two parts called the long head and the short head. The short head arises from the supraglenoid tubercle within the capsule of the shoulder joint. It descends between the greater and lesser tubercle of the humerus. It has been shown during the model development that a model with this "configuration" is very unstable in lateral impact simulations, and therefore a simplified model of the biceps muscle is used instead. The long head of the biceps is connected directly to the humerus at the lower margin of the head of the humerus. The short head is located medially to the long head and arises from the tip of the coracoid process of the scapula. This upper part is modelled by 124 membrane elements that also perform the functions of the coracobrachialis muscle, which runs parallel to the short head of the biceps muscle. The lower part of the biceps muscle also models the brachialis muscle that is connected to the humerus in a simplified form. 878 solid elements are used for the FE-model of the biceps muscle.

The triceps muscles on the back of the humerus are modelled in a similar way, shown in Figure 3.6.11. The long head of the triceps is connected to the lower margin of the scapula by membrane elements, close to the shoulder joint. It joins the lateral head of the triceps at the humerus and is modelled by 502 solid elements downwards along the shaft of the humerus.

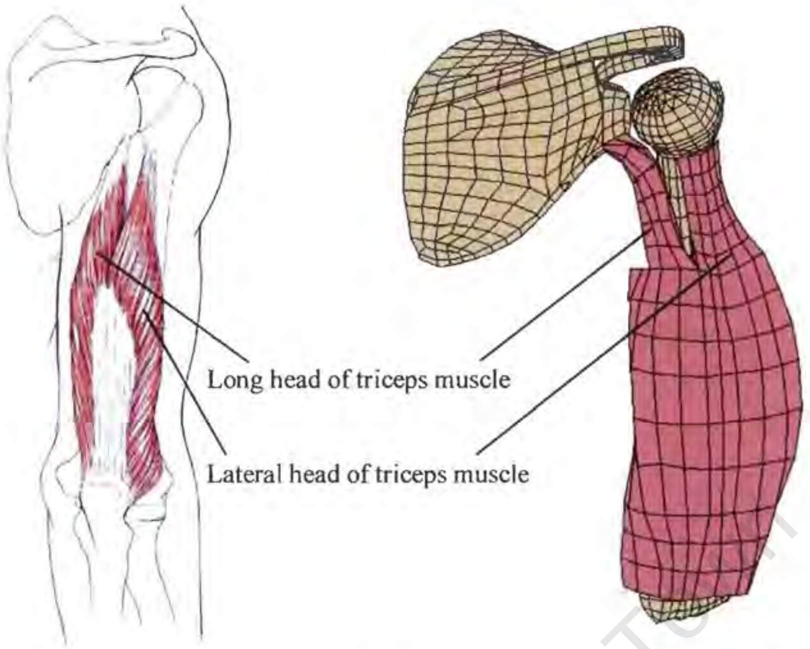

a) Triceps muscles [Hei62] *b) FE-model of triceps muscles*

Figure 3.6.11 Muscles of the arm

The lateral head is modelled by 300 solid elements and originates below the head of the humerus. The lower ends of the biceps and triceps are simplified at the lower end of the humerus, where 120 membrane elements build the bridge between the elbow joint and the ulna of the forearm, in order to stabilize the joint.

For simplification, the muscles of the forearm are not modelled according to their geometrical shape, as shown in Figure 3.6.12.

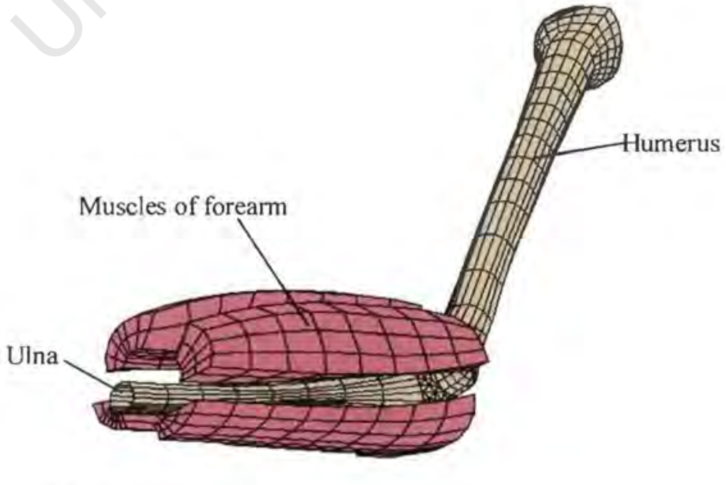

Figure 3.6.12 Muscles of the forearm

These muscles are simply represented by 380 solid elements used to fill the space occupied by the muscles of the forearm between the ulna and the skin of the forearm. A more complex model of the forearm, including the fibia and several muscle groups of the forearm, would require significantly more elements than the present model. The simplifications of the FE-model of the forearm are supported by the fact that injuries of the forearm have a low priority in side impact [Ott93, Rou85].

3.7 The Lower Limb

The functions of the lower limb are weight bearing and locomotion. The weight of the trunk is transmitted from the sacrum, through the almost immobile sacroiliac joints to the pelvic bones and from these through the hip joints to the femur. At the knee joint the femur is connected to the tibia of the leg, which in turn is connected to the foot at the ankle joint.

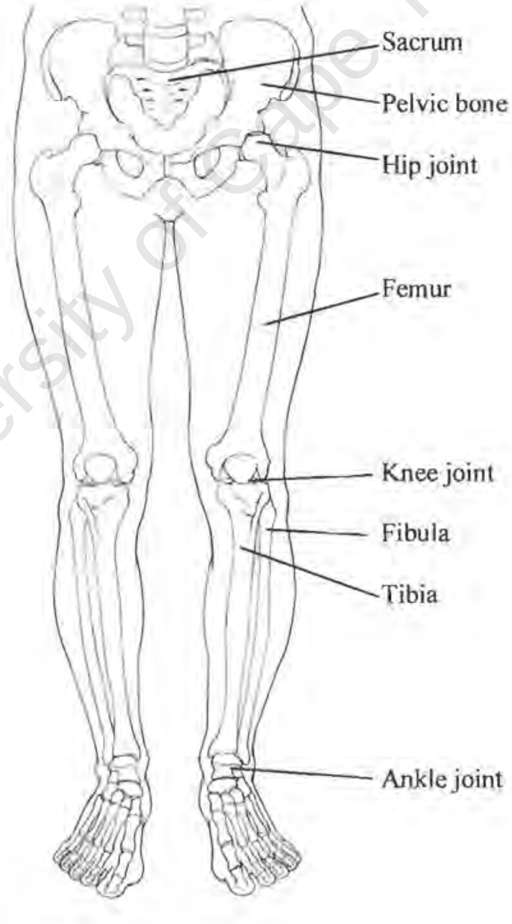

Figure 3.7.1 Skeleton of the lower limb [Hei62]

3.7.1 The Bones of the Lower Limb

The three bones of the pelvis: the pubis, ischium and ilium, have been described more fully in section 3.4, together with the sacroiliac joint and the pubic symphysis. The hip joint is the third joint of the pelvis and is formed by the acetabulum and the femur. The acetabulum lies at the site where the three parts of the hip bone fuse. It is a cup-shaped cavity facing laterally and slightly downwards and forwards. The surface of the acetabulum is partially covered by an incomplete ring of cartilage. The non-articular floor of the acetabulum contains a pad of fat. A fibrous capsule is attached proximally to the margin of the acetabulum. This capsule is reinforced by three strong ligaments extending from the pelvic bone to the femur. These are the pubofemoral, ischiofemoral and iliofemoral ligaments. All three ligaments take a spiral course around the neck of the femur and are arranged in such a way that they become taut in full extension.

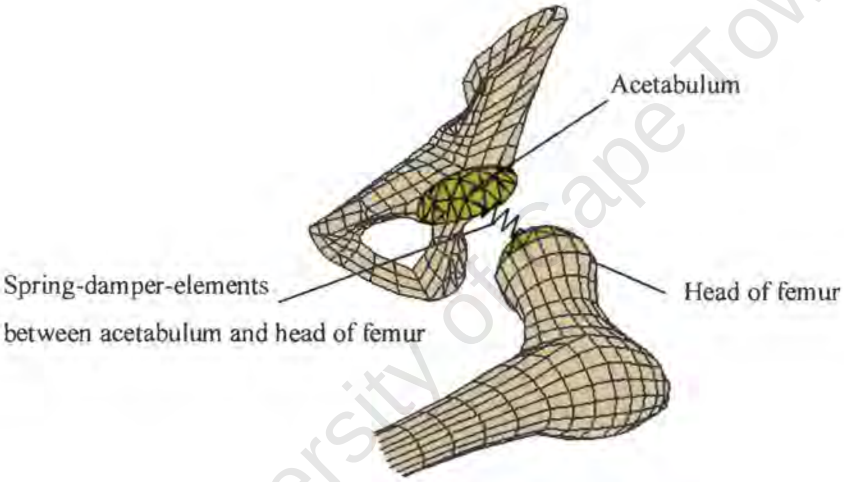

Figure 3.7.2 FE-model of the hip joint and schematical spring-damper element

The damping effects of the cartilage material within the ball socket joint are considered by a system of spring-damper elements between the femoral head and the acetabulum. The complex arrangement of ligaments is not included in the model, since they are of minor importance during side-impact loading, as they do not bear compression forces. The acetabulum consists of 74 triangular shell elements that have the same configuration as the triangular shell elements of the femoral head, with which they form a contact pair.

The femur, illustrated in Figure 3.7.3, is the longest, strongest and heaviest bone of the body. Distal to the head is a stout neck, which is directed laterally and tilts slightly backwards forming an angle of about 125 degrees with the long axis of the shaft. At the point where the neck joins the shaft, are two substantial projections, the greater and the lesser trochanter. They provide attachments for several muscles of the gluteal region.

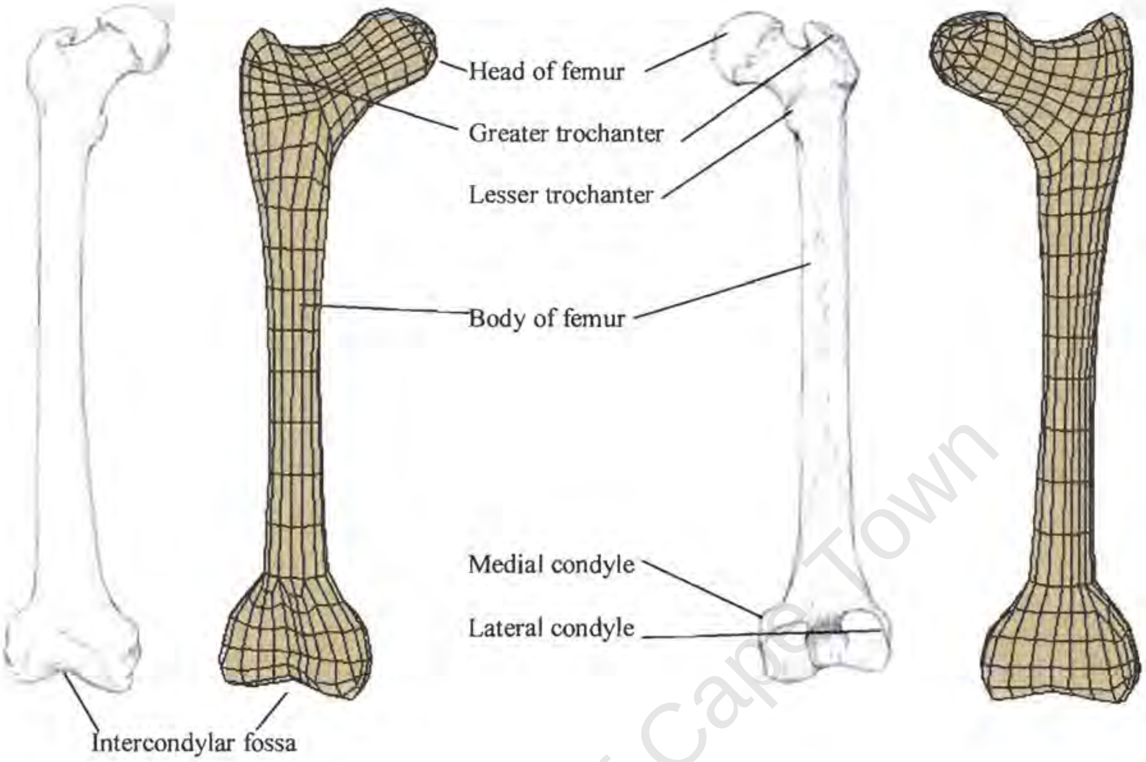

a) Front view *b) Rear view*

Figure 3.7.3 Femur and FE-model of the femur [Hei62]

The body of the femur is slightly bowed anteriorly and is narrowest at its midpoint. Its middle two-quarters are approximately circular in transverse section. The lower end is formed by two condyles that are separated by an intercondylar fossa. The femoral condyles articulate with the corresponding condyles of the tibia. The FE-model of the femur consists of 620 shell elements.

The tibia and fibula are the bones of the lower leg of which the tibia supports most of the weight. For reasons of simplification only the tibia is included in the FE-model and consists of 480 shell elements as shown in Figure 3.7.4. The upper end of the tibia is formed by the medial and lateral condyles. The shaft of the tibia is triangular in section. The lower end of the tibia is bigger and more quadrangular in section than the shaft.

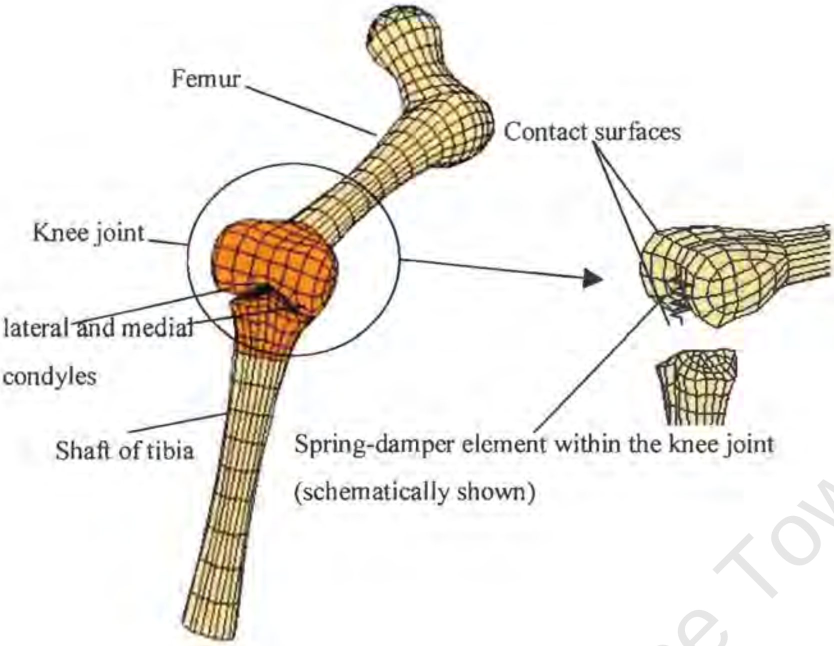

Figure 3.7.4 FE-model of knee joint and tibia

At the knee joint the thigh articulates with the leg. The bony articulating surfaces, covered by hyaline cartilage, consist of the two disc-like femoral condyles and intervening bony bridge, the patella, and the superior surfaces of the tibia. Although it permits some rotation, it is primarily a hinge joint. Its stability depends on the strength of a complex system of ligaments and muscles, which are simply modelled by a system of spring-damper elements as illustrated in Figure 3.7.4.

3.7.2 The Muscles of the Lower Limb

Figure 3.7.5 illustrates the musculature of the gluteal region, which is represented by 1948 solid elements that simply surround the femur and pelvis. The muscles of the lower leg are modelled by 432 solid elements. A lumped mass at the lower end of the tibia model takes into account the mass of the foot.

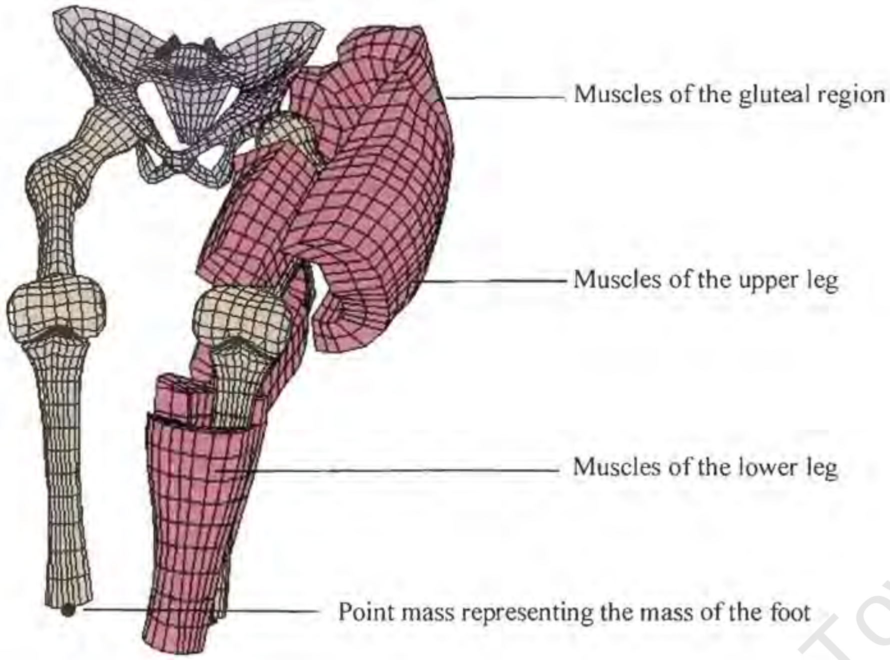

Figure 3.7.5 Muscles of the lower limb

3.8 Summary of FE-Model Data

Figure 3.8 shows the entire FE-model of the human body.

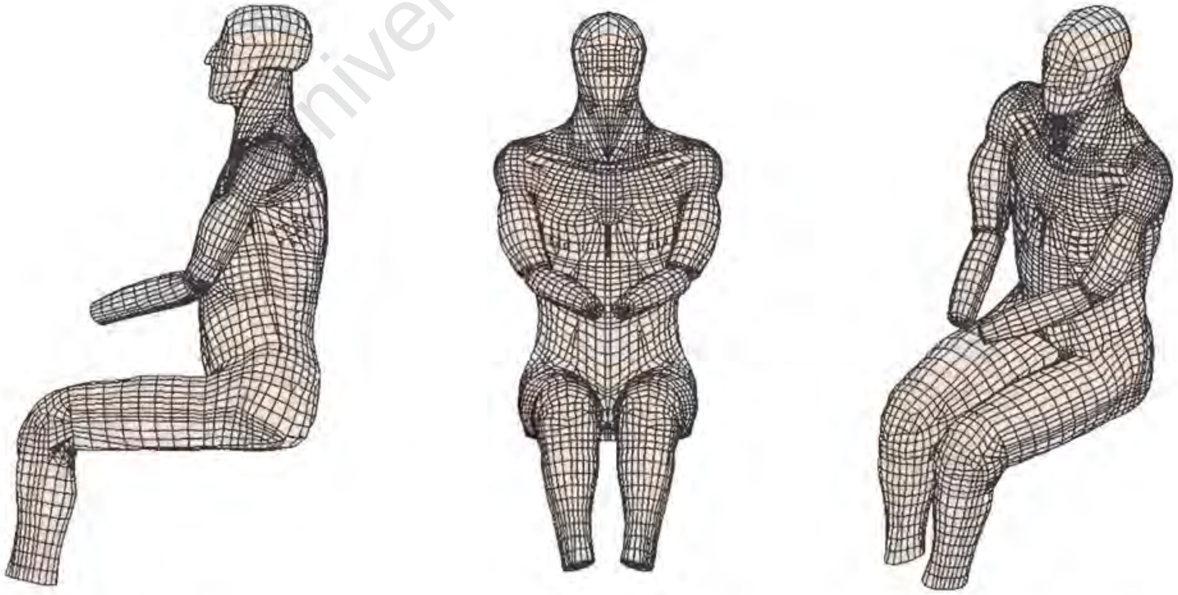

a) Side view *b) front view* *c) Oblique front view*

Figure 3.8.1 Entire FE-model of the human body

The outer skin is modelled using 4800 membrane elements, which are defined as a contact surface with the surfaces of impactors and the sled test wall.

Table 3.8.1 summarises the number of elements used for the bones and joints, Table 3.8.2 for the muscles and ligaments and Table 3.8.3 for the visceral contents.

Bones						
	Number of shell elements	Young's modulus [Mpa]	Yield Stress [Mpa]	Ultimate Stress [Mpa]	Poisson 's ratio	Density [g/cm^3]
Back						
T1 – T12	3360	5000	150	180	0.3	2.5
L1 – L5	1400	5000	150	180	0.3	2.5
Thorax						
Ribs	1962	1000	9	10	0.3	2.0
Costal cartilage	478	2500	10	13	0.3	2.5
Sternum	148	5000	10	13	0.3	2.5
Pelvis						
Pelvic bones	1180	2500	120	150	0.3	2.5
Acetabulum		5000	150	180	0.3	2.5
Sacrum	320	5000	150	180	0.3	2.5
Head and Neck						
Head rigid elements	520					
C1	162	5000	150	180	0.3	2.5
C2	278	5000	150	180	0.3	2.5
C3 – C7	1200	5000	150	180	0.3	2.5
Upper Limbs						
Clavicle (each)	588	1000	9	10	0.3	2.5
Scapula (each)	596	12000	150	180	0.3	2.5
Humerus (each)	504	12000	150	180	0.3	2.5
Ulna (each)	400	12000	150	180	0.3	2.5
Lower Limbs						
Femur (each)	620	5000	150	180	0.3	2.5
Tibia (each)	480	5000	150	180	0.3	2.5

Table 3.8.1 Number of elements used for bone models

Muscles							
	Number of solid elements	Number of membrane elements	Young’s modulus [Mpa]	Yield Stress [Mpa]	Ultimate Stress [Mpa]	Poisson ‘s ratio	Density [g/cm^3]
Back							
Erector Spinae	678	128	20	0.2	0.4	0.3	1
Trapezius	767	-	20	0.2	0.4	0.3	1
Latissimus	720	-	20	0.2	0.4	0.3	1
Thorax							
Intercostal muscles inner + outer layer	-	1144	20	0.6	0.8	0.3	1
Abdomen							
Rectus abdominis	178	-	20	0.6	0.8	0.3	1
Abdominis muscles	768	-	20	0.6	0.8	0.15	1.3
Fat	318	-	20	0.6	0.8	0.15	1.3
Head and Neck							
Spenius capitis	-	128	20	0.6	0.8	0.3	1
Semispinalis capitis	648	-	20	0.2	0.4	0.3	1
Sternocleido mastoid	192	-	20	0.6	0.8	0.3	1
Upper Limbs							
Serratus anterior muscle (each)	324	128	20	0.2	0.4	0.3	1
Subscapularis (each)	228	24	20	0.2	0.4	0.3	1
Infraspinatus (each)	278		20	0.2	0.4	0.3	1
Rhomboid (each)	-	244	100	0.8	1.0	0.3	1
Deltoid (each)	648	354	20	0.6	0.8	0.3	1
Pectoralis (each)	584	344	20	0.2	0.4	0.3	1
Biceps (each)	878	124	20	0.2	0.4	0.3	0.8
Triceps (each)	802	120	20	0.2	0.4	0.3	0.8
Muscles of forearm (each)	380	-	20	0.6	0.8	0.3	1
Lower Limbs							
Gluteal region	1948	-	20	0.2	0.4	0.3	1
Upper Leg (each)	864	-	20	0.6	0.8	0.3	1
Lower Leg (each)	520		20	0.6	0.8	0.3	1

Table 3.8.2 Number of elements used for muscle models

Joints, Ligaments and Visceral contents									
	No of solid elements	No of membr. elments	Young's modulus [Mpa]	Yield Stress [Mpa]	Ultimate Stress [Mpa]	Poisson 's ratio	Density [g/cm^3]	Spring No / (N/mm)	Damper No / (Ns/mm)
Back									
Intervert. Disc	384								96 /
Cervical			500	1.0	1.2	0.3	2.0		0.05
Thoracic			500 / 700	1.0 / 1.2	1.2 / 1.4	0.3	2.0		0.05
Lumbar			500	1.0	1.2	0.3	2.0		0.05
Supraspinous ligament									48 / 0.05
Anterior longitudinal ligament		60	1.5	0.2	0.4	0.3	1.0		
ligament flava		60	1.5	0.2	0.4	0.3	1.0		
interspinous ligament		80	10	0.2	0.4	0.3	1.0		
Abdomen									
Inguinal ligament		86	1.5	0.2	0.4	0.3	1.0		
Head and Neck									
Cruciform ligament		12	10	0.2	0.4	0.3	1.0		4 / 0.05
Alar ligament		18	1.5	0.2	0.4	0.3	1.0		
Upper Limbs									
Shoulder joint (each)								12 / 0.1	12 / 0.05
Elbow joint (each)								76 / 0.1	16 / 0.05
Lower Limbs									
Hip joint								28 / 0.1	28 / 0.05
Knee joint								22 / 0.15	22 / 0.05
Thoracic contents	518		0.3	0.1	0.2	0.2	1.6		
Heart	120		1.0	0.2	0.4	0.2	1.6		
Abdominal contents	442		0.5	0.2	0.35	0.2	1.6		
Pelvic contents	244		0.4	0.2	0.3	0.2	1.6		
Skin		4800	10	0.6	0.8	0.3	1.0		

Table 3.8.3 Number of elements used for joint, ligament and viceral contents models

4. Validation of the FE-Model

This chapter describes the validation procedure of the FE-model of the human body. The biomechanical responses of the simulations are compared to those of the corresponding experimental cadaver tests that have been described in section 2.1. The following tests were examined:

a) Shoulder impactor and sled tests (Section 4.2)

b) Head-Neck sled tests (Section 4.3)

c) Thorax impactor and sled tests (Section 4.4)

d) Abdomen impactor and sled tests (Section 4.5)

e) Pelvis impactor and sled tests (Section 4.6)

The validation of a numerical model is one of the most important part of the model development. During the validation process, results of the model are compared to the results of the corresponding cadaver experiments. This feedback is used to investigate the influence of the model on the simulation. This procedure is intended not only to determine the correct values of the parameters, as these are mainly the properties of the bone, muscles and ligaments, but also to investigate the sensitivity of these parameters. These material properties, presented in Tables 3.1.1 to 3.1.4, have been chosen to optimise the entire model.

Some general principles need to be considered for the validation procedure. A single test validation may be misleading since it is possible that the model parameters may only be valid for that test. Therefore validation should be conducted over various test severities that cover the range of expected severities in which the model may be used. The tests themselves may not be repeatable, so that several tests of the same severity should be considered. The results of cadaver tests are often presented in the form of corridors that include a wide range of responses of different cadavers subjected to the same impact load. The quality of a model to simulate the cadaver tests can be determined by how closely the simulated response falls within the corridor defined by the experiments. However, a model with known systematic differences between the model and the test result might still be valuable. Furthermore, it is important that a model is able to predict to some extent the outcome of certain experiments. A simple model with a few parameters might be validated for a single test condition but might not be able to predict the results of more complex tests.

In complex FE-models the number of parameters exceeds the number of experiments, resulting in a mathematically undetermined system. Therefore, assumptions in terms of parameter definition are inevitable.

The computational time needed to simulate 60 ms of a cadaver sled test event is about 48-58 hours on a SGI Origin 2000 computer. The number of evaluation steps to validate the FE-model is therefore limited by practical time considerations.

In section 3.1 the problematic nature of defining the mechanical properties of biological materials has already been discussed. For many of the material parameters, values have to be estimated prior to the validation. These values need to be within the range of experimental values. During the validation process, these values are then adjusted according to the model's response, to find a configuration of model parameters that satisfies almost all of the tests.

4.1 Visual comparison of the sled test kinematics

4.1.1 Visual comparison of 6.7 m/s WSU sled test

The series of pictures in Figure 4.1.1 shows the kinematics of the FE-model in a 6.7 m/s WSU sled test in comparison with the original cadaver test recorded as sic07. The time frame at which the pictures of the cadaver motion are captured is estimated, because the time could not be extracted from the experiment film. Animation files of the simulated cadaver sled tests can be found on the accompanying CD.

a) Cadaver test *b) FE-model*

Figure 4.1.1 Comparison of the impact dynamics in the 6.7 m/s WSU sled test after ~25 ms

The first picture shows the impact after about 25 ms, at which point significant shoulder deformation can be observed for the cadaver and the FE-model. In both cases there is no head or thorax movement visible at this stage of the impact relative to the sled.

a) Cadaver *b) FE-model*

Figure 4.1.2 Comparison of the impact dynamics in the 6.7 m/s WSU sled test after ~40 ms

The second picture presents the impact after about 40 ms. The motion of the impacted shoulder cannot be observed in the cadaver experiment, as it intrudes laterally into the body. The shoulder motion seems to be different in the simulation, as the FE-shoulder tends to move slightly downwards, which cannot be observed to the same extent in the cadaver experiment. This shoulder motion causes the non-impacted shoulder and arm to raise more than in the experiment. The motion of the shoulder probably influences the head rotation. It can be seen that the cadaver's head rotates slightly more after 40 ms than in the simulation. The movement of the lower part of the body differs between the cadaver and FE-model. While the legs of the cadaver tend to move slightly forward, the legs of the FE-model hardly show any forward movement. Furthermore, the pelvis of the FE-model is lifted upwards on the non impacted side, which cannot be observed in the cadaver experiment.

a) Cadaver *b) FE-model*

Figure 4.1.3 Comparison of the impact dynamics in the 6.7 m/s WSU sled test after ~60 ms

After 60 ms some rotation around a vertical axis can be observed in the cadaver motion, which does not happen in the simulation. The rotation of the head is similar in both cases. The head impacts the shoulder beam after 65 ms in the simulation and it is assumed that the cadaver head impact occurs at the same time.

a) Cadaver *b) FE-model*

Figure 4.1.4 Comparison of the impact dynamics in the 6.7 m/s WSU sled test after ~70 ms

After about 70 ms the impact is almost over. The cadaver continues to rotate around the vertical axes while the FE-model rebounces laterally without significant rotation. In contrast to the cadaver motion, the pelvis of the FE-model lifts off the seat for a short duration. The right leg, which does not impact the wall, bounces back laterally after a short contact with the left leg in the simulation. In the cadaver experiment both legs move closer together after the impact, which might be due to influence by the body rotation around the vertical axis.

4.1.2 Visual comparison of 8.9 m/s WSU sled test

The following picture series shows the impact dynamics of a cadaver in a more severe WSU sled test at the higher velocity of 8.9 m/s in comparison to the response of the FE-model. The cadaver test was recorded as sic04.

a) Cadaver *b) FE-model*

Figure 4.1.5 Comparison of the impact dynamics in the 8.9 m/s WSU sled test after ~25 ms

After about 25 ms the FE-model shows significant shoulder deformation already, which is difficult to observe in the cadaver experiment. The legs of the FE-model are in contact at this stage already, which cannot be observed in the experiment due to greater initial distance between the legs of the cadaver prior to impact. The head rotation is similar in both cases and is still small at this stage of the impact.

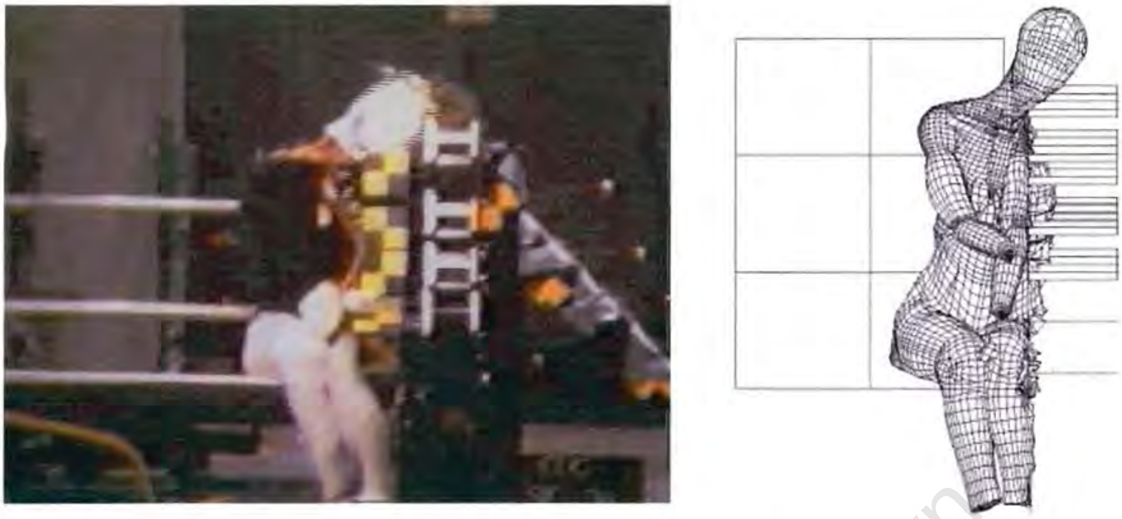

a) Cadaver *b) FE-model*

Figure 4.1.6 Comparison of the impact dynamics in the 8.9 m/s WSU sled test after ~40 ms

Figure 4.1.6 shows the comparison of the impact after about 40 ms. It is assumed that the shoulder of the FE-model penetrates deeper into the thorax than in cadaver case, although it cannot be well observed. The different shoulder deformation probably influences the head rotation, which is less in the case of the FE-model at this stage of the impact. The simulated leg motion correlated well with that observed in the cadaver test.

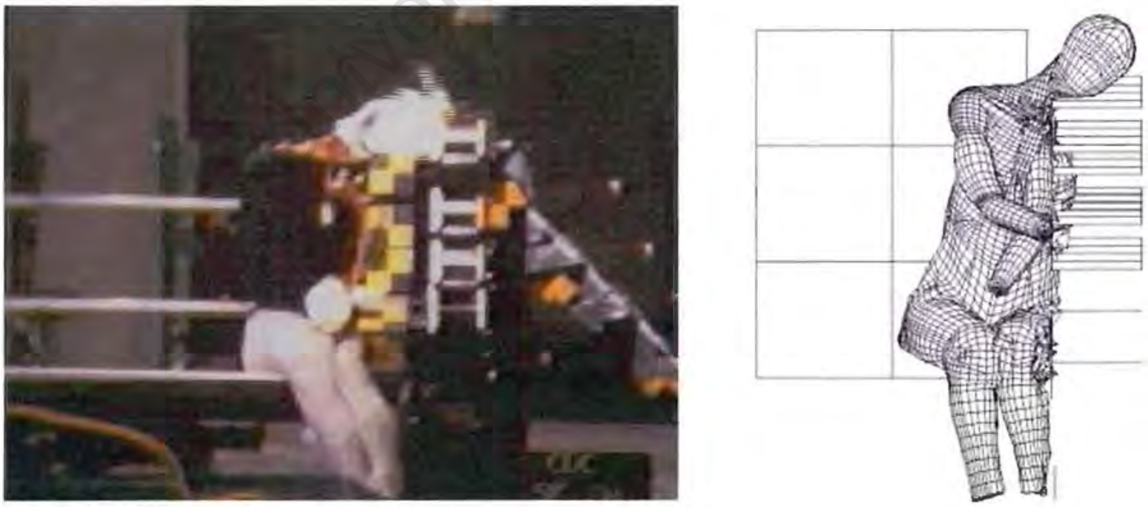

a) Cadaver *b) FE-model*

Figure 4.1.7 Comparison of the impact dynamics in the 8.9 m/s WSU sled test after ~45 ms

Figure 4.1.7 shows the impact after about 45 ms, when almost the entire side of the head of the cadaver impacts the shoulder beam. The head of the FE-model impacts the shoulder beam only at the area of the jaw or chin, which leads to significant strain of the neck. The upper limb of the impacted side of the FE-model is significantly deformed and pushed downwards, which in turn causes the neck to impact the shoulder beam. The legs of the FE-model have started to bounce off the wall again, which cannot be observed in the cadaver test at this stage.

a) Cadaver *b) FE-model*

Figure 4.1.8 Comparison of the impact dynamics in the 8.9 m/s WSU sled test after ~55 ms

Figure 4.1.8 shows the impact after about 55 ms, when the rebounce phase starts. The cadaver does not show the same body rotation around the vertical axis as the cadaver at 6.7 m/s illustrated before. The head rotation of the FE-model still differs from that observed of the cadaver. The pelvis of the FE-model lifts upwards and the non impacted lower leg of the FE-model bounces off, which does not happen in the cadaver experiment.

The visual comparisons give a first impression that the FE-model behaves similar to the cadaver in the WSU sled tests. This qualitative comparison may be considered as a first validation step to examine differences in the gross motion of the cadaver and the FE-model. For parameter investigations a quantitative comparison is needed, as for example the comparison of measured force and acceleration responses.

4.2 Shoulder Validation Results

4.2.1 Shoulder impactor test

In the first shoulder validation test, a 23 kg impactor is aimed at the shoulder, the centre aligned with the shoulder joint. It impacts the cadaver or model at an initial velocity of 4.5 m/s. A picture series of this test simulation is shown in Figure 4.2.1 and can be found in movie-format on the accompanying CD.

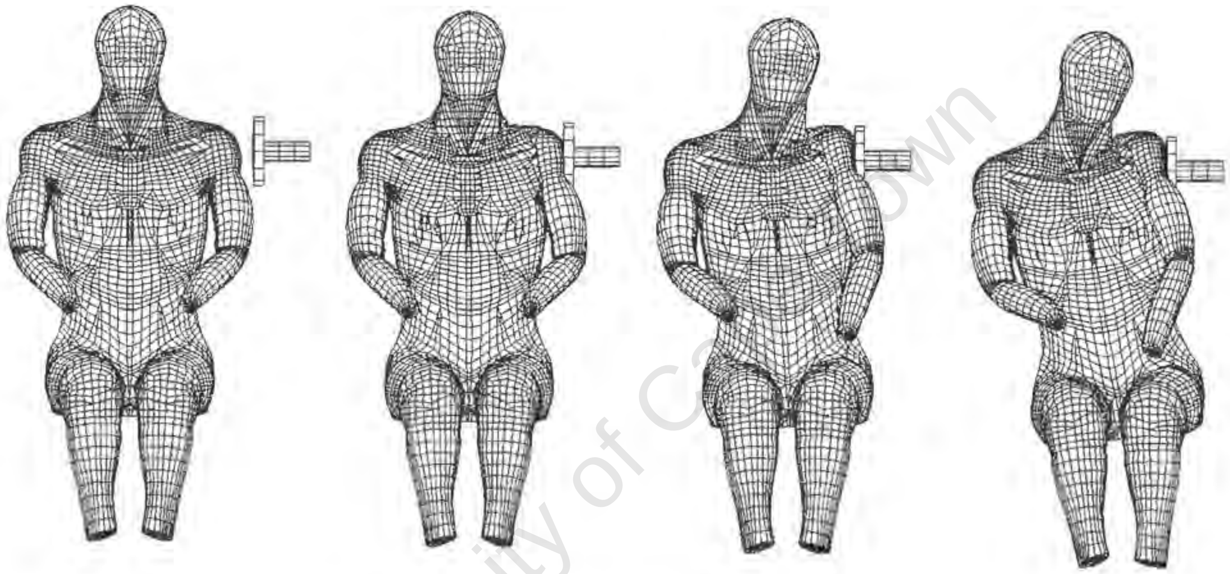

a) time = 0ms
Initial conditions prior to impact

b) time = 5 ms
Impactor starts to deform deltoid muscle

c) time = 10 ms
Scapula moves inwards

d) time = 25 ms
Maximum shoulder deflection of 39.8 mm

Figure 4.2.1 Shoulder impactor test

Figure 4.2.1 a) shows the initial condition of the model prior to impact. At time = 5 ms the impactor starts to deform the deltoid muscle which does not dissipate much energy. The impactor pushes the tubercle of the humerus against the scapula, which moves inwards at time = 10 ms. The dynamics of the FE-shoulder model are determined by the buckling behaviour of the clavicle at this stage of the impact. It is assumed that in real life the clavicle deforms and breaks without a significant buckling process, which in turn describes a different motion as observed in the simulation. In section 3.1 it was stated that no material failure criterion is used in the FE-model. This influences the dynamics of the clavicle, because the deformation behaviour is not determined by the fracture of the clavicle but by its buckling pattern. The clavicle motion is presented in more detail in Figure 4.2.2. Nevertheless, this shoulder model does perform well in terms of maximum shoulder deflection, which is reached at time = 25 ms, with a maximum value of 39.8 mm. In the cadaver experiments a maximum shoulder deflection relative to the thoracic spine showed an average value of 37.5 mm [ISO89]. Allowing a ± 10% deviation from this value gives a range of 34 to 41 mm for the maximum shoulder deflection. The result of the FE-model lies within this range.

Figure 4.2.2 shows a picture series of the shoulder impact, illustrating the deformation of the clavicle and the movement of the bony shoulder parts.

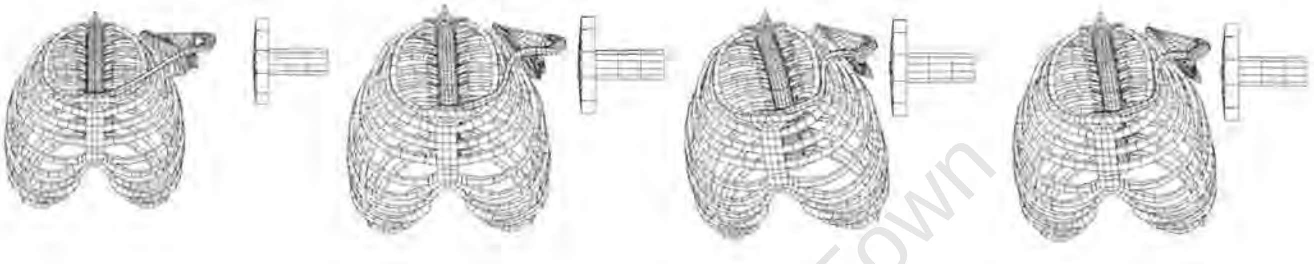

a) time = 0 ms
Initial conditions
prior to impact

b) time = 5 ms
The clavicle starts
to buckle

c) time = 10 ms
The clavicle
deforms into an
s-shaped curve

d) time = 25 ms
Maximum
shoulder deflection
of 39.8 mm

Figure 4.2.2 Deflection response of the bony shoulder parts

As can be seen in Figure 4.2.2, the clavicle deforms into an s-shaped curve between 5 ms and 10 ms. In real life the clavicle would probably have been fractured at only one section resulting in a different clavicle-scapula motion. The rib cage, on the other hand, does not deform significantly during the shoulder impact, as can be observed at time = 25 ms, when the maximum shoulder deflection occurs.

The resulting forces are calculated by multiplying the recorded acceleration of the impactor with its mass. Figure 4.2.3 compares the response of the model with the results of the corresponding cadaver test as defined in the ISO requirements.

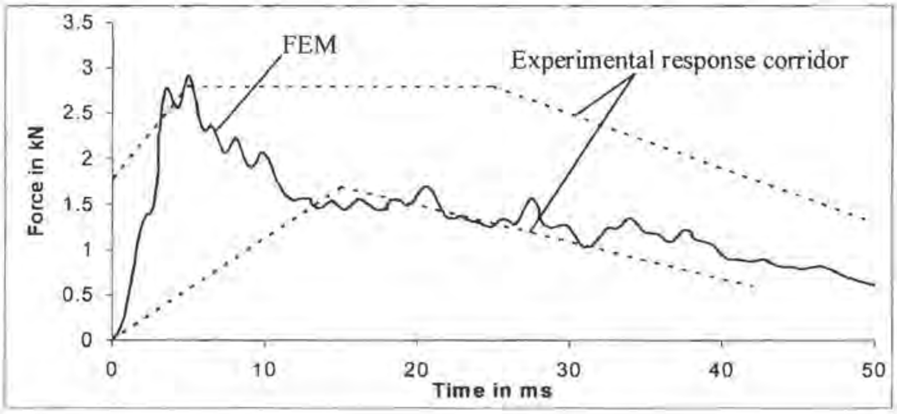

Figure 4.2.3 Shoulder impactor force-time history

As is evident from the figure above, the simulated force-time history of this impact begins with a steep upward slope within the first 5 ms, at which time the force value peaks at a level of ~2.7 kN, which is slightly higher than the upper boundary of the experimental response corridor defined by the ISO-requirements. The buckling effect of the clavicle causes the force to drop to ~1.4 kN at ~10 ms when it reaches the force level of the lower response boundary. The force then "swings" around the lower border of the response corridor. In terms of force-time and maximum deflection response, the FE-model fulfils the response requirements defined by the ISO-standard.

4.2.2 Shoulder sled test

The impact response of the shoulder in a series of cadaver sled tests performed at Wayne State University described in Section 2.1.1 was investigated in detail by Irwin et al. [Irw93]. The relevant tests that were used for the validation of the FE-model were the two unpadded tests, shown in Section 4.1 with initial velocities of 8.9 m/s and at 6.7 m/s respectively.

Figure 4.2.4 consists of a series of photographs taken by an overhead camera during the cadaver sled test. Alongside is the corresponding series of images generated by the FE-model with regard to the shoulder impact dynamics.

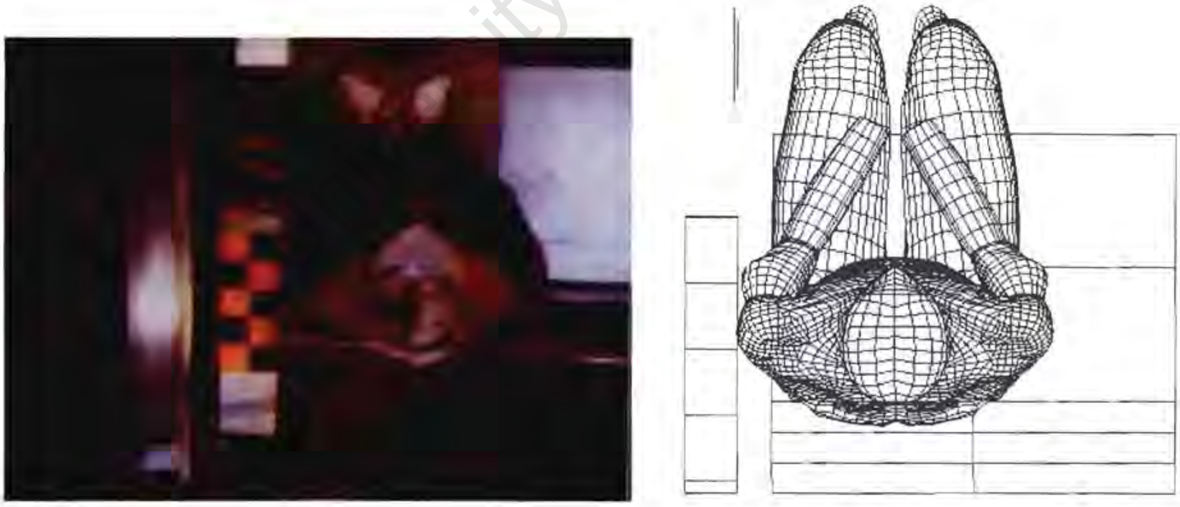

a) time = 0 ms

Figure 4.2.4 Comparison of the shoulder deformation between cadaver and FE-model

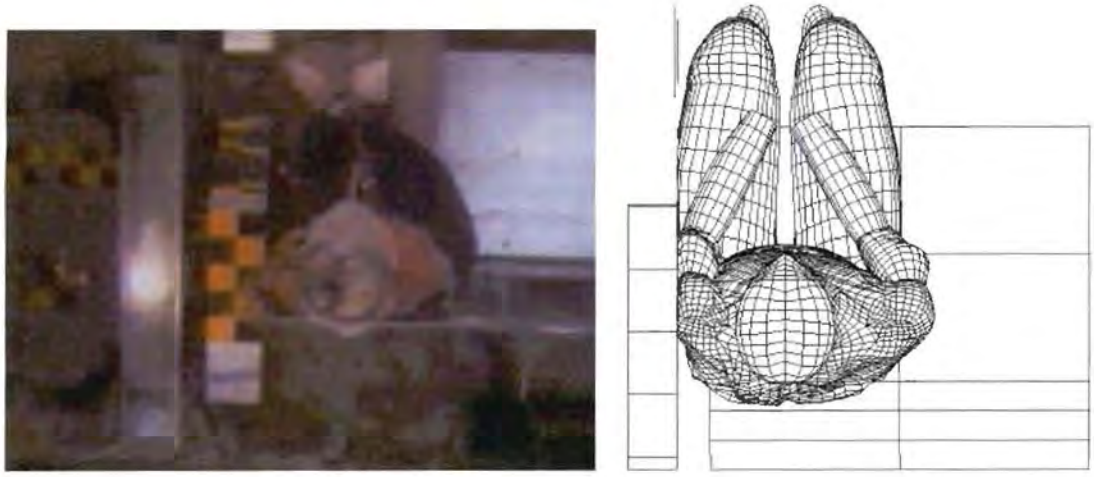

b) time = 30 ms

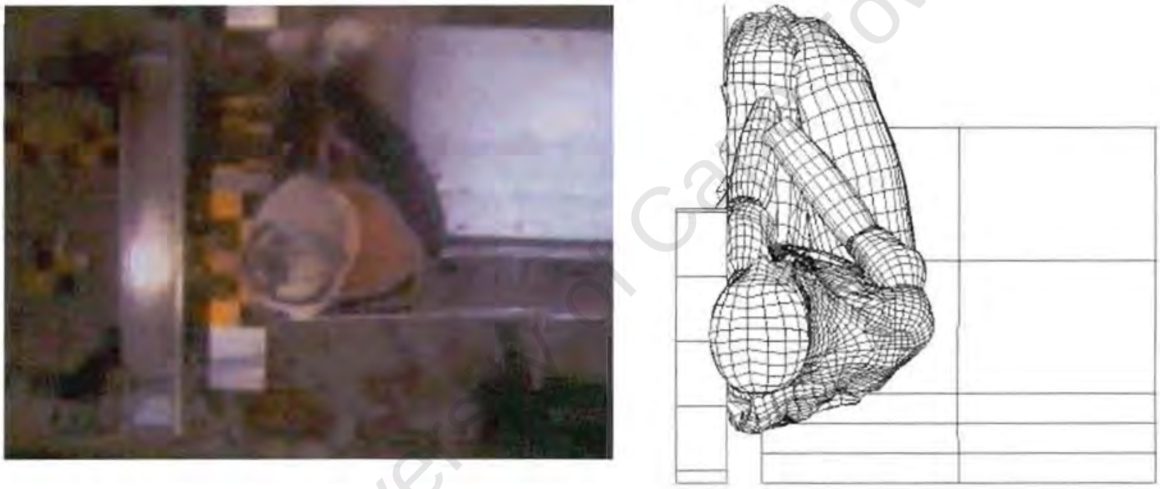

c) time = 40 ms

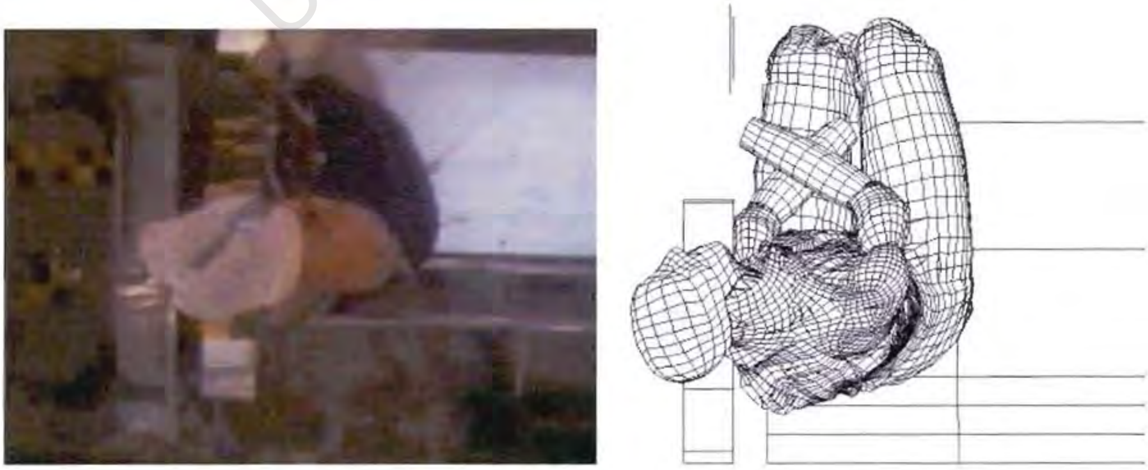

d) time = 60 ms

Figure 4.2.4 Comparison of the shoulder deformation between cadaver and FE-model

The first picture shows the initial state prior to impact. After 30 ms the shoulder has started to deform without significant influence on the motion of the upper body. At time = 40 ms the shoulder has intruded into the body and the head has started to rotate. At time = 60 ms the maximum shoulder deflection has been reached. The shoulder motion cannot be observed any longer, as the head rotates between shoulder and overhead camera. Although the visual comparison of the simulated dynamics with those observed in the cadaver experiments is difficult, the picture series gives the impression that the simulated shoulder and head-neck dynamics correlate fairly well with the cadaver experiment.

The shoulder structure is perhaps the most difficult skeletal structure to observe in side impacts, because it seems to disappear completely into the body. Since the WSU sled tests were multipurpose tests, it was not always possible to place the cameras at optimal locations for filming the photographic targets attached to the shoulder of the cadaver [Irw93]. As described in Section 2.1.1, pressure transducers were built into the shoulder beam, which the cadaver impacts, to measure the force response during the impact. Figure 4.2.5 compares the force-time responses of these shoulder beams of the FE-model with the corresponding experimental result obtained during the sled test.

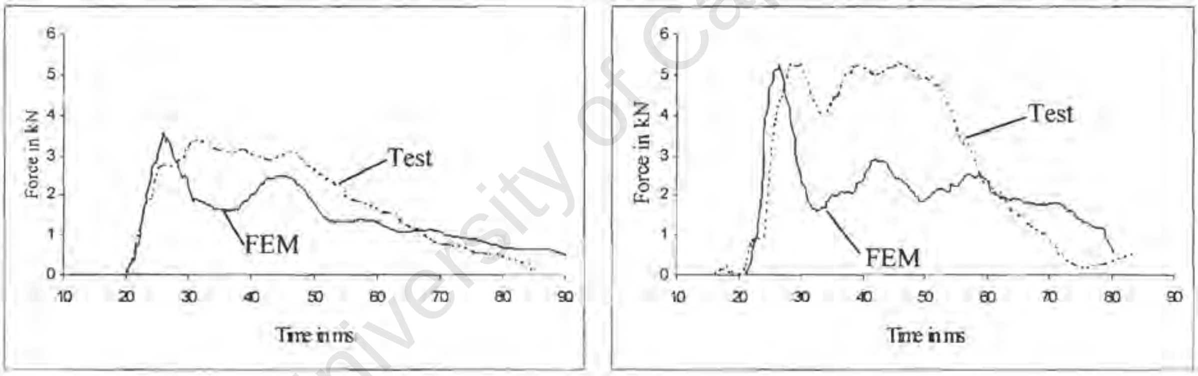

a) 6.7 m/s impact velocity b) 8.9 m/s *impact velocity*

Figure 4.2.5 Comparison of the shoulder impact force: WSU cadaver test – FE-model

In Figure 4.2.5 a) the force response of the FE-model is compared to the corresponding cadaver sled test at an impact velocity of 6.7 m/s. The simulated force curve has almost the same slope as the experimental curve, but reaches the peak value of ~3.7 kN earlier. The force then drops significantly, which is not the case in the cadaver experiments. Thereafter, the force curve recovers and reaches a second peak at about 45 ms. After that the curves again decline in a similar way, and the impact at shoulder level is completed after 90 ms. A similar pattern is shown in Figure 4.2.5 b) where the force response of the FE-model is compared with the experimental result for the more severe sled test at an initial velocity of 8.9 m/s. After a similar ascent the simulated force curve reaches a maximum of ~5 kN, whereas the experimental curve peaks slightly higher at ~5.3 kN after ~28 ms. The force level decreases to 4 kN in the experiment and to ~1.7 kN for the FE-model. The shapes of both curves are similar, although the force drops significantly in the simulation. The experimental force thereafter reaches the same level as the simulated force, before it begins to decline at about 50 ms. The simulated force also recovers to a level of about 3 kN before decreasing until the impact is completed after ~80 ms. It is assumed that the significant drop of the simulated force curve after reaching the first peak is mainly caused by the buckling behaviour of the clavicle as described earlier.

Three scapular bone mounts would be required for the definition of the motion of the scapula. As the scapula is a thin and fragile bone, it is difficult to attach more than one bone mount. However, to track scapula displacement, in the WSU cadaver tests a singular scapular target was mounted to the spinous process, which is the most superficial region on the posterior aspect of the scapula. In the experiments, pronounced differences for the scapula displacements were observed in both the padded and the unpadded tests. It is hypothesised [Irw93] that these may be attributed to different deformation patterns of the rib cage. In the unpadded impact tests the cadavers suffered significantly more rib fractures than in the padded test, which in turn lead to different shoulder motion. Figure 4.2.6 illustrates the two different rib cage deformation patterns that influence the motion of the scapula.

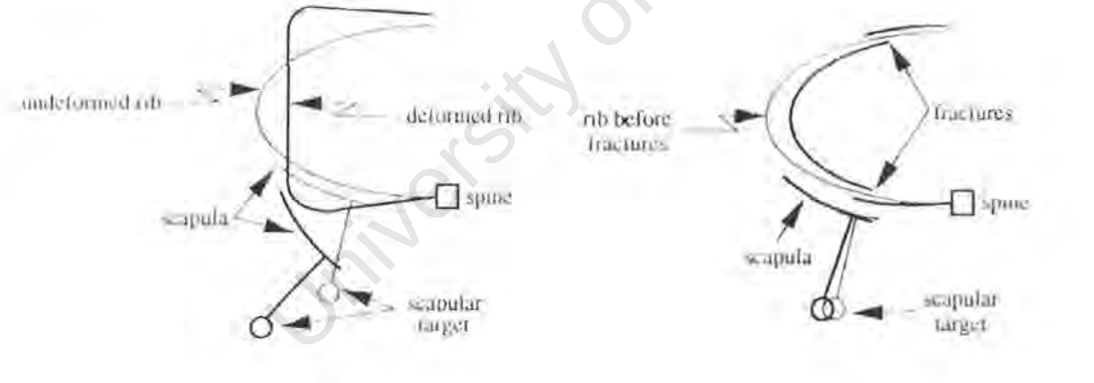

a) Scapula deflection without rib fracture *b) Scapula deflection with rib fracture*

Figure 4.2.6 Scapula deflection depending on rib cage deformation [Irw93]

The posterior bulk causes the scapula to wing outward; thus the displacement of the scapula is fairly large. When the ribs fracture on the other hand, the scapula translates and rotates less, as shown in Figure 4.2.6 b). The scapula in the FE-model shows a motion more like type a) without rib fractures and moves out laterally as shown in Figure 4.2.7.

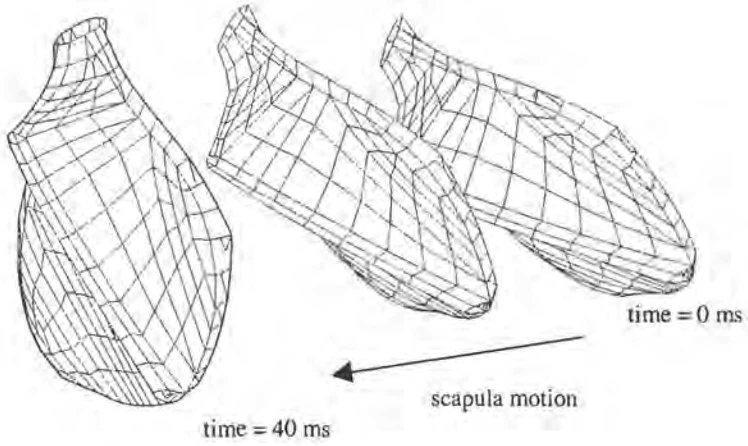

Figure 4.2.7 FE-model scapula motion

The cadavers in tests sic04 and sic07, which were examined in more detail in the shoulder investigations by Irwin et al. [Irw93], displayed a deformation pattern with several rib fractures. Table 4.2.1 lists the shoulder injuries of sic04 and sic07. The shoulder injuries were similar in both cases, with an acromion separation and fraction on the impacted side. Although the FE-model shows stress concentration in the acromion region, the yield stress is not exceeded at that region. This might be influenced by the deformation behaviour of the clavicle, which does not show enough resistance and results in higher stress levels at the acromion.

	Shoulder	**Thorax**
SIC04 8.9 m/s	left acromion separation left acromion fracture	19 left rib fractures 3 right rib fractures
SIC07 6.7 m/s	left acromion separation left acromion fracture	13 left rib fractures 3 right rib fractures

Table 4.2.1 Shoulder and thorax injuries in WSU sled test

The kinematics of the shoulder bones on the non-impacted side were tracked by the displacement of the acromion. Figure 4.2.8 shows the displacement-time history of the non-impacted acromion and compares the simulated result with the corresponding experimental result at 6.7 and 8.9 m/s.

In both cases the simulation closely follows the experimental displacement. The displacement of the acromion on the non-impacted side is not influenced by as many factors as on the impacted side, because there is less interaction between the different muscle groups.

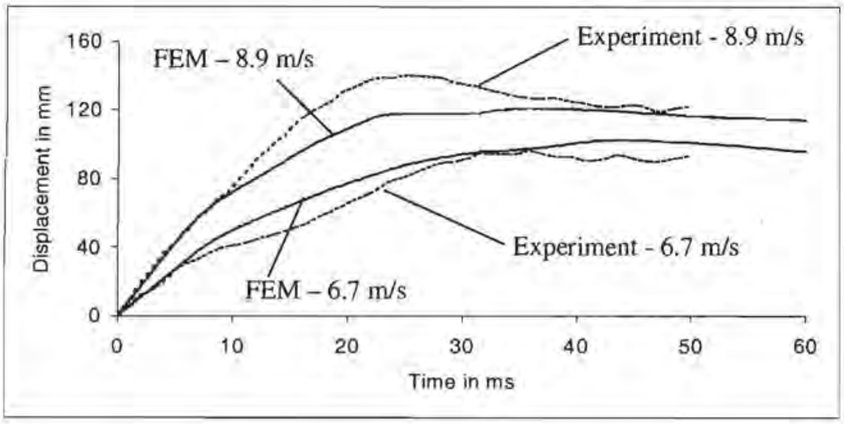

Figure 4.2.8 Acromion displacement on non-impacted side.

4.3 Head Neck Validation Results

Some results of accident research [Dan76, Ott82] show that neck injuries in vehicle side collisions do not often exceed injuries more severe than AIS 1. However, the neck plays an essential role for the dynamics of an occupant's head in an impact situation, as it connects the head to the impacted torso. The significance of head injuries in lateral vehicle collisions is presently shown by many car manufacturer's developments of inflatable curtains for head protection in such situations. Head injuries account for many fatal injuries, as shown by the statistics presented in Section 1.1. The present section deals with the validation of the head-neck complex, part of which has been published by the author in [Jos00]. Results from two different tests are used for the validation of the head-neck FE-model, namely low g-level volunteer tests and high g-level cadaver sled tests. The principle test set up, shown in Figure 4.3.1, for both types of tests for the lateral loading direction, has been described in detail in section 2.1.2. The relative motion of the head-neck complex is described within the local coordinate system, with its origin at the first thoracic vertebrae, as presented in Figure 4.3.1 b) in both tests and the simulation.

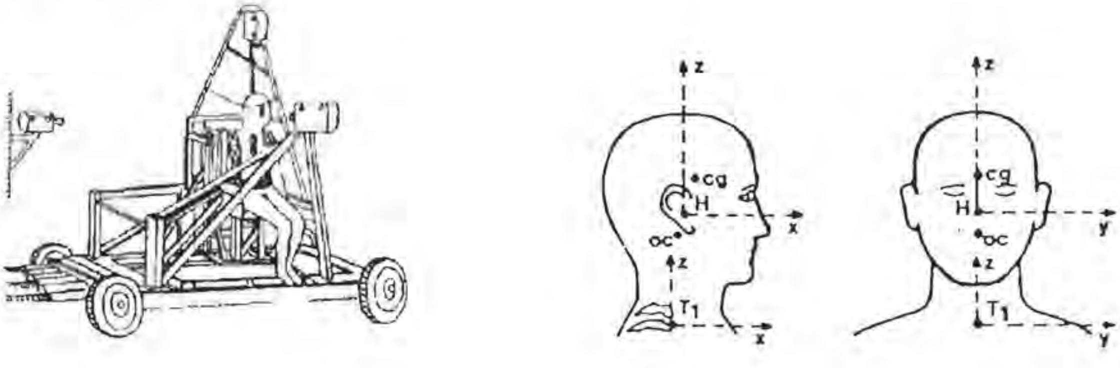

Figure 4.3.1 a) Lateral acceleration sled test [Ben87] *b) Coordinate system [Wis86]*

Accelerometers were placed at significant positions to provide translational and rotational acceleration, velocity and displacement of the head and first thoracic vertebra. This data can be used as input acceleration of a mathematical model of the neck, considered separately from the thorax.

4.3.1 Low g-level volunteer test

The predicted responses of the low g-level volunteer tests of the FE head-neck model are illustrated in Figure 4.3.2.

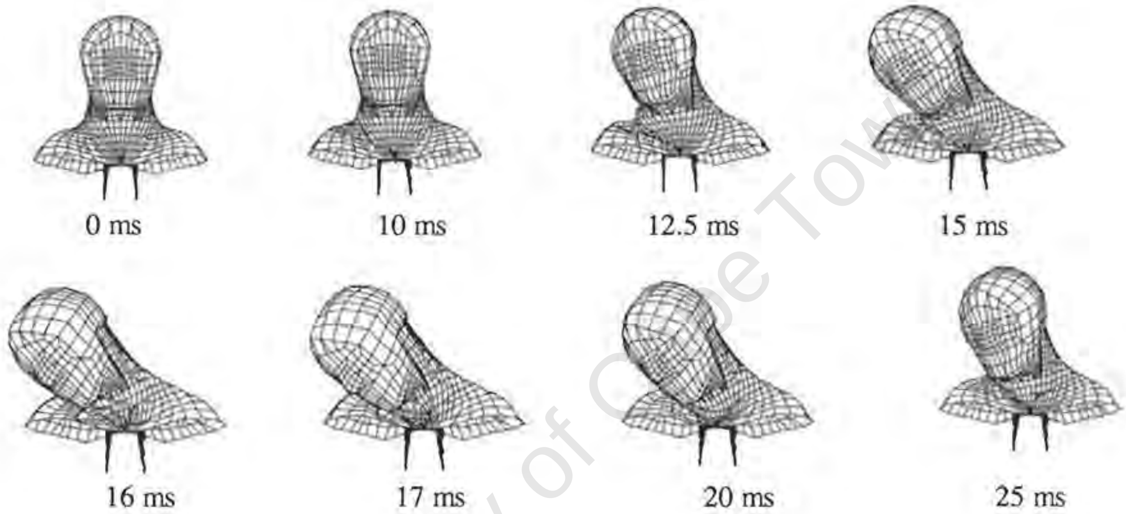

Figure 4.3.2 Picture series showing the FE-model response of a volunteer sled test

The volunteer's head's centre of gravity describes a translational movement, followed by a rotation in which lateral flexion and torsion dominates. This has also been reported in [Ewi77]. The rotational movement can be better observed than the translational movement in the picture series. A quantitative comparison between the predicted translational acceleration responses of the model and the experimental volunteer test results is presented in Figure 4.3.3. The dotted lines show the upper and lower limits of the volunteer response corridor. In Figure 4.3.3 a) the predicted translational y-acceleration shows good agreement as it closely follows the volunteer corridor. A similar agreement can also be seen for the FE-model response of the z-acceleration, although the peak values do not match exactly as shown in Figure 4.3.3 b).

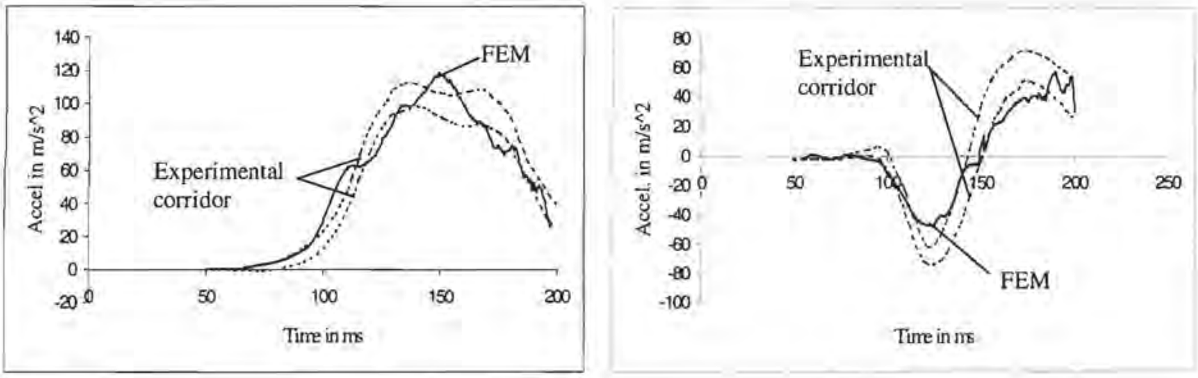

a) Translational y-acceleration *b) Translational z-acceleration*

Figure 4.3.3 Comparison of the experimental and simulated head translational acceleration

Although most of the kinematics take place in the y-z plane, the head-neck also moves forward. This is shown in Figure 4.3.4, in which the simulated x-acceleration is compared to the experimental counterpart.

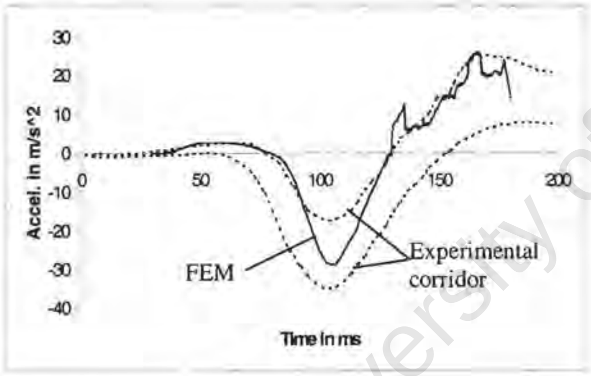

Figure 4.3.4. Translational x-acceleration

The simulated acceleration correlates very well with the experimental result. From the beginning up to 90 ms the simulated curve closely follows the upper border of the experimental response corridor. The acceleration peak value of -28.8 m/s^2 is reached at the same time as observed in the experiments after 100 ms. Apart from some minor irregularities after 130 ms, the simulated curve again follows the upper border of the response corridor.

The rotational acceleration of the head around the longitudinal and vertical axes is shown in Figure 4.3.5.

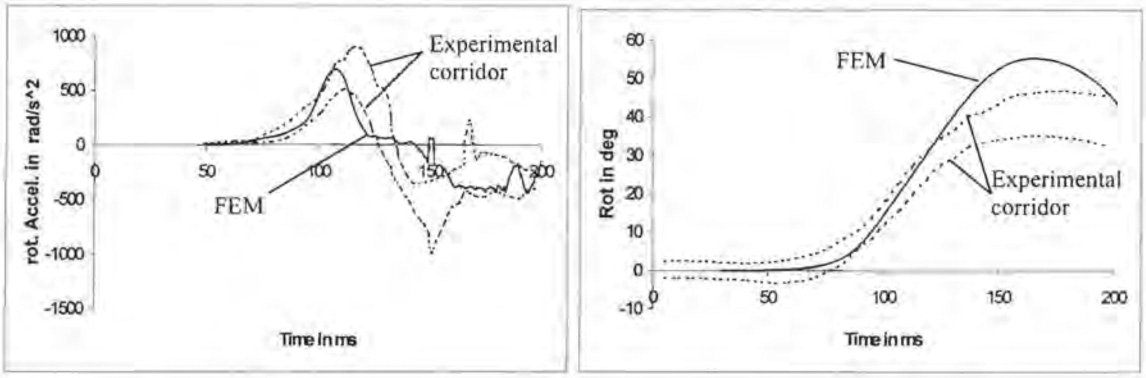

a) Rotational x-acceleration *b) X-rotation*

Figure 4.3.5 Comparison of the experimental and simulated head rotation around x-axis

The rotational x-acceleration prediction of the finite element model shows a similar shape to the upper limit of the volunteer corridor in Figure 4.3.5 a). The peak value is reached earlier but falls within the corridor. The following decline of the predicted acceleration curve also starts earlier and follows the upper limit. The resulting head rotation around the x-axis is shown in Figure 4.3.5 b). The simulated curve follows the lower border of the response corridor closely up to 100 ms. It exceeds the values of the upper border after 120 ms and peaks at a higher maximum of 55.2°. This higher level of x-rotation in the simulation is due to the lower level of negative acceleration after 130 ms, as can be observed in Figure 4.3.5 a). A similar correlation can be observed in Figure 4.3.6 a) comparing the rotational acceleration around the z-axis.

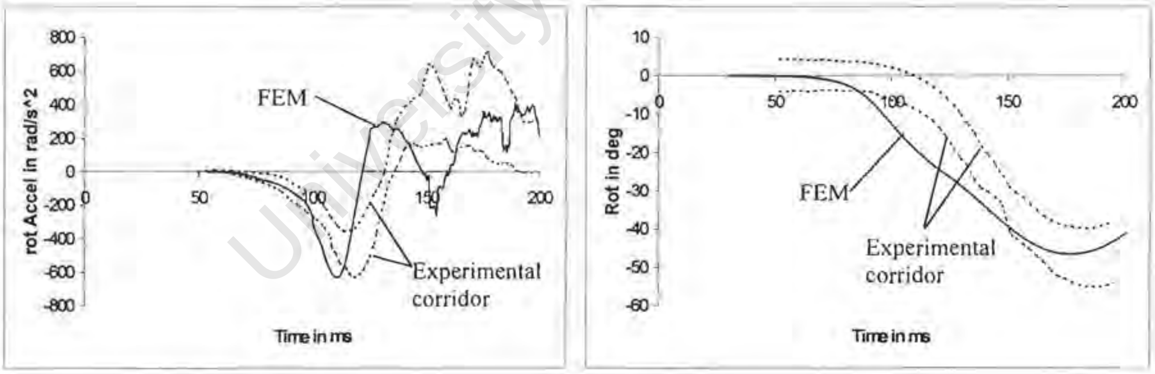

a) Rotational z-acceleration *b) Z-rotation*

Figure 4.3.6 Comparison of the experimental and simulated head rotation around z-axis

The shape of the predicted response looks similar to the upper limit of the volunteer response corridor, although the peak value matches that of the lower limit. The simulated curve peaks earlier after 110 ms, instead of after 118 ms as in the experiment. This influences the curve of the simulated head rotation shown in Figure 4.3.6 b). The simulated curve starts declining earlier than the experimental borders, but reaches a peak value that falls within the corridor limits.

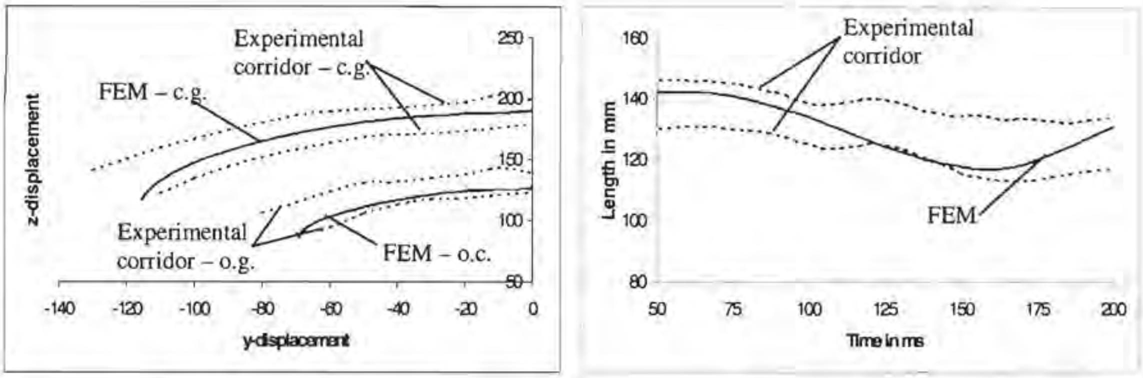

a) o.c. and c.g. trajectory *b) Neck length*

Figure 4.3.7 Head and neck displacement responses

The trajectories of the occipital condyles (o.c.) and the head's centre of gravity (c.g.) are shown in Figure 4.3.7 a). Both simulation curves fall between the borders of the experiments. A very good agreement of the simulated displacement can also seen in Figure 4.3.7 b) which graphically portrays a comparison of the simulated change of the neck length with the corresponding experimental results. The neck length is defined as the distance between the first thoracic vertebra and the head anatomical origin. The simulated neck length-time history falls between the limits of the experimental corridor.

4.3.2 High g-level cadaver test

The acceleration time history of the first thoracic vertebra is only given for the cadaver test described as MS375, which in turn was used for the FE-model validation.

The predicted kinematics of the head in the high g-level test show a very similar pattern with a first translational movement and a subsequent rotation, as was also observed in the experiment. This can be seen in Figure 4.3.8, which shows a series of pictures of the head movement.

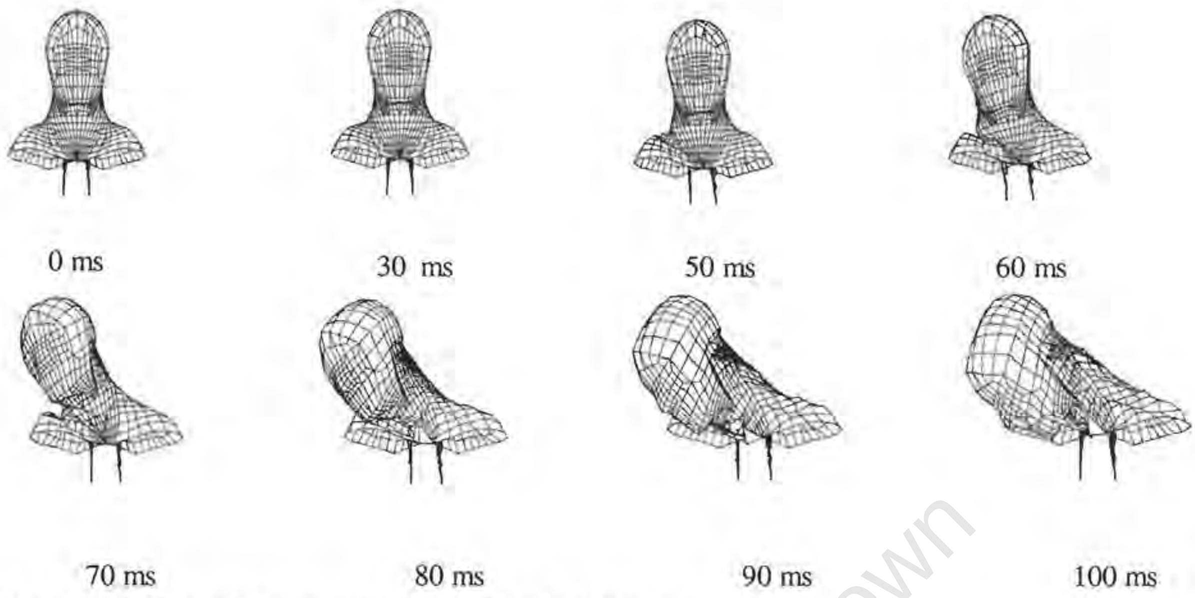

Figure 4.3.8 FE-model response of high g-level cadaver test

In comparison to the low g-level volunteer tests, the head motion for the cadaver test takes place within a much shorter time period. The optical impression is that up to 50 ms the translational movement dominates, while thereafter rotation prevails from there onwards. At 60 ms distorted shoulder elements can be seen that might influence the head rotation. A refinement of the mesh in that region might prevent these elements from distorting, but would increase the number of elements significantly.

Comparing the simulated results with the corresponding cadaver test, Figure 4.3.9 a) shows the translational and Figure 4.3.9 b) the rotational acceleration-time histories.

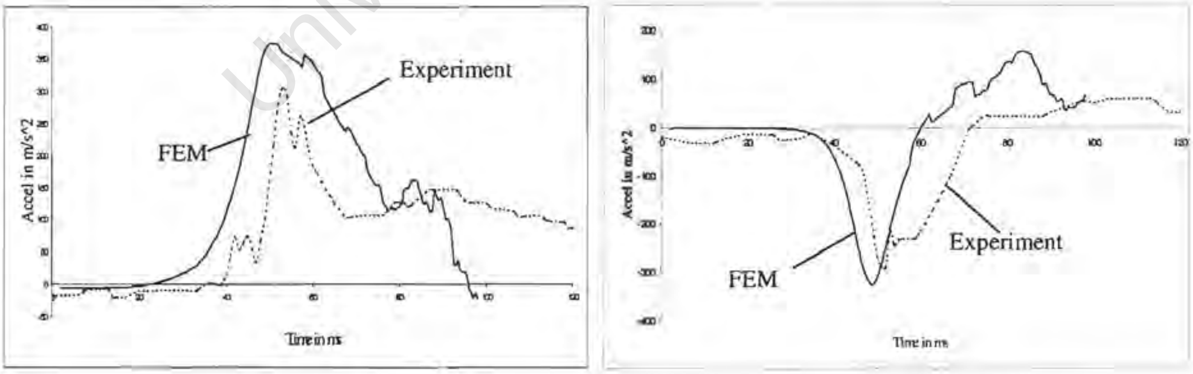

a) Translational y-acceleration *b) Translational z-acceleration*

Figure 4.3.9 Comparison of the experimental and simulated head translational acceleration

The predicted dominant translational movement of the head can be seen in the y-acceleration-time curve in Figure 4.3.9 a). The FE-model response starts inclining earlier and peaks at a higher value than the experimental cadaver result. However, the translational z-acceleration shows a fairly good agreement with the corresponding experimental response, as the peak values and the shapes of the curves match. The rotational model response is compared to the corresponding experimental result in Figure 4.3.10.

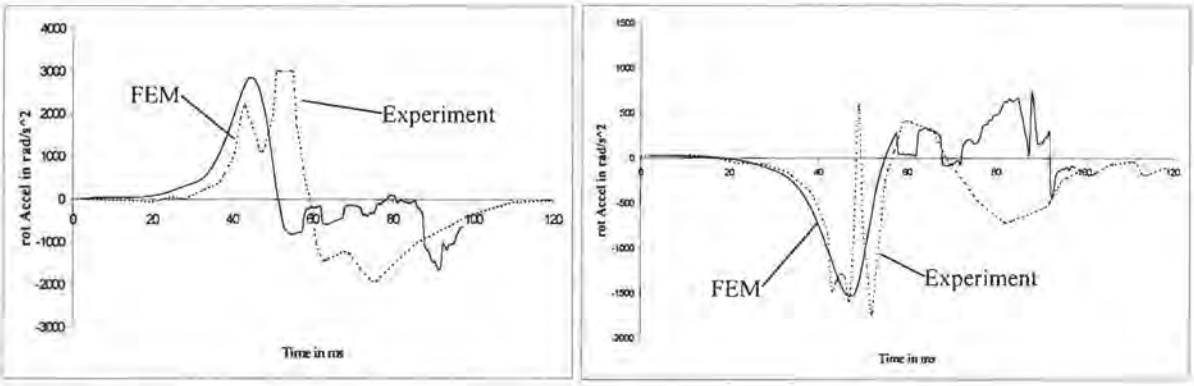

a) Rotational x-acceleration *b) Rotational z-acceleration*

Figure 4.3.10 Comparison of the experimental and simulated head rotational acceleration

The predicted rotational response around the longitudinal direction in Figure 4.3.10 a) shows a fairly good agreement with the corresponding experimental result. The dominant translational response is possibly the reason for the early decline of the rotational acceleration curve. The correlation of the overall shape of the predicted z-rotational acceleration curve is satisfactory and is shown in Figure 4.3.10 b). The predicted curve does not show a sharp peak at about 50 ms, as does the corresponding experimental result. It is possible that this peak is caused by a measuring problem, because it cannot be observed in second cadaver test [Ben87]. Figure 4.3.11 shows the trajectory of the head's centre of gravity, comparing the simulated result with that of the corresponding experiment.

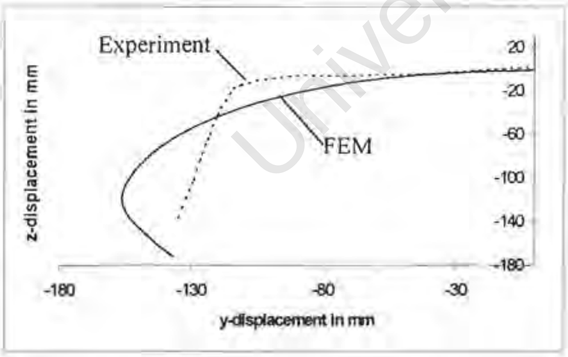

Figure 4.3.11 Trajectory of centre of gravity

The simulated motion of the centre of gravity agrees very well with the one observed in the experiments for the first 50 mm of lateral displacement. Thereafter the influence of the vertical motion becomes more apparent, so that the simulated curve starts to decline earlier than in the experiments. In the experiment the vertical component is prevalent up to 120 mm lateral displacement, whereafter the motion in z-direction dominates. The maximum lateral displacement is higher for the simulation.

4.4 Thorax Validation Results

It has been stated before that thoracic injuries are an acute problem in vehicle side impacts. The following section focuses on the comparison between the dynamic responses of the FE-model thorax and the corresponding cadaver impactor and sled tests.

4.4.1 Thorax impactor tests

The thoracic impactor tests focus specifically on the dynamic response of the area defined by Eppinger [Epp78] as the "hard thorax" and usually do not include the arms.

In compliance with the thoracic ISO impactor requirements, a 23.4 kg mass impacts the thorax laterally at an initial velocity of 4.5 m/s. The picture series in Figures 4.4.1 and 4.4.2 show the dynamic behaviour of the FE-model during this impact test. An animated movie of this simulated impactor test can be found on the accompanying CD.

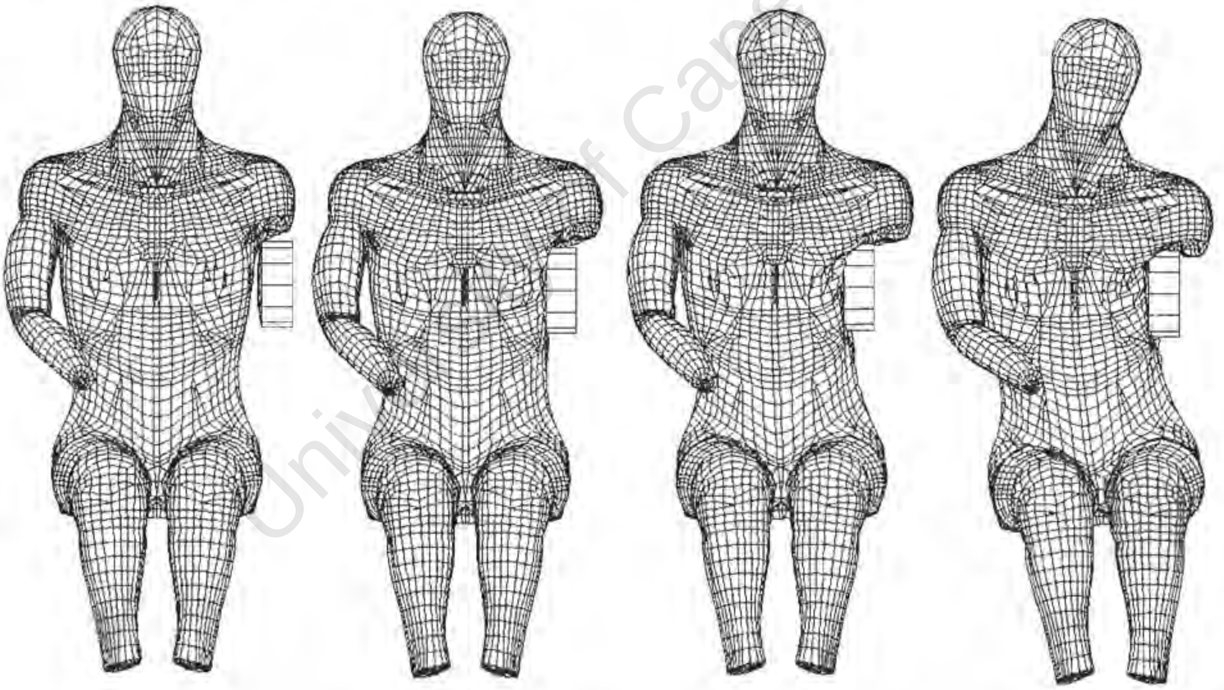

a) time = 0 ms
Initial state prior to impact

b) time = 10 ms
Compression of thin fat and skin layer; rib cage starts to deform

c) time = 18 ms
Highest impactor deceleration of 14.5 g

d) time = 30 ms
Highest ribcage deformation of 93 mm

Figure 4.4.1 ISO Impactor test at 4.3 m/s

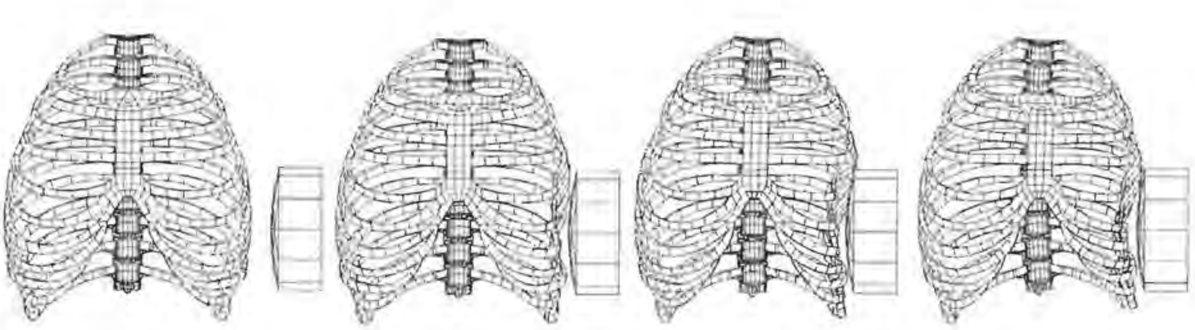

a) time = 0 ms *b) time = 10 ms* *c) time = 18 ms* *d) time = 30 ms*

Figure 4.4.2 FE-Thorax-model response to ISO impactor test

The impactor begins to deform the rib cage in Figures 4.4.1/2 b) after compressing the thin fat and skin layers at 10 ms. Most of the resistance against the impactor is caused by the stiffness of the rib cage. The highest impactor deceleration is reached at time = 18 ms shown in Figures 4.4.1/2 c), whereas Figures 4.4.1/2 d) capture the state of the highest deformation at time = 30 ms. Even this impact at a relatively low initial velocity deforms the rib cage remarkably.

The ISO requirements define a response corridor of the impactor's acceleration response with an upper and lower limit. Figure 4.4.3 compares the simulated impactor acceleration with the corresponding response corridor for this cadaver impactor test.

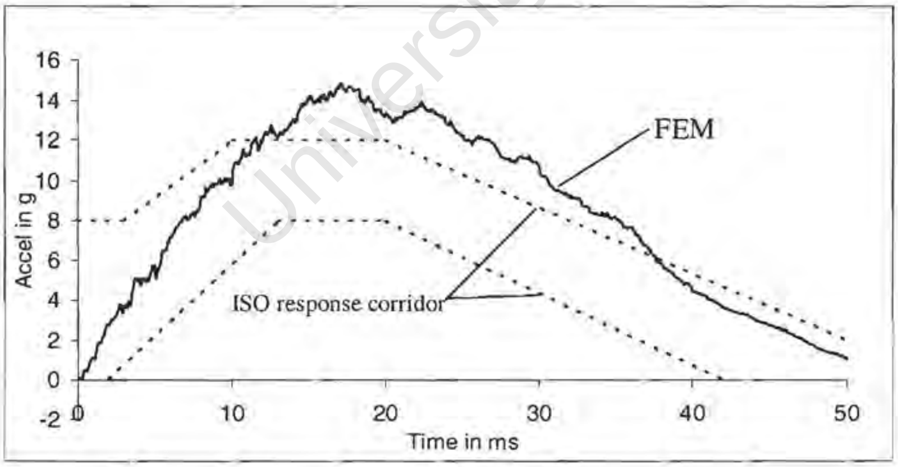

Figure 4.4.3 Impactor acceleration response

For the first 10 ms the simulated acceleration curve falls within the limits of the experimental results. After 10 ms the simulation predicts up to 2 g's higher acceleration than the upper limit of the corridor. This indicates that the FE-thorax is stiffer than those of the cadavers used in the experiments. It is possible to vary the mechanical properties, mainly those of the rib cage, to lower the acceleration level of the simulation, but it has been found that this would deteriorate the performance of the model at higher impact velocities. However, since the overall shape of the simulated acceleration response closely follows the upper limit, the FE-model response correlates fairly well with the experimental counterpart.

The second ISO requirement concerns the acceleration response of the first thoracic vertebra, shown in Figure 4.4.4.

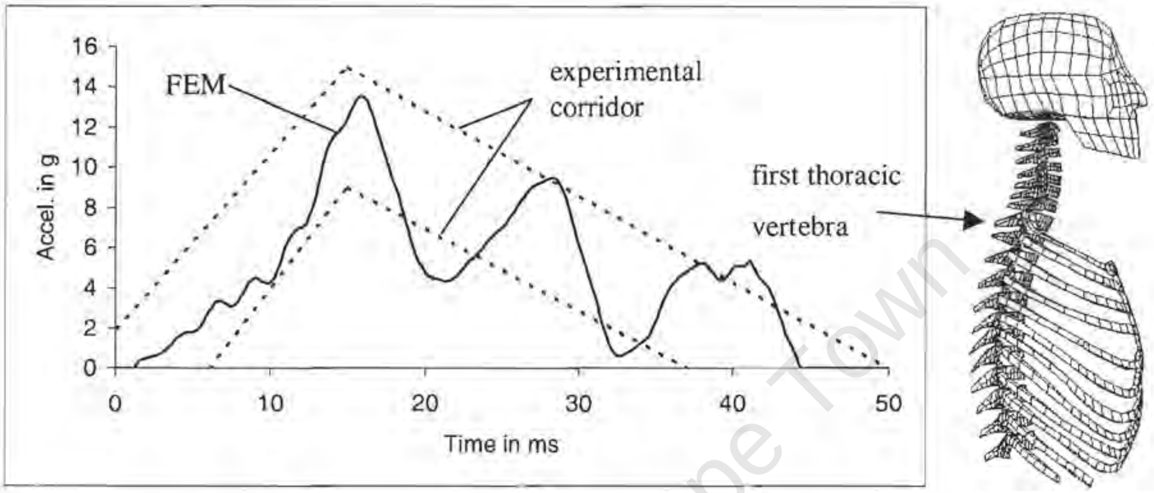

Figure 4.4.4 Acceleration response of first thoracic vertebra in the FE-model

For the first 18 ms the simulated curve falls between the upper and lower limits of the response corridor. The peak value of 13.6 g is also reached at the peak value of the corridor at 16 ms. The phase after 16 ms shows an oscillatory curve that slightly dips twice below the lower border and once exceeds the upper limit after 40 ms, but generally does fall within the corridor.

Viano impactor test

Viano conducted thoracic impactor tests using a 23.4 kg impactor at three initial velocities of 4.5, 6.7 and 9.5 m/s respectively. The 150 mm diameter impactor is modelled with non-deformable rigid elements. The impact responses of all three test simulations are summarised in Appendix A. The validation results of the severest test at 9.5 m/s are discussed below. This test may be considered a benchmark test for the stability of the thorax impact simulation. The picture series in Figure 4.4.5 shows the impact simulation that can be found on the accompanying CD.

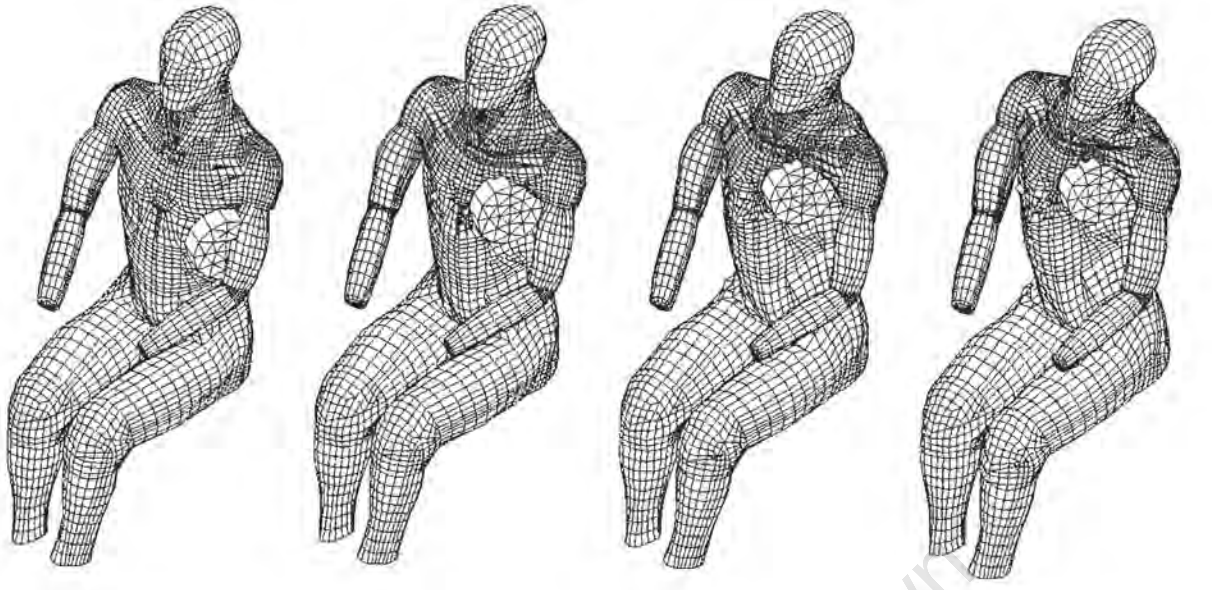

a) time = 0 ms

Initial state prior to impact

b) time = 10 ms

Rib cage deformation started

c) time = 16 ms

Highest impactor deceleration of 26.3 g

d) time = 30 ms

Maximum impactor intrusion of 195 mm

Figure 4.4.5 Viano impactor test 60°-lateral at 9.5 m/s

Figure 4.4.5 a) shows the initial state of the model at time = 0 ms when the impactor is about to hit the thorax. In the experiments the cadaver was suspended in an upright position with the hands and arms overhead. The position of the FE-model was not changed to comply with this test procedure, because it would have required too many geometric changes. The FE-model was therefore impacted in the seated position. No contact was defined between the impactor and the arm, so that the impactor could "penetrate" the FE-model of the arm as seen in Figure 4.4.5 a). The centre of the impactor was aligned 75 mm below the midsternum, so that the rib cage was fully hit by the whole impactor, and the pectoralis muscle was hit only by the upper part of the impactor. At time = 10 ms, when the impactor intrudes the rib cage, the solid elements of the pectoralis muscle are already severely distorted. Up to this stage no significant body motion has happened, whereas at time = 16 ms the upper body motion can be clearly observed. At this stage the impactor has already intruded into the chest by ~150 mm. At time = 30 ms it achieves the maximum intrusion of ~195 mm and the entire upper body moves to the side. Due to head inertia, the neck bends laterally and slightly forward, but despite this no significant stress can be observed for this region during this impact test.

Figure 4.4.6 shows a frontal view of this impact, while Figure 4.4.7 illustrates the extreme deformation of the rib cage for the same time in detail.

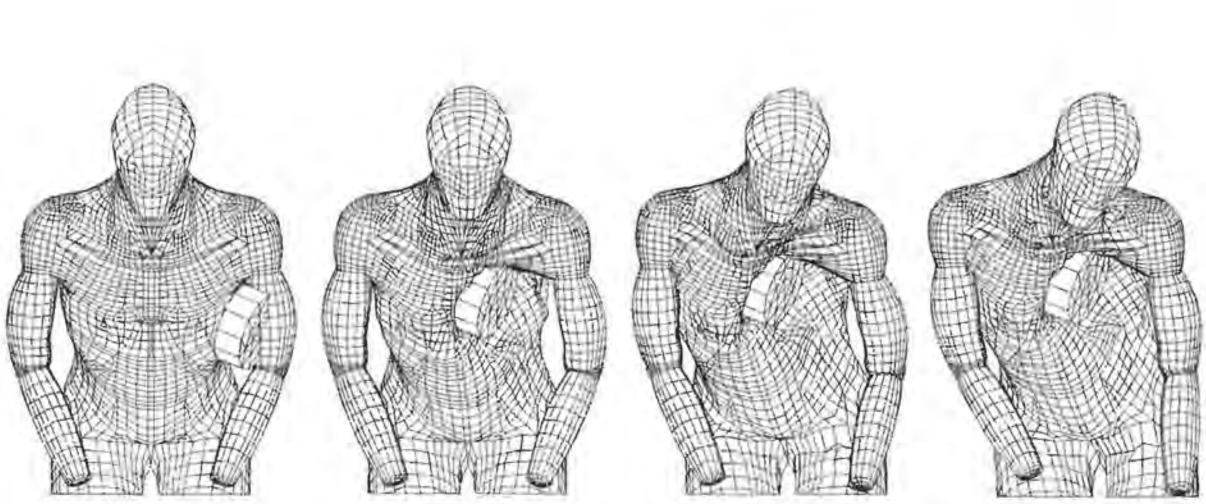

a) time = 0ms *b) time = 10ms* *c) time =16ms* *d) time =30ms*

Figure 4.4.6 Viano impactor test 60°-lateral at 9.5 m/s

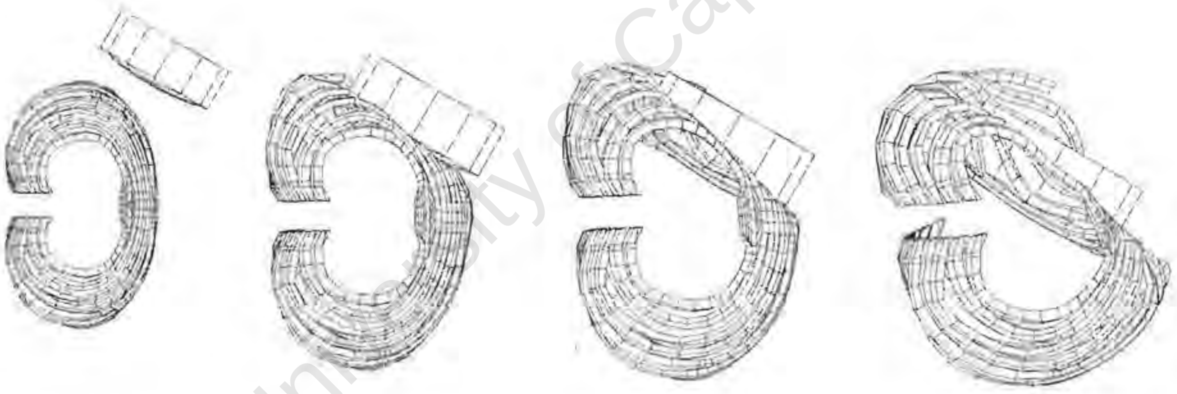

a) time = 0ms *b) time = 10ms* *c) time =16ms* *d) time =30ms*

Figure 4.4.7 Rib cage deformation

The extreme rib deformation starts at time = 10 ms followed by a fatal rib cage deformation. The value of 48.85 % for the chest compression slightly exceeds the upper limit of the experimental result of 43.2% (± 3.92), but can still be considered to be close enough to the experimental value. Table 4.3.1 summarises the thorax responses of the experiments and the FE-model simulation. The "ticks - ✓" indicate that the simulated response falls within the experimental range, whereas the ticks in brackets "(✓)" show that the simulated response is relatively close to the experimental range with less than 5% difference.

	Impact velocity: 4.3 m/s		**Impact velocity: 6.5 m/s**		**Impact velocity: 9.5 m/s**	
	Experiment	**FEM**	**Experiment**	**FEM**	**Experiment**	**FEM**
Force in kN	2.67 ± 0.99	2.59 ✓	3.1 ± 0.46	3.6 (✓)	6.3 ± 0.9	6.04 ✓
Deflection in mm	84 ± 13	112.8	112 ± 13.5	152.4	141.8±17.9	195.4
Compression in %	26.1 ± 4.1	28.2 ✓	34.9 ± 4.5	38.1 ✓	43.2 ± 3.92	48.85 (✓)
VC in m/s	0.62 ± 0.23	0.66 ✓	1.1 ± 0.18	1.35 (✓)	2.05 ± 0.41	2.66
G T1-y	14.0 ± 6.0	13.82 ✓	-	24.93	46.1 ± 8.3	59.97
G T8-y	16.5 ± 6.5	13.16 ✓	33.6 ± 8.1	19.65	62.5 ± 20.4	41.95 ✓
G T12-y	12.6 ± 8.5	13.4 ✓	25.4 ± 5.1	21.3 ✓	54.6 ± 25.3	23.58
Rib fractures	0.4 ± 0.9	-	5.2 ± 1.5	-	12.7 ± 4.5	-

Table 4.4.1 Comparison of Thorax responses [Via89] – FE-model

As expected, all response values increase with increasing impact velocity. The high number of rib fractures (12.7 ± 4.5) for the 9.5 m/s impact again highlights the severity of this type of impact. The fracture of the ribs can only be predicted indirectly by the FE-model, as no failure criterion is included in the model. One can only speculate that the ribs will break when many of the elements show significant plastic strain, which did in fact happen with many of the ribs during the impact simulation. Although the dynamics of a rib cage with fracturing ribs cannot be simulated at this stage, the overall impact response closely resembles that of the corresponding experiments. This is supported by the comparison of the maximum impactor force of the simulation, which falls within the range of the experimental values for all three velocities. Although the values of the chest deflection exceed the average experimental values, the simulated chest deformation is within a realistic range, because the chest compression, which takes into account the original size of the thorax, falls within the range of the experimental responses. The simulated results for the viscous response (VC) slightly exceed the upper limits generated by the experiments.

The simulated acceleration peak values of the 1st, 8th and 12th thoracic vertebra are generally within the range of the experimental responses. Due to the fact that this range of peak values is fairly wide, this correlation and its significance has to be considered carefully. The force and deformation responses are considered as being more accurate for the validation of the FE-model than the acceleration responses as they do not vary within a wide range. Therefore, the force and deformation responses are described in more detail in the subsequent paragraphs. Figure 4.4.8 shows the comparison of the simulated impact force-time history of the 9.5 m/s impact with the corresponding experimental corridor.

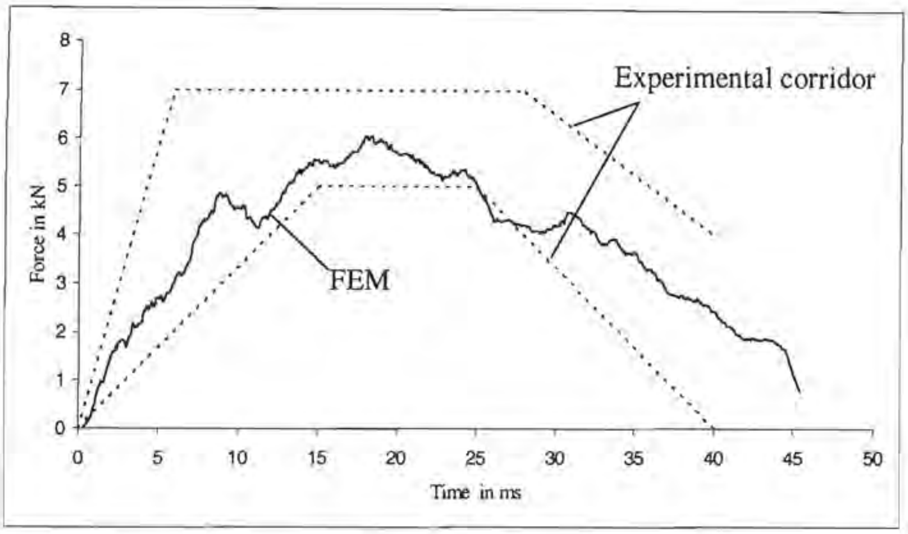

Figure 4.4.8 Comparison of force-time responses in Viano impactor test at 9.5 m/s

The simulated force curve falls between the limits of the experimental response corridor, with only one minor exception at about 26 ms, where the force is lower than the lower boundary. The FE-model seems to respond with a rather low force level, which is close to the lower border of the response corridor of this particular test. The force deflection curve, shown in Figure 4.4.9, also demonstrates that the FE-model does in fact predict this high velocity impact, because the simulated force-deflection response falls between the corridor borders for most of the deformation range. It can also be observed in this figure that the simulation response is rather on the "soft" side, as the simulated curve closely follows the lower corridor limit.

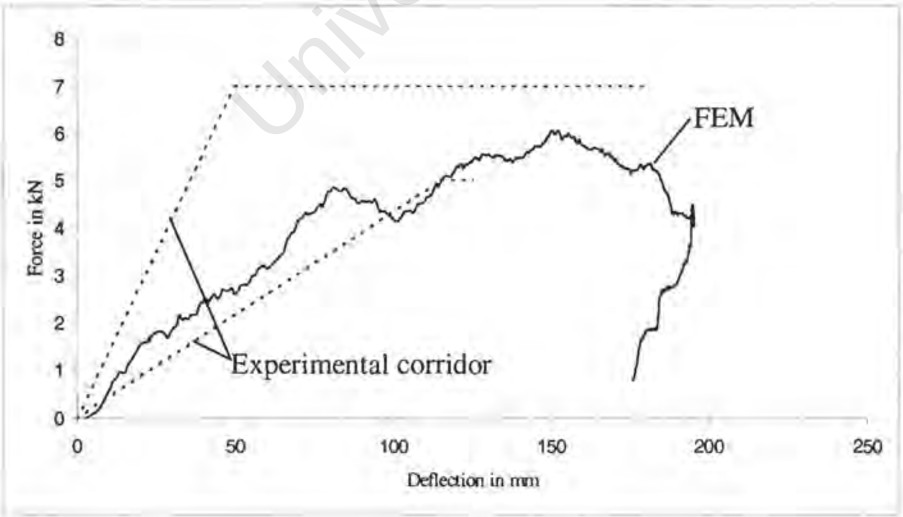

Figure 4.4.9 Comparison of force-deflection responses in Viano impactor test at 9.5 m/s

WSU impactor test with limited stroke

The impactor test set up used by Chung [Chu98] differs from the "normal" impactor test as described in Section 2.1.1 in so far as that it describes a predefined motion with a limited stroke to simulate the door motion in a real accident. The resistance of the cadaver thorax during this impact is measured by a load cell at the impactor. Figure 4.4.10 shows the velocity-displacement history that was defined for the impactor.

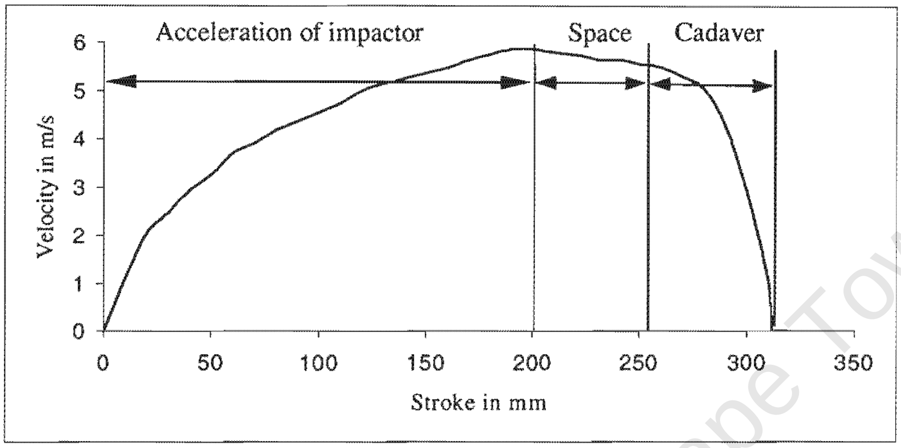

Figure 4.4.10 Velocity-displacement history of impactor in a limited stroke test [Chu98]

The first 200 mm of the 305 mm stroke were used to accelerate the impactor, the next 55 mm to traverse the space occupied by padding material or air space, and the last 50 mm to traverse the space occupied by the struck side of the occupant. For the FE-simulation only the unpadded cadaver data were used, so that only the last part of the impact needed to be simulated. Therefore, the impactor is positioned closely to the body and only the last part of the velocity history was defined for the impactor motion.

The simulated response forces are shown in Figure 4.4.11 in comparison with the force curves of the two cadaver tests. The cadaver peak forces differ by more than 40 %, which demonstrates that there is a wide range of biomechanical responses of cadavers subjected to impact.

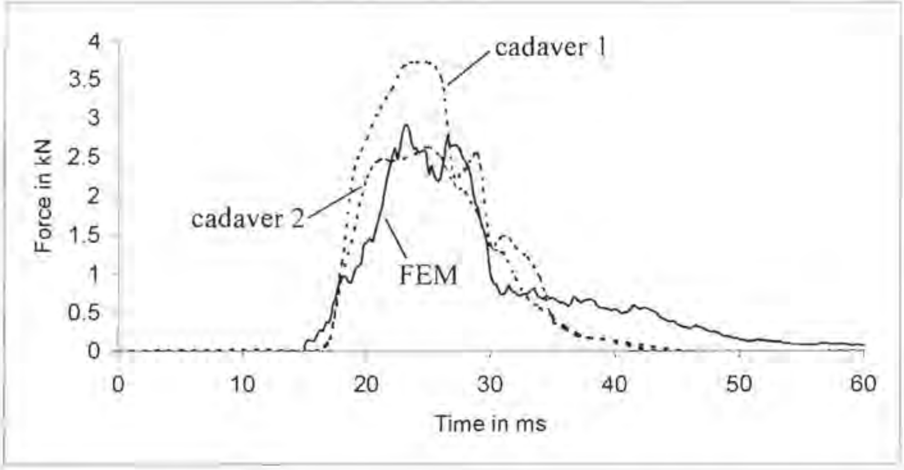

Figure 4.4.11 Comparison of force-time histories in the WSU limited stroke test

The simulated force curve has a softer slope at the beginning, but reaches a peak value that falls between the peak forces given by the experiments. The shapes of the force-time histories look very similar. After about 30 ms the force level of the simulation is higher than that measured in the experiments.

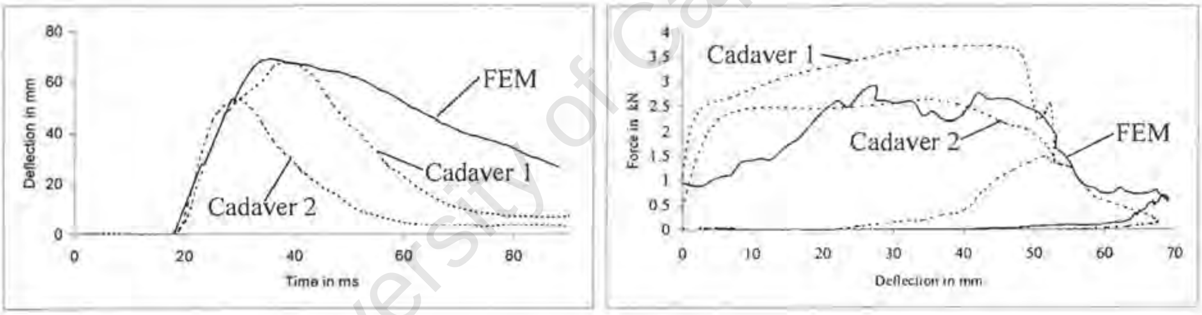

a) Deflection time response *b) Force deflection response*

Figure 4.4.12 Comparison of chest deflection in the limited stroke tests

The chest deflection curve of the FE-model in Figure 4.4.12 a) has a similar rising slope as the two experiments. The simulated peak value matches that of the first cadaver. After about 38 ms it can be observed in Figure 4.4.12 that chest recovering pattern of the FE-model is slightly different to that of the two cadavers. Both cadavers show a faster reduction of chest deflection than the FE-model, which might indicate that the damper elements, which serve for the visco-elastic properties of the visceral contents absorb more energy than the visceral contents of the cadavers.

The simulated force deflection curve, shown in Figure 4.4.12 b), differs from cadaver responses at the beginning but closely follows the force deflection curve of the second cadaver after 20 mm deflection.

The acceleration response of the impacted rib cage measured at rib 4, 6 and 8 and the acceleration of the thoracic spine, measured at T1, T6 and T12, are shown in Figure 4.4.13.

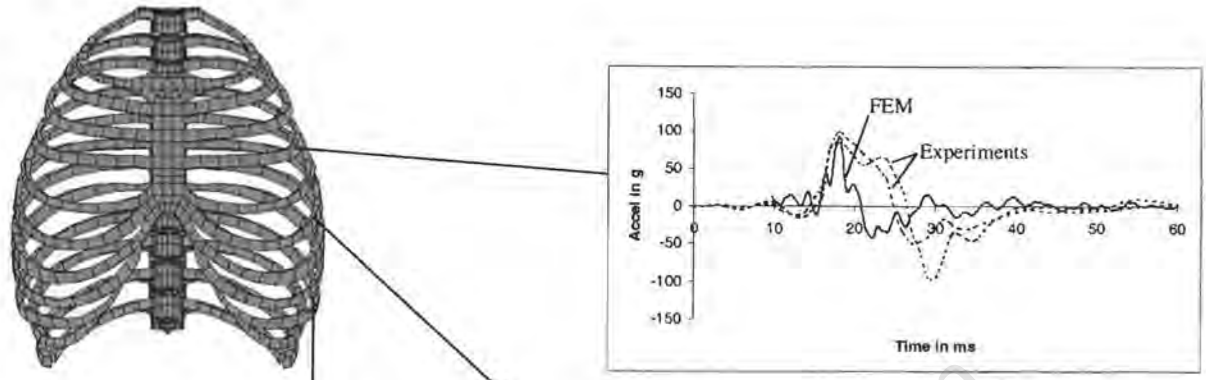

a) Location of rib accelerometers

b) Rib 4 acceleration

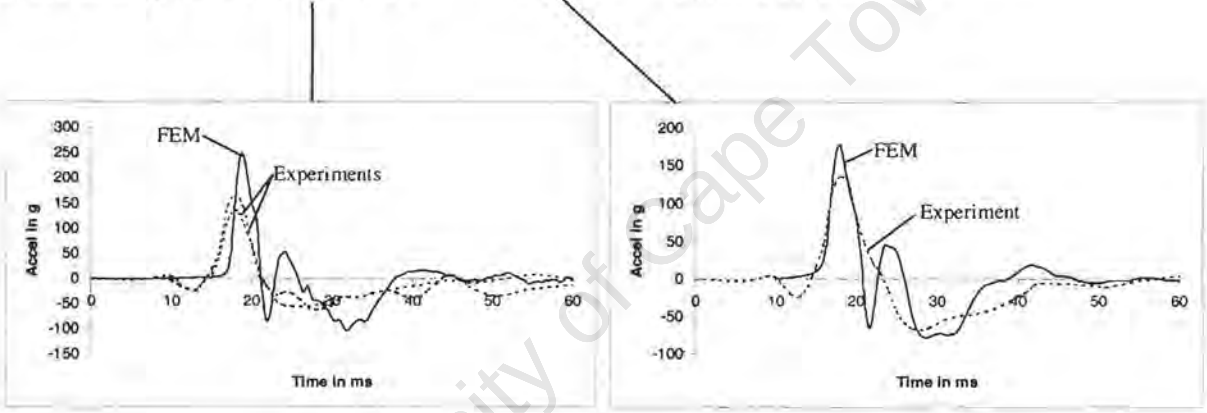

c) Rib 8 acceleration

d) Rib 6 acceleration

Figure 4.4.13 Comparison of rib acceleration-time histories

As shown in Figure 4.4.13 b) the acceleration curve of the impacted fourth rib in the simulation shows almost the same peak value as that of the experimental result, although the shape of the simulated curve differs from the experimental curve. As can be observed in Figure 4.4.13 d), the slope of the acceleration curve of the sixth rib is very similar to its experimental counterpart, and the peak values only differ slightly. The simulated curve, however, shows a different decline after 18 ms with a dip in the acceleration curve down to -65 g, which cannot be observed in the experiments. Although this behaviour cannot be explained, the overall performance seems to be similar to that observed in the experiment. The same can be stated for the acceleration response of the eighth rib, shown in Figure 4.4.13 c). The simulated peak value exceeds the experimental value by 30 g. However, the overall shape of the simulated response shows a relatively good agreement with the experimental curve.

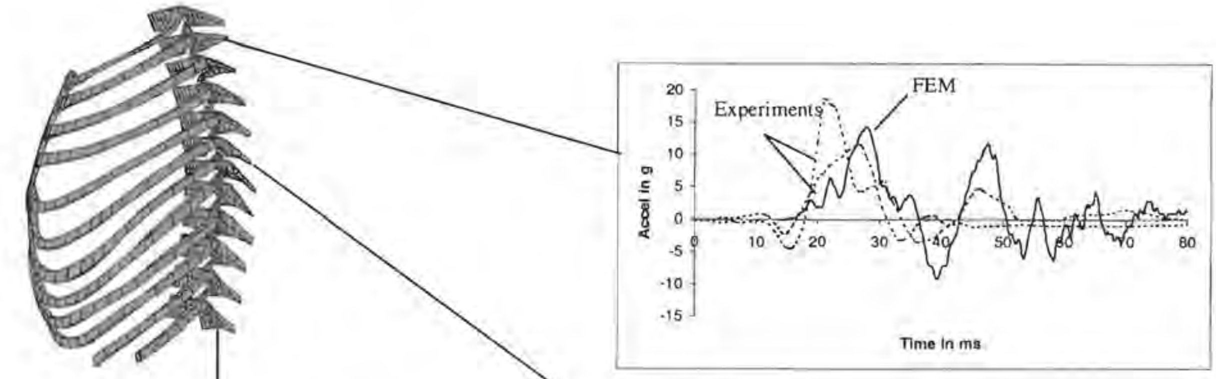

a) Location of thoracic accelerometer *b) T1 acceleration*

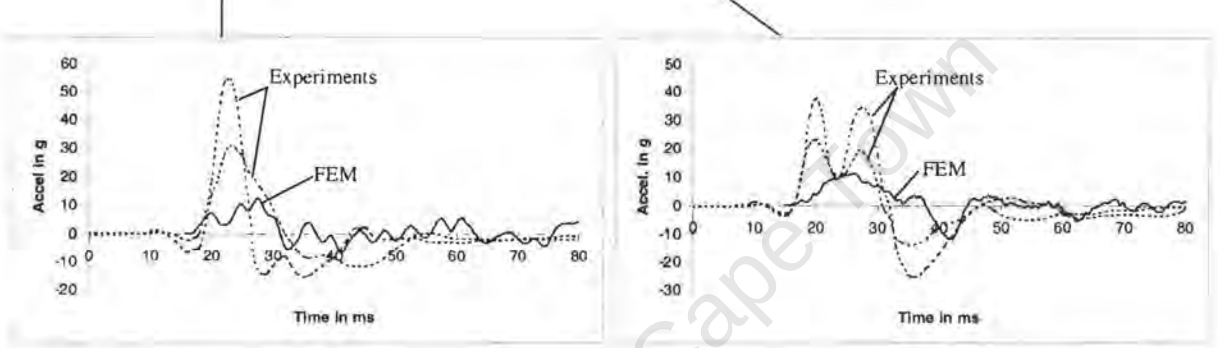

c) T12 acceleration *d) T6 acceleration*

Figure 4.4.14 Comparison of thoracic vertebrae acceleration-time histories

In contrast to the fairly good performance of the simulated rib acceleration curve in Figure 4.4.13, the acceleration responses of the thoracic vertebrae in Figure 4.4.14 do not show the same agreement with their experimental counterparts. The simulated acceleration of the first thoracic vertebra may be considered as being within the range of the experimental curves, as seen in Figure 4.4.14 b). However, the simulated curves of the sixth and twelfth thoracic vertebra in Figures 4.4.14 c) and d) do not show such a reasonable agreement with the experimental results. This discrepancy between the simulated and experimental vertebral accelerations is probably determined by the different deformation pattern of the thorax. Although the force-deflection behaviour of the thorax can be simulated well by using a simplified elastic-plastic material model for the ribs, the load transfer into the thoracic spine differs in comparison to the experiments. When ribs fracture in real life, the load transfer to the corresponding thoracic vertebrae decreases significantly. This does not happen to the same extent in the FE-model, because the ribs only deform plastically but do not break, which leads to a higher load transfer into the thoracic vertebrae and therefore to higher vertebral accelerations.

The Viscous Criterion shows a better agreement between simulation and experiment, as can be seen in Figure 4.4.15. Although the simulated curve does not reach the exact peak, the overall shape of the simulated curve looks similar to those of the experiments. It has been observed in the Viano tests that at higher impact velocities the simulated Viscous Criterion generally shows higher values than in the experiments. It may therefore be speculated that the impact velocity in the limited stroke test is not fast enough to show a similar viscous response as has been observed in the Viano tests.

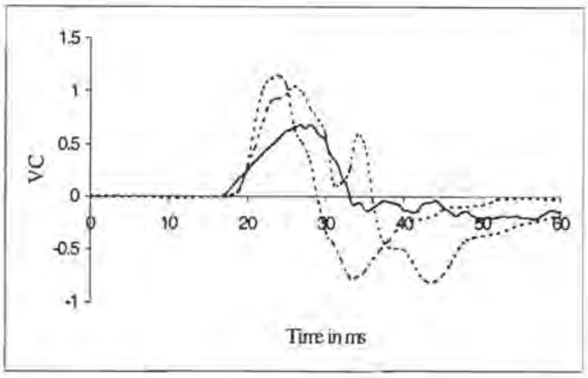

Figure 4.4.15 Viscous response in the limited stroke test

The most important cadaver responses are summarised in Table 4.4.2, which again highlights the wide range of responses for cadaver tests.

	cadaver 1 male, 54 years, 103 kg	**cadaver 2** male, 71 years, 76 kg	**FEM** ("62.5 years" for TTI)
Rib fractures	4	15	-
TTI [g]	189.0	214.0	217.45 (✓)
VCmax [m/s]	1.17	1.07	0.681
Force max [kN]	2.666	3.742	2.908 ✓
Peak Acceleration Rib 4 [g]	98.4	91.8	92.23 ✓
Peak Acceleration Rib 6 [g]	-	140.2	176.89
Peak Acceleration Rib 8 [g]	138.7	172.0	247.61
Peak Acceleration T1 [g]	19.1	12.3	14.27 ✓
Peak Acceleration T6 [g]	35.6	37.2	11.41
Peak Acceleration T12 [g]	31.3	56.6	12.29
Peak Deflection Rib 6 [mm]	46.4	60.8	65.3

Table 4.4.2 Impact response – limited stroke test

The second cadaver suffered significantly more injuries than the first with 15 rib fractures, while the first cadaver suffered only 4 fractures. Therefore, one clearly cannot expect the same biomechanical responses for both cadaver tests. Numerically, the TTI would have predicted the severity of the injuries better than the Viscous Criterion, as the TTI shows a bigger value for the second cadaver test.

The simulation shows that almost the same TTI value can be achieved by different impact dynamics, for example high rib acceleration – low vertebral acceleration, or the other way around. However, the Viscous Criterion may be criticised for not being sensitive enough to predict the different rib cage injuries in terms of 4 and 15 rib fractures respectively. The force and deflection values on the other hand seem to be more on the intuitive side, with higher values for the more severely injured cadaver. One has to bear in mind that these two tests cannot be considered as sufficient for generalised statements about both injury criteria.

4.4.2 Thorax sled test

The Heidelberg sled tests were the first cadaver sled tests to investigate the biomechanical responses of cadavers subjected to lateral impact. The tests conducted at Wayne State University had a similar set up; it differed insofar as the impacted wall consisted of four force plates instead of two, as used in the Heidelberg tests. The test procedures are described in Section 2.1.2, and the results are used for the FE-model validation. The body's gross motion in the Heidelberg tests does not differ significantly from the motion in the WSU tests, as the test set ups are similar. The initial velocities of the sled were 6.7 m/s and 8.9 m/s (15 and 20 miles per hour) respectively. It is assumed [Cav90] that the initial velocity of the cadaver prior to impact is slightly less, because the cadaver slides over a low friction surface before impacting the wall. As a result, initial velocities of 6.5 m/s and 8.7 m/s were defined for the FE simulation.

Force response

The first quantitative validation results compare the simulated impact force with the corresponding Heidelberg test result [ISO89]. Figure 4.4.16 a) shows the force response corridor that has been developed from the Heidelberg test data for the ISO requirements. Figure 4.4.16 b) shows the force response recorded in the WSU sled tests, combining the force-time histories of the shoulder and thoracic beams, since both of then together cover the same area as the thoracic plate in the Heidelberg tests.

The force-time curve of the FE-model falls entirely within the response corridor defined in the ISO requirements. The shape of the force curve is also very similar to the force curve of one of the experiments shown in Figure 4.4.16 a). The simulated force curve has a steep slope up to 7 ms, where it reaches a peak of ~4 kN. The force then drops down to ~2 kN at 11 ms, and rises once again to a maximum of about 8 kN between 20 and 30 ms. The following decline completes the thoracic impact after about 60 ms. The first peak and the subsequent decrease in the simulated force curve are influenced by the deformation of the shoulder, and especially the clavicle, as described in the shoulder validation (Section 4.2).

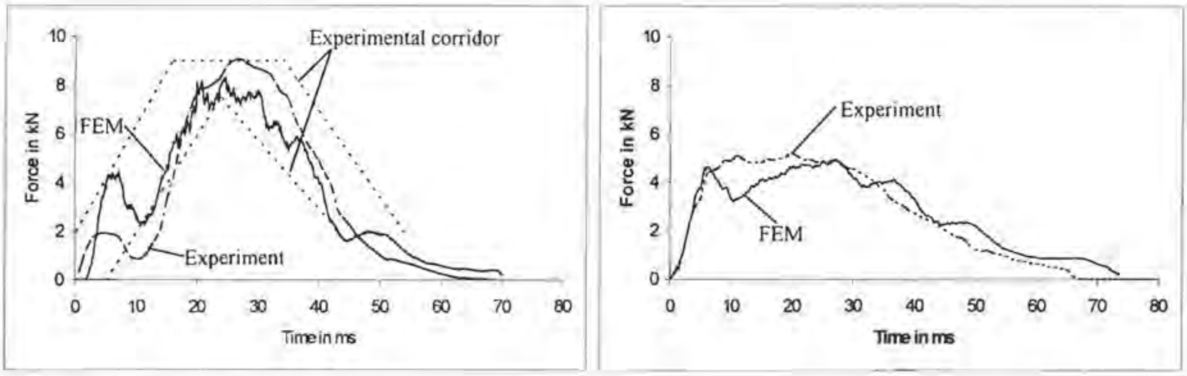

a) Thoracic force Heidelberg test *b) Thoracic + Shoulder force WSU test*

Figure 4.4.16 Comparison of thoracic cadaver sled test responses at 6.7 m/s

The simulated force time history of the WSU tests shown in Figure 4.4.16 b) closely resembles that of the experimental result. The simulated curve closely follows its experimental counterpart, with only a relatively small difference after about 10 ms in the form of a small descent in the force curve. Although the thoracic and shoulder beams cover the same area as the thoracic plate in the Heidelberg test, the peak forces are significantly higher in the latter. It was speculated [Cav90] that the initial velocities in the Heidelberg tests might have been higher than those in the WSU tests. The comparison between the simulated Heidelberg tests and the simulated WSU tests at the same initial velocity of 6.7 m/s shows the same difference, which has been observed by the comparison of the experimental results of both tests. It might be concluded that the two sled test configurations in fact differ more than originally expected. The results obtained from the FE-model demonstrate that it is sensitive enough to simulate these differences. The same comparison between the FE-model and the high severity sled tests at an initial velocity of 8.9 m/s is illustrated in Figure 4.4.17 a) for the Heidelberg test and in Figure 4.4.17 b) for the WSU test.

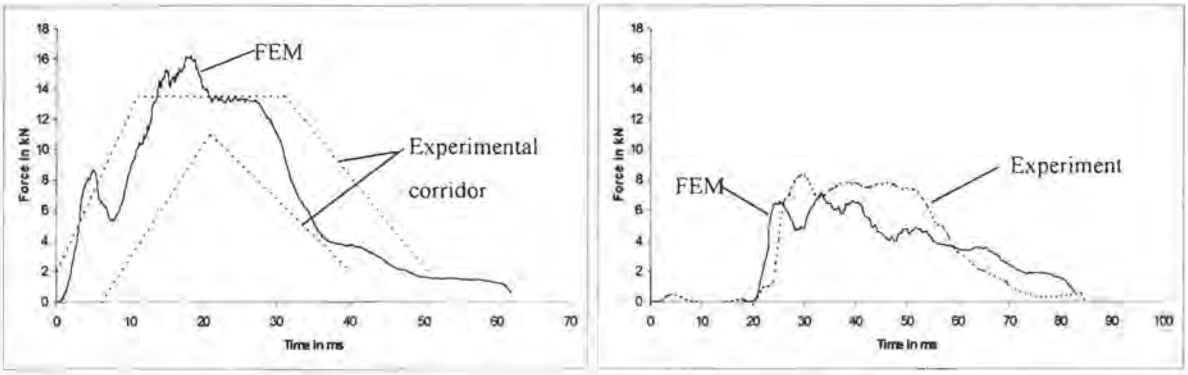

a) Thoracic force Heidelberg test *b) Thoracic + Shoulder force WSU test*

Figure 4.4.17 Comparison of thoracic cadaver sled test responses at 8.9 m/s

The simulated force curve in Figure 4.4.17 a) shows a steep rising slope as observed previously in the 6.7 m/s test. Although the curve generally falls within the experimental response corridor, it exceeds the upper border slightly at 5 ms and between 12 ms and 19 ms. The descent of the curve again falls within the corridor borders.

The thoracic force in the Heidelberg test is again significantly higher than the sum of the thoracic and shoulder force in the WSU test as can be seen in Figures 4.4.17 a) and b). The simulated force response in Figure 4.4.17 b) shows a similar slope at the beginning as observed in the WSU experiment although it starts 3 ms earlier. The simulated force peak does not reach the experimental value and starts declining earlier. However, the duration of both impacts is almost identical.

The separation of the shoulder and thoracic beams in the WSU tests permits the examination of the thoracic force response with less interference from the shoulder motion. Figure 4.4.18 compares the experimental and simulated force responses of the thorax with the WSU tests at 6.7 m/s and 8.9 m/s respectively.

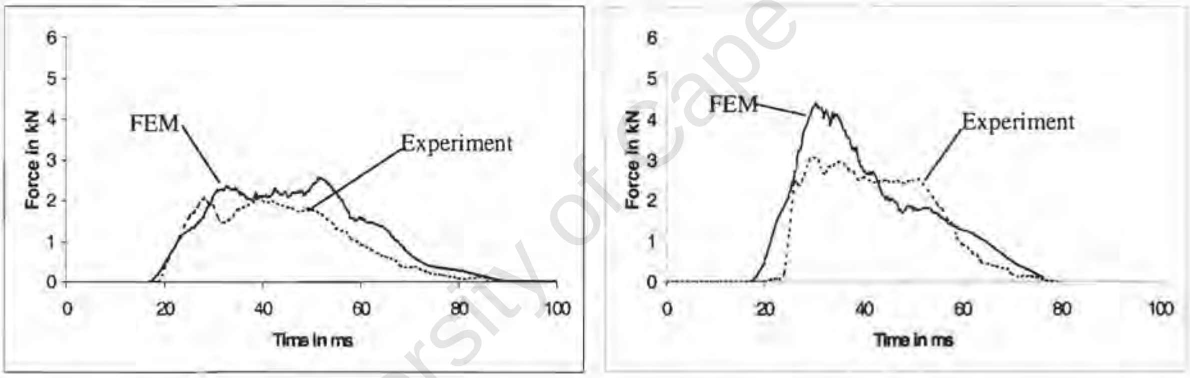

a) Thoracic force WSU- 6.7 m/s *b) Thoracic force WSU- 8.9 m/s*

Figure 4.4.18 Comparison of thoracic WSU responses

For the first 15 ms, until the experimental curve reaches the first maximum value of about 2 kN, the slopes of both curves in Figure 4.4.18 a) are almost identical. The simulated curve continues to ascend to ~2.5 kN at 30 ms. It remains at this level until 55 ms, whereafter it declines. The experimental curve displays a similar shape, although the maximum force level of about 2 kN is less than that of the FE-model. The declines of both curves are also similar, both ending at about 80 ms, so that the total thoracic impact lasts for about 60 ms.

For the more severe impact at 8.9 m/s initial velocity, the simulated force has a distinct peak at about 30 ms, which cannot be observed in the experiment in that form. The simulated force peak value of 4.4 kN exceeds the averaged experimental peak force significantly, with 3.1 kN at 30 ms. However, the shapes of both curves are similar and the force curves do peak at almost the same time. The decline of the simulated curve also closely resembles its experimental counterpart.

Deformation of the Thorax

The sled tests display a deformation pattern of the thorax different to that of the impactor tests. The impacted wall provides a larger impact area than the pendulum impactor, which leads to a wider load distribution. Furthermore, the pendulum impacts usually did not include the arm, whereas the arm is an unavoidable part of the thorax impact in the sled test. Figure 4.4.19 shows the deformation pattern of the rib cage for the 6.7 m/s WSU tests.

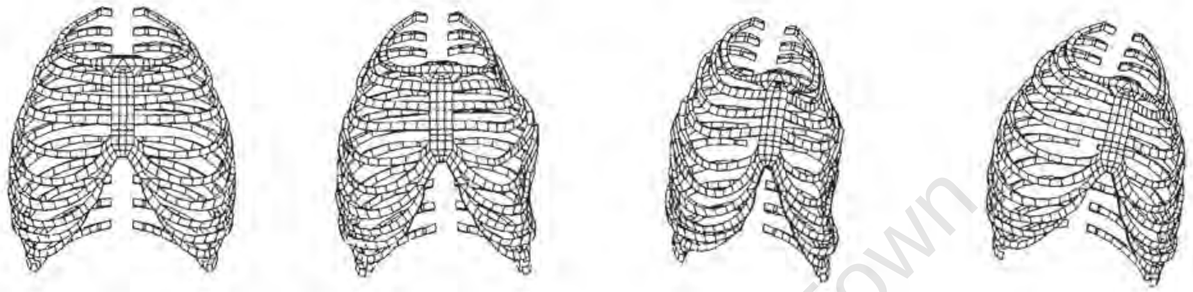

a) Time = 0 ms
Initial state prior to impact

b) Time = 35 ms
Rib cage deforms by intruding arm and shoulder

c) Time = 50 ms
Maximum rib cage compression of 38.6 %

d) Time = 65 ms
Deformation recovering

Figure 4.4.19 Rib cage deformation in WSU simulation

The initial state prior to impact is shown in Figure 4.4.19 a). After 35 ms the arm moves laterally inwards and deforms the lower part of the rib cage for a short duration. Then the arm slides away from the body in a forward direction. The shoulder deforms the upper part of the rib cage as the scapula moves inwards. The maximum rib cage deformation relative to the spine is reached after 50 ms, whereafter the recovery phase starts, as shown in Figure 4.4.19 d).

6.7 m/s	**Compression** in %	**$V_{max} * C_{max}$** in m/s	**Injuries**
cadaver SIC05	38.0	2.55	left flail chest, 8 right rib fractures
cadaver SIC07	41.2	2.75	left flail chest, 3 right rib fractures
cadaver SIC08	63.0	4.15	left flail chest, aortic laceration
FE-model	38.6 ✓	1.34	-
8.9 m/s			
cadaver SIC04	33.0	2.99	left flail chest, 3 right rib fractures
cadaver SIC06	42.3	3.83	left flail chest, 2 right rib fractures
FE-model	46.8	2.63	-

Table 4.4.3 Compression data and viscous response

The compression of the thorax in the WSU tests was defined as the compression of the half-thorax measured at T5 level, divided by half of the chest width including the arm. The peak compression data and the maximum viscous response are summarised in Table 4.4.3 for the WSU experiments and the FE-model. The maximum compression of the FE-model is almost identical to that observed in the sic05 cadaver test at an initial velocity of 6.7 m/s. At the higher velocity of 8.9 m/s the simulation shows a peak compression value (46.8 %) that slightly exceeds those observed in the experiments. For both velocities the Viscous Criterion is lower in the simulation than in the experiments

Acceleration responses

The cadavers in the Heidelberg sled tests were fitted with accelerometers at the ribs and vertebrae, as described in Section 2.1.2. Figures 4.4.20 a) and b) compare the simulated acceleration curves of the 1st and 12th thoracic vertebrae to the acceleration curves obtained in the corresponding Heidelberg sled tests.

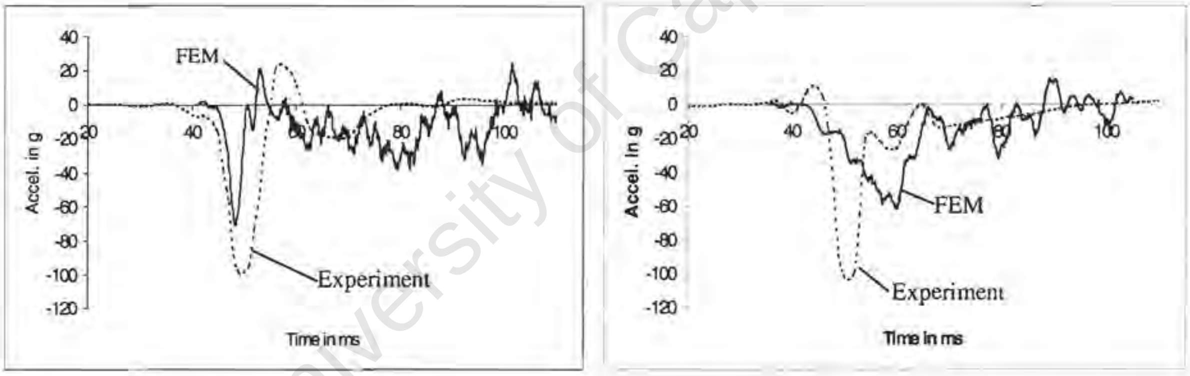

a) T1- lateral acceleration *b) T12- lateral acceleration*

Figure 4.4.20 Comparison of thoracic vertebrae acceleration-time response in Heidelberg test 6.7 m/s

For the acceleration of the first and twelfth thoracic vertebrae, the peak values of the simulated responses are lower than the corresponding experimental values. Although the shapes of the simulated curves look similar to their experimental counterparts, the simulated peak values are lower for both vertebrae, which in turn influences the value of the injury criterion TTI that is based on the acceleration peak of the twelfth thoracic vertebra. The same problem was described earlier in the thoracic impactor tests: the peak values of the rib acceleration were too high, which in turn compensated for the low vertebral acceleration in the calculation of the TTI. This can also be observed in the sled test simulation of the Heidelberg tests.

Figure 4.4.21 shows a comparison of the simulated acceleration of the fourth rib on the impacted side.

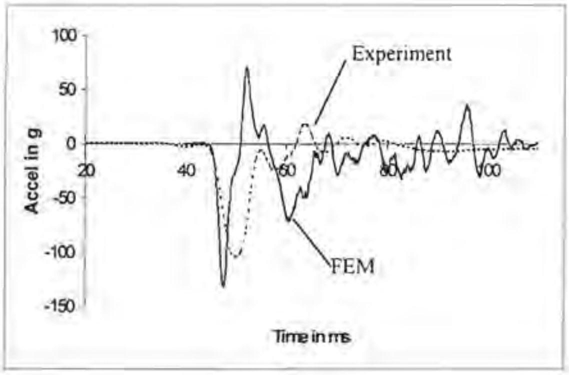

Figure 4.4.21 Rib 4 acceleration: FE-model -Heidelberg test at 6.7 m/s

The simulated acceleration exceeds the experimental peak value by 30 g. However, the overall shape of the simulated curve looks fairly similar to the experiment, although the experimental acceleration does seem to be more damped overall.

4.5 Abdomen Validation Results

Abdominal organs are a significant source of injuries in side impact. Injuries to the kidney, liver and spleen account for 32% of all injuries to the abdomen [Sie93]. Contact with the intruding door in lateral vehicle impact may also cause lung and aortic injuries. The abdominal organs are only partially protected by the rib cage and are therefore vulnerable to impact injuries. This section describes the biomechanical impact response of the abdominal area of the FE-model in comparison to cadaver test results.

4.5.1 Abdomen impactor test

In Viano's 60° lateral impactor test a 23.4 kg pendulum was used to impact the abdominal area of human cadavers at initial velocities of 4.8, 6.8 and 9.4 m/s. The impactor was aimed at 150 mm below the midsternum in order to partially impact the rib cage and the underlying abdominal organs. Figure 4.5.1 shows the dynamic response of the FE-model subjected to the 6.8 m/s abdominal impactor test.

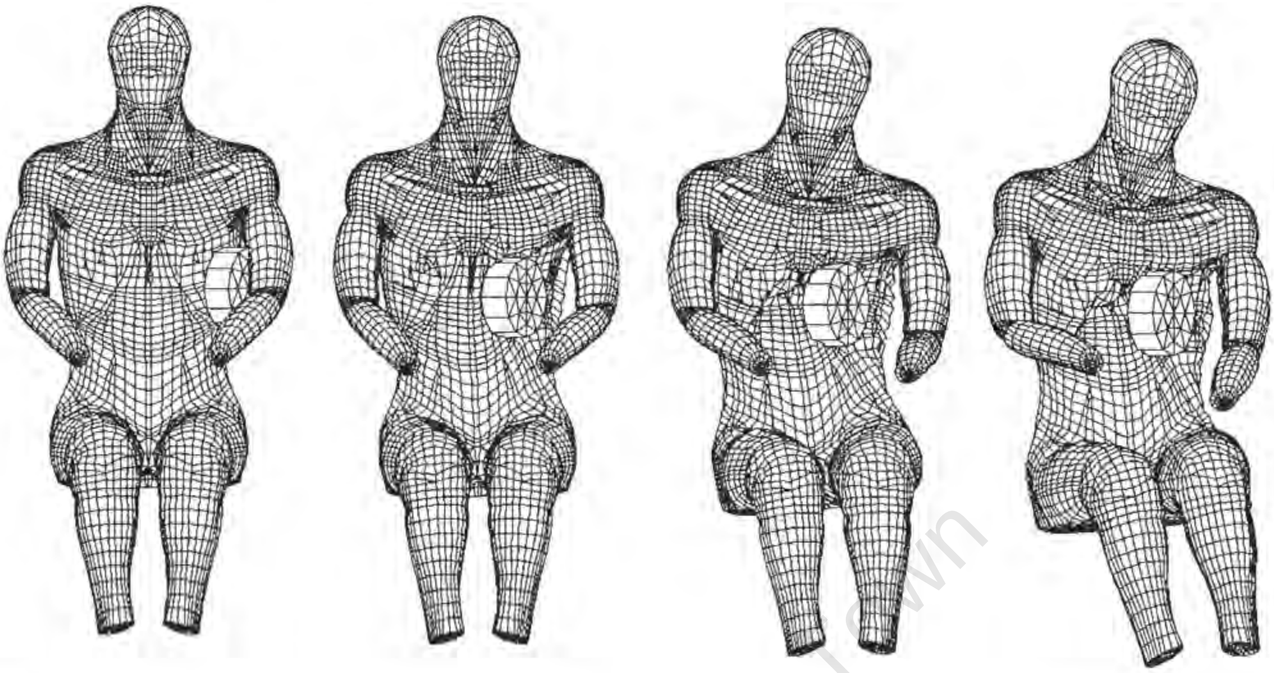

a) time = 0.0 ms *b) time = 10.5 ms* *c) time = 35 ms* *d) time = 50 ms*

Figure 4.5.1 Abdominal impactor test at 6.8 m/s

The first picture shows the FE-model prior to impact at time = 0.0 ms. At time = 10.5 ms the impact force peaks and the rib cage has started to deform while the remaining body is still at rest. At time = 35ms the maximum deformation is reached and the body has started to move. The recovering phase can be seen at time = 50 ms, in which the upper and lower body moves laterally. Animation files of the abdominal impacts can be found on the accompanying CD. The picture series in Figure 4.5.2 shows the deformation of the rib cage, spine and pelvis during this impact.

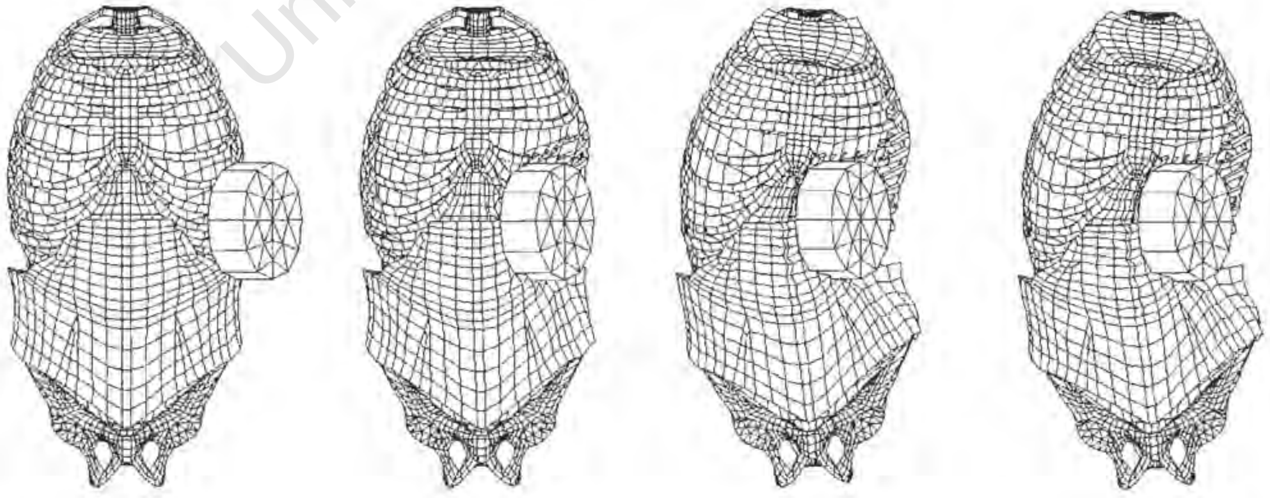

a) time = 0.0ms *b) time = 10.5ms* *c) time = 35ms* *d) time = 50ms*

Figure 4.5.2 Rib cage deformation of FE-model to Viano abdominal impactor test at 6.8 m/s

The rib cage is not entirely impacted by the front surface of the pendulum in the abdominal tests, which in turn influences the deformation pattern of the rib cage. In Figure 4.5.2 at time = 10.5 ms and 35 ms it is shown that mainly the lower ribs are deformed. The abdominal muscles do not show much resistance against the impactor. The muscle deformation around the impactor can be seen in Figure 4.5.2. Parameter modifications of the muscle material have not shown a significant influence on the force response and are therefore not illustrated. The force-time histories of the abdominal impacts at 6.8 and 9.4 m/s initial velocity are shown in Figure 4.5.3 in comparison with the force response corridor defined by the experiments.

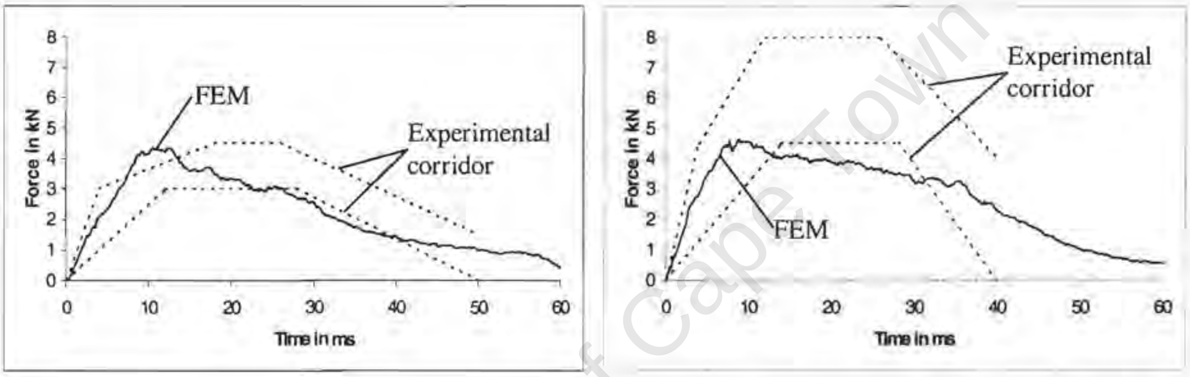

a) Abdominal impact at 6.8 m/s *b) Abdominal impact at 9.4 m/s*

Figure 4.5.3 Comparison of abdominal force-time histories

In Figure 4.5.3 a) and b) the simulated force curves for the 6.8 m/s and 9.4 m/s impactor tests show similar response curves. Although the initial velocity is 38% higher in the second case, the peak forces are only slightly higher than in the 6.8 m/s impact. Due to the higher initial velocity the peak force is reached earlier and the force level decreases at a slower rate. In both cases the simulated force curve falls mostly between the upper and lower border of the corresponding experimental response corridor, although the peak forces of the 6.8 m/s impact briefly exceed the upper border at about 8 ms. The model parameters, such as the stiffness of the rib cage or the material properties of the visceral contents, might be selected in such a way that either the response curve of the 6.8 m/s or that of the 9.4 m/s impact are optimised for one particular impact, but the overall performance seems to be best with this compromise. The force-deflection responses for these tests are shown in Figure 4.5.4.

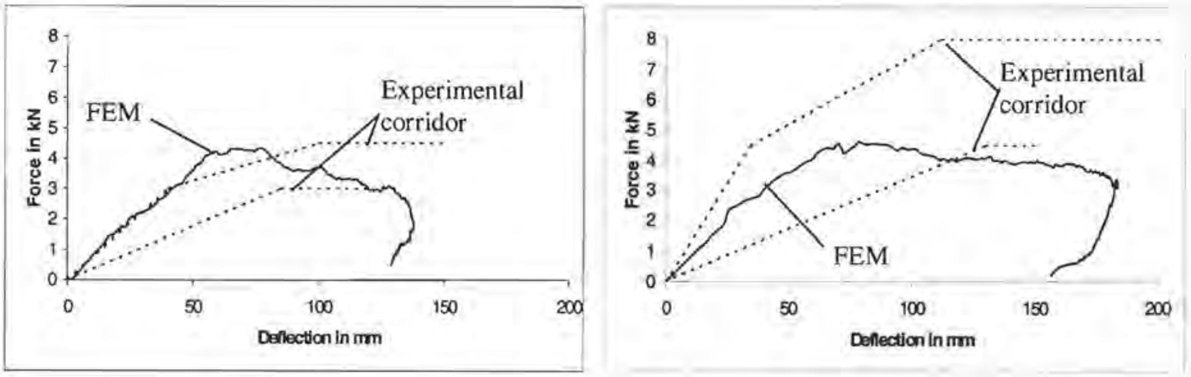

a) Abdominal impact at 6.8 m/s *b) Abdominal impact at 9.4 m/s*

Figure 4.5.4 Comparison of abdominal force-deformation histories

The simulated force-deflection response of the 6.8 m/s test follows the upper limit of the corridor at the beginning, but exceeds it after about 50 mm of abdominal deflection, as shown in Figure 4.5.4 a). The maximum force-deflection values however are not exceeded, but are only reached at lower deflection levels. Figure 4.5.4 b) shows the force-deflection response of the more severe abdominal test at an initial velocity of 9.4 m/s. It can be seen that the maximum deflection values are significantly higher than in the 6.8 m/s impact test, although the maximum force does not differ much. This deformation pattern of the abdominal region differs from that of the thorax. It is encouraging that both simulated force-deflection responses fall mostly between the borders of the response corridor.

Table 4.5.1 compares the maximum values of the simulated force, deflection and acceleration responses of the abdominal impactor tests to the corresponding experimental data. The graphical comparisons of response-time histories are shown in Appendix A.

	Experiment 4.8 m/s	**FE-model 4.8 m/s**	**Experiment 6.8 m/s**	**FE-model 6.8 m/s**	**Experiment 9.8 m/s**	**FE-model 9.8 m/s**
Force in kN	2.41 ± 0.49	2.79 ✓	3.71 ± 0.48	4.32 (✓)	6.50 ± 1.10	4.6
Deflection in mm	108.3 ± 2.30	108.09 ✓	114.3 ±7.6	136.42	146.0 ± 23.6	183.5
Compression in %	32.0 ± 6.6	31.79 ✓	36.2 ± 1.65	38.28 (✓)	45.8 ± 3.1	53.9
VC in m/s	0.77 ± 0.23	0.74 ✓	1.26 ± 0.12	1.32 ✓	2.22 ± 0.41	2.56 ✓
Acceleration T1 in g	6.9 ± 2.0	11.04	17.5 ± 1.9	15.1 (✓)	37.5 ± 11.0	19.66
Acceleration T6 in g	10.8 ± 4.4	11.36 ✓	28.9 ± 7.1	15.92	29.1 ± 5.9	20.86
Acceleration T12 in g	11.6 ± 1.6	17.64	29.8 ± 12.4	23.47	44.3 ± 9.0	20.45

Table 4.5.1 Abdominal responses: Viano impactor test – FE-model

The peak force of the FE-model exceeds the value of the experiment in the 6.8 m/s test as described earlier, while the simulated value is lower in the 9.8 m/s test and falls within the range of experimental values for the 4.8 m/s test. The maximum deformation of the FE-model is virtually identical with the experiment in the 4.8 m/s test, but exceeds the experimental values for the higher impact velocities at 6.8 and 9.8 m/s. The simulated compression of the abdomen in the 4.8 and 6.8m/s tests correlates fairly well with the experimental result, which indicates that the abdominal width of the cadavers must have been slightly smaller than that of the FE-model. The simulated Viscous Criterion (VC) also correlates well with the corresponding experimental result, which again indicates the capability of the FE-model to predict force and compression responses fairly well. The problematic nature of the acceleration responses has been mentioned earlier, and can also be seen in Table 4.5.1 with regard to the acceleration of the vertebrae T1, T6 and T12. In contrast to the thoracic simulation results, the acceleration peaks in the abdominal impacts are smaller than those of the experimental counterpart.

4.5.2 Abdominal response in the WSU sled test

The experimental set up of the WSU cadaver sled test was described in detail in Section 2.1.2. Figures 4.5.5 a) and b) compare the simulated force curves with the experimental counterpart for the initial velocities of 6.7 m/s and 8.9 m/s respectively.

As expected, the force level in the 6.8 m/s test is lower than in the 8.9 m/s test. The experimental force curve of the 6.8 m/s test has a slightly steeper ascending slope to ~25 ms than the simulation and reaches a first force peak of 1.8 kN. This is followed by a small descent for about 6 ms, before a second peak value of 3.1 kN is reached. The simulated curve does not show the first peak and reaches up to almost the same peak force within the same time as observed in the experiment. The decrease of the experimental force curve after 40 ms differs from the simulated curve by a slightly softer decline.

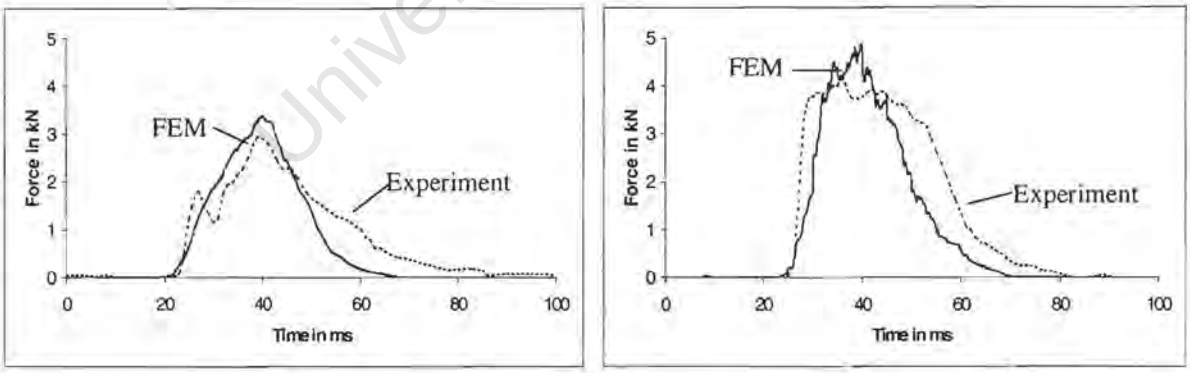

a) WSU sled test 6.7 m/s *b) WSU sled test 8.9 m/s*

Figure 4.5.5 Comparison of abdominal force-time histories in WSU sled tests

The slope of the simulated force curve in Figure 4.5.6 b) has a slightly lower gradient than the experimental counterpart, but reaches a higher peak force of 4.8 kN at 40 ms. The experimental force curve reaches a lower force level, which is held for a longer period than in the simulation. The experimental abdominal impact events seem to last longer than in the simulation, observed in Figures 4.5.5 a) and b) for both velocities. The cause of this discrepancy might be the difference in fat volume between the cadavers and the FE-model. This soft mass probably influences the duration of the abdominal impact.

Table 4.5.2 summarises the important abdominal cadaver data and FE-model responses of the WSU sled tests.

6.7 m/s	**age**	**mass** [kg]	**sex**	**internal abdominal injuries**	**Rib 8** [g]	**T12** [g]	**Force** [kN]
SIC05	67	44.0	m	none	100.4	92.3	3.75
SIC07	66	74.8	m	none	117.8	42.0	2.82
SIC08	64	73.9	f	25 mm laceration of spleen 10 mm laceration of liver	-	51.4	2.83
average	66	64.2	-	-	109.1	61.9	3.13
FE-model	-	73.4 √		-	108.0 √	40.5 (√)	3.84 (√)
8.9 m/s							
SIC04	69	57.6	m	two 25x13 mm lacerations of spleen	149	75.5	4.49
SIC06	60	61.2	m	none	136	92.8	4.69
average	65	59.4	-	-	142.5	84.2	4.59
FE-model	-	73.4	-	-	160.96	57.97	4.18

Table 4.5.2 Abdominal responses: WSU test – FE-model

The comparison of the impact responses of the FE-model and the experimental results shows a good agreement of the peak values of the acceleration of the 8th rib with the experimental results for the initial velocity of 6.7 m/s. At the higher velocity of 8.9 m/s, the simulation responses have higher peak values than the experiments. The acceleration of the 12th thoracic vertebra shows an even greater difference between the simulation responses and the experiments themselves. The peak values for sic05 and sic07, for example, differ by almost 120%. The values for the simulated impact forces fall within the range of the experimental responses, as described earlier.

4.6 Pelvis Validation Results

The frequency of pelvic fractures is 10%-14% [Gui97, Cav93, Hue92, Dan76] in vehicle side impact crashes. Fractures of the pubic rami, pubic symphysis, iliac wing, sacroiliac junction and the acetabulum can occur. Within the pelvic cavity, fractures are associated with potentially severe injuries to the blood vessels, bladder and urinary tract.

The comparison of accident and test injuries shows a good correlation with some minor differences. The fracture of the pelvic rami is most frequent. These fractures occur mainly on one side in cadaver sled tests, whereas they often involve both sides in accidents [Ces82]. The other differences concern the number of femoral neck fractures, which might be influenced by the test subject's age. The mechanical resistance of the femoral neck decreases with age and the cadavers used were usually older than the victims of car accidents.

Section 4.6.1 describes the validation of the pelvic region of the FE-model of the human body subjected to impactor loads. Section 4.6.2 presents the validation results of the FE-model in cadaver sled test simulations.

4.6.1 Pelvic impactor tests

The biomechanical impact response of the pelvis has been investigated experimentally in impactor tests on isolated pelvises and on the whole body as described in detail in Section 2.1.2.

Impactor test on isolated pelvic bone

Guillemot et al. [Gui97] conducted dynamic impactor tests on 12 pelvic bones as described in detail in section 2.1.2. The pelvises were impacted with a falling mass of 3.68 kg at a speed of 4 km/h, and the resultant displacement and impact force were obtained. This test configuration was simulated for the pelvic bone validation of the FE-model and is shown in Figure 4.6.1.

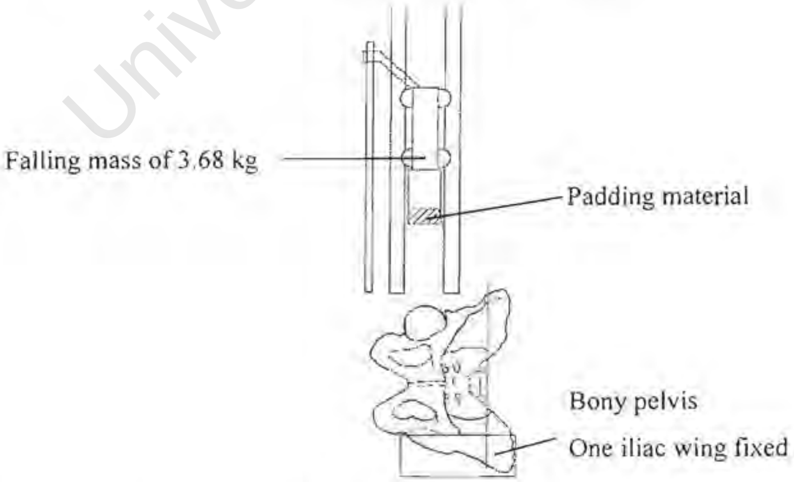

Figure 4.6.1 Experimental test set up [Gui97]

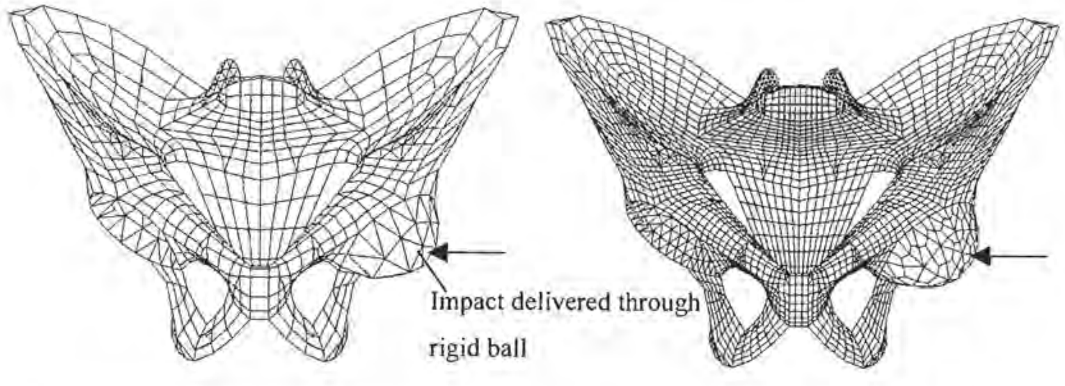

a) Coarse mesh 1180 shell elements *b) Fine mesh 4714 shell elements*

Figure 4.6.2 Impactor drop test on isolated pelvic bones

Regarding the simulation, the same orientation of the FE-pelvis was used as in the normal seated position, so that the impact was delivered laterally. In the impact test, the pelvis was loaded through a rigid ball positioned in the acetabulum. For the simulation, the FE-model of the femoral head with non-deformable elements was used to simulate this rigid ball. The load on the pelvis was defined through this non-deformable ball using the profile of a standard force, measured in the experimental tests [Bes98]. This procedure simplifies the simulation and reduces the influence of the impact of the falling mass and the rigid ball inside the acetabulum. Two different meshes have been developed for the FE-model of the pelvic bone shown in Figures 4.6.2 a) and b) to examine the differences in accuracy between a fine mesh with 4714 shell elements and a relatively coarse mesh with 1180 shell elements. Figure 4.6.3 compares the force-deflection response of the two FE-models with fine and coarse meshes respectively. The fine mesh has a softer slope at the beginning up to ~4 mm deflection, at which point the maximum force is reached.

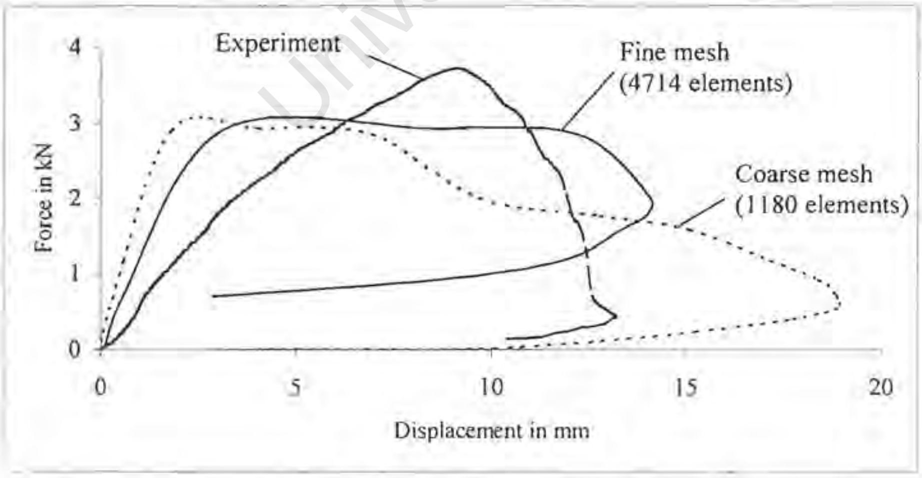

Figure 4.6.3 Comparison between fine mesh and coarse mesh [Gui97]

The descent of the force-deflection curve of the coarse mesh has a lower gradient than the fine mesh, and it reaches larger displacement values. However, the differences in the force-deflection responses between the coarse and the fine mesh do not justify the significantly longer simulation time for the fine mesh. Therefore, the coarse mesh is used in the FE-model of the human body.

Three different groups of pelvises were constituted to classify the fracture behaviour of the pelvis. In the first classification no fractures happened, and the impact forces were therefore high and the deformation low. In the second group, pubic fractures occurred, resulting in lower forces and more deformation. When anterior and posterior fractures took place, as in the third group, the force level was very low and the deformation accordingly high. The FE-model is intended to simulate the deformation behaviour of the pelvis that occurs most frequently, which is that of pubic fractures. As can be seen in Figure 4.6.4, the force deflection curve of the FE-model correlates well with the corresponding curve of the second group. As described in Section 3.1, no material failure is included in the model, so that the fracture is simulated by large plastic deformation of the upper pubic bone.

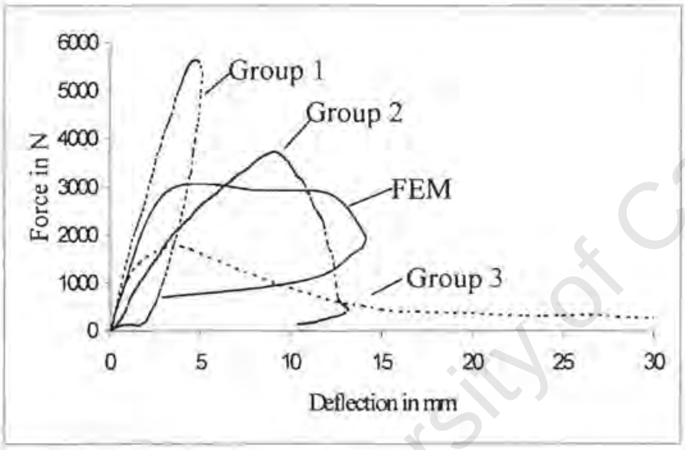

Figure 4.6.4 Comparison of force-deflection responses of FE-model and experiments [Bes98]

ISO pelvic impactor test

The test procedure for the lateral pelvic impactor test that is included in the ISO requirements is described in detail in Section 2.1.1. This test is based on a study conducted at ONSER, in which 22 unbelted cadavers were impacted laterally on the greater trochanter area with a 17.3 kg impactor at different initial velocities and the impact forces were measured. Figure 4.6.5 a) shows the impact force-time response of the FE-model subjected to this pelvic impactor test.

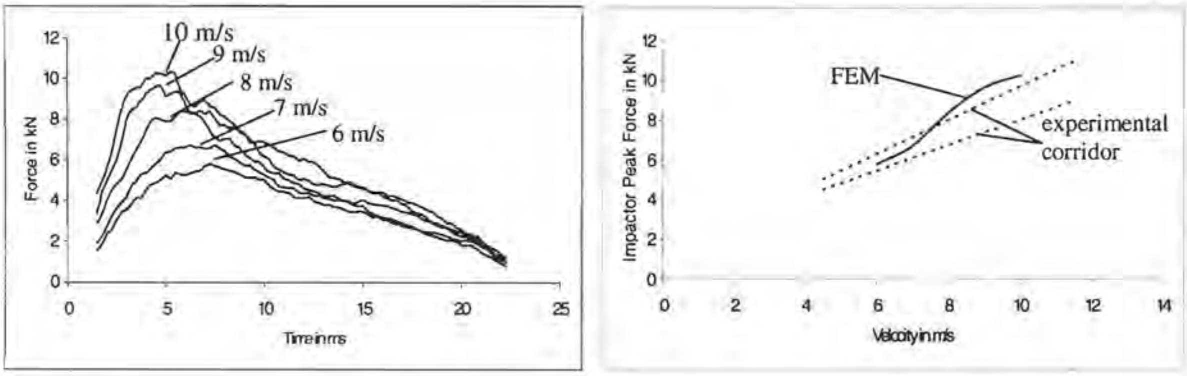

a) Force-time response FE-model *b) Peak impact force-velocity plot*

Figure 4.6.5 Comparison of pelvis impactor test

As expected, the impact peak forces increase with increasing impact velocity. Figure 4.6.5 b) shows the response corridor proposed in the ISO requirements that defines the range of peak forces depending on the impact velocity. For initial velocities up to 7 m/s the simulated response falls between the upper and lower limits of the experimental corridor. At higher velocities the simulated peak force exceeds the upper border of this corridor. This might be explained by the fact that with higher velocities the probability of pelvic fractures increases, and therefore the deviations of the non-fracturing material used in the FE-model become more apparent. It is possible to adjust the material properties of the model to fit the peak forces within the corridor at higher velocities. This would, however, deteriorate the performance of the model at lower velocities and in the pelvic impactor tests described below.

Viano pelvic impactor test

The pendulum impactor test procedure of the Viano is described in detail in Section 2.1.2. These impactor tests were conducted with a 23.4 kg pendulum that impacts the pelvic region at initial velocities of 4.8, 6.8 and 9.8 m/s. The Force-time histories of the 4.3 m/s and 9.8 m/s tests are shown in Figure 4.6.6 a) and b) in comparison with the corresponding response corridors developed from the experimental results.

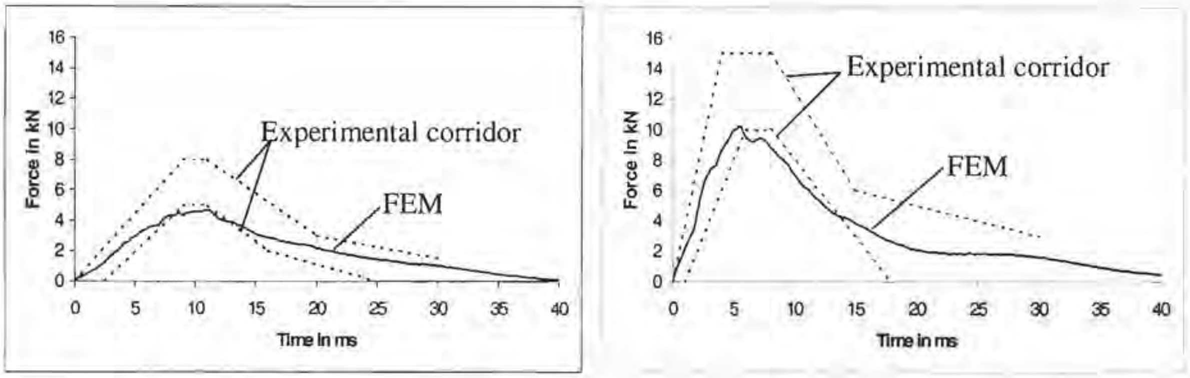

a) Pelvis impactor test 4.8 m/s *b) Pelvis impactor test 9.8 m/s*

Figure 4.6.6 Comparison of force-time histories in Viano pelvis impactor tests

The force-time curve of the 4.8 m/s test falls right between the borders of the response corridor, up to 8 m/s. The level of the peak force is slightly lower than the experimental values between 8 and 13 ms. The declining curve after 13 ms again falls between the upper and lower limit of the response corridor. The force response in the more severe test at 9.8 m/s shows a similar behaviour with a peak force that is near the lower limit. Furthermore, the descent of the curve closely follows the lower limit. The simulated responses in the Viano pendulum tests are closer too the lower border of the response corridor for both impact velocities, which in turn implies a rather soft deformation behaviour of the FE-pelvis. The comparison of the simulated peak impact forces in the ISO pelvis impactor tests in Figure 4.6.5 b) on the other hand illustrates, that the FE-model shows higher peak forces than the experiments at higher velocities. This discrepancy might be explained by the wide range of influencing factors on the biomechanical responses in cadaver tests. However, the simulated force responses correlate well with the corresponding experimental results, as can also be seen in Figure 4.6.7 a) and b), showing the force-deflection curves of the 4.8 m/s and 9.8 m/s impacts.

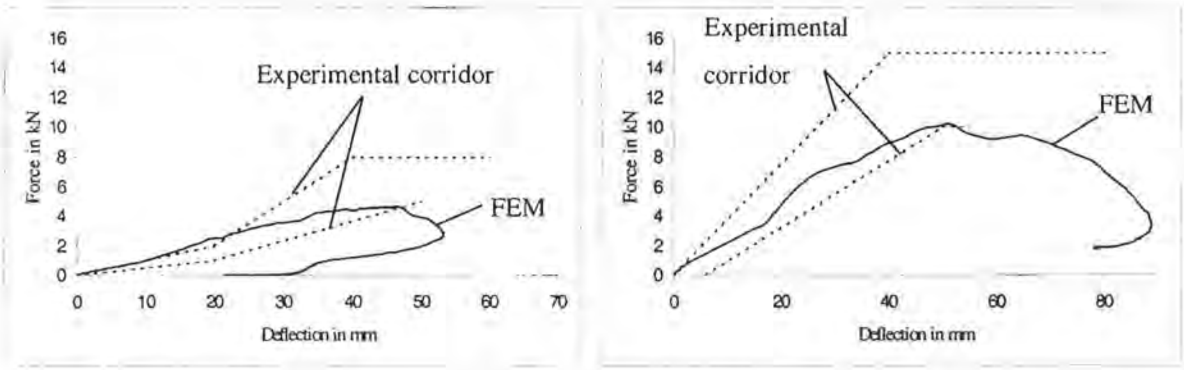

a) Pelvis impactor test 4.8 m/s *b) Pelvis impactor test 9.8 m/s*

Figure 4.6.7 Comparison of force-deflection responses in Viano pelvis impactor tests

The simulated force-deflection curve at the lower velocity shows a slightly stiffer behaviour than the experimental results for the first 20 mm. Thereafter the simulated curve falls between the corridor borders. At the highest velocity of 9.8 m/s, the simulated response correlates very well with the experiments, as the curve fits right into the corridor and shows a force-deflection behaviour that is closer to the lower corridor limit.

Table 4.6.1 summarises the most important responses of the FE-model in comparison with the corresponding experimental results.

	Experiment 4.8 m/s	**FE-model 4.8 m/s**	**Experiment 9.8 m/s**	**FE-model 9.8 m/s**
Force in kN	5.45 ± 1.65	4.64 ✓	11.20 ± 1.48	10.23 ✓
Deflection in mm	49.0 ± 16.0	53.3 ✓	78.3 ± 22.7	88.8 ✓
Compression in %	13.5 ± 4.0	14.8 ✓	22.9 ± 6.0	24.6 ✓
Acceleration T8 in g	7.7 ± 3.1	7.5 ✓	-	9.30
Acceleration T12 in g	15.0 ± 12.6	14.0 ✓	31.6 ± 1.0	28.9
Acceleration S3 in g	34.4 ± 15.0	29.8 ✓	39.9 ± 26.8	71.3

Table 4.6.1 Pelvic impact response data

As set out in the table above, the simulated force and deflection peak values correspond well with the experiments. The acceleration responses of the 8th and 12th thoracic vertebra show good agreement for both impact velocities. The acceleration response measured at the sacrum at S3 level shows fairly good agreement at low velocities, but gives a poor prediction for the high velocity. However, the experimental results of the S3 acceleration show a wide range, with over ± 67% in the case of the 9.8 m/s impacts and therefore the S3 acceleration does not seem be an ideal criterion for model validation and injury prediction.

4.6.2 Pelvic sled tests

The biomechanical impact response of the pelvis has been investigated experimentally in the Heidelberg and WSU sled tests that are described in detail in section 2.2.2. In contrast to the pelvic impactor test, a larger area of the body is involved when the cadaver impacts the rigid wall in sled tests. The leg and partially the abdomen generates impact forces at the pelvic beam. The different sizes of the pelvic beams distinguish the pelvis responses in the Heidelberg and the WSU sled tests.

Pelvis response in Heidelberg sled test

Figure 4.6.8 shows the force-time histories measured at the pelvic beam in the Heidelberg sled test for the 6.7 m/s and 8.9 m/s initial velocities.

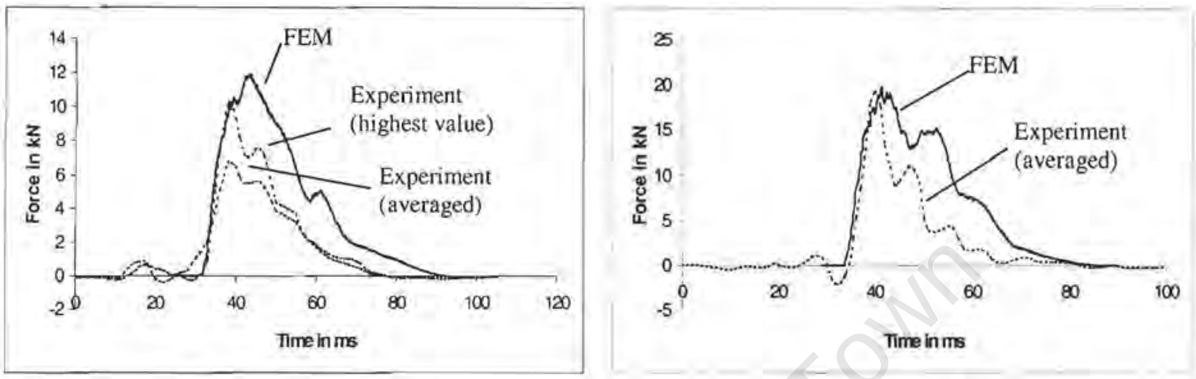

a) Pelvis force response at 6.7 m/s *b) Pelvis force response at 8.9 m/s*

Figure 4.6.8 Comparison of pelvis force-time histories in Heidelberg sled test

The simulated force curve in Figure 4.6.8 a) is compared to the averaged experimental force response and the curve with the highest force level. The simulated curve has a very similar slope compared with both experimental curves but exceeds the peak forces of 10.2 kN by the simulated force peak of 11.9 kN at time = 43 ms. The following descent of the curve looks similar to that of the experiments, although the simulated impact lasts about 15 ms longer. No explanation could be found for the discrepancies between the experimental and simulated force responses in the 6.7 m/s Heidelberg sled test. The simulated response of the 8.9 m/s impact in Figure 4.6.8 b), shows a closer correlation with the experiments. The slope of the simulated curve is almost identical with the experiments as is the force peak value. The shape of the descent following also looks very similar, although the simulated force levels exceed those of the experimental curve.

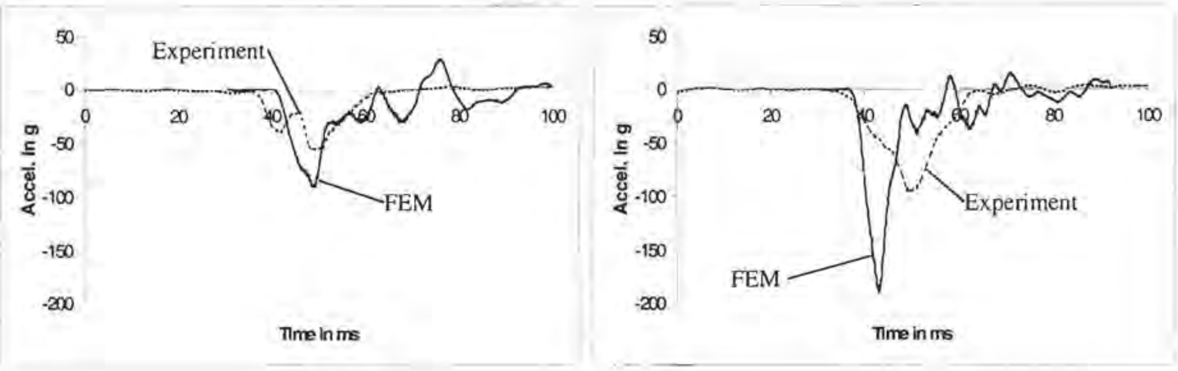

a) Pelvis acceleration response at 6.7 m/s *b) Pelvis acceleration response at 8.9 m/s*

Figure 4.6.9 Pelvic acceleration-time history - Heidelberg sled test

The simulated acceleration response at the 3rd sacral vertebra is shown for the 6.7 m/s and 8.9 m/s test in Figure 4.6.9 a) and b) respectively. It has been stated earlier that the simulated acceleration responses of the vertebrae exceed the experimental values, which can also be observed for the pelvis acceleration. The peak value of the FE-model exceeds the experimental values significantly and would require a more detailed investigation.

Pelvis response in WSU sled test

The pelvic beam in the WSU test is smaller than the Heidelberg pelvic beam, which partially covers the abdominal area. The responses measured in the WSU are therefore more concentrated on the impact forces generated by the pelvic body part. Figures 4.6.10 a) and b) compare the simulated pelvic force responses with the corresponding experimental results at the initial velocities of 6.7 m/s and 8.9 m/s respectively.

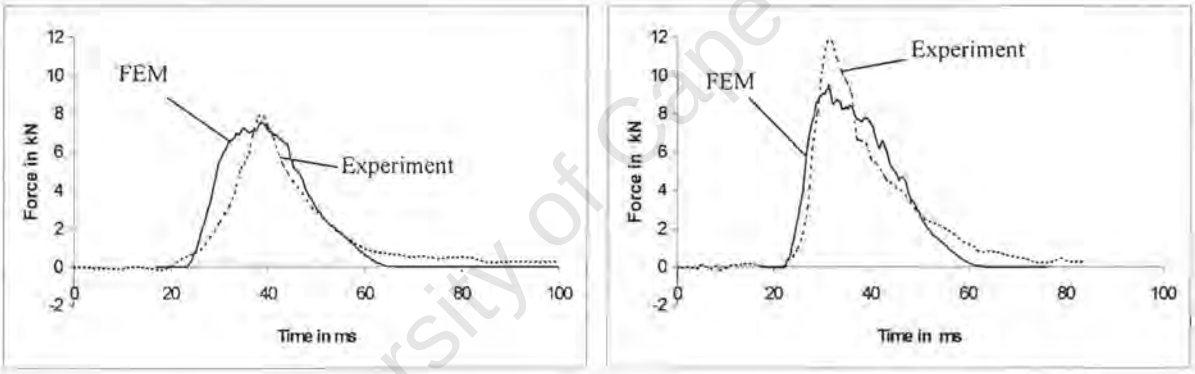

a) Pelvis force-time response at 6.7 m/s *b) Pelvis force-time response at 8.9 m/s*

Figure 4.6.10 Comparison of pelvis force-time histories in WSU sled test

The simulated pelvic force of the 6.7 m/s test shown in Figure 4.6.10 a) has a steeper slope than its experimental counterpart and reaches the maximum force level earlier, namely after 30 ms. The maximum forces are almost identical, with 7.48 kN for the simulation and 7.89 kN on average for the experiments. This high force level is only of short duration in the experiment, while it lasts for almost 20 ms in the simulation. The descents of both curves, as well as the duration of the entire impact event show a very similar pattern. The comparison of the pelvic forces in the more severe test at 8.9 m/s is shown in Figure 4.6.10 b). The slope of the simulated curve closely follows the experiments up to 9 kN, whereafter the simulated peak value of 9.48 kN is reached. The experiments on average show a higher peak value of 11.83 kN. The descent of the simulated curve shows a similar shape as the experiment, and the duration of the impact differs only slightly.

The compression responses are compared in Figure 4.6.11 for the 6.7 m/s and 8.9 m/s tests. The compression is defined here by the pelvic deflection of the struck side, divided by half of the pelvic width.

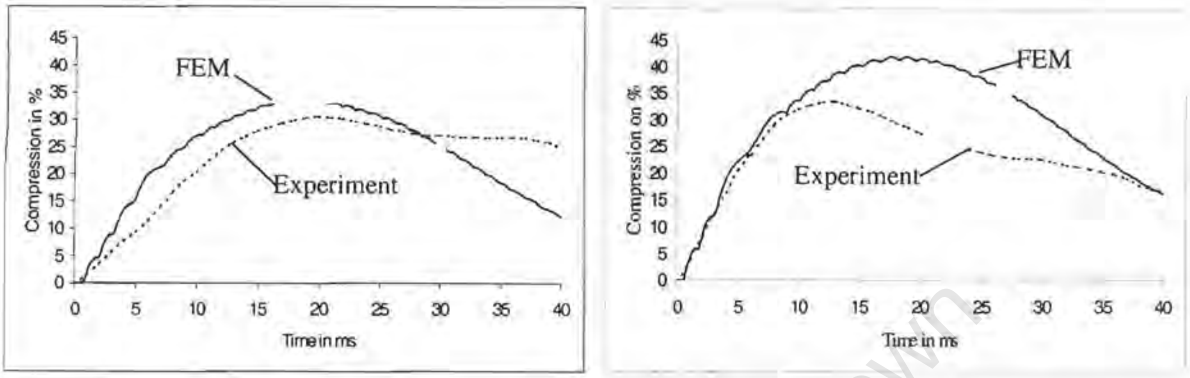

a) Pelvis compression response at 6.7 m/s *b) Pelvis compression response at 8.9 m/s*

Figure 4.6.11 Comparison of pelvis compression in WSU sled test

The pelvis compression in the 6.7 m/s test is generally higher in the simulation up to 27 ms, as shown in Figure 4.6.11 a). After the maximum value of 33.59 % is reached at 18 ms, the pelvis compression continuously decreases, whereas the compression in the experiment does not recover significantly. A similar behaviour is observed in the 8.9 m/s test, as shown in Figure 4.6.11 b). The simulated curve closely follows the experiment up to 10 ms whereafter the maximum compression of 31.4 % in the experiments is reached at 12 ms. After the maximum compression of 41.86 % is reached in the simulation, the compression continuously decreases as could be observed in the 6.7 m/s test.

The half pelvic width indicates the differences in cadaver statures in the 6.7 m/s and the 8.9 m/s tests. The average value of 179.7 mm in the 6.7 m/s test is virtually the same as the value of 180 mm of the FE-model, whereas the average width of 134.4 mm in the 8.9 m/s tests differs significantly. This might explain the bigger differences between the simulated and experimental compression in the 8.9 m/s test.

Table 4.6.2 summarises important pelvic response data comparing the simulation results with the corresponding experiments.

	6.7 m/s					8.9 m/s			
	SIC05	SIC07	SIC08	average	FEM	SIC04	SIC06	average	FEM
Pelvic Acceleration [g]	68.9	116.1	36.8	**73.9**	**60.0** ✓	62.9	103.4	**83.2**	**73.1**(✓)
compression [%]	23.7	33.4	36.9	**31.3**	**33.6** ✓	29.8	33.0	**31.4**	**41.9**
half pelvic width [mm]	168.8	190.5	-	**179.7**	**180.0** ✓	137.9	130.8	**134.4**	**180.0**
max. Force [kN]	10.79	6.68	6.20	**7.89**	**7.48** ✓	12.92	10.74	**11.83**	**9.48**

Table 4.6.2 Comparison of the pelvis responses – WSU test

It has been mentioned earlier that the pelvic acceleration values differ greatly among the cadaver tests. This can also be observed in the 6.7 m/s and the 8.9 m/s tests, with wide ranges between 36.8 g and 116.1 g peak acceleration. Although the simulated values do not differ too much from the averaged experimental data, the pelvic acceleration of the FE-model might only be used qualitatively.

The simulated peak values of the compression and the peak force correlate better for the 6.7 m/s than for the 8.9 m/s test.

5. Discussion and Conclusion

This final chapter discusses the simulated impact responses of the different body regions. The biomechanical responses of the FE-model of the human body are compared with those of existing side impact dummies and the important differences are illustrated. Conclusions are drawn from this comparison and the scope for future work will be presented.

5.1 Discussion of the Impact Responses

5.1.1 Shoulder response

The validation of the FE-model of the shoulder was conducted comparing the biomechanical impact response of the FE-shoulder subjected to a pendulum impactor test and the WSU sled test. The simulated results, presented in Section 4.2, showed satisfactory correlation with the corresponding experimental cadaver impactor and sled tests. The simulated impactor force time history falls between the borders of the experimental response corridor defined by the experiments. The comparison of the simulated force time histories with the corresponding sled test results showed the same level of peak values, but a steeper decline of the simulated force curve.

The simulation showed that the shoulder dynamics are strongly influenced by the deformation of the clavicle, which in turn determines the dynamics of all bony parts of the shoulder. The muscle groups of the shoulder, thoracic and neck region do not influence the shoulder dynamics to the same extent as the clavicle, the scapula and the rib cage. Two different shoulder deflection patterns were assumed to take place in lateral shoulder impacts, and both are strongly influenced by the rib cage deformation. In the first case, the ribs do not fracture, but bulge forward and rearward which in turn causes the scapula to wing outwards. The second rib cage deformation pattern is influenced by numerous rib fractures, which prevent the rib cage from bulging rearwards and therefore causes the scapula to exhibit a large motion. The FE-model confirms this hypothesis for the case of a non-fracturing rib cage. Since no material failure was included in the FE-model, the rib cage bulged rearwards, causing the scapula to wing outwards.

The complex deformation pattern of the human shoulder subjected to a lateral impact is difficult to simulate by a human surrogate or side impact dummy. The shoulder deformation of the FE-model and the cadaver show different characteristics to those observed in the current side impact dummies. This is illustrated in Figure 5.1.1a), which shows the force time history of the SID subjected to the shoulder impactor test at an impact velocity of 4.3 m/s in comparison to the cadaver and FE-model responses. Figure 5.1.1 b) illustrates the shoulder force time history of the SID in the 8.9 m/s WSU sled test in comparison with the corresponding responses of the FE-model and the cadaver test.

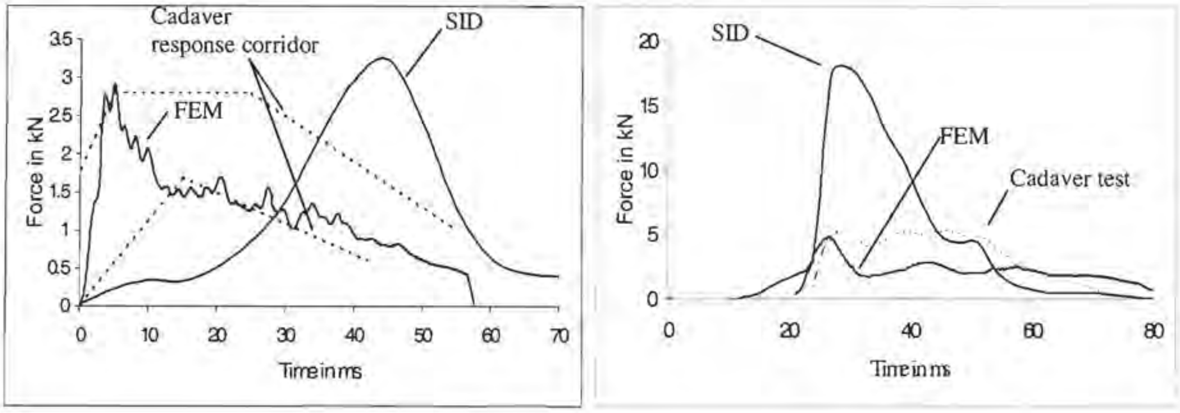

a) Shoulder impactor test at 4.3 m/s *b) Shoulder force WSU test at 8.9 m/s*

Figure 5.1.1 Comparison of the shoulder impact response of the SID with the corresponding responses of the FE-model and cadaver tests.

The shoulder deformation of the SID shows a different behaviour in comparison to that of the FE-model and the cadavers. The force curve for the SID does not fall within the response corridor shown in Figure 5.1.1 a). Although the SID shoulder seems to be too soft at the beginning, the peak impact force reaches a higher value than observed in the simulation and cadaver response. The maximum shoulder deflection was 157 mm for the SID, whereas in the cadaver test an average value of 37.5 mm was measured. The FE-model response, with a value of 39.8 mm compares well with the cadaver shoulder deflection. The deformation characteristics of the SID observed in the WSU sled test configuration does not correlate well with those of the cadavers, because the impact force exceeds the experiment value significantly. The FE-model shows a much higher biofidelity than the SID.

5.1.2 Head and neck response

The dynamics of the head-neck complex subjected to lateral acceleration were examined by two sled test conditions; a low g-level volunteer test and a high g-level cadaver test, presented in Section 4.3. The head-neck responses of the FE-model were compared to the corresponding experimental head acceleration time histories in the longitudinal, lateral and vertical direction, as well as the rotational acceleration and displacement around the longitudinal and vertical direction. The comparison of the low g-level simulation results showed good agreement for the simulated accelerations and displacements in all three directions with the experimental counterparts. The dynamic responses of the FE-model of the head and neck subjected to high g-level lateral acceleration showed reasonable agreement with the experiments.

Figures 5.1.2 a) and b) shows the trajectories of the centre of gravity of the head of the SID, the FE-model, volunteers in low g-level sled tests and a cadaver in high g-level sled test.

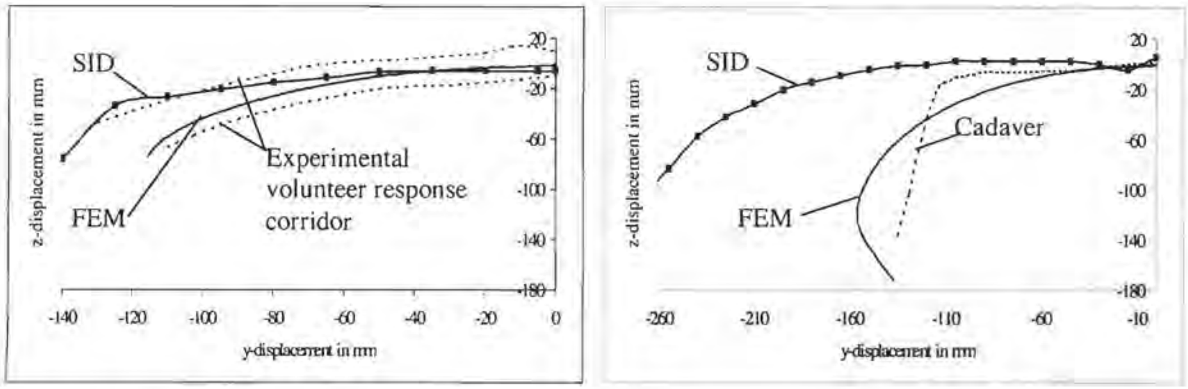

a) Low g-level lateral sled test *b) High g-level lateral sled test*

Figure 5.1.2 Comparison of the head trajectory of the SID with the corresponding responses of the FE-model, volunteer and cadaver in low and high g level lateral sled tests.

The trajectory curve of the SID-head follows closely the upper border of the volunteer response corridor as shown in Figure 5.1.2 a). The curve of the FE-model also falls between the borders of the experimental response corridor. The dynamic head-neck responses differ more at higher lateral acceleration illustrated in Figure 5.1.2 b). The curve of the SID follows closely that of the cadaver to about 110 mm of lateral y-displacement. The dynamics of the cadaver head is then dominated by a motion in the vertical z-direction, which cannot be observed for the head of the SID. The head of the SID moves more into the lateral then in the vertical direction. The curve of FE-model follows the experimental cadaver response closer than the SID.

5.1.3. Thorax response

For the thorax validation, presented in Section 4.4, the FE-model was subjected to lateral and oblique impactor tests at different impact velocities and compared to sled test impacts against a rigid wall at 6.7 m/s and 8.9 m/s initial velocity. The impact force, the thorax compression and the lateral acceleration of thoracic vertebrae and ribs were important biomechanical responses that were compared with the corresponding experimental counterparts.

The simulated impact responses showed an exceptionally good agreement with the corresponding impactor tests in terms of force-time histories and force-deflection responses. The correlation between the simulated rib acceleration and the accelerations in the experiments was fairly good. Some differences were observed between the simulated acceleration of the thoracic vertebrae and the corresponding experimental results.

The force responses in the simulated cadaver sled tests showed a very good agreement with the corresponding Heidelberg- and WSU tests at 6.7 m/s. The peak forces predicted by the FE-model in the 8.9 m/s sled tests, exceeded the experimental values slightly. The acceleration responses of the 4th rib and the 1st and 12th thoracic vertebrae exceeded the corresponding experimental values less, as observed in the thoracic impactor tests.

As expected, the simulation of the thoracic impact showed that the rib cage contributes most to thorax stiffness. Although no material failure model was included in the material properties of the ribs, the simulated force and deformation responses seemed to be realistic. Although the force-deflection behaviour can be simulated well by using a simplified elastic-plastic material model for the ribs, the load transfer into the thoracic spine differs in comparison to the experiments. When ribs fracture in real life, the load transfer to the corresponding thoracic vertebrae decreases significantly. This does not happen to the same extent in the FE-model, where fracture is simulated by a large amount of strain. This deformation behaviour helps to explain the discrepancies between the simulated and experimental acceleration values of the thoracic vertebrae.

The deformation of the thorax plays an important role in assessing the biofidelity of the FE-model in the thoracic impactor test. The deformation pattern is characterised by the impactor force, which represents the resistance of the rib cage against the impactor and the resulting deflection response. A high level of biofidelity of the thorax can only be achieved by using a very flexible rib cage, as shown in the validation results of the FE-thorax in Section 4.4. A stiff and relatively inflexible thorax design, as found in the present side impact dummies, generates impact forces that exceed those of the cadaver experiments significantly and cannot be considered as "human-like". Figure 5.1.3 a) illustrates the force time response of the present Eurosid subjected to the Viano thoracic pendulum test at an impact velocity of 9.8 m/s in comparison to the corresponding FE-model and cadaver responses.

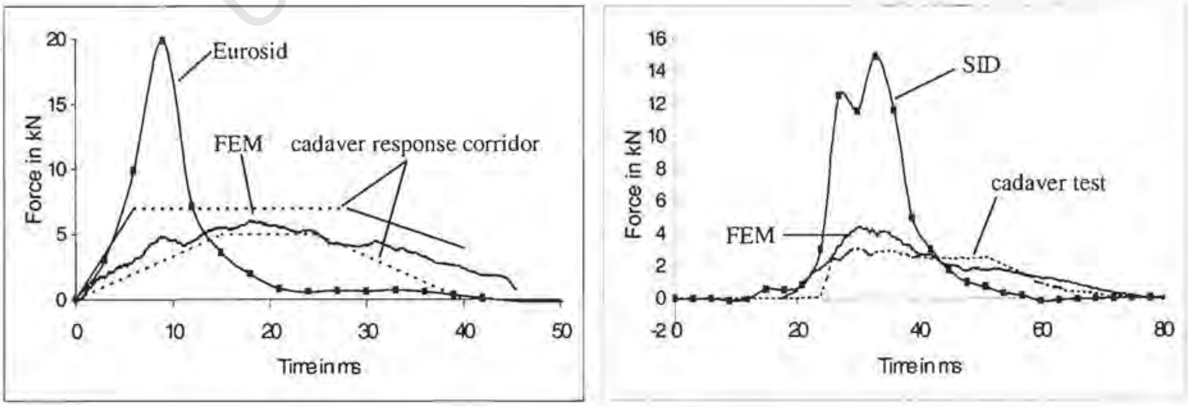

a) Viano thoracic impact at 9.8 m/s *b) WSU sled test at 8.9 m/s*

Figure 5.1.3 Comparison of the thorax impact response of the Eurosid and SID with the corresponding responses of the FE-model and cadaver tests

5.1.4 Abdomen response

For the validation of the abdomen, presented in Section 4.5, the FE-model was subjected to oblique impactor tests at different impact velocities and to sled test impacts against a rigid wall at 6.7 m/s and 8.9 m/s initial velocity. The impact force and the abdominal compression were the important biomechanical responses that were compared to the corresponding experimental counterparts. The simulated force-time and force-deflection responses showed a satisfactory agreement with the corresponding experimental results.

In contrast to the experimental results, which showed significantly higher peak force between the 6.8 and 9.8 m/s impactor test, the simulation did not show this difference to the same extent. However the simulated force-time and force-deflection responses fell between the upper and lower limits defined by the experimental corridors. The simulated force response of the abdomen in the 6.7 and 8.9 m/s WSU sled tests correlate well with the corresponding experimental counterparts in terms of peak values, shape of force curves and duration of impact.

In the abdominal impactor tests, the rib cage is not entirely impacted by the front of the pendulum impactor, which influences the deformation pattern of the rib cage. Therefore only the lower part of the rib cage is impacted and more deformed than in the thoracic tests. The influence of properties of the visceral contents that are covered by the rib cage is higher in the abdominal impact than in the thoracic impact. However, the rib cage still contributes most to the impact resistance of the abdominal region in these tests. The compliance of the abdomen is essential for the biomechanical impact response of this body region. Figure 5.1.4 a) shows the abdominal impact response of the Eurosid subjected to the Viano pendulum test at a velocity of 6.8 m/s, in comparison with the corresponding cadaver and FE-model responses. The generated impact forces exceed those of the cadavers significantly as illustrated in Figure 5.1.4 a), which indicates that the abdomen part of the Eurosid is too stiff. To achieve a biomechanical response similar to that of the cadavers, the abdominal region needs to be as soft as demonstrated with the FE-model. In contrast to the poor performance of the dummies in the abdominal impactor test, the SID abdominal response under WSU sled test condition correlates fairly well with the corresponding experiment as illustrated in Figure 5.1.4 b).

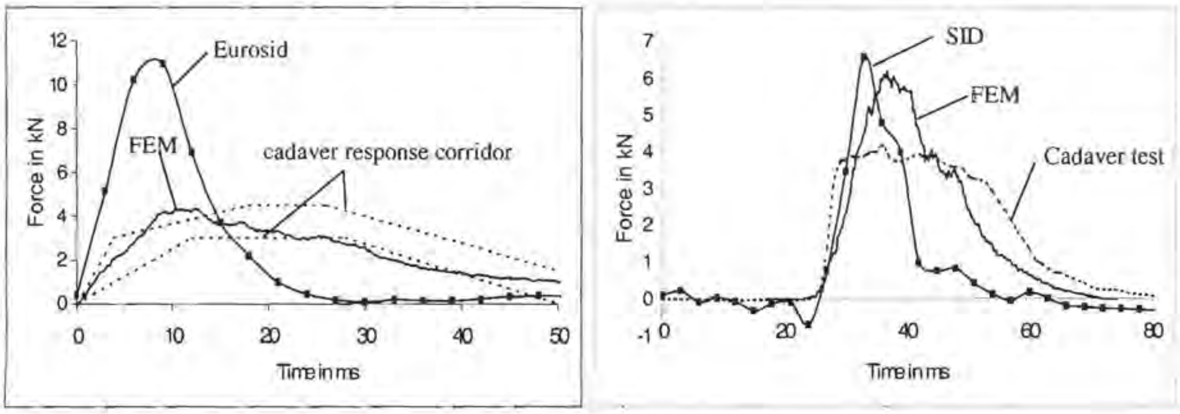

a) Viano abdominal impact 6.8 m/s *b) WSU sled test 6.8 m/s*

Figure 5.1.4 Comparison of the abdominal impact response of the Eurosid and SID with the corresponding responses of the FE-model and cadaver tests

The peak force measured in the SID experiment does not exceed the cadaver values too same extent as generally observed in dummy tests. The abdominal response need to be considered together with the thoracic response of the same test shown earlier in Figure 5.1.3 b). The thoracic force response exceeds the cadaver values significantly, so that one might conclude that the thoracic beam takes up the largest amount of the impact load. This impact is therefore dominated by the thoracic region and might not be useful for abdominal impact investigation. The FE-model on the other hand fulfils the biofidelity requirements of both the impactor and the sled tests.

5.1.5 Pelvis response

For the validation of the pelvis, presented in Section 4.6, the FE-model was subjected to lateral impactor tests at different impact velocities and to sled test impacts against a rigid wall at 6.7 m/s and 8.9 m/s initial velocity. The impact force and the pelvis compression were the important biomechanical responses that were compared to the corresponding experimental counterparts. The simulated force-time and force-deflection responses showed a satisfactory agreement with the corresponding experimental results. The simulated peak pelvic force was slightly smaller than the experimental counterparts, whereas the pelvis compression values of the FE-model matched those of the experiments. The pelvis acceleration responses did not show a satisfactory agreement with the cadaver experiment, although it must be said that the experimental results varied within a wide range.

Figure 5.1.5 depicts the impact response of the Eurosid pelvis subjected to the impact load in the 9.8 m/s Viano pendulum test.

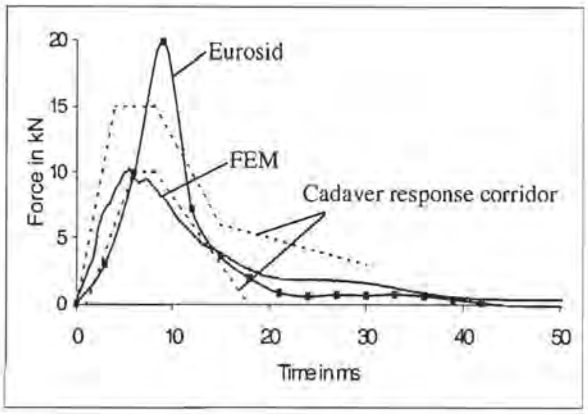

Figure 5.1.5 Comparison of the pelvis force in Viano test 9.8 m/s

The impact force generated by the Eurosid pelvis does not exceed the upper border of the cadaver response corridor to the same extent as observed in the thoracic and abdominal impacts. However, the dummy pelvis turned out to be too stiff as the high impact forces indicate. The softer pelvis of the FE-model showed an impact response that closely follows the lower border of the response corridor.

For the cadaver and the FE-model, the pelvis compression is significantly lower than the compression of the abdomen and thorax under the same impact condition, and the impact force is accordingly higher. The stiff structure of the bony pelvis does not allow the impactor to deform the pelvic region to the same extent as the abdomen and thorax. The influence of the surrounding muscles of the pelvic region contributes mostly for the inertial properties rather than for the structural stiffness.

The stiffer deformation pattern is easier to achieve with the mechanical design of the dummy, which leads to a better biomechanical performance of the pelvis in comparison to the thoracic and abdominal dummy regions.

5.2 Conclusion and Scope for Future Work

The objective of this thesis was to build a FE-model of the human body for vehicle side impact simulations. This FE-model was required to be complex enough to model the biofidelity of the human body.

The FE-model developed by the author has been described in detail in Chapter 3. All relevant skeletal parts of the human body are modelled by shell elements in greater detail than in previous models. The different joints and ligaments of the human body are represented by FE-models of a high geometrical complexity. All major muscles of the back, the neck, the abdomen and the complex shoulder muscles are included as separate FE-models. These model groups interact through contact conditions, which allow for realistic movements among the different muscle layers. Three modelling techniques are applied for the different muscle groups of the body using one-dimensional spring-damper elements, two-dimensional membrane elements and three-dimensional solid elements.

Chapter 4 compared the impact responses of the FE-model with the results of all relevant cadaver lateral impactor tests, as well as to all relevant sled tests. The material properties were determined in order to optimise the entire FE-model and not to improve the impact performance for a particular test. This validation procedure has demonstrated the high level of biofidelity of the FE-model. When comparing the impact response curves of the FE-model with those obtained from impact dummies, it becomes clear that the potential of simulating the response of the human body in lateral side impact with the use of FE-models is greater than that of using dummies.

The main conclusions drawn from the described work are:

- The FE-model showed a significantly higher biofidelity than the existing dummies. The source of the poor biofidelity of the present dummies was concluded to be the high stiffness of the dummies.
- Despite its complexity, the FE-model proved to operate numerically stable even under severe impact conditions as localised impacts at 9.8 m/s.
- The head-neck validation was conducted for low and high g-level accelerations and proved the high biofidelity of that body region of the FE-model
- The shoulder dynamics are mainly influenced by the clavicle and the deformation of the rib cage, and to a lesser extent by the deformation of the muscles. This influence of the rib cage deformation on the shoulder dynamics was assumed by Irwin et al. [Irw93] and was illustrated by the FE-model
- The impact performance of the thorax and abdomen is determined by the rib cage deformation.
- Differences between the Heidelberg sled test and the WSU sled test were described and verified.

The scope for future work includes:

- Improvement of the material model, including material failure. This would cause stability problems, because muscle elements undergo large strain as they are connected to "breaking bones".
- Development of visco-elastic materials for muscles and visceral contents.
- Including the FE-model of the human body into a FE-model of a crash-vehicle.
- Validation of the FE-model for other impact directions.

References

[AISyear] The Abbreviated Injury Scale (year of revison)
American Association for Automotive Medicine

[Ast98] Astori, P. and Raballo, M. "Multi-body numerical model of the human neck", Proc. of the International Crashworthiness Conference, IJcrash98, pp. 63-72, 1998.

[Bau96] Baudrit, P.; Domont, A.; Trosseille, X. and Tarriere, C. "Influence of test condition on protection criteria in side impact", 40th Stapp Car Crash Conference, SAE 962420, pp. 131-136, 1996.

[Bea97] Beaugonin, M; Haug, E.; Cesari, D "Improvement of a numerical ankle-foot model: deformable bones", 41st Stapp Car Crash Conference, SAE 973331, 1997

[Ben87] Bendjellal, F.; Tarriere, C.; Gillet, D.; Mack, P. and Guillon, F."Head and neck responses under high G-level lateral deceleration", 31st Stapp Car Crash Conference, SAE 872196, pp. 29-47, 1987.

[Ben88] Bendjellal, F.; Tarriere, C. and Brun-Cassan, F. "Comparative evaluation of the biofidelity of Eurosid and SID side impact dummies", 32nd Stapp Car Crash Conference, SAE 881717, 1988.

[Ben91] Bendjellal, F.; Fuid, E; Hautmann, E; Koch, M.; Marks, H; Pastorino, A. "Eurosid-1 and Biosid impact response characteristics vs. ISO Biofidelity requirements" 13th ESV conference, 1991.

[Ber93] Bermond, F., Ramet, M., Bouquet, R. and Cesari, D., "A Finite Element Model of the Pedestrian Knee Joint in Lateral Impact", Proceedings of the 1993 International IRCOBI Conference on the Biomechanics of Impacts, pp. 117-129, Eindhoven, September 8-10, 1993.

[Bes98] Besnault, B.; Guillemont, H.; Robin, S.; Lavaste, F. and LeCoz, J.Y. "A parametric finite element model of the human pelvis", 42nd Stapp Car Crash Conference, SAE 983147, 1998.

[Bos86] Bosio, A.C. and Bowman, B.M. "Simulation of head-neck dynamic response in -Gx and +Gy", 30th Stapp Car Crash Conference, SAE 861895, pp. 345-378, 1986.

[Bou94] Bouquet, R.; Ramet, M.; Bermond, F. and Cesari, D. "Thoracic and pelvic human response to impact", 14th Int. Conference on Experimental Safety Vehicle, 94-S1-O-03, 1994.

[Bow84] Bowman, B.M. and Schneider, L.W. "Simulation analysis of head and neck dynamic response", 28th Stapp Car Crash Conference, SAE 841668, pp. 173-205, 1984.

[Cam97] Camacho, D.L.; Nightingale, R.W.; Robinette, J.J.; Vanguri, S.K.; Coates, D.J. and Myers, B.S. "Experimental flexibility measurements for the development of a computational head-neck model validated for near vertex head impact", 41st Stapp Car Crash Conference, SAE973345, pp. 473-486, 1997.

[Car91] Careme, L. M. "Occupant kinematics and injury causation in side impacts – field accident experience", SAE 910316, 1991.

[Cav90a] Cavanaugh, J.M.; Walilko, T.; Malhotra, A.; Zhu, Y. and King, A.I. "Biomechanical response and injury tolerance of the pelvis in twelve sled side impacts", 34th Stapp Car Crash Conference, SAE 902305, 1990.

[Cav90b] Cavanaugh, J.M.; Walilko, T.; Malhotra, A.; Zhu, Y. and King, A.I. "Biomechanical response and injury tolerance of the thorax in twelve sled side impacts", 34th Stapp Car Crash Conference, SAE 902307, 1990.

[Cav93] Cavanaugh, J.M.; Zhu, Y.; Huang, Y. and King, A.I. "Injury and response of the thorax in side impact cadaveric tests", 37th Stapp Car Crash Conference, SAE 939127, 1993.

[Cav96] Cavanaugh, J.M.; Walilko, T.; Chung, J. and King, A.I. "Abdominal injury and responses in side impact", 34th Stapp Car Crash Conference, SAE 902307, 1990.

[Ces76] Cesari, D.; Ramet, M. and Cavallero, C. "Influence of intrusion in side impact", 6th Int. Conference on Experimental Safety Vehicle, pp. 703-714, 1976.

[Ces80] Cesari, D.; Ramet, M. and Clair, P. "Evaluation of pelvic fracture tolerance in side impact", 24th Stapp Car Crash Conference, SAE 801306, 1980.

[Ces82] Cesari, D.; Ramet, M. and Clair, P. "Pelvic tolerance and protection criteria in side impact", 26th Stapp Car Crash Conference, SAE 821159, 1982.

[Ces81] Cesari, D.; Ramet, M. and Bloch, J. "Influence of arm position on thoracic injuries in side impact", 25th Stapp Car Crash Conference, SAE 811007, 1981.

[Che88] Chen, H.H. and Guenther, D.A. "Computer simulation and evaluation of the effect of padding on the thorax in lateral impact", 32nd Stapp Car Crash Conference, SAE 881722, 1988.

[Chu98] Chung, J. "Biomechanical responses of the thorax in lateral velocity pulse impacts" PhD Thesis, Department of Biomechanical Engineering, Wayne State University, 1998

[Dal95] Dalstra, M.; Huiskes, R. and Van Erning, L "Development and validation of a three dimensional finite element model of the pelvic bone Journal of Biomechanical Engineering, 117, pp.272-278, 1995

[Dal95b] Dalstra, M.; Huiskes, R. , "Load transfer across the pelvic bone", Journal of Biomechanics, 28(6), pp.715-724, 1995

[Dan76] Danner, M. and Langwieder, K. "Car/vehicle side impacts – a study of accident characteristics and occupant injuries", 6th Int. Conference on Experimental Safety Vehicles, pp. 516-540, 1976.

[Dau94] Dauvilliers, F.; Bendjellal, F.; Weiss, M.; Lavaste, F. and Tarriere, C. "Development of a finite element model of the neck", 38th Stapp Car Crash Conference, SAE 942210, pp. 77-91, 1994.

[Den87] Deng, Y.C. and Goldsmith, W. "Response of a human head/neck/upper-torso replica to dynamic loading part II. Analytical/numerical model", Journal of Biomechanics, Vol.20, pp. 487-497, 1987.

[Den88] Deng, Y.C. "Design considerations for occupant protection in side impact – a modelling aproach", 32nd Stapp Car Crash Conference, SAE 881713, 1988.

[Den89] Deng, Y.C. "Side impact simulation and thoracic injury assessment", 11th Int. Conference on Experimental Safety Vehicle, pp. 77-86, 1989.

[Den93] Deng, Y.C. and Ng, P. "Simulation of vehicle structure and occupant response in side impact", 37th Stapp Car Crash Conference, SAE 933125, 1993.

[dJa96] de Jager, M.; Sauren, A.; Thunissen, J. and Wismans, J. "A global and a detailed mathematical model for head-neck dynamics", 40th Stapp Car Crash Conference, SAE 962430, pp. 269-281, 1996.

[Dum75] Dumpleton, J.H.; Black, J. "An introduction to orthopaedic materials" Charles C. Thomas Publisher, 1975

[Epp78] Eppinger, R.H.; Augustyn, K. and Robbins, D.H. "Development of a promising thoracic trauma prediction methodology", 22nd Stapp Car Crash Conference, SAE 780891, 1978.

[Epp84] Eppinger, R.H.; Marcus, J.H. and Morgan, M.M. "Development of dummy and injury index for NHTSA's thoracic side impact protection research program", 28th Stapp Car Crash Conference, SAE 840885, 1984.

[Epp89] Eppinger, R.H. "On the development of a deformation measurement system and its application toward mechanically based injury index", 33rd Stapp Car Crash Conference, SAE 892426, 1989.

[Ewi76] Ewing, C.L.; Thomas, D.J. and Lustick, L. "The effect of duration, rate of onset and peak sled acceleration on the dynamic response of the human head and neck", 20th Stapp Car Crash Conference, SAE 760800, pp. 3-41, 1976.

[Ewi77] Ewing, C.L.; Thomas, D.J. and Lustick, L. "Dynamic response of the human head and neck to +Gy impact", 21st Stapp Car Crash Conference, SAE 770928, pp. 509-545, 1977.

[Fun93] Fung, Y.C. "Biomechanics: Material properties of living tissue", Springer Verlag, 1993.

[Goe89] Goel, V.K. and Witerbottom, J.M. "Ligamentous laxity across C0-C1-C2 complex", Spine, Vol. 15, No. 10, pp. 990-996, 1989.

[Gui97] Guillemot, H.; Besnault, B.; Robin, S.; Got, C.; LeCoz, JY.; Lavast, F. and Lassau, JP. "Pelvic injuries in side impact collisions: a field accident analysis and dynamic tests on isolated pelvic bones", 39th Stapp Car Crash Conference, SAE 973322, pp. 91-100, 1997.

[Hal90] Hall-Craggs, E.C.B. "Anatomy", Williams and Wilkins Co., Baltimore, 1990.

[Har91] Harigae, T.; Ohsaki, K. and Ohmae, H. "Evaluation of impact responses of the Eurosid-1 and Biosid", 13th Int. Conference on Experimental Safety Vehicle, pp. 837-849, 1991.

[Har76] Hartemann, F.; Thomas, C.; Foret-Bruno, J.Y.; Henry, C.; Fayon, A. and Tarriere, C. "Occupant protection in lateral impacts", 20th Stapp Car Crash Conference, SAE 760806, 1976.

[Hay99] Hayamizu, N. ; King, A.; Miki, K.;
"Analysis of Head and Neck Response During Side Impact", International Congress & Exposition, March 1999, Detroit, MI, USA, SAE Document No: 1999-01-0717; SP-1432

[Hei62] Heidegger, G.W. "Atlas of human anatomy", Hafner Publishing Company, New York, 1962.

[Hob95] Hobbs, C.A. "Dispelling the misconceptions about side impact protection", 39th Stapp Car Crash Conference, SAE 950879.

[Hua94a] Huang, Y.; King, A.I. and Cavanaugh, J.M. "Finite element modeling of gross motion of human cadavers in side impact", 38th Stapp Car Crash Conference, SAE 942207, 1994.

[Hua94b] Huang, Y.; King, A.I. and Cavanaugh, J.M. "A Madymo model of near-side human occupants in side impact", Journal of Biomechanical Engineering, Vol. 116, May 1994.

[Hue92] Huelke, D.F. and Compton, C.P.
"Analysis of passenger car side impacts – crash location, injuries, AIS and contacts" SAE920353, 1992

[Irw93] Irwin, A. and Walilko, T.J. "Displacement responses of the shoulder and thorax in lateral sled impacts", 37th Stapp Car Crash Conference, SAE 933124, 1993.

[ISO89] ISO/TR 9790, "Road vehicles – anthropomorphic side impact dummy", Part 1-6, 1989.

[Jos99] Jost, R., Nurick, G.N., "Finite element modelling of the human body in vehicle side impact", International Journal of Crashworthiness, Vol. 4, No.1, pp 31-37, 1999

[Jos00a] Jost, R., Nurick, G.N., "Development of a finite element model of the human neck subjected to high g-level deceleration", International Journal of Crashworthiness, Vol. 5, No.3, pp. 259-270, 2000

[Jos00b] Jost, R., Nurick, G.N., "Finite Element Simulation of Biomechanical Responses of the Human Body Subjected to Lateral Impact", ICRASH2000, International Crashworthiness Conference, London, September 2000

[Kal81] Kallieris, D.; Mattern, R.; Schmidt, G. and Eppinger, R.H. "Quantification of side impact responses and injuries", 25th Stapp Car Crash Conference, SAE 811009, pp. 329-366, 1981

[Kal86] Kallieris, D.; Mattern, R. and Härdle, W. "Belastbarkeitsgrenzen und Verletzungsmechanik der angegurteten Fahrzeuginsassen beim Seitenaufprall", FAT-Schriftenreihe, No. 60, 1986.

[Kal86] Kallieris, D. "Belastbarkeitsgrenzen und Verletzungsmechanik des angegurteten PKW-Insassen beim Seitenaufprall", FAT-Schriftenreihe, No. 60, Phase II: Ansätze für Verletzungsprädiktoren, 1986.

[Kal91] Kallieris, D.; Mattern, R.; Miltner, E.; Schmidt, G. and Stein, K. "Considerations for a neck injury criterion", 35th Stapp Car Crash Conference, SAE 912916, pp. 401-417, 1991.

[Kan91] Kanianthra, J.N.; Willke, D.T.; Gabler, H.C. and Zuby, D.S. "Comparative performance of SID, Biosid and Eurosid in lateral, pendulum, sled and car impacts", 13th Int. Conference on Experimental Safety Vehicle, ESV paper No. S5-0-16.

[Kin91] King, A.I.; Huang, Y. and Cavanaugh, J.M. "Protection occupants against side impact", 13th Int. Conference on Experimental Safety Vehicle, Paris, 1991.

[Kin96] King, A.I. "Occupant kinematics and impact biomechanics", Proc. of the NATO-Advanced Study Institute on Crashworthiness of Transportation Systems: Structural Impact and Occupant Protection, Troia, Portugal, pp. 3-23, 1996.

[Kla84] Klaus, G.; Sinnhuber, R. and Hoffmann, G. "Side impact – a comparison between dummies and cadavers, correlation bewteen cadaver loads and injury severity", 28th Stapp Car Crash Conference, SAE 841655, 1984.

[Kle93] Kleinberger, M. "Application of finite element techniques to the study of cervical spine mechanics", 37th Stapp Car Crash Conference, SAE 933131, pp. 261-272, 1993.

[Lau86] Lau, I.V. and Viano, D.C. "The viscous criterion – bases and applications of an injury severity index for soft tissues", 30th Stapp Car Crash Conference, SAE 861882, 1986.

[Lau89] Ian, V. Lau, "An analysis of the MVMA sponsored full scale side impact tests", 33rd Stapp Car Crash Conference, SAE 892431, pp.101-112, 1989.

[Lau91] Lau, I.V.; Capp, J. and Obermeyer, J.A. "A comparison of frontal and side impact: crash dynamics, countermeasures and subsystem tests", 35th Stapp Car Crash Conference, SAE 912896, 1991.

[Lau88] Lau, I.V. and Viano, D.C. "How and when blunt injury occurs – implications to frontal and side impact protection", 32nd Stapp Car Crash Conference, SAE 881714, 1988.

[Lob73] Lobdell, T.E. and Neathery, R.F. "Mechanical simulation of human thorax under impact", SAE 730982, 1973.

[Low90] Low, T.C. and Prasad, P. "Dynamic response and mathematical model of the side impact dummy", 34th Stapp Car Crash Conference, SAE 902321.

[Liz98] Lizee, E.; Robin, S.; Song, E.; Bertholon, N.; LeCoz, JY.; Besnault, B. and Lavaste, F. "Development of a 3d finite element model of the human body", 42nd Stapp Car Crash Conference, SAE 983152, pp. 115-138, 1998.

[Mac89] Mack, P.; Chamouard, F.; Bendjellal, F.; Song, D.; Talantikite, Y. and Tarriere, C. "Development of a modelization of human being in lateral impact, to mitigate the insufficiencies of actual side impact dummies", 12th Int. Conference on Experimental Safety Vehicle, pp. 705-725, 1989.

[Mal82] Malliaris, A.C.; Hitchcock, R. and Hedlund, J. "A search for priorities in crash protection", SAE Technical Paper, No. 820242, 1982.

[Mat95] Mattern, R.; Haerdele, W. and Kallieris, D. "Biomechanik der Seitenkollision", Berichte der Bundesanstalt für Strassenwesen, Heft M 43, 1995.

[Mar83] Marcus, J.H.; Morgan, R.M.; Eppinger, R.H.; Kallieris, D.; Mattern, R. and Schmidt, G. "Human response to injury from lateral impact", 27th Stapp Car Crash Conference, SAE 831634, 1983.

[Mer84] Merz, H.J. "A procedure for normalizing impact response data", 28th Stapp Car Crash Conference, SAE 840884, 1984

[Mer84] Merril, T.; Goldsmith, W. and Deng, Y.C. "Three dimensional response of a lumped parameter head-neck model due to impact and impulsive loading", Journal ofBiomechanics, Vol. 17, No. 2, pp. 81-95, 1984.

[Mil91] Miltner, E.; Kallieris, D.; Wiedmann, B.; Leutwein, B.; Hepp, H.P.; Fischer, R.; Salwender, H.J. and Frobenius, H. "About the threshold of fatal or potentially fatal injuries in car-to-car side collisions – a comparison between real accidents and PMHS-tests", 35th Stapp Car Crash Conference, pp. 125-143, 1991.

[Mon77] Monk, M.; Burgett, A. and DeLarm, L. "Computerized side impact injury analysis", 21st Stapp Car Crash Conference, SAE 770940, 1977.

[Mor81] Morgan, M.M.; Marcus, J.H. and Eppinger, R.H. "Correlation of side impact dummy/cadaver tests", 25th Stapp Car Crash Conference, SAE 811008, 1981.

[Mor86] Morgan, M.M.; Marcus, J.H. and Eppinger, R.H. "Side impact – The biofidelity of NHTSA's proposed ATD and efficacy of TTI", 30th Stapp Car Crash Conference, SAE 861877, 1986.

[Mye95] Myers, B.S.; van Ee, C.A.; Camacho, D.L.; Wooley, C.T. and Best, T.M. "On the structural and material properties of mammalian skeletal muscle and its relevance to human cervical impact dynamics", 39th Stapp Car Crash Conference, SAE 952723, pp. 203-214, 1995.

[Myk88] Myklebust, J.B.; Pintar, F.; Yogonandan, N.; Cusik, J.F.; Mainman, D.; Myers, T.J. and Sances, A."Tensile strength of spinal ligaments", Spine, Vol. 13, No. 5, pp. 526-531, 1988.

[Net89] Netter, F.; " Atlas of human anatomy", CIBA-GEIGY corp, 1989

[Nus79] Nusholtz, G.S.; Melvin J.W.; Alem, N.M "Head impact response comparisons of human surrogates ", 23rd Stapp Car Crash Conference, SAE 791020, 1979.

[Ott82] Otte, D.; Kühnel, A.; Suren, E.G.; Weber, H.; Gotzen, L.; Schockenhoff, G. and Vu Han, V. "Erhebungen am Unfallort", Unfall und Sicherheitsforschung Strassenverkehr 37, pp. 1-100, 1982.

[Ott84] Otte, D.; Suren, E.G.; Appel, H. and Nehmzow, J. "Vehicle parts causing injuries to front-seat car passengers in lateral impacts", 28th Stapp Car Crash Conference, SAE 841651, 1984.

[Ott90] Otte, D. "Comparison and realism of crash simulation tests and real accident situations for the biomechanical movements in car collisions", 34th Stapp Car Crash Conference, pp. 329-348, 1990.

[Ott93] Otte, D. "Deformation characteristics and occupant load capacity in lateral impacts for nearside belted front car passengers", 37th Stapp Car Crash Conference, SAE 933126, pp. 185-197, 1993.

[Pan91] Panjabi, M.M.; Dvorak, J.; Crisco, J.J.; Oda, T.; Hilibrand, A. and Grob, D. "Flexion, extension and lateral bending of the upper cervical spine in response to alar ligament transections", Journal of Spinal Disorders, Vol. 4, pp. 157-167, 1991.

[Par83] Partyka, S.C. and Rezabek, S.E. "Occupant injury patterns in side impacts – a coordinated industry/government accident data analysis", SAE Technical Paper, No. 830459, 1983.

[Pat63] Patrick, L.M.; Lissner, H.R. and Gurdjian, E.S. "Survival by design – Head protection", 7th Stapp Car Crash Conference, pp. 483-499.

[Pla89] Plank, G. and Eppinger, R.H. "Computed dynamic response of the human thorax from finite element model", 12th Int. Conference on Experimental Safety Vehicle, pp. 665-672.

[Pla94] Plank, G.R.; Kleinberger, M. and Eppinger, R.H. "FE modeling and analysis of thorax/restraint system interaction", 14th Int. Conference on Experimental Safety Vehicle, pp. 210-219, 1994.

[Plu96] Plummer, J.W.; Bidez, M.W. and Alonso, J. "Parametric FE studies of the human pelvis: The influence of load magnitude and duration on pelvic tolerance during side impact", 40th Stapp Car Crash Conference, SAE 962411, 1996.

[Pra96] Prasad, P. "Occupant simulation models: experiment and practice", Proc. of the NATO-Advanced Study Institute on Crashworthiness of Transportation Systems: Structural Impact and Occupant Protection, Troia, Portugal, pp. 209-219, 1996.

[Pre87] Preuss, C.A. and Wasko, R.J. "Results of MVMA sixteen full vehicle side impact tests using the proposed NHTSA test procedure", SAE 871115, 1987.

[Ren93] Renaudin, F.; Guillemont, F.; LaVaste, W.; Skalii, W.; LeSage, F. and Pecheux, C. "A 3-d finite element model of the pelvis in side impact", 37th Stapp Car Crash Conference, SAE 933130, 1993.

[Rid90] Ridella, S.A. and Viano, D.C. "Determining tolerance to compression and viscous injury in frontal and lateral impacts", 34th Stapp Car Crash Conference, SAE 902330, 1990.

[Rob76] Robbins, D.H.; Melvin, J.W. and Stalnaker, R.L. "The prediction of thoracic impact injuries", 20th Stapp Car Crash Conference, SAE 760822, 1976.

[Rou85] Rouhana, S.W; Foster, M.E. "Lateral impact – an analysis of the statistics in the NCSS", 29th Stapp Car Crash Conference, pp. 79-98, 1985.

[Rou86] Rouhana, S.W.; Ridella, S.A. and Viano, D.C. "The effect of limiting impact force on abdominal injuries", 30th Stapp Car Crash Conference, pp. 65-85, 1986.

[Sac82] Sacreste, J.; Brun-Cassan, F. and Fayon, A. "Proposal for a thorax tolerance level in side impacts based on 62 tests performed with cadavers having known bone conditions", 26th Stapp Car Crash Conference, SAE 821157.

[She89] Shea, M.; Edwards, W.T.; White, A.A. and Hayes, W.C. "Variation stiffness and strength along the human cervical spine", Journal of Biomechanics, Vol. 24, pp. 95-107, 1991.

[Sie93] Siegel, JH; Mason-Gonzales. S; Dischinger, P. "Safety belt restraints and compartment intrusions in frontal and lateral motor vehicle crashes: mechanisms of injuries, complications and acute care costs", J of Trauma 5(34):736-759, 1993.

[Sta79] Stalnaker, R.L.; Tarriere, C.; Fayon, A.; Walfish, G.; Balthazard, M.; Masset, J.; Got, C.; Patel, A. "Modification of part 572 dummy for lateral impact according to biomechanical data", 23rd Stapp Car Crash Conference 1979, SAE 791031.

[Tar79] Tarriere, C.; Walfisch, G. and Fayon, A. "Synthesis of human tolerances obtained from lateral impact simulation", 7th Int. Conference on Experimental Safety Vehicle, pp. 359-373, 1979.

[Tan96] Tannous, R.E.; Bandak, F.A.; Toridis, T.G.; Eppinger, R.H "A three-dimensional finite element model of the human ankle: development and preliminary application to axial impulsive loading " 40th Stapp Car Crash Conference 1996, SAE 962427.

[Tie87] Tien, C.S. and Huston, R.L. "Numerical advances in gross-motion simulations of head/neck dynamics", Journal of Biomechanical Engineering, Vol. 109, pp. 163-168, 1987.

[Vee98] van Ee, C.A.; Chasse, A.L. and Myers, B.S. "The effect of post-mortem time and freezer storage on the mechanical properties of skeletal muscle", 42nd Stapp Car Crash Conference, SAE 983155, pp. 169-178.

[vdS98] van der Spuy, J., Dr.; Head of National Trauma Research Programme of South Africa, Personal communications, 1998.

[vdH97] van der Horst, M.J.; Thunissen, J.G.M.; Happee, R.; van Haaster, R.M.H.P. and Wismans, J.S.H.M. "The influence of muscle activity on head-neck response during impact", 41st Stapp Car Crash Conference, SAE 973346, pp. 487-507, 1997.

[Via85] Viano, D.C. and Lau, I.V. "Thoracic impact: a viscous tolerance criterion", 10th Int. Conference on Experimental Safety Vehicle, pp. 104-114, 1985.

[Via86] Viano, D.C. "Biomechanics of bone and tissue: a review of material properties and failure characteristics", SAE 861923, 1986.

[Via87a] Viano, D.C. "Evaluation of the benefit of energy-absorbing material in side impact protection: Part 1", 31st Stapp Car Crash Conference, SAE 872212, 1987.

[Via87b] Viano, D.C. "Evaluation of the benefit of energy-absorbing material in side impact protection: Part 2", 31st Stapp Car Crash Conference, SAE 872212, 1987.

[Via89a] Viano, D.C.; Lau, I.V.; Asbury, C.; King, A.I. and Begeman, P. "Biomechanics of the human chest, abdomen and pelvis in lateral impact", 33rd Annual Proceedings of Association for the Advancement of Automotive Medicine, Baltimore, Maryland, 1989.

[Via89b] Viano, D.C. "Biomechanical responses and injuries in blunt lateral impact", 33rd Stapp Car Crash Conference, SAE 892432, 1989.

[Via91] Viano, D.C. "Evaluation of armrest loading in side impacts", 35th Stapp Car Crash Conference, SAE 912899, 1991.

[Via95] Viano, D.; Fan, A; Ueno, K.; Wallilko, T; Cavanaugh, J.; King. A "Biofidelity and inury assessment in Eurosid-1 and Biosid", 40th Stapp Car Crash Conference, pp.307-325, SAE952731, 1995

[Via96] Viano, D.C. and King, A.I. "Injury mechanisms and biofidelity of dummies", Proc. of the NATO-Advanced Study Institute on Crashworthiness of Transportation Systems: Structural Impact and Occupant Protection, Troia, Portugal, pp. 25-51, 1996.

[Vispr] http://www.npac.syr.edu/projects/vishuman/VisibleHuman.html

[Wis86] Wismans, J.; Woltring, J.H. and Van Oorschot, E. "Omni-directional human head-neck response", 30th Stapp Car Crash Conference, SAE 861893, pp. 313-331, 1986.

[Wil83] Williams, J.L. and Belytschko, T.B. "A three-dimensional model of the human cervical spine for impact simulation", Journal of Biomechanical Engineering, Vol. 105, pp. 321-331, 1983.

[Yam70] Yamada, H. "Strength of biological materials", The Williams and Wilkins Company, Baltimore, 1970.

[Yan98] Yang, K.H.; Zhu, F.; Luan, F.; Zhao, L. and Begeman, P.C. "Development of a finite element model of the human neck", 42nd Stapp Car Crash Conference, SAE 983157, pp. 195-205, 1998.

[Yog89] Yoganandan, N.; Pintar, F.; Butler, J.; Reinartz, J.; Sances, A.; Larson, SJ. "Dynamic response of human cervical spine ligaments", Spine, Vol. 14, No. 10, pp. 1102-1110, 1989.

[Zho96] Zhou, Q.; Rouhana, S.W. and Melvin, J.W. "Age effects on thoracic injury tolerance", 40th Stapp Car Crash Conference, SAE 962421, 1996.

[Zhu93] Zhu, J.Y.; Cavanaugh, J.M. and King, A.I. "Pelvic biomechanical responses and padding benefits in side impact based on a cadaveric test series", 37th Stapp Car Crash Conference, SAE 933128, 1993.

Appendix A

A1. Shoulder impact response plots

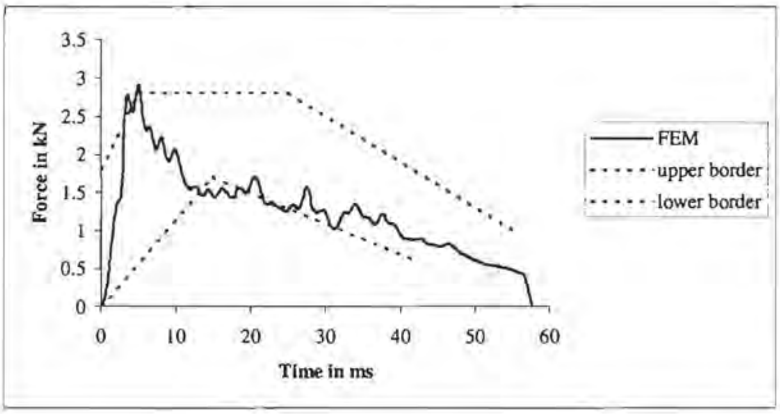

Figure A1.1 Force-time response FE-model – ISO-cadaver response

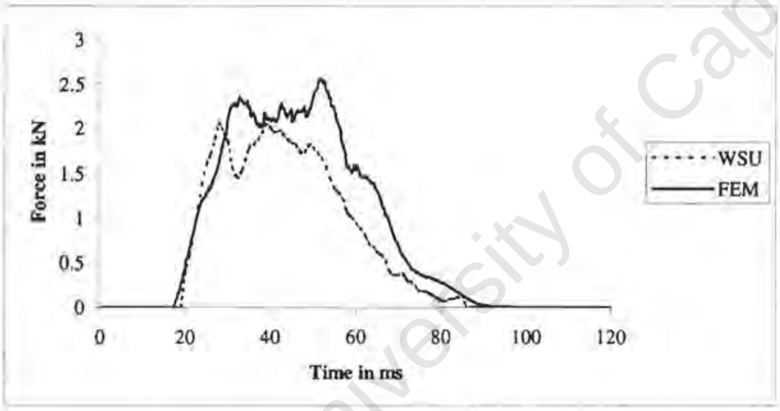

Figure A1.2 Shoulder force-time response FE-model – WSU sled test 6.7 m/s

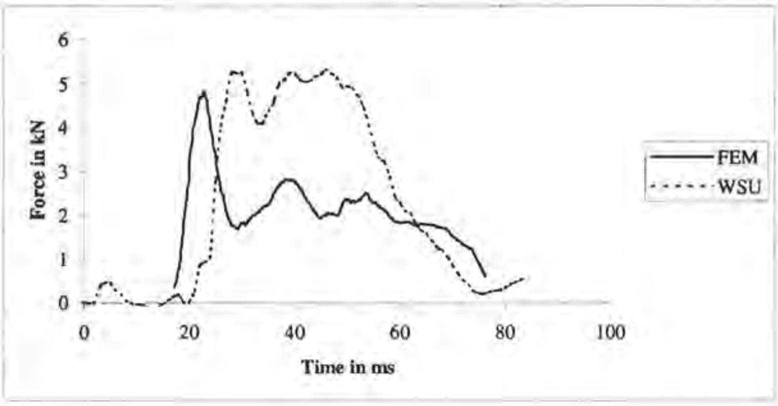

Figure A1.3 Shoulder force-time response FE-model – WSU sled test 8.9 m/s

A2. Thorax impact response plots

Viano – impactor test at 4.3 m/s

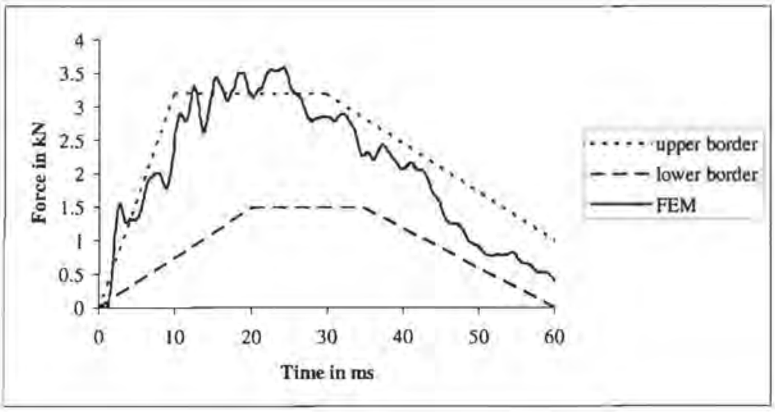

Figure A2.1: Thorax force-time response FE-model – Viano impactor test at 4.3 m/s

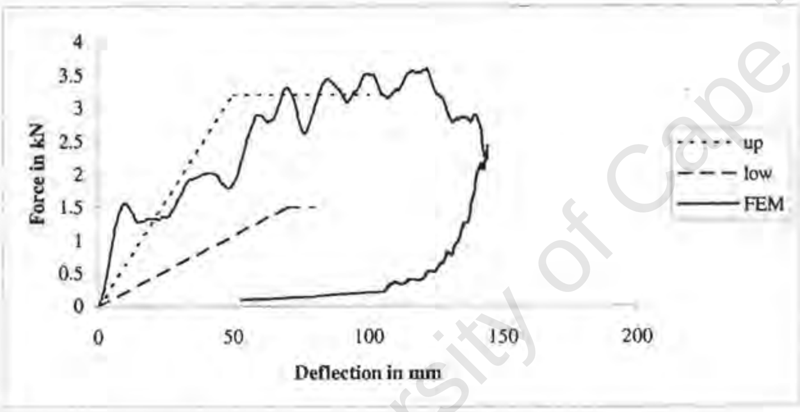

Figure A2.2: Thorax force-deflection response FE-model – Viano impactor test at 4.3 m/s

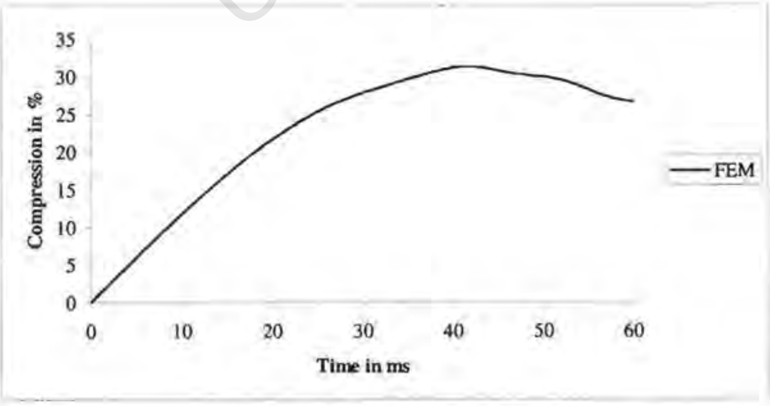

Figure A2.3: Thorax compression-time response FE-model – Viano impactor test at 4.3 m/s

Viano – impactor test at 6.5 m/s

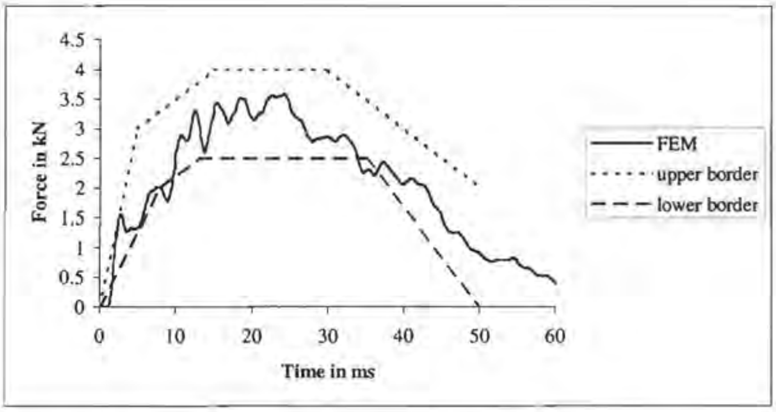

Figure A2.4: Thorax force-time response FE-model – Viano impactor test at 6.5 m/s

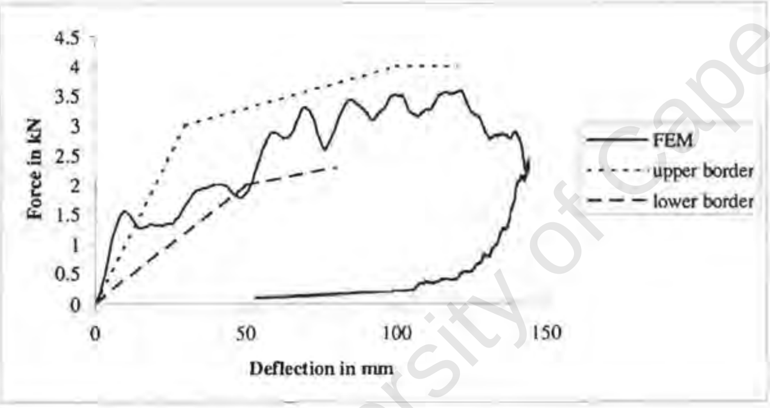

Figure A2.5: Force-deflection response FE-model – Viano impactor test at 6.5 m/s

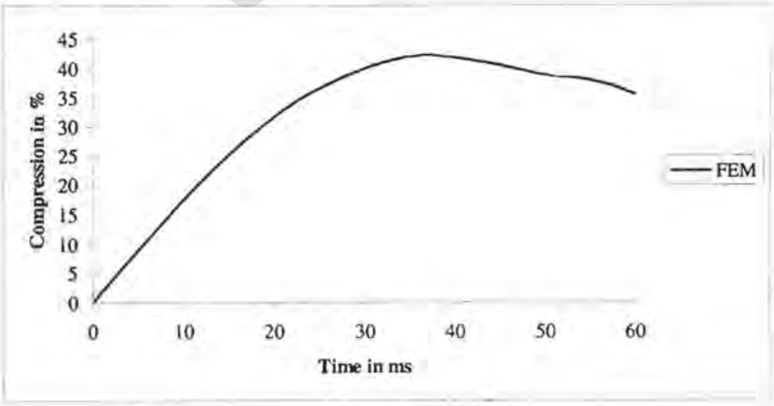

Figure A2.6: Compression-time response FE-model – Viano impactor test at 6.5 m/s

Viano – impactor test at 9.5 m/s

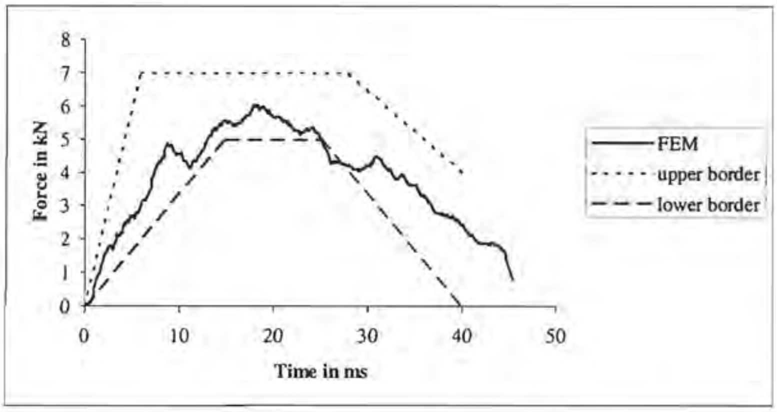

Figure A2.7: Thorax force-time response FE-model – Viano impactor test at 9.5 m/s

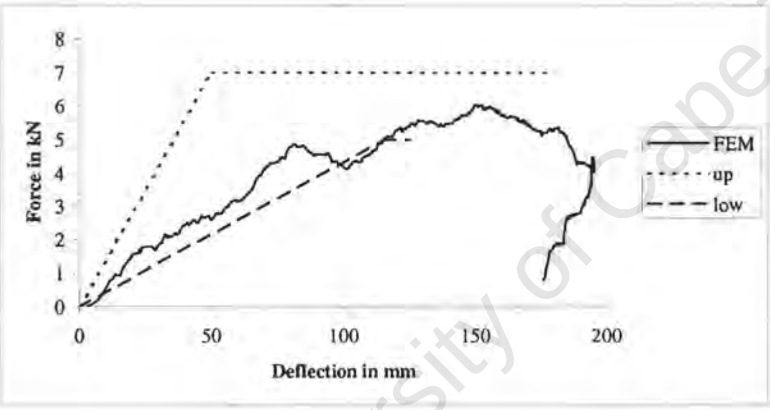

Figure A2.8: Force-deflection response FE-model – Viano impactor test at 9.5 m/s

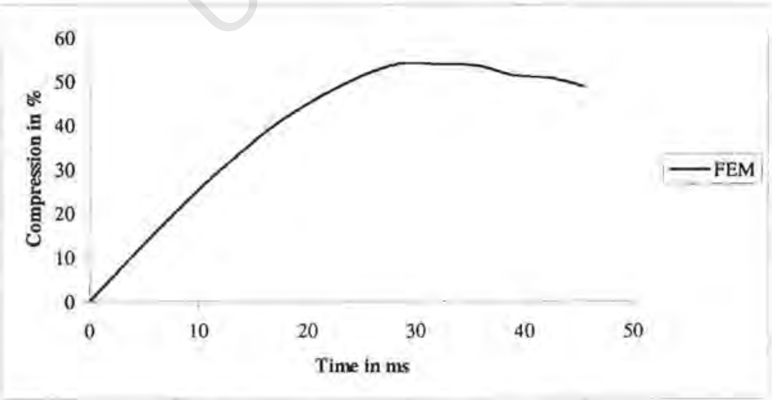

Figure A2.9: Compression-time response FE-model – Viano impactor test at 9.5 m/s

Thorax force - WSU sled test

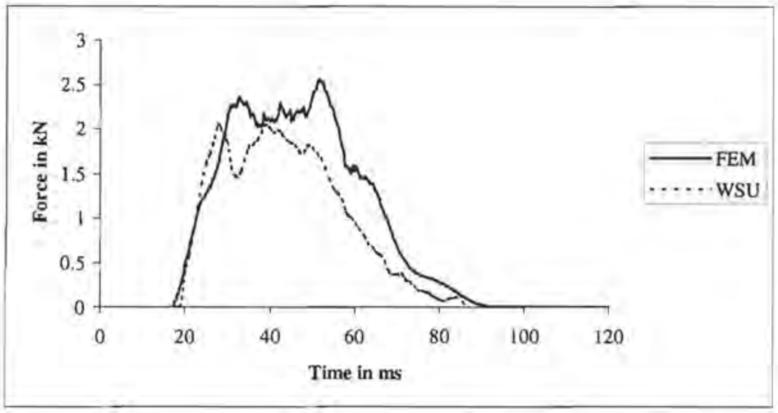

Figure A2.10 Thorax force-time response FE-model – WSU sled test 6.7 m/s

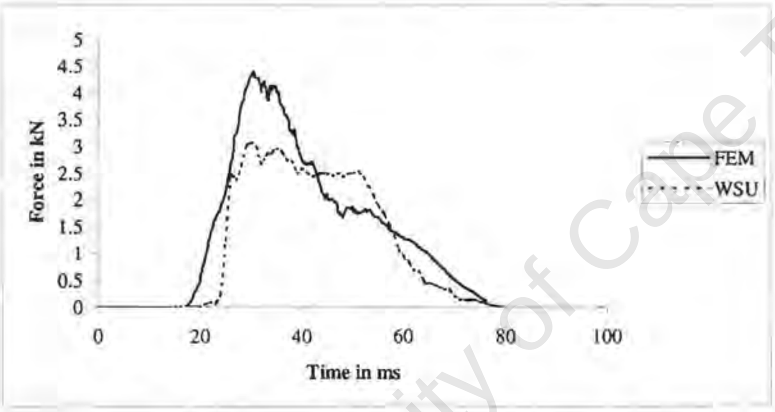

Figure A2.11 Thorax force-time response FE-model – WSU sled test 8.9 m/s

Thorax force - Heidelberg sled test

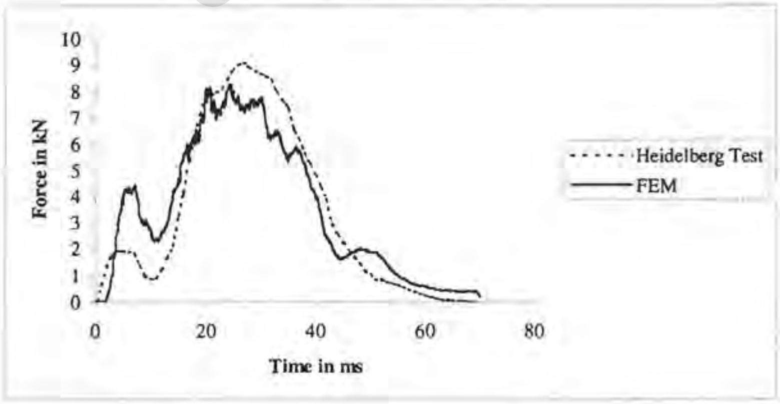

Figure A2.12 Thorax force-time response FE-model – Heidelberg sled test 6.7 m/s

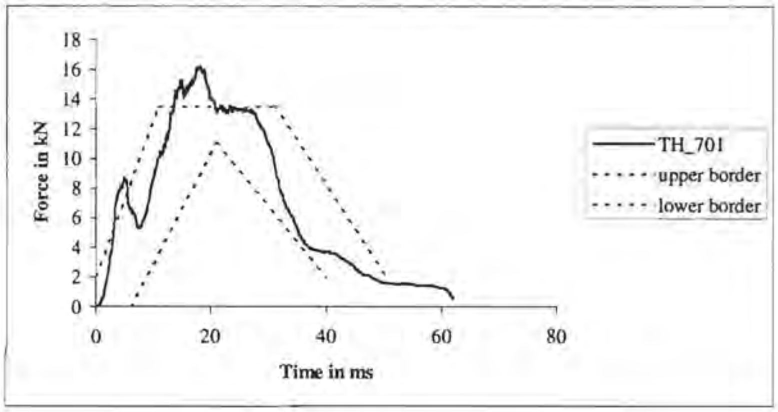

Figure A2.13 Thorax force-time response FE-model – Heidelberg sled test 8.9 m/s

A3. Abdomen impact response plots

Viano – impactor test at 4.8 m/s

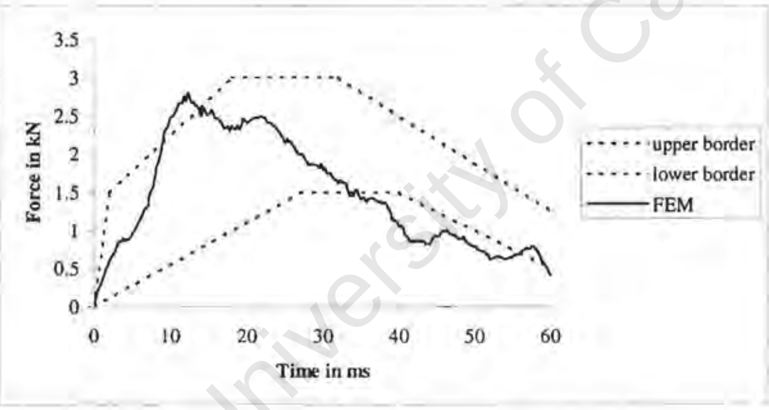

Figure A3.1 Abdomen force-time response FE-model – Viano pendulum test 4.8 m/s

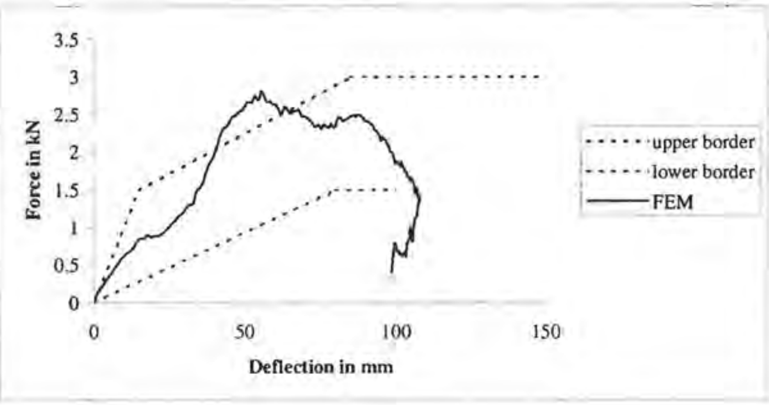

Figure A3.2 Abdomen force-deflection response FE-model – Viano pendulum test 4.8 m/s

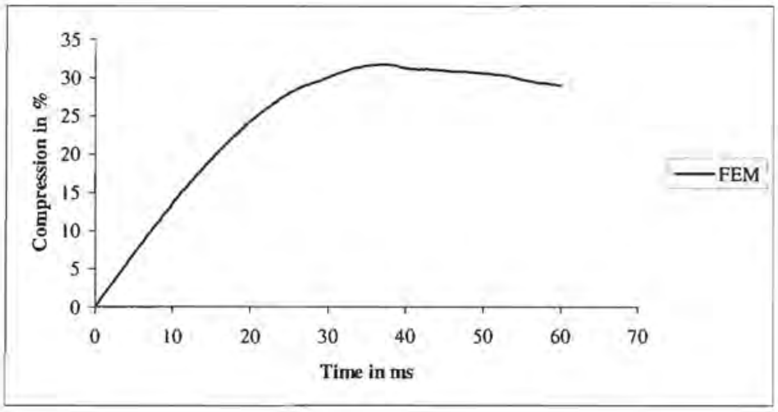

Figure A3.3 Abdomen compression-time response FE-model – Viano pendulum test 4.8 m/s

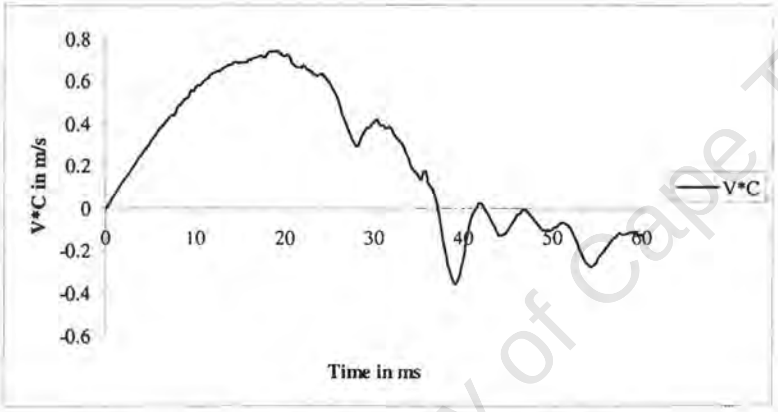

Figure A3.4 Abdomen VC-time response FE-model – Viano pendulum test 4.8 m/s

Viano – impactor test at 6.8 m/s

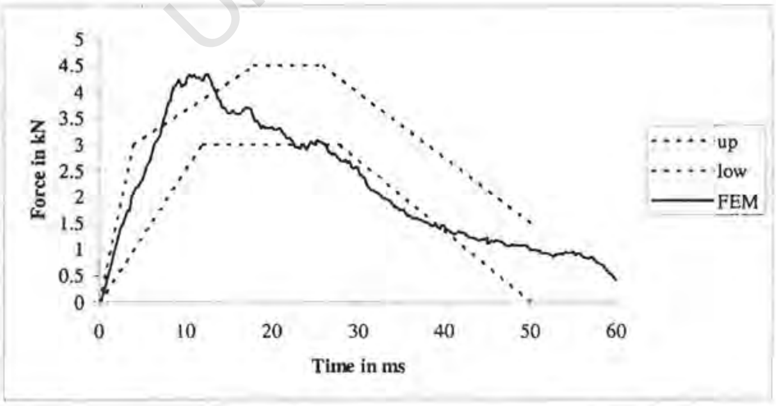

Figure A3.5 Abdomen force-time response FE-model – Viano pendulum test 6.8 m/s

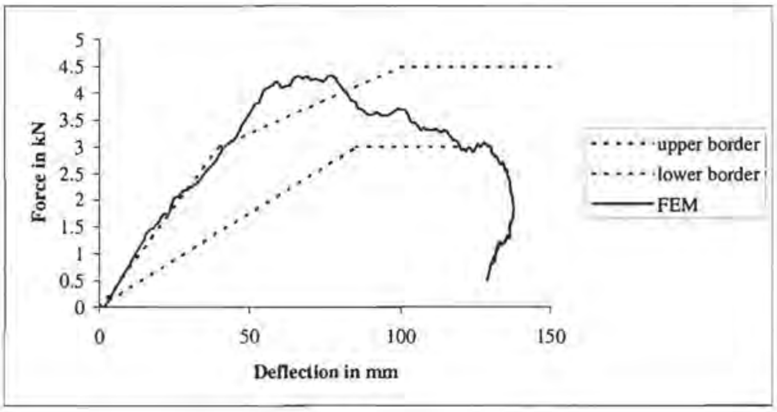

Figure A3.6 Abdomen force-deflection response FE-model – Viano pendulum test 6.8 m/s

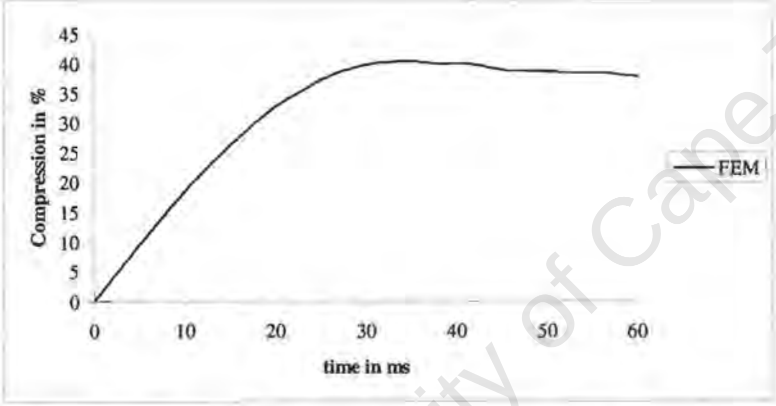

Figure A3.7 Abdomen compression-time response FE-model – Viano pendulum test 6.8 m/s

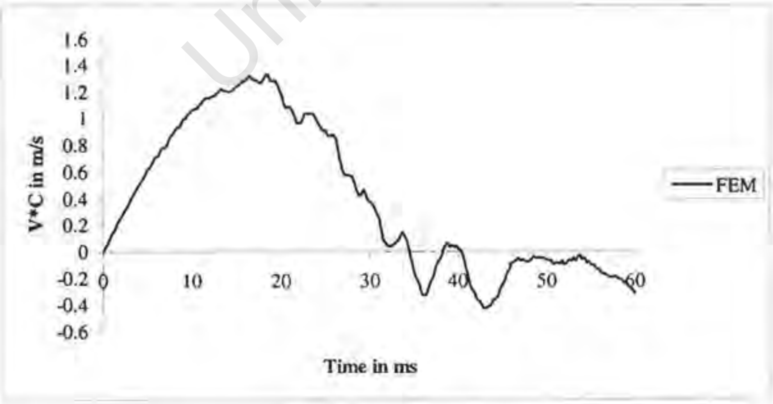

Figure A3.8 Abdomen VC-time response FE-model – Viano pendulum test 6.8 m/s

Viano – impactor test at 9.8 m/s

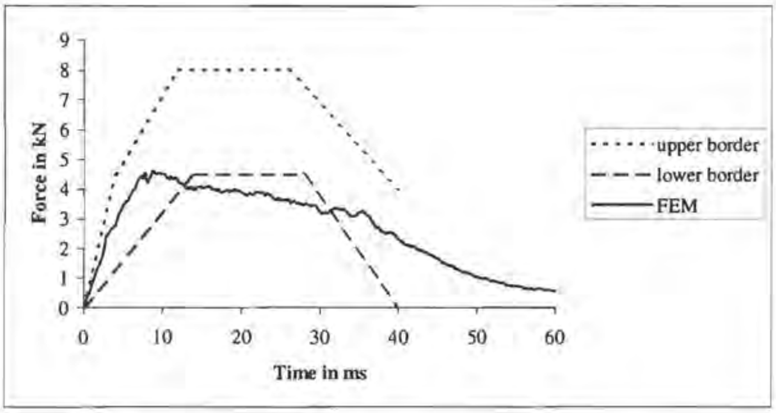

Figure A3.9 Abdomen force-time response FE-model – Viano pendulum test 9.8 m/s

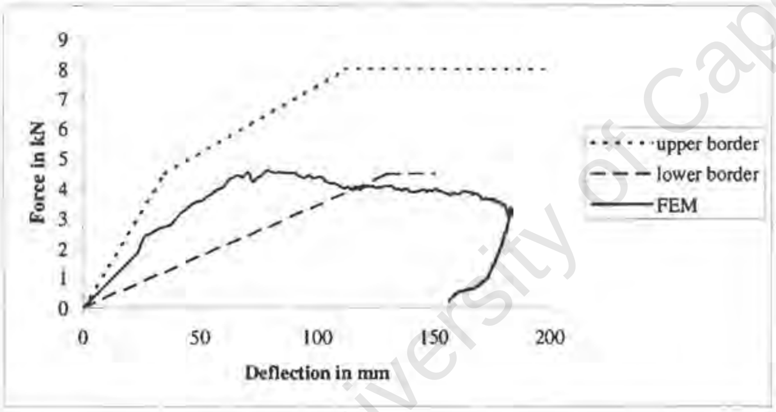

Figure A3.10 Abdomen force-deflection response FE-model – Viano pendulum test 9.8 m/s

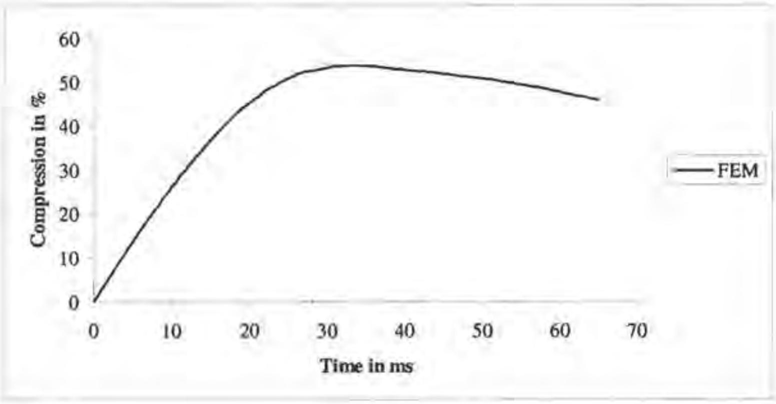

Figure A3.11 Abdomen compression-time response FE-model – Viano pendulum test 9.8 m/s

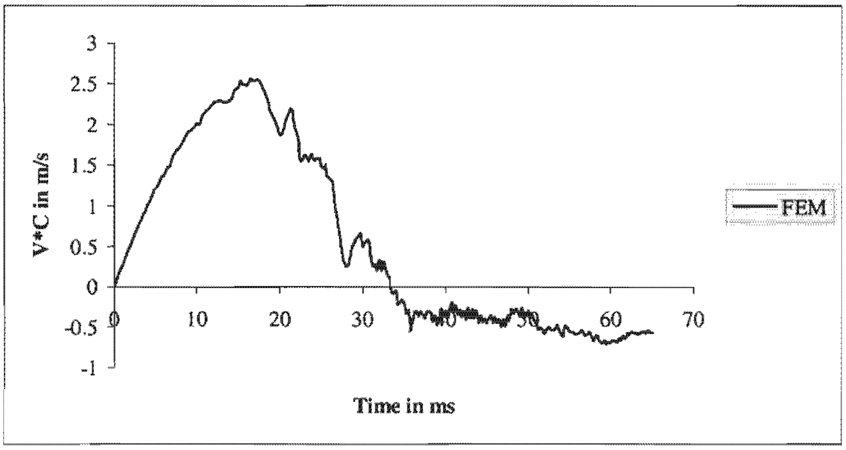

*Figure A3.12 Abdomen V*C-time response FE-model – Viano pendulum test 9.8 m/s*

Abdomen force - WSU sled test

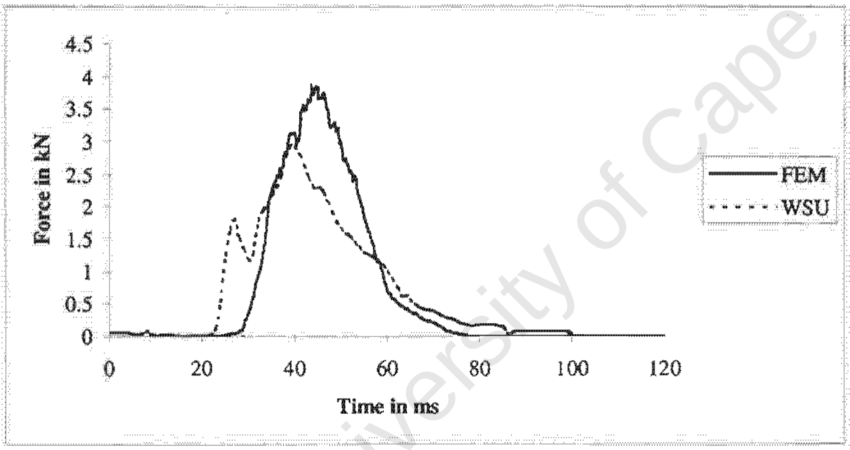

Figure A3.13 Abdomen force-time response FE-model – WSU sled test 6.7 m/s

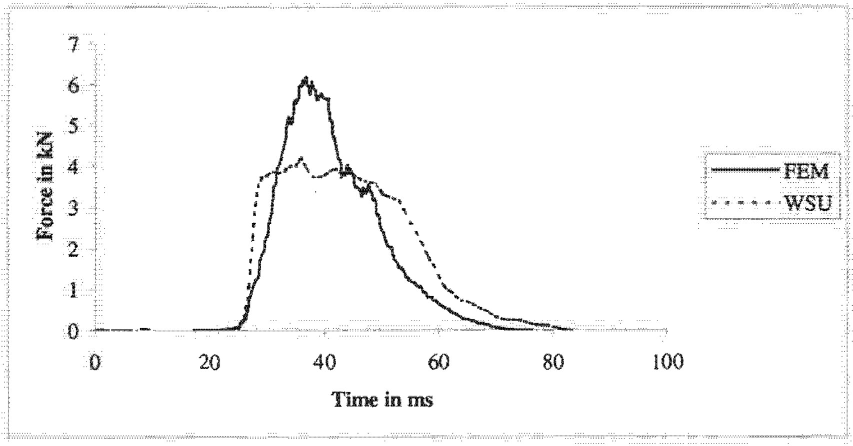

Figure A3.14 Force-time response FE-model – WSU sled test 8.9 m/s

A4. Pelvis impact response plots

Viano – Pelvis impactor test at 4.8 m/s

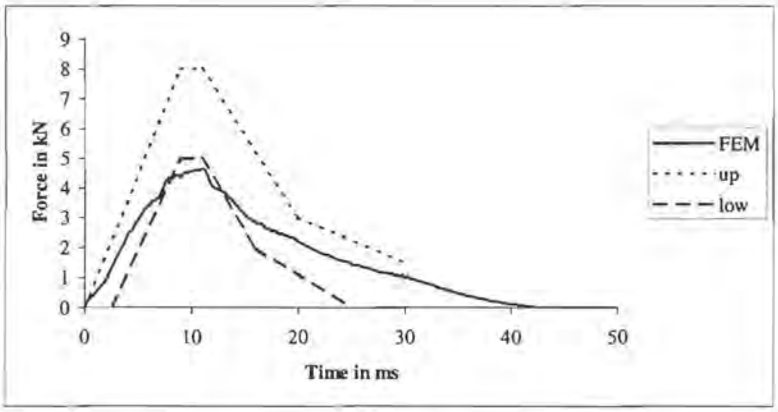

Figure A4.1 Pelvis force-time response FE-model – Viano pendulum test 4.8 m/s

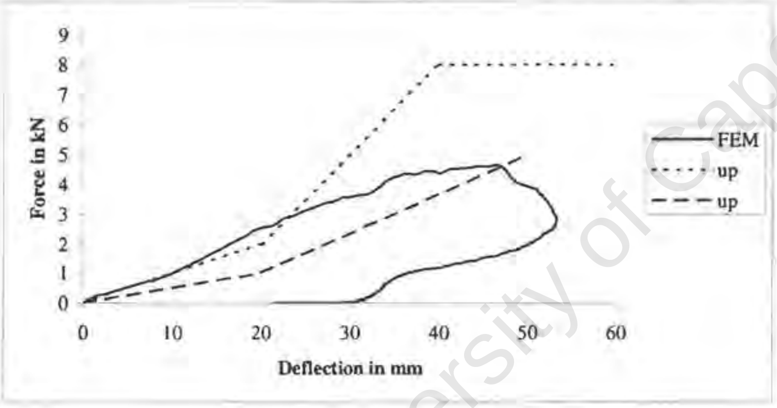

Figure A4.2 Pelvis force-deflection response FE-model – Viano pendulum test 4.8 m/s

Pelvis force – WSU test

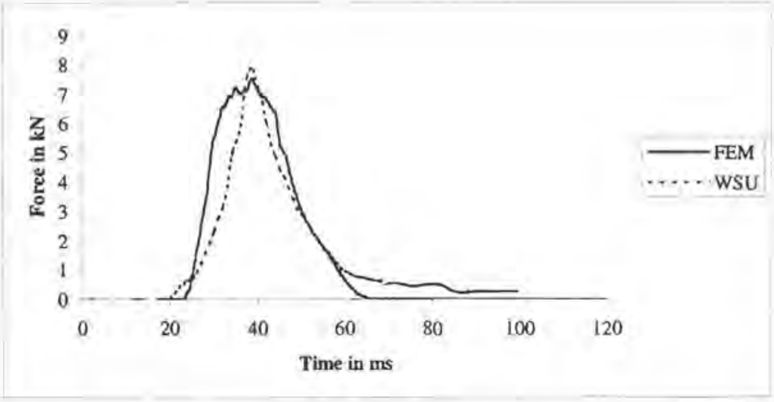

Figure A4.3 Pelvis force-time response FE-model – WSU sled test 6.7 m/s

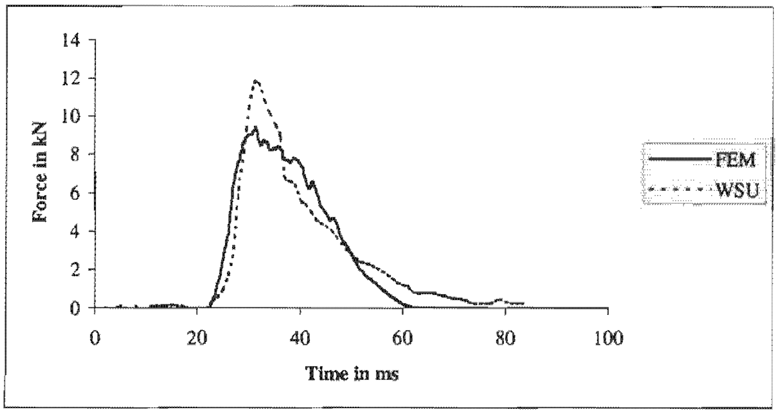

Figure A4.4 Pelvis force-time response FE-model – WSU sled test 8.9 m/s

Pelvis force – Heidelberg test

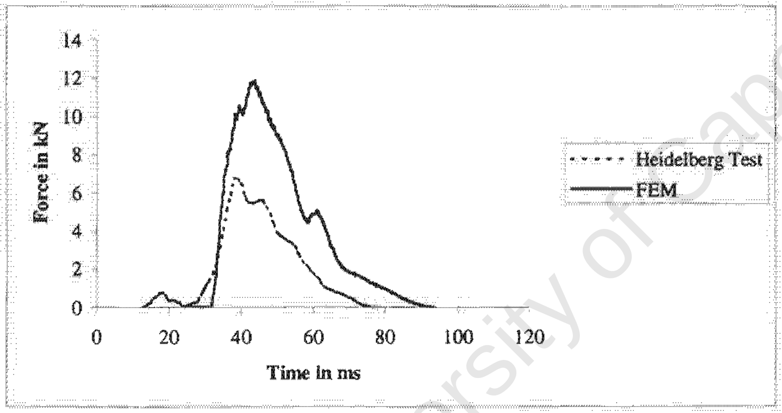

Figure A4.5 Pelvis force-time response FE-model – Heidelberg sled test 6.7 m/s

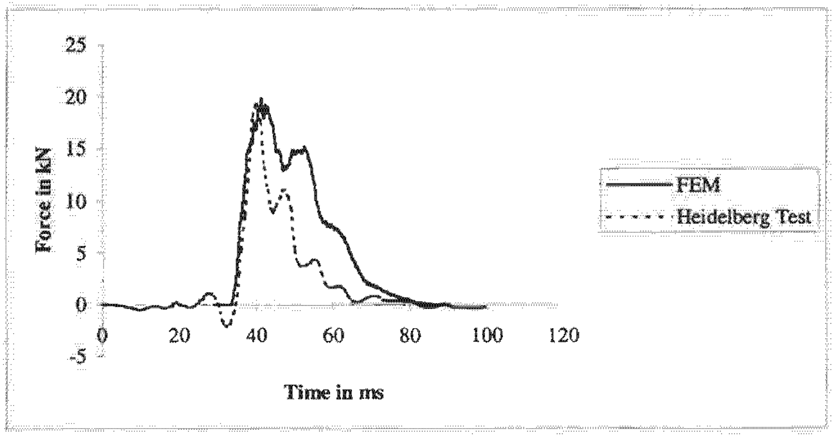

Figure A4.6 Pelvis force-time response FE-model – Heidelberg sled test 8.9 m/s

Normalisation Procedure [ISO89]

For the normalisation of the measured impactor acceleration-time curve, two factors need to be determined, one to be multiplied with the impactor acceleration values and one with the corresponding time. These factors are calculated by:

$$R_a = (R_K)^{\frac{1}{2}} \ (R_m)^{\frac{1}{2}} \ (M_p + M_e)^{\frac{1}{2}} (M_p + M_s)^{-\frac{1}{2}}$$ Impactor acceleration factor

$$R_a = (R_K)^{-\frac{1}{2}} \ (R_m)^{\frac{1}{2}} \ (M_p + M_e)^{\frac{1}{2}} \ (M_p + M_s)^{-\frac{1}{2}}$$ Time factor

$$R_m = \frac{M_s}{M_e}$$ Mass ratio

$$R_K = \frac{K_s}{K_e} = \frac{L_s}{L_e}$$ Stiffness ratio = ratio of characteristic length

	L_e - characteristic length	M_s - of the standard subject
Shoulder	236 mm [ISO89]	20.5 kg [ISO89]
Thorax	349 mm [Via89]	32.7 kg [ISO89]
Abdomen	314 mm [Via89]	16.4 kg [ISO89]
Pelvis	385 mm [Via89]	14.5 kg [ISO89]

Table B1 Characteristic lengths and masses of standard subject

The effective cadaver mass M_e is calculated for the different body regions:

$$M_e = \frac{\int M_p \cdot a_p \cdot dt}{\int a_T \cdot dt}$$

M_p - Impactor mass
a_p - Pendulum acceleration
$a_{S/T/A/P}$ - Acceleration of shoulder / thorax / abdomen or pelvis
M_s - Mass of test subject
$L_{T/A/P}$ - Length or width of thorax, abdomen or pelvis of test subject
K_s - Equivalent standard stiffness of cadaver
K_e - Equivalent stiffness of cadaver subject

The first part of Appendix C1 contains all material properties defined in the FE-model in tabular form. The second part contains the original ABAQUS input file of the WSU sled test simulation including the original ABAQUS material input file.

Cortical Bone	**1a**	**1b**	**1c**	**1d**	**1e**	**1f**
***Young's modulus* [Mpa]**	1.0E+3	2.5E+3	5.0E+3	7.5E+3	10.0E+3	12.5E+3
***Yield Stress* [Mpa]**	9	9	9	9	9	9
***Ultimate Stress* [Mpa]**	10	10	10	10	10	10
***Density* [g/cm^3]**	2	2	2	2	2	2
	2a	**2b**	**2c**	**2d**	**2e**	**2f**
***Young's modulus* [Mpa]**	2.5E+3	2.5E+3	2.5E+3	2.5E+3	2.5E+3	2.5E+3
***Yield Stress* [Mpa]**	10	10	20	50	80	120
***Ultimate Stress* [Mpa]**	13	15	30	80	100	150
***Density* [g/cm^3]**	2.5	2.5	2.5	2.5	2.5	2.5
	3a	**3b**	**3c**	**3d**	**3e**	**3f**
***Young's modulus* [Mpa]**	5.0E+3	5.0E+3	5.0E+3	5.0E+3	5.0E+3	5.0E+3
***Yield Stress* [Mpa]**	10	20	50	80	120	150
***Ultimate Stress* [Mpa]**	13	30	80	120	150	180
***Density* [g/cm^3]**	2.5	2.5	2.5	2.5	2.5	2.5
	4a	**4b**	**4c**	**4d**	**4e**	**4f**
***Young's modulus* [Mpa]**	7.5E+3	7.5E+3	7.5E+3	7.5E+3	7.5E+3	7.5E+3
***Yield Stress* [Mpa]**	10	20	80	120	150	180
***Ultimate Stress* [Mpa]**	13	30	120	150	180	200
***Density* [g/cm^3]**	2.5	2.5	2.5	2.5	2.5	2.5
	5a	**5b**	**5c**	**5d**	**5e**	**5f**
***Young's modulus* [Mpa]**	10.0E+3	10.0E+3	10.0E+3	10.0E+3	10.0E+3	10.0E+3
***Yield Stress* [Mpa]**	10	20	80	120	150	250
***Ultimate Stress* [Mpa]**	13	30	120	150	180	500
***Density* [g/cm^3]**	2.5	2.5	2.5	2.5	2.5	2.5
	6a	**6b**	**6c**	**6d**	**6e**	**6f**
***Young's modulus* [Mpa]**	12.0E+3	12.0E+3	12.0E+3	12.0E+3	12.0E+3	12.0E+3
***Yield Stress* [Mpa]**	10	20	80	120	150	500
***Ultimate Stress* [Mpa]**	13	30	120	150	180	650
***Density* [g/cm^3]**	2.5	2.5	2.5	2.5	2.5	2.5
	7a	7b	7c	7d	7e	7f
***Young's modulus* [Mpa]**	20.0E+3	20.0E+3	20.0E+3	20.0E+3	20.0E+3	20.0E+3
***Yield Stress* [Mpa]**	10	20	80	120	150	500
***Ultimate Stress* [Mpa]**	13	30	120	150	180	650
***Density* [g/cm^3]**	2.5	2.5	2.5	2.5	2.5	2.5

Cartilage	**1**	**1b**	**1c**	**1d**	**1e**	**1f**
Young's modulus **[Mpa]**	200	400	400	400	400	400
Yield Stress **[Mpa]**	-	0.8	1.0	1.2	1.4	2
Ultimate Stress **[Mpa]**	-	1.0	1.2	1.4	1.6	3
Density **[g/cm^3]**	2.0	2.0	2.0	2.0	2.0	2.0
	2a	**2b**	**2c**	**2d**	**2e**	**2f**
Young's modulus **[Mpa]**	500	500	500	500	500	500
Yield Stress **[Mpa]**	0.6	0.8	1.0	1.2	1.4	2
Ultimate Stress **[Mpa]**	0.8	1.0	1.2	1.4	1.6	3
Density **[g/cm^3]**	2.0	2.0	2.0	2.0	2.0	2.0
	3a	**3b**	**3c**	**3d**	**3e**	**3f**
Young's modulus **[Mpa]**	600	600	600	600	600	600
Yield Stress **[Mpa]**	0.6	0.8	1.0	1.2	1.4	2
Ultimate Stress **[Mpa]**	0.8	1.0	1.2	1.4	1.6	3
Density **[g/cm^3]**	2.0	2.0	2.0	2.0	2.0	2.0
	4a	**4b**	**4c**	**4d**	**4e**	**4f**
Young's modulus **[Mpa]**	700	700	700	700	700	700
Yield Stress **[Mpa]**	0.6	0.8	1.0	1.2	1.4	2
Ultimate Stress **[Mpa]**	0.8	1.0	1.2	1.4	1.6	3
Density **[g/cm^3]**	2.0	2.0	2.0	2.0	2.0	2.0
	5a	**5b**	**5c**	**5d**	**5e**	**5f**
Young's modulus **[Mpa]**	1000	1000	1000	1000	1000	1000
Yield Stress **[Mpa]**	0.6	0.8	1.0	1.2	1.4	2
Ultimate Stress **[Mpa]**	0.8	1.0	1.2	1.4	1.6	3
Density **[g/cm^3]**	2.0	2.0	2.0	2.0	2.0	2.0
	6a	**6b**	**6c**	**6d**	**6e**	**6f**
Young's modulus **[Mpa]**	2500	2500	2500	2500	2500	2500
Yield Stress **[Mpa]**	1.2	1.4	5	10	10	20
Ultimate Stress **[Mpa]**	1.4	1.6	10	13	15	30
Density **[g/cm^3]**	2.5	2.5	2.5	2.5	2.5	2.5
	7a	**7b**	**7c**	**7d**	**7e**	**7f**
Young's modulus **[Mpa]**	5000	5000	5000	5000	5000	5000
Yield Stress **[Mpa]**	1.4	5	10	10	20	30
Ultimate Stress **[Mpa]**	1.6	10	13	15	30	50
Density **[g/cm^3]**	2.5	2.5	2.5	2.5	2.5	2.5

Soft Tissue – Muscle, Ligament, Visceral contents

	1a	1b	1c	1d	1e	1f
Young's modulus **[Mpa]**	10	10	10	10	10	
Yield Stress **[M pa]**	-	0.4	0.6	1.0	2	
Ultimate Stress **[Mpa]**	-	0.6	0.8	1.2	3	
Density **[g/cm^3]**	1.0	1.0	1.0	1.0	1.0	
	2a	**2b**	**2c**	**2d**	**2e**	**2f**
Young's modulus **[Mpa]**	20	20	20	20	20	
Yield Stress **[Mpa]**	0.2	0.4	0.6	1.0	2	
Ultimate Stress **[Mpa]**	0.4	0.6	0.8	1.2	3	
Density **[g/cm^3]**	0.8	0.8	0.8	0.8	0.8	
	3a	**3b**	**3c**	**3d**	**3e**	**3f**
Young's modulus **[Mpa]**	20	20	20	20	20	
Yield Stress **[Mpa]**	0.2	0.4	0.6	1.0	2	
Ultimate Stress **[Mpa]**	0.4	0.6	0.8	1.2	3	
Density **[g/cm^3]**	1.0	1.0	1.0	1.0	1.0	
	4a	**4b**	**4c**	**4d**	**4e**	**4f**
Young's modulus **[Mpa]**	20	20	20	20	20	
Yield Stress **[Mpa]**	0.2	0.4	0.6	1.0	2	
Ultimate Stress **[Mpa]**	0.4	0.6	0.8	1.2	3	
Density **[g/cm^3]**	1.3	1.3	1.3	1.3	1.3	
	5a	**5b**	**5c**	**5d**	**5e**	**5f**
Young's modulus **[Mpa]**	100	100	100	500	1000	2000
Yield Stress **[Mpa]**	0.6	0.8	2	-	-	-
Ultimate Stress **[Mpa]**	0.8	1.2	3	-	-	-
Density **[g/cm^3]**	1.0	1.0	1.0	1.0	1.0	1.0
	6a	**6b**	**6c**	**6d**	**6e**	**6f**
Young's modulus **[Mpa]**	0.3	0.3	0.4	0.4	0.5	0.5
Yield Stress **[Mpa]**	0.1	0.15	0.2	0.3	0.1	0.2
Ultimate Stress **[Mpa]**	0.2	0.2	0.3	0.4	0.2	0.35
Density **[g/cm^3]**	1.6	1.6	1.6	1.6	1.6	1.6
	7a	7b	7c	7d	7e	7f
Young's modulus **[Mpa]**	0.3	0.3	0.4	0.4	1.0	1.0
Yield Stress **[Mpa]**	0.1	0.1	0.1	0.1	0.2	0.4
Ultimate Stress **[Mpa]**	0.3	0.35	0.15	0.2	0.4	0.6
Density [g/cm^3]	1.6	1.6	1.6	1.6	1.6	1.6

```
*HEADING
**
*INCLUDE,INPUT=wall6.inp
***INCLUDE,INPUT=wall4.inp
*** (depending on position and posture)
*INCLUDE,INPUT=no3.inp
*INCLUDE,INPUT=el.inp
**
*node
120000,  415.800,  0.0,  176.300
120001,  414.600,   0.0,  173.500
120002,  414.000,   0.0,  170.600
120003,  413.800,   0.0,  167.700
**
*element,type=m3d4r,elset=armtape
70000,  93610, 120003, 120002,  93609
70001, 120003,  93205,  93204, 120002
70002,  93609, 120002, 120001,  93608
70003, 120002,  93204,  93203, 120001
70004,  93608, 120001, 120000,  93607
70005, 120001,  93203,  93202, 120000
**
***(no armtape for impactor tests)
*membrane section,elset=armtape,material=cart1a
4.0,
**
**  ----------------  wall  ---------------------------
*NODE,NSET=WALLN
701,0,0,0
702,0,0,0
703,0,0,0
704,0,0,0
705,0,0,0
706,0,0,0
707,0,0,0
708,0,0,0
709,0,0,0
710,0,0,0
**
*RIGID BODY,ELSET=WSH,REF NODE=701,POSITION=CENTER OF MASS,DENSITY=1E-5
0.00001
*RIGID BODY,ELSET=WTH,REF NODE=702,POSITION=CENTER OF MASS,DENSITY=1E-5
0.00001
*RIGID BODY,ELSET=WAB,REF NODE=703,POSITION=CENTER OF MASS,DENSITY=1E-5
0.00001
*RIGID BODY,ELSET=WPE,REF NODE=704,POSITION=CENTER OF MASS,DENSITY=1E-5
0.00001
*RIGID BODY,ELSET=WSE,REF NODE=705,POSITION=CENTER OF MASS,DENSITY=1E-5
0.00001
*RIGID BODY,ELSET=Wkn,REF NODE=706,POSITION=CENTER OF MASS,DENSITY=1E-5
0.00001
*RIGID BODY,ELSET=WTH2,REF NODE=707,POSITION=CENTER OF MASS,DENSITY=1E-5
0.00001
*RIGID BODY,ELSET=WAB2,REF NODE=708,POSITION=CENTER OF MASS,DENSITY=1E-5
0.00001
*RIGID BODY,ELSET=Wfo,REF NODE=709,POSITION=CENTER OF MASS,DENSITY=1E-5
0.00001
*RIGID BODY,ELSET=WPE2,REF NODE=710,POSITION=CENTER OF MASS,DENSITY=1E-5
0.00001
*BOUNDARY
WALLN,ENCASTRE
**  ----------------  BL  ---------------------------
*SHELL SECTION, ELSET=BL1, MATERIAL=BONE3f
          4.,        5
*SHELL SECTION, ELSET=BL2, MATERIAL=BONE3f
          4.,        5
*SHELL SECTION, ELSET=BL3, MATERIAL=BONE3f
          4.,        5
*SHELL SECTION, ELSET=BL4, MATERIAL=BONE3f
          4.,        5
*SHELL SECTION, ELSET=BL5, MATERIAL=BONE3f
          4.,        5
**
**
*SOLID SECTION, ELSET=intdh, MATERIAL=CART2c
          1.,
*SOLID SECTION, ELSET=intdi, MATERIAL=CART2c
          1.,
*SOLID SECTION, ELSET=intdj, MATERIAL=CART2c
          1.,
**
**
**  ----------------  BC  ---------------------------
**
*SHELL SECTION, ELSET=BC1, MATERIAL=BONE3f
          4.,        5
```

```
*SHELL SECTION, ELSET=BC2, MATERIAL=BONE3f
           4.,        5
*SHELL SECTION, ELSET=BC3, MATERIAL=BONE3f
           4.,        5
*SHELL SECTION, ELSET=BC4, MATERIAL=BONE3f
           4.,        5
*SHELL SECTION, ELSET=BC5, MATERIAL=BONE3f
           4.,        5
*SHELL SECTION, ELSET=BC6, MATERIAL=BONE3f
           4.,        5
*SHELL SECTION, ELSET=BC7, MATERIAL=BONE3f
           4.,        5
**
**
*SOLID SECTION, ELSET=intdb, MATERIAL=CART2c
           1.,
*SOLID SECTION, ELSET=intdc, MATERIAL=CART2c
           1.,
**
**
**  ----------------  BT  ---------------------------
**
*SHELL SECTION, ELSET=BT1, MATERIAL=BONE3f
           4.,        5
*SHELL SECTION, ELSET=BT2, MATERIAL=BONE3f
           4.,        5
*SHELL SECTION, ELSET=BT3, MATERIAL=BONE3f
           4.,        5
*SHELL SECTION, ELSET=BT4, MATERIAL=BONE3f
           4.,        5
*SHELL SECTION, ELSET=BT5, MATERIAL=BONE3f
           4.,        5
*SHELL SECTION, ELSET=BT6, MATERIAL=BONE3f
           4.,        5
*SHELL SECTION, ELSET=BT7, MATERIAL=BONE3f
           4.,        5
*SHELL SECTION, ELSET=BT8, MATERIAL=BONE3f
           4.,        5
*SHELL SECTION, ELSET=BT9, MATERIAL=BONE3f
           4.,        5
*SHELL SECTION, ELSET=BT10, MATERIAL=BONE3f
           4.,        5
*SHELL SECTION, ELSET=BT11, MATERIAL=BONE3f
           4.,        5
*SHELL SECTION, ELSET=BT12, MATERIAL=BONE3f
           4.,        5
**
**
*SOLID SECTION, ELSET=intdd, MATERIAL=CART4d
           1.,
*SOLID SECTION, ELSET=intde, MATERIAL=CART2c
           1.,
*SOLID SECTION, ELSET=intdf, MATERIAL=CART2c
           1.,
*SOLID SECTION, ELSET=intdg, MATERIAL=CART2c
           1.,
**
**
**  ----------------  HEAD  ---------------------------
**
**
***SHELL SECTION, ELSET=Bhead, MATERIAL=BONE3f
**           12.,       5
**
*NODE
999,122,0,710
*rigid body,elset=bhead,ref node=999
*ELEMENT, TYPE=MASS, ELSET=headm
999,999
*MASS,ELSET=HEADM
**4.1
4.3
*ELEMENT, TYPE=ROTARYI, ELSET=HEADR
998,999
*ROTARY INERTIA,ELSET=HEADR
2.7E+4,2.8E+4,2.5E+4
**
**  ----------------  NECKMUSCLES  ---------------------------
**
*SOLID SECTION, ELSET=BSTEL, MATERIAL=stis1c
           1.,
**
*SOLID SECTION, ELSET=BSTER, MATERIAL=stis1c
           1.,
*MEMBRANE SECTION, ELSET=BNSUR, MATERIAL=stis1c
           8.,
```

```
*MEMBRANE SECTION, ELSET=BCLIG, MATERIAL=stis1c
          8.,
**
**
**  ----------------  SHOULDER MUSCLES  ---------------------------
**
**
*SOLID SECTION, ELSET=SHLAT, MATERIAL=stis2a
          1.,
**
*SOLID SECTION, ELSET=SHLAT5, MATERIAL=stis2a
          1.,
**
*MEMBRANE SECTION, ELSET=SHlatsu, MATERIAL=stis1c
          6.,
**
*SOLID SECTION, ELSET=SHINL, MATERIAL=stis2a
          1.,
**
*SOLID SECTION, ELSET=SHINR, MATERIAL=stis2a
          1.,
**
*MEMBRANE SECTION, ELSET=SHINLs, MATERIAL=stis1c
          6.,
*MEMBRANE SECTION, ELSET=SHINrs, MATERIAL=stis1c
          6.,
*MEMBRANE SECTION, ELSET=SHINCL, MATERIAL=stis1c
          6.,
*MEMBRANE SECTION, ELSET=SHINCr, MATERIAL=stis1c
          6.,
**
*SOLID SECTION, ELSET=SHDEL, MATERIAL=stis1c
          1.,
**
*SOLID SECTION, ELSET=SHDER, MATERIAL=stis1c
          1.,
**
*MEMBRANE SECTION, ELSET=SHdes, MATERIAL=stis1c
          6.,
**
**
*SOLID SECTION, ELSET=SHpec, MATERIAL=stis2a
          1.,
**
*MEMBRANE SECTION, ELSET=SHPcl, MATERIAL=stis1c
          6.,
**
*MEMBRANE SECTION, ELSET=SHPcr, MATERIAL=stis1c
          6.,
**
**
*SOLID SECTION, ELSET=SHSER, MATERIAL=stis2a
          1.,
**
*SOLID SECTION, ELSET=SHSEL, MATERIAL=stis2a
          1.,
**
*MEMBRANE SECTION, ELSET=SHSERS, MATERIAL=stis1c
          6.,
**
*MEMBRANE SECTION, ELSET=SHSELS, MATERIAL=stis1c
          6.,
**
**
*SOLID SECTION, ELSET=SHSul, MATERIAL=stis2a
          1.,
**

*SOLID SECTION, ELSET=SHSur, MATERIAL=stis2a
          1.,
**
*MEMBRANE SECTION, ELSET=SHSuls, MATERIAL=stis1c
          6.,
**
*MEMBRANE SECTION, ELSET=SHSurs, MATERIAL=stis1c
          6.,
**
**  ----------------  SHOULDER BONES  --------------------------
**
*SHELL SECTION, ELSET=shgll, MATERIAL=BONE6e
          5.,       5
*SHELL SECTION, ELSET=shglr, MATERIAL=BONE6e
          5.,       5
*SHELL SECTION, ELSET=shscapl, MATERIAL=BONE6e
          8.,       5
*SHELL SECTION, ELSET=shscapr, MATERIAL=BONE6e
```

```
          8.,       5
**
*SHELL SECTION, ELSET=shclvl1, MATERIAL=BONE1a
          3.,       5
*SHELL SECTION, ELSET=shclvr1, MATERIAL=BONE1a
          3.,       5
**
*SHELL SECTION, ELSET=shcopl, MATERIAL=BONE6e
          3.,       5
*SHELL SECTION, ELSET=shcopr, MATERIAL=BONE6e
          3.,       5
*MEMBRANE SECTION, ELSET=shclvl2, MATERIAL=cart1
          16.,      5
*MEMBRANE SECTION, ELSET=shclvr2, MATERIAL=cart1
          16.,      5
**
**  ----------------  BACK LIGAMENTs  -------------------------
*MEMBRANE SECTION, ELSET=Bcfllig, MATERIAL=stis2a
          4.,       5
*MEMBRANE SECTION, ELSET=Btfllig, MATERIAL=stis2a
          4.,       5
*MEMBRANE SECTION, ELSET=Blfllig, MATERIAL=stis2a
          4.,       5
*MEMBRANE SECTION, ELSET=Bclolig, MATERIAL=stis2a
          4.,       5
*MEMBRANE SECTION, ELSET=Btlolig, MATERIAL=stis2a
          4.,       5
*MEMBRANE SECTION, ELSET=Bllolig, MATERIAL=stis2a
          4.,       5
*MEMBRANE SECTION, ELSET=Bcsulig, MATERIAL=stis2a
          4.,       5
*MEMBRANE SECTION, ELSET=Btsulig, MATERIAL=stis2a
          4.,       5
*MEMBRANE SECTION, ELSET=Blsulig, MATERIAL=stis2a
          4.,       5
**
**  ----------------  BACK MUSCLES  ---------------------------
**
*SOLID SECTION, ELSET=BERECT, MATERIAL=stis2a
          1.,
*MEMBRANE SECTION, ELSET=BERECTsl, MATERIAL=stis2a
          3.,       5
*MEMBRANE SECTION, ELSET=BERECTsr, MATERIAL=stis2a
          3.,       5
**
*SOLID SECTION, ELSET=BTRAP, MATERIAL=stis2a
          1.,
**
*SOLID SECTION, ELSET=BTRAP2, MATERIAL=stis2a
          1.,
**
*MEMBRANE SECTION, ELSET=BTRAPF, MATERIAL=stis1c
          6.,       5
*MEMBRANE SECTION, ELSET=Brhoml, MATERIAL=stis5a
          16.,      5
*MEMBRANE SECTION, ELSET=Brhomr, MATERIAL=stis5a
          16.,      5
**
*SOLID SECTION, ELSET=BSEMSOL, MATERIAL=stis2a
          1.,
*MEMBRANE SECTION, ELSET=BSEMsur, MATERIAL=stis1c
          6.,
*MEMBRANE SECTION, ELSET=BSPLL, MATERIAL=stis1c
          8.,
**
*MEMBRANE SECTION, ELSET=BSPLR, MATERIAL=stis1c
          8.,
**
**
**  ----------------  RIB  ---------------------------
**
*SHELL SECTION, ELSET=R1, MATERIAL=BONE1a
          2.,       5
*SHELL SECTION, ELSET=R2, MATERIAL=BONE1a
          2.,       5
*SHELL SECTION, ELSET=R3, MATERIAL=BONE1a
          2.,       5
*SHELL SECTION, ELSET=R4, MATERIAL=BONE1a
          2.,       5
*SHELL SECTION, ELSET=R5, MATERIAL=BONE1a
          2.,       5
*SHELL SECTION, ELSET=R6, MATERIAL=BONE1a
          2.,       5
*SHELL SECTION, ELSET=R7, MATERIAL=BONE1a
          2.,       5
*SHELL SECTION, ELSET=R8, MATERIAL=BONE1a
```

```
          2.,       5
*SHELL SECTION, ELSET=R9, MATERIAL=BONE1a
          2.,       5
*SHELL SECTION, ELSET=R10, MATERIAL=BONE1a
          2.,       5
*SHELL SECTION, ELSET=R11, MATERIAL=BONE1a
          2.,       5
*SHELL SECTION, ELSET=R12, MATERIAL=BONE1a
          2.,       5
**
*SHELL SECTION, ELSET=RCOCART, MATERIAL=cart6d
          2.,       5
*SHELL SECTION, ELSET=rSTERN, MATERIAL=BONE2a
          3.,       5
**
*MEMBRANE SECTION, ELSET=RINTIN, MATERIAL=stis1c
          8.,
**
*MEMBRANE SECTION, ELSET=Rintout, MATERIAL=stis1c
          8.,
**
**
**  ----------------  ABDOMINAL MUSCLES  ---------------------------
**
*SOLID SECTION, ELSET=ASOL1, MATERIAL=stis4c
          1.,
**
*SOLID SECTION, ELSET=ASOL2, MATERIAL=stis4c
          1.,
**
*MEMBRANE SECTION, ELSET=ABDsur, MATERIAL=stis1c
          8.,
**
*MEMBRANE SECTION, ELSET=ABDin, MATERIAL=stis1c
          8.,
*MEMBRANE SECTION, ELSET=ABdou, MATERIAL=stis1c
          8.,
**
*SOLID SECTION, ELSET=ABD3L, MATERIAL=stis1c
          1.,
**
*SOLID SECTION, ELSET=ABD3R, MATERIAL=stis1c
          1.,
****
*MEMBRANE SECTION, ELSET=ABD3S, MATERIAL=stis1c
          8.,
**
**  ----------------  ARM BONES  ---------------------------
**
*SHELL SECTION, ELSET=AHUML, MATERIAL=BONE6e
          5.,       5
*SHELL SECTION, ELSET=ATUBL, MATERIAL=BONE6e
          5.,       5
*SHELL SECTION, ELSET=AHUMR, MATERIAL=BONE6e
          5.,       5
*SHELL SECTION, ELSET=ATUBR, MATERIAL=BONE6e
          5.,       5
*SHELL SECTION, ELSET=Aulnal, MATERIAL=BONE6e
          5.,       5
*SHELL SECTION, ELSET=Aulnar, MATERIAL=BONE6e
          5.,       5
**
**
**  ----------------  ARM MUSCLES  --------------------------
**
*SOLID SECTION, ELSET=ABIsoll, MATERIAL=stis1b
          1.,
**
*SOLID SECTION, ELSET=ABIsolr, MATERIAL=stis1b
          1.,
**
*MEMBRANE SECTION, ELSET=Abisull, MATERIAL=stis1c
          4.,
**
*MEMBRANE SECTION, ELSET=Abisulr, MATERIAL=stis1c
          4.,
**
**
*SOLID SECTION, ELSET=ATRisol, MATERIAL=stis1b
          1.,
**
*SOLID SECTION, ELSET=ATRisor, MATERIAL=stis1b
          1.,
**
*MEMBRANE SECTION, ELSET=ATRisul, MATERIAL=stis1c
          6.,
```

```
**
*MEMBRANE SECTION, ELSET=ATRisur, MATERIAL=stis1c
          6.,
**
*SOLID SECTION, ELSET=Aforeal, MATERIAL=stis1c
          1.,
*SOLID SECTION, ELSET=Aforear, MATERIAL=stis1c
          1.,
**
*MEMBRANE SECTION, ELSET=Asurfl, MATERIAL=stis1c
          6.,
*MEMBRANE SECTION, ELSET=Asurfr, MATERIAL=stis1c
          6.,
**
*MEMBRANE SECTION, ELSET=aelbligl, MATERIAL=stis5e
          8.,
*MEMBRANE SECTION, ELSET=aelbligr, MATERIAL=stis5e

         8.,
*MEMBRANE SECTION, ELSET=ACOLIGR, MATERIAL=stis5e
          12.,
*MEMBRANE SECTION, ELSET=ACOLIGl, MATERIAL=stis5e
         12.,
**
*MEMBRANE SECTION, ELSET=afosul, MATERIAL=stis2a
          8.,
*MEMBRANE SECTION, ELSET=afosur, MATERIAL=stis2a
          8.,
*MEMBRANE SECTION, ELSET=aelsul, MATERIAL=stis2a
          4.,
*MEMBRANE SECTION, ELSET=aelsur, MATERIAL=stis2a
          4.,
*MEMBRANE SECTION, ELSET=awl, MATERIAL=stis2a
          4.,
*MEMBRANE SECTION, ELSET=awr, MATERIAL=stis2a
          4.,
**
**  ----------------  PELVIS  ---------------------------
**
*SHELL SECTION, ELSET=P1, MATERIAL=BONE2f
          4,        5
*SHELL SECTION, ELSET=P2, MATERIAL=BONE2f
          6,        5
*SHELL SECTION, ELSET=P3, MATERIAL=BONE2f
          6,        5
*SHELL SECTION, ELSET=P4, MATERIAL=BONE2f
          4,        5
*SHELL SECTION, ELSET=Pacetl, MATERIAL=BONE3f
          6.,       5
**
*SHELL SECTION, ELSET=P1r, MATERIAL=BONE2f
          4,        5
*SHELL SECTION, ELSET=P2r, MATERIAL=BONE2f
          6,        5
*SHELL SECTION, ELSET=P3r, MATERIAL=BONE2f
          6,        5
*SHELL SECTION, ELSET=P4r, MATERIAL=BONE2f
          4,        5
*SHELL SECTION, ELSET=Pacetr, MATERIAL=BONE3f
          6.,       5
**
*SHELL SECTION, ELSET=PSACRUM, MATERIAL=BONE3f
          3.,       5
**
*SOLID SECTION, ELSET=PSYMPh, MATERIAL=CART2c
          1.,
**
*MEMBRANE SECTION, ELSET=PGs, MATERIAL=stis2b
          1.,
**
*SOLID SECTION, ELSET=PGlm, MATERIAL=stis2a
          1.,
**
**
*SHELL SECTION, ELSET=Pfhl, MATERIAL=BONE3f
          6.,       5
**
*SHELL SECTION, ELSET=Pfhr, MATERIAL=BONE3f
          6.,       5
**
*SHELL SECTION, ELSET=Pfhal, MATERIAL=BONE3f
          6.,       5
**
*SHELL SECTION, ELSET=Pfhar, MATERIAL=BONE3f
          6.,       5
**
```

```
**
**  ----------------  VISCERAL CONTENTS  ---------------------------
*SOLID SECTION, ELSET=VISOL1, MATERIAL=stis6a
          1.,
*SOLID SECTION, ELSET=VISOL1B, MATERIAL=stis7e
          1.,
**
*SOLID SECTION, ELSET=VISOL2, MATERIAL=stis6f
          1.,
**
*SOLID SECTION, ELSET=VISOL3, MATERIAL=stis6c
          1.,
**
*MEMBRANE SECTION, ELSET=VISC1S, MATERIAL=stis2c
          4.,
*MEMBRANE SECTION, ELSET=VISC2S, MATERIAL=stis2c
          4.,
*MEMBRANE SECTION, ELSET=VISC3S, MATERIAL=stis2c
          4.,
**
**
**
**  ----------------  LEG  ---------------------------
**
*SHELL SECTION, ELSET=ptibl, MATERIAL=BONE3f
          6.,        5
*SHELL SECTION, ELSET=ptibr, MATERIAL=BONE3f
          6.,        5
**
**
*SOLID SECTION, ELSET=plegsor, MATERIAL=stis2a
          1.,
*SOLID SECTION, ELSET=plegsol, MATERIAL=stis2a
          1.,
**
*MEMBRANE SECTION, ELSET=plegl, MATERIAL=stis5b
          6.,
*MEMBRANE SECTION, ELSET=plegr, MATERIAL=stis5b
          6.,
*SOLID SECTION, ELSET=pksol, MATERIAL=stis1c
          1.,
*SOLID SECTION, ELSET=pksor, MATERIAL=stis1c
          1.,
**
*MEMBRANE SECTION, ELSET=pksul, MATERIAL=stis5b
          6.,
*MEMBRANE SECTION, ELSET=pksur, MATERIAL=stis5b
          6.,
**
**
**
**  ----------------  MATERIAL  PROPERTIES  ---------------------------
*INCLUDE,INPUT=material.inp
*INCLUDE,INPUT=elsets3.inp
** ----------------  -------------------  ---------------------------
**
*NSET,NSET=OUTN
WALLN
onode
15313
999
** ----------------  provisional arm contact---------------------------
*elset,elset=ac,generate
21151,21159,1
** ----------------  -------------------  ---------------------------
**
*nset,nset=alln2
alln
999
**
**
*INITIAL CONDITIONS,TYPE=VELOCITY
ALLN2,2,6500
**
*STEP
*DYNAMIC,EXPLICIT
,0.0000005
*variable mass scaling,type=below min,dt=11.0e-7,elset=alel,number interval=1
*RESTART,WRITE,NUMBER INTERVAL=1
*END STEP
*STEP
*DYNAMIC,EXPLICIT
,0.005
**
**
***adaptive mesh,elset=ABIsol1,frequency=20,mesh sweeps=1
```

```
**
***DLOAD
**ALEL,-9800,0,0,1.0
**
*HISTORY OUTPUT,TIME=0.0001
*NODE HISTORY,NSET=OUTN
U,V,A,RF1,RF2,RF3
**
*INCLUDE,INPUT=spine.inp
*INCLUDE,INPUT=joint.inp
*INCLUDE,INPUT=cont.inp
*surface definition,name=ac
ac,spos
*contact pair,penalty
wth,ac
**
*RESTART,WRITE,NUMBER INTERVAL=1
*END STEP
*STEP
*DYNAMIC,EXPLICIT
,0.005
*RESTART,WRITE,NUMBER INTERVAL=1
*END STEP
*STEP
*DYNAMIC,EXPLICIT
,0.005
*RESTART,WRITE,NUMBER INTERVAL=1
*END STEP
*STEP
*DYNAMIC,EXPLICIT
,0.005
*RESTART,WRITE,NUMBER INTERVAL=1
*END STEP
*STEP
*DYNAMIC,EXPLICIT
,0.005
*RESTART,WRITE,NUMBER INTERVAL=1
*END STEP
***     ----- 7th Step  ---------
*STEP
*DYNAMIC,EXPLICIT
,0.005
*RESTART,WRITE,NUMBER INTERVAL=1
*END STEP
*STEP
*DYNAMIC,EXPLICIT
,0.005
*RESTART,WRITE,NUMBER INTERVAL=1
*END STEP
*STEP
*DYNAMIC,EXPLICIT
,0.005
*RESTART,WRITE,NUMBER INTERVAL=1
*END STEP
***     ----- 10th Step  ---------
*STEP
*DYNAMIC,EXPLICIT
,0.005
*RESTART,WRITE,NUMBER INTERVAL=1
*END STEP
*STEP
*DYNAMIC,EXPLICIT
,0.005
*RESTART,WRITE,NUMBER INTERVAL=1
*END STEP
*STEP
*DYNAMIC,EXPLICIT
,0.005
*RESTART,WRITE,NUMBER INTERVAL=1
*END STEP
*STEP
*DYNAMIC,EXPLICIT
,0.005
*RESTART,WRITE,NUMBER INTERVAL=1
*END STEP
*STEP
*DYNAMIC,EXPLICIT
,0.005
*RESTART,WRITE,NUMBER INTERVAL=1
*END STEP
***     ----- 15th Step  ---------
*STEP
*DYNAMIC,EXPLICIT
,0.005
*RESTART,WRITE,NUMBER INTERVAL=1
*END STEP
```

Material input

```
**  ----------------  MATERIAL  PROPERTIES  -----
----------------------
**
**  ------------------------   BONE   -----------
--------
**  ------------------------ BONE1a-f  E = 1 -
12.5E+6, -------------------
**
*MATERIAL, NAME=BONE1a
*DENSITY
      2.0E-6,
*ELASTIC, TYPE=ISO
      1.0E+6,         0.3
*PLASTIC
 9.0E+3,0
10.0E+3,1.0
**
*MATERIAL, NAME=BONE1b
*DENSITY
      2.0E-6,
*ELASTIC, TYPE=ISO
      2.5E+6,         0.3
*PLASTIC
 9.0E+3,0
10.0E+3,1.0
**
*MATERIAL, NAME=BONE1c
*DENSITY
      2.0E-6,
*ELASTIC, TYPE=ISO
      5.0E+6,         0.3
*PLASTIC
 9.0E+3,0
10.0E+3,1.0
**
*MATERIAL, NAME=BONE1d
*DENSITY
      2.0E-6,
*ELASTIC, TYPE=ISO
      7.5E+6,         0.3
*PLASTIC
 9.0E+3,0
10.0E+3,1.0
**
*MATERIAL, NAME=BONE1e
*DENSITY
      2.0E-6,
*ELASTIC, TYPE=ISO
      10.0E+6,         0.3
*PLASTIC
 9.0E+3,0
10.0E+3,1.0
**
*MATERIAL, NAME=BONE1f
*DENSITY
      2.0E-6,
*ELASTIC, TYPE=ISO
      12.5E+6,         0.3
*PLASTIC
 9.0E+3,0
10.0E+3,1.0
**
**  ------------------------ BONE2a-f  E =
2.5E+6, Yield: 10 - 150 -------------
**
*MATERIAL, NAME=BONE2a
*DENSITY
      2.5E-6,
*ELASTIC, TYPE=ISO
      2.5E+6,         0.3
*PLASTIC
10.0E+3,0
13.0E+3,1.0
**
**
*MATERIAL, NAME=BONE2b
*DENSITY
      2.5E-6,
*ELASTIC, TYPE=ISO
      2.5E+6,         0.3
*PLASTIC
10.0E+3,0
15.0E+3,1.0
**
*MATERIAL, NAME=BONE2c
*DENSITY
      2.5E-6,
*ELASTIC, TYPE=ISO
      2.5E+6,         0.3
*PLASTIC
20.0E+3,0
30.0E+3,1.0
**
*MATERIAL, NAME=BONE2d
*DENSITY
      2.5E-6,
*ELASTIC, TYPE=ISO
      2.5E+6,         0.3
*PLASTIC
50.0E+3,0
80.0E+3,1.0
**
*MATERIAL, NAME=BONE2e
*DENSITY
      2.5E-6,
*ELASTIC, TYPE=ISO
      2.5E+6,         0.3
*PLASTIC
 80.0E+3,0
100.0E+3,1.0
**
*MATERIAL, NAME=BONE2f
*DENSITY
      2.5E-6,
*ELASTIC, TYPE=ISO
      2.5E+6,         0.3
*PLASTIC
120.0E+3,0
150.0E+3,1.0
**  ------------------------ BONE3a-f  E =
5.0E+6, Yield: 10 - 180 -------------
**
*MATERIAL, NAME=BONE3a
*DENSITY
      2.5E-6,
*ELASTIC, TYPE=ISO
      5.0E+6,         0.3
*PLASTIC
10.0E+3,0
13.0E+3,1.0
**
**
*MATERIAL, NAME=BONE3b
*DENSITY
      2.5E-6,
*ELASTIC, TYPE=ISO
      5.0E+6,         0.3
*PLASTIC
20.0E+3,0
30.0E+3,1.0
**
*MATERIAL, NAME=BONE3c
*DENSITY
      2.5E-6,
*ELASTIC, TYPE=ISO
      5.0E+6,         0.3
*PLASTIC
50.0E+3,0
80.0E+3,1.0
**
*MATERIAL, NAME=BONE3d
*DENSITY
      2.5E-6,
*ELASTIC, TYPE=ISO
      5.0E+6,         0.3
*PLASTIC
 80.0E+3,0
120.0E+3,1.0
**
*MATERIAL, NAME=BONE3e
*DENSITY
      2.5E-6,
*ELASTIC, TYPE=ISO
      5.0E+6,         0.3
*PLASTIC
```

```
120.0E+3,0
150.0E+3,1.0
**
*MATERIAL, NAME=BONE3f
*DENSITY
      2.5E-6,
*ELASTIC, TYPE=ISO
      5.0E+6,         0.3
*PLASTIC
150.0E+3,0
180.0E+3,1.0
**  ------------------------- BONE4a-f  E =
7.5E+6, Yield: 10 - 200 -------------
**
*MATERIAL, NAME=BONE4a
*DENSITY
      2.5E-6,
*ELASTIC, TYPE=ISO
      7.5E+6,         0.3
*PLASTIC
10.0E+3,0
13.0E+3,1.0
**
*MATERIAL, NAME=BONE4b
*DENSITY
      2.5E-6,
*ELASTIC, TYPE=ISO
      7.5E+6,         0.3
*PLASTIC
20.0E+3,0
30.0E+3,1.0
**
*MATERIAL, NAME=BONE4c
*DENSITY
      2.5E-6,
*ELASTIC, TYPE=ISO
      7.5E+6,         0.3
*PLASTIC
 80.0E+3,0
120.0E+3,1.0
**
*MATERIAL, NAME=BONE4d
*DENSITY
      2.5E-6,
*ELASTIC, TYPE=ISO
      7.5E+6,         0.3
*PLASTIC
120.0E+3,0
150.0E+3,1.0
**
*MATERIAL, NAME=BONE4e
*DENSITY
      2.5E-6,
*ELASTIC, TYPE=ISO
      7.5E+6,         0.3
*PLASTIC
150.0E+3,0
180.0E+3,1.0
**
*MATERIAL, NAME=BONE4f
*DENSITY
      2.5E-6,
*ELASTIC, TYPE=ISO
      7.5E+6,         0.3
*PLASTIC
180.0E+3,0
200.0E+3,1.0
**
**  ------------------------- BONE5a-f  E =
10.0E+6, Yield: 10 - 500 -----------
**
*MATERIAL, NAME=BONE5a
*DENSITY
      2.5E-6,
*ELASTIC, TYPE=ISO
      10.0E+6,         0.3
*PLASTIC
10.0E+3,0
13.0E+3,1.0
**
*MATERIAL, NAME=BONE5b
*DENSITY
      2.5E-6,
*ELASTIC, TYPE=ISO
      10.0E+6,         0.3
*PLASTIC
20.0E+3,0
30.0E+3,1.0
**
*MATERIAL, NAME=BONE5c
*DENSITY
      2.5E-6,
*ELASTIC, TYPE=ISO
      10.0E+6,         0.3
*PLASTIC
 80.0E+3,0
120.0E+3,1.0
**
*MATERIAL, NAME=BONE5d
*DENSITY
      2.5E-6,
*ELASTIC, TYPE=ISO
      10.0E+6,         0.3
*PLASTIC
120.0E+3,0
150.0E+3,1.0
**
*MATERIAL, NAME=BONE5e
*DENSITY
      2.5E-6,
*ELASTIC, TYPE=ISO
      10.0E+6,         0.3
*PLASTIC
150.0E+3,0
180.0E+3,1.0
**
*MATERIAL, NAME=BONE5f
*DENSITY
      2.5E-6,
*ELASTIC, TYPE=ISO
      10.0E+6,         0.3
*PLASTIC
250.0E+3,0
500.0E+3,1.0
**
**  ------------------------- BONE6a-f  E =
12.0E+6, Yield: 10 - 650 -----------
**
*MATERIAL, NAME=BONE6a
*DENSITY
      2.5E-6,
*ELASTIC, TYPE=ISO
      12.0E+6,         0.3
*PLASTIC
10.0E+3,0
13.0E+3,1.0
**
*MATERIAL, NAME=BONE6b
*DENSITY
      2.5E-6,
*ELASTIC, TYPE=ISO
      12.0E+6,         0.3
*PLASTIC
20.0E+3,0
30.0E+3,1.0
**
*MATERIAL, NAME=BONE6c
*DENSITY
      2.5E-6,
*ELASTIC, TYPE=ISO
      12.0E+6,         0.3
*PLASTIC
 80.0E+3,0
120.0E+3,1.0
**
*MATERIAL, NAME=BONE6d
*DENSITY
      2.5E-6,
*ELASTIC, TYPE=ISO
      12.0E+6,         0.3
*PLASTIC
120.0E+3,0
150.0E+3,1.0
**
*MATERIAL, NAME=BONE6e
*DENSITY
      2.5E-6,
*ELASTIC, TYPE=ISO
      12.0E+6,         0.3
*PLASTIC
150.0E+3,0
180.0E+3,1.0
```

```
**
*MATERIAL, NAME=BONE6f
*DENSITY
      2.5E-6,
*ELASTIC, TYPE=ISO
      12.0E+6,         0.3
*PLASTIC
500.0E+3,0
650.0E+3,1.0
**
**  ------------------------ BONE7a-f  E =
20.0E+6, Yield: 10 - 650 -----------
**
*MATERIAL, NAME=BONE7a
*DENSITY
      2.5E-6,
*ELASTIC, TYPE=ISO
      20.0E+6,         0.3
*PLASTIC
10.0E+3,0
13.0E+3,1.0
**
*MATERIAL, NAME=BONE7b
*DENSITY
      2.5E-6,
*ELASTIC, TYPE=ISO
      20.0E+6,         0.3
*PLASTIC
20.0E+3,0
30.0E+3,1.0
**
*MATERIAL, NAME=BONE7c
*DENSITY
      2.5E-6,
*ELASTIC, TYPE=ISO
      20.0E+6,         0.3
*PLASTIC
 80.0E+3,0
120.0E+3,1.0
**
*MATERIAL, NAME=BONE7d
*DENSITY
      2.5E-6,
*ELASTIC, TYPE=ISO
      20.0E+6,         0.3
*PLASTIC
120.0E+3,0
150.0E+3,1.0
**
*MATERIAL, NAME=BONE7e
*DENSITY
      2.5E-6,
*ELASTIC, TYPE=ISO
      20.0E+6,         0.3
*PLASTIC
150.0E+3,0
180.0E+3,1.0
**
*MATERIAL, NAME=BONE7f
*DENSITY
      2.5E-6,
*ELASTIC, TYPE=ISO
      20.0E+6,         0.3
*PLASTIC
 500.0E+3,0
650.0E+3,1.0
**
**
**  -------------------------- Cartilage -------
--------------------
**  --------------------- CART1a-f   E = 400E+3,
-------------------
**
***
*MATERIAL, NAME=CART1
*DENSITY
       2.E-6,
*ELASTIC, TYPE=ISO
      200.E+3,         0.3
**
**
*MATERIAL, NAME=CART1b
*DENSITY
       2.E-6,
*ELASTIC, TYPE=ISO
      400.E+3,         0.3
*PLASTIC
0.8E+3,0
1.0E+3,1.0
**
*MATERIAL, NAME=CART1c
*DENSITY
       2.E-6,
*ELASTIC, TYPE=ISO
      400.E+3,         0.3
*PLASTIC
1.0E+3,0
1.2E+3,1.0
**
*MATERIAL, NAME=CART1d
*DENSITY
       2.E-6,
*ELASTIC, TYPE=ISO
      400.E+3,         0.3
*PLASTIC
1.2E+3,0
1.4E+3,1.0
**
*MATERIAL, NAME=CART1e
*DENSITY
       2.E-6,
*ELASTIC, TYPE=ISO
      400.E+3,         0.3
*PLASTIC
1.4E+3,0
1.6E+3,1.0
**
*MATERIAL, NAME=CART1f
*DENSITY
       2.E-6,
*ELASTIC, TYPE=ISO
      400.E+3,         0.3
*PLASTIC
2.0E+3,0
3.0E+3,1.0
**
**  ---------------------  CART2a-f   E = 500E+3,
-------------------
**
***

*MATERIAL, NAME=CART2a
*DENSITY
       2.E-6,
*ELASTIC, TYPE=ISO
      500.E+3,         0.3
*PLASTIC
0.6E+3,0
0.8E+3,1.0
**
*MATERIAL, NAME=CART2b
*DENSITY
       2.E-6,
*ELASTIC, TYPE=ISO
      500.E+3,         0.3
*PLASTIC
0.8E+3,0
1.0E+3,1.0
**
*MATERIAL, NAME=CART2c
*DENSITY
       2.E-6,
*ELASTIC, TYPE=ISO
      500.E+3,         0.3
*PLASTIC
1.0E+3,0
1.2E+3,1.0
**
*MATERIAL, NAME=CART2d
*DENSITY
       2.E-6,
*ELASTIC, TYPE=ISO
      500.E+3,         0.3
*PLASTIC
1.2E+3,0
1.4E+3,1.0
**
*MATERIAL, NAME=CART2e
*DENSITY
       2.E-6,
*ELASTIC, TYPE=ISO
      500.E+3,         0.3
```

```
*PLASTIC
1.4E+3,0
1.6E+3,1.0
**
*MATERIAL, NAME=CART2f
*DENSITY
       2.E-6,
*ELASTIC, TYPE=ISO
      500.E+3,         0.3
*PLASTIC
2.0E+3,0
3.0E+3,1.0
**
**  ---------------------  CART3a-f   E = 600E+3,
-------------------
**
***
*MATERIAL, NAME=CART3a
*DENSITY
       2.E-6,
*ELASTIC, TYPE=ISO
      600.E+3,         0.3
*PLASTIC
0.6E+3,0
0.8E+3,1.0
**
*MATERIAL, NAME=CART3b
*DENSITY
       2.E-6,
*ELASTIC, TYPE=ISO
      600.E+3,         0.3
*PLASTIC
0.8E+3,0
1.0E+3,1.0
**
*MATERIAL, NAME=CART3c
*DENSITY
       2.E-6,
*ELASTIC, TYPE=ISO
      600.E+3,         0.3
*PLASTIC
1.0E+3,0
1.2E+3,1.0
**
*MATERIAL, NAME=CART3d
*DENSITY
       2.E-6,
*ELASTIC, TYPE=ISO
      600.E+3,         0.3
*PLASTIC
1.2E+3,0
1.4E+3,1.0
**
*MATERIAL, NAME=CART3e
*DENSITY
       2.E-6,
*ELASTIC, TYPE=ISO
      600.E+3,         0.3
*PLASTIC
1.4E+3,0
1.6E+3,1.0
**
*MATERIAL, NAME=CART3f
*DENSITY
       2.E-6,
*ELASTIC, TYPE=ISO
      600.E+3,         0.3
*PLASTIC
2.0E+3,0
3.0E+3,1.0
**
**  ---------------------  CART4a-f   E = 700E+3,
-------------------
**
***
*MATERIAL, NAME=CART4a
*DENSITY
       2.E-6,
*ELASTIC, TYPE=ISO
      700.E+3,         0.3
*PLASTIC
0.6E+3,0
0.8E+3,1.0
**
*MATERIAL, NAME=CART4b
*DENSITY
       2.E-6,
*ELASTIC, TYPE=ISO
      700.E+3,         0.3
*PLASTIC
0.8E+3,0
1.0E+3,1.0
**
*MATERIAL, NAME=CART4c
*DENSITY
       2.E-6,
*ELASTIC, TYPE=ISO
      700.E+3,         0.3
*PLASTIC
1.0E+3,0
1.2E+3,1.0
**
*MATERIAL, NAME=CART4d
*DENSITY
       2.E-6,
*ELASTIC, TYPE=ISO
      700.E+3,         0.3
*PLASTIC
1.2E+3,0
1.4E+3,1.0
**
*MATERIAL, NAME=CART4e
*DENSITY
       2.E-6,
*ELASTIC, TYPE=ISO
      700.E+3,         0.3
*PLASTIC
1.4E+3,0
1.6E+3,1.0
**
*MATERIAL, NAME=CART4f
*DENSITY
       2.E-6,
*ELASTIC, TYPE=ISO
      700.E+3,         0.3
*PLASTIC
2.0E+3,0
3.0E+3,1.0
**
**  ---------------------  CART5a-f   E =
1000E+3, -------------------
**
***
*MATERIAL, NAME=CART5a
*DENSITY
       2.E-6,
*ELASTIC, TYPE=ISO
      1000.E+3,        0.3
*PLASTIC
0.6E+3,0
0.8E+3,1.0
**
*MATERIAL, NAME=CART5b
*DENSITY
       2.E-6,
*ELASTIC, TYPE=ISO
      1000.E+3,        0.3
*PLASTIC
0.8E+3,0
1.0E+3,1.0
**
*MATERIAL, NAME=CART5c
*DENSITY
       2.E-6,
*ELASTIC, TYPE=ISO
      1000.E+3,        0.3
*PLASTIC
1.0E+3,0
1.2E+3,1.0
**
*MATERIAL, NAME=CART5d
*DENSITY
       2.E-6,
*ELASTIC, TYPE=ISO
      1000.E+3,        0.3
*PLASTIC
1.2E+3,0
1.4E+3,1.0
**
*MATERIAL, NAME=CART5e
*DENSITY
       2.E-6,
```

```
*ELASTIC, TYPE=ISO
      1000.E+3,         0.3
*PLASTIC
1.4E+3,0
1.6E+3,1.0
**
*MATERIAL, NAME=CART5f
*DENSITY
       2.E-6,
*ELASTIC, TYPE=ISO
      1000.E+3,         0.3
*PLASTIC
2.0E+3,0
3.0E+3,1.0
**
**  ---------------------  CART6a-f   E =
2500E+3, -------------------
**
***
*MATERIAL, NAME=CART6a
*DENSITY
       2.5E-6,
*ELASTIC, TYPE=ISO
      2500.E+3,         0.3
*PLASTIC
1.2E+3,0
1.4E+3,1.0
**
*MATERIAL, NAME=CART6b
*DENSITY
       2.5E-6,
*ELASTIC, TYPE=ISO
      2500.E+3,         0.3
*PLASTIC
1.4E+3,0
1.6E+3,1.0
**
*MATERIAL, NAME=CART6c
*DENSITY
       2.5E-6,

*ELASTIC, TYPE=ISO
      2500.E+3,         0.3
*PLASTIC
5.0E+3,0
10.0E+3,1.0
**
*MATERIAL, NAME=CART6d
*DENSITY
       2.5E-6,
*ELASTIC, TYPE=ISO
      2500.E+3,         0.3
*PLASTIC
10E+3,0
13E+3,1.0
**
*MATERIAL, NAME=CART6e
*DENSITY
       2.5E-6,
*ELASTIC, TYPE=ISO
      2500.E+3,         0.3
*PLASTIC
10E+3,0
15E+3,1.0
**
*MATERIAL, NAME=CART6f
*DENSITY
       2.5E-6,
*ELASTIC, TYPE=ISO
      2500.E+3,         0.3
*PLASTIC
20E+3,0
30E+3,1.0
**
**  ---------------------  CART7a-f   E =
5000E+3, -------------------
**
***
*MATERIAL, NAME=CART7a
*DENSITY
       2.E-6,
*ELASTIC, TYPE=ISO
      5000.E+3,         0.3
*PLASTIC
1.4E+3,0
1.6E+3,1.0
```

```
**
*MATERIAL, NAME=CART7b
*DENSITY
       2.5E-6,
*ELASTIC, TYPE=ISO
      5000.E+3,         0.3
*PLASTIC
5E+3,0
10E+3,1.0
**
*MATERIAL, NAME=CART7c
*DENSITY
       2.5E-6,
*ELASTIC, TYPE=ISO
      5000.E+3,         0.3
*PLASTIC
10E+3,0
13E+3,1.0
**
*MATERIAL, NAME=CART7d
*DENSITY
       2.5E-6,
*ELASTIC, TYPE=ISO
      5000.E+3,         0.3
*PLASTIC
10E+3,0
15E+3,1.0
**
*MATERIAL, NAME=CART7e
*DENSITY
       2.5E-6,
*ELASTIC, TYPE=ISO
      5000.E+3,         0.3
*PLASTIC
20E+3,0
30E+3,1.0
**
*MATERIAL, NAME=CART7f
*DENSITY
       2.5E-6,
*ELASTIC, TYPE=ISO
      5000.E+3,         0.3
*PLASTIC
30E+3,0
50E+3,1.0
**
**
**  --------------------------  Soft Tissue -----
----------------------
**  -------------- Muscle, Ligament, Visceral
Contents   -------------------
**
*MATERIAL, NAME=stis1
*DENSITY
       1.0E-6,
*ELASTIC, TYPE=ISO
      20.E+3,         0.3
**
*MATERIAL, NAME=stis1a
*DENSITY
       1.0E-6,
*ELASTIC, TYPE=ISO
      10.E+3,         0.3
*PLASTIC
0.2E+3,0
0.4E+3,1.0
**
*MATERIAL, NAME=stis1b
*DENSITY
       1.0E-6,
*ELASTIC, TYPE=ISO
      10.E+3,         0.3
*PLASTIC
0.4E+3,0
0.6E+3,1.0
**
*MATERIAL, NAME=stis1c
*DENSITY
       1.0E-6,
*ELASTIC, TYPE=ISO
      10.E+3,         0.3
*PLASTIC
0.6E+3,0
0.8E+3,1.0
**
*MATERIAL, NAME=stis1d
```

```
*DENSITY
       1.0E-6,
*ELASTIC, TYPE=ISO
      10.E+3,         0.3
*PLASTIC
1.0E+3,0
1.2E+3,1.0
**
*MATERIAL, NAME=stis1e
*DENSITY
       1.0E-6,
*ELASTIC, TYPE=ISO
      10.E+3,         0.3
*PLASTIC
2.0E+3,0
3.0E+3,1.0
**
*MATERIAL, NAME=stis2a
*DENSITY
       0.8E-6,
*ELASTIC, TYPE=ISO
      20.E+3,         0.3
*PLASTIC
0.2E+3,0
0.4E+3,1.0
**
*MATERIAL, NAME=stis2b
*DENSITY
       0.8E-6,
*ELASTIC, TYPE=ISO
      20.E+3,         0.3
*PLASTIC
0.4E+3,0
0.6E+3,1.0
**
*MATERIAL, NAME=stis2c
*DENSITY
       0.8E-6,
*ELASTIC, TYPE=ISO
      20.E+3,         0.3
*PLASTIC
0.6E+3,0
0.8E+3,1.0
**
*MATERIAL, NAME=stis2d
*DENSITY
       0.8E-6,
*ELASTIC, TYPE=ISO
      20.E+3,         0.3
*PLASTIC
1.0E+3,0
1.2E+3,1.0

**
*MATERIAL, NAME=stis2e
*DENSITY
       0.8E-6,
*ELASTIC, TYPE=ISO
      20.E+3,         0.3
*PLASTIC
2.0E+3,0
3.0E+3,1.0
**
*MATERIAL, NAME=stis3a
*DENSITY
       1.0E-6,
*ELASTIC, TYPE=ISO
      20.E+3,         0.3
*PLASTIC
0.2E+3,0
0.4E+3,1.0
**
*MATERIAL, NAME=stis3b
*DENSITY
       1.0E-6,
*ELASTIC, TYPE=ISO
      20.E+3,         0.3
*PLASTIC
0.4E+3,0
0.6E+3,1.0
**
*MATERIAL, NAME=stis3c
*DENSITY
       1.0E-6,
*ELASTIC, TYPE=ISO
      20.E+3,         0.3
*PLASTIC
0.6E+3,0
0.8E+3,1.0
**
*MATERIAL, NAME=stis3d
*DENSITY
       1.0E-6,
*ELASTIC, TYPE=ISO
      20.E+3,         0.3
*PLASTIC
1.0E+3,0
1.2E+3,1.0
**
*MATERIAL, NAME=stis3e
*DENSITY
       1.0E-6,
*ELASTIC, TYPE=ISO
      20.E+3,         0.3
*PLASTIC
2.0E+3,0
3.0E+3,1.0
**
*MATERIAL, NAME=stis4a
*DENSITY
       1.3E-6,
*ELASTIC, TYPE=ISO
      20.E+3,         0.3
*PLASTIC
0.2E+3,0
0.4E+3,1.0
**
*MATERIAL, NAME=stis4b
*DENSITY
       1.3E-6,
*ELASTIC, TYPE=ISO
      20.E+3,         0.3
*PLASTIC
0.4E+3,0
0.6E+3,1.0
**
*MATERIAL, NAME=stis4c
*DENSITY
       1.3E-6,
*ELASTIC, TYPE=ISO
      20.E+3,         0.3
*PLASTIC
0.6E+3,0
0.8E+3,1.0
**
*MATERIAL, NAME=stis4d
*DENSITY
       1.3E-6,
*ELASTIC, TYPE=ISO
      20.E+3,         0.3
*PLASTIC
1.0E+3,0
1.2E+3,1.0
**
*MATERIAL, NAME=stis4e
*DENSITY
       1.3E-6,
*ELASTIC, TYPE=ISO
      20.E+3,         0.3
*PLASTIC
2.0E+3,0
3.0E+3,1.0
**
*MATERIAL, NAME=stis5a
*DENSITY
       1.0E-6,
*ELASTIC, TYPE=ISO
      100.E+3,         0.3
*PLASTIC
0.8E+3,0
1.0E+3,1.0
**
*MATERIAL, NAME=stis5b
*DENSITY
       1.0E-6,
*ELASTIC, TYPE=ISO
      100.E+3,         0.3
*PLASTIC
1.2E+3,0
1.4E+3,1.0
**
*MATERIAL, NAME=stis5c
```

```
*DENSITY
       1.0E-6,
*ELASTIC, TYPE=ISO
      100.E+3,         0.3
*PLASTIC
2.0E+3,0
3.0E+3,1.0
**
*MATERIAL, NAME=stis5d
*DENSITY
       1.0E-6,
*ELASTIC, TYPE=ISO
      500.E+3,         0.3
**
*MATERIAL, NAME=stis5e
*DENSITY
       1.0E-6,
*ELASTIC, TYPE=ISO
      1000.E+3,         0.3
**
*MATERIAL, NAME=stis5f
*DENSITY
       1.0E-6,
*ELASTIC, TYPE=ISO
      2000.E+3,         0.3
**
*MATERIAL, NAME=stis6a
*DENSITY
       1.6E-6,
*ELASTIC, TYPE=ISO
      0.3E+3,         0.3
*PLASTIC
0.1E+3,0
0.2E+3,1.0
**
*MATERIAL, NAME=stis6b
*DENSITY
       1.6E-6,
*ELASTIC, TYPE=ISO
      0.3E+3,         0.3
*PLASTIC
0.15E+3,0
0.2E+3,1.0
**
*MATERIAL, NAME=stis6c
*DENSITY
       1.6E-6,
*ELASTIC, TYPE=ISO
      0.4E+3,         0.3
*PLASTIC
0.2E+3,0
0.3E+3,1.0
**
*MATERIAL, NAME=stis6d
*DENSITY
       1.6E-6,
*ELASTIC, TYPE=ISO
      0.4E+3,         0.3
*PLASTIC
0.3E+3,0
0.4E+3,1.0
**
*MATERIAL, NAME=stis6e
*DENSITY
       1.6E-6,
*ELASTIC, TYPE=ISO
      0.5E+3,         0.3
*PLASTIC
0.1E+3,0
0.2E+3,1.0
**
*MATERIAL, NAME=stis6f
*DENSITY
       1.6E-6,
*ELASTIC, TYPE=ISO
      0.5E+3,         0.3
*PLASTIC
0.2E+3,0
0.35E+3,1.0
**
*MATERIAL, NAME=stis7a
*DENSITY
       1.6E-6,
*ELASTIC, TYPE=ISO
      0.3E+3,         0.3
*PLASTIC
```

```
0.1E+3,0
0.3E+3,1.0
**
*MATERIAL, NAME=stis7b
*DENSITY
       1.6E-6,
*ELASTIC, TYPE=ISO
      0.3E+3,         0.3
*PLASTIC
0.1E+3,0
0.35E+3,1.0
**
*MATERIAL, NAME=stis7c
*DENSITY
       1.6E-6,
*ELASTIC, TYPE=ISO
      0.4E+3,         0.3
*PLASTIC
0.1E+3,0
0.15E+3,1.0
**
*MATERIAL, NAME=stis7d
*DENSITY
       1.6E-6,
*ELASTIC, TYPE=ISO
      0.4E+3,         0.3
*PLASTIC
0.1E+3,0
0.2E+3,1.0
**
*MATERIAL, NAME=stis7e
*DENSITY
       1.6E-6,
*ELASTIC, TYPE=ISO
      1.0E+3,         0.3
*PLASTIC
0.2E+3,0
0.4E+3,1.0
**
*MATERIAL, NAME=stis7f
*DENSITY
       1.6E-6,
*ELASTIC, TYPE=ISO
      1.0E+3,         0.3
*PLASTIC
0.4E+3,0
0.6E+3,1.0
**
```

Model Optimisation

The validation of a numerical model is one of the most important part of the model development. Figure C2 .1 shows the diagram of the basic steps of the procedure used for FE-model validation. This procedure is described generally and by examples of the validation procedure of the pelvic part of the FE-model.

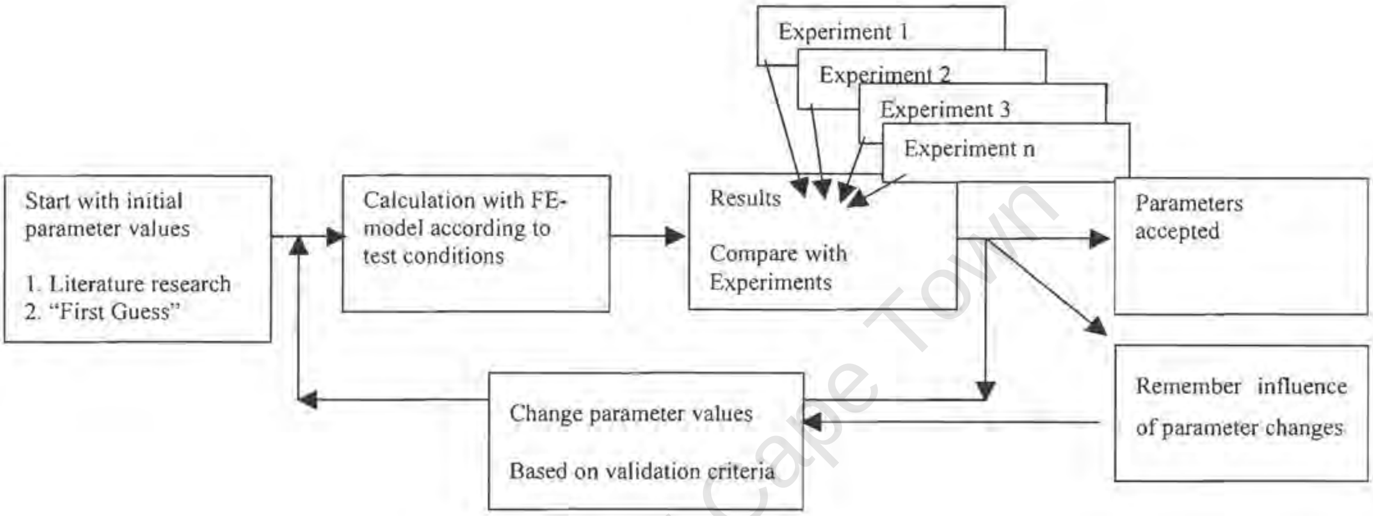

Figure C2.1: Diagram of validation process

Defining the intial parameter values is the first part of the validation process. At the begining of the FE-model development it was planned to use only purely elastic material properties with the basic material parameters: Young's moduls, Poisson's ratio and Density found in wider literature. An overview of these material properties are presented in Tables 3.1.1, 3.1.2, 3.1.3 and 3.1.4. For biological materials like the visceral contents no properties are published and the initial values were estimated. The second part of the validation includes the modification of the FE-model according to the experimental test that is intended to be simulated. The pelvis was the first part of the FE-model that could be tested separately from the entire body model. The experimental impact tests used for the validation are described in Section 4.6 (page 135). The FE-pelvis needed to be modelled according to the test setup, shown in Figure C2.2 and the simulation performed according to the given experimental test conditions.

The simulation results consist of e.g. force-deflection-, force-time, deflection-time curves, etc., which in turn are compared with the corresponding experimental results in the third validation step. The criteria that describe the "goodness of fit" in comparison to the corresponding experimental results are described in the following example of the pelvis validation.

1. Subjective validation criterion: Overall shape of the response curves

In Section 4.6.1 (page 136) a dynamic test procedure is described in which isolated pelvises were impacted with a falling mass of 3.68 kg at a speed of 4 km/h. The resultant displacements and impact forces were obtained for the different pelvises that are catergorised into 3 different groups as described in Section 4.6.1.

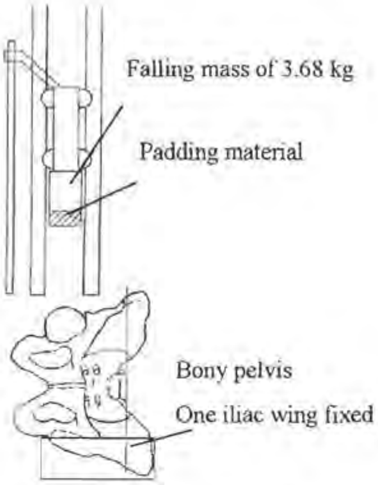

Figure C2.2 Experimental test set up [Gui97] (original Figure 4.6.1)

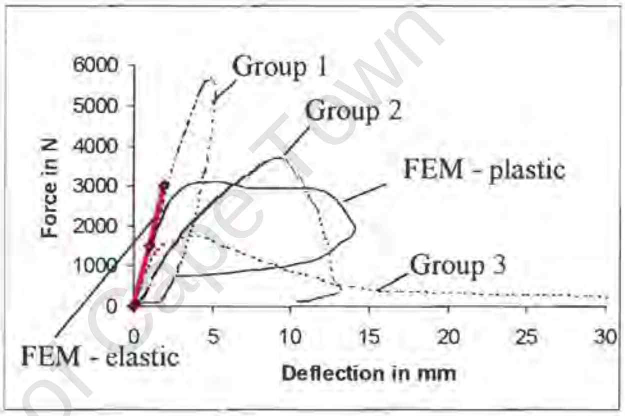

Figure C2.3 Comparison of force-deflection responses of FE-model and experiments [Bes98] (original Figure 4.6.4)

The first validation criteria that describes the "goodness of fit" is the first subjective impression of the shape of the simulated curve in comparions to the experimental results. The FE-pelvis model with purely linear elastic material properties shows a force-deflection curve that differs significantly from all three experimental results as can be seen in Figure C2.3. The simulated curve shows a force-deflection response with a steep and almost linear slope while the experimentally obtained curves show a non-linear behaviour with higher deflection. Any modifications of the property parameters, in this case the Young's modulus results in a different gradient of the force-deflection slope but does not influence the overall shape of the curve.

In contrast to the experimental tests, the FE-model with the purely elastic material does not show permant deformation which in turn is not realistic. Therefore the material model needed to be expanded to show an elastic-plastic behaviour. The next iteration loops were performed to find the range of the yield stress. It was observed that this parameter mainly determines the maximum force and maximum deflection. The ranges and increments of material property changes can be found in Appendix C 1, showing the original material data sheets. The aim was to get a simulated force-defelection curve with an overall shape that looks similar to the curve of the second group pelvises reaching similar force and deflection levels. No specific statistical method was applied because this first validation criterion is too subjective.

2. Validation criteria: slope of the curve, duration and time of maxima, duration of response descent

One of the most important part of the validation of the FE-model of the human body is the performance of the enitre FE-model subjected to impactor and sled tests. The typical criteria used for the comparison between the simulated and experimental results are demonstrated at the example of the pelvis validation process.

Figures C2.4 a) and b) show the force-time histories of the simulated Viano impactor tests at initial velocities of 4.8 m/s and 9.8 m/s in comparison to the experimental corridors.

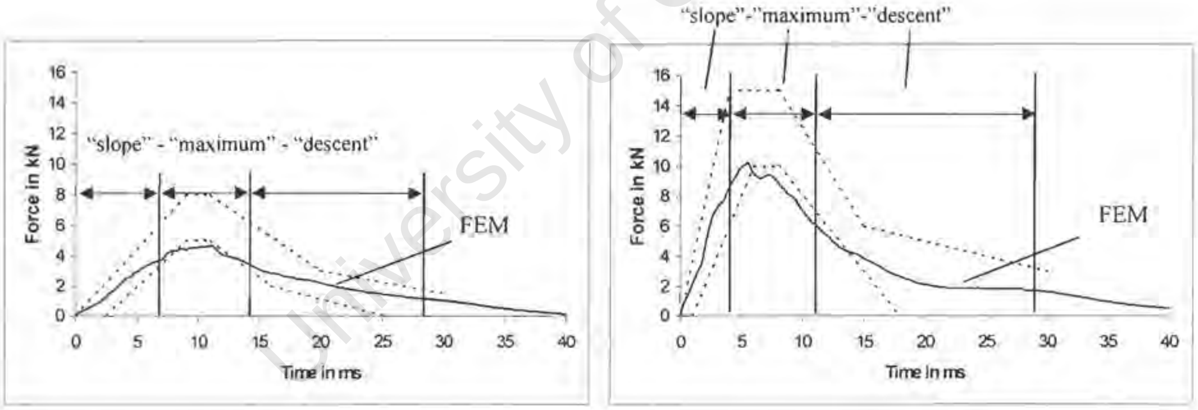

a) Pelvis impactor test 4.8 m/s *b) Pelvis impactor test 9.8 m/s*

Figure C2.4 (original: Figure 4.6.6) Comparison of force-time histories in Viano pelvis impactor tests

The force-time response can be roughly devided into three stages. The first is the slope of the curve that covers the period from 0 to 7 ms in the 4.8 m/s test and from 0 to 4.5 ms in the 9.8 m/s test as shown in Figures C2.4 a) and b). The gradient is mainly influenced by the Young's modulus of the biological materials and can be accepted when the slope of force-time and force-deflection curves falls either within the response corridor given by the experiments or within a range of ± 30 % of the experimental curve. The latter is applied when an experimental curve is given instead of a corridor.

The range of ± 30 % might appear to be too wide but it is realistic in comparison to the range of responses of experimental results.

The next criterion focuses on the shape of the curve around the peak values. In this case a time period of ± 3 ms was defined around the maximum at t = 10 ms for the 4.8 m/s and t = 4.5 ms for the 9.8 m/s pelvic impact test. Prior to this period of maximum values the "slope"- stage is defined and afterwards the "descent"- stage of the curve.

For the 4.8 m/s test the simulated curve shows a similar duration of the maximum as observed in the experiments. At the higher velocity of 9.8 m/s the maximum and the maximum is reached earlier than in the experiments. An optimisation of this particular event can be achieved by increasing the Young's modulus and the Yield stress. In the following validation loop, these parameters were changed with the result of a deteriorated performance of the FE-model, in particular the pelvis impact force results in the Heidelberg and WSU sled tests. It can be seen in Figures C2.5 a) and b) that the pelvic impact forces in the Heidelberg sled tests already exceed the experimental values and would fall out of the 30% range in case of a higher Young's modulus and yield stress. If the parameter changes result into a bad performance of more than one other test, which means the simulated results fall out of the ± 30 % range of the experiment, the validation procedure stops following this optimisation direction.

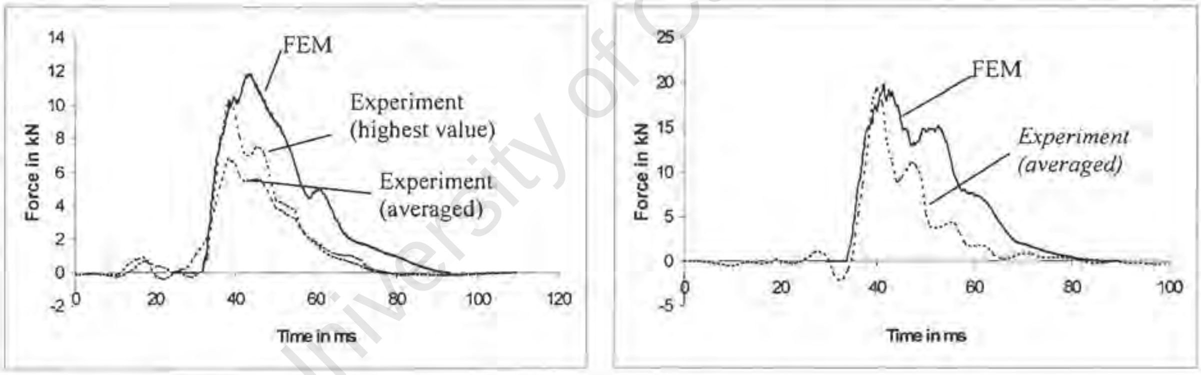

a) Pelvis force response at 6.7 m/s *b) Pelvis force response at 8.9 m/s*

Figure C2.5 (original: Figure 4.6.8) Comparison of pelvis force-time histories in Heidelberg sled test

The third stage of the force-time response is the duration of the descent which is less important than the slope an the maximum stage, because the descent of the response curve cannot be influenced without significant changes of the slope and the maximum stage. However, the overall shape of response curve is influenced by the descent as well as the overall duration of the impact response. Although the slope and the maximum of the simulated curve corresponds extremly well with the experimental results in Figure C2.5 b), the descent of the curve differs and exceeds the 30% range. The slope and the maximum are considered to be important because most of the energy is dissipated within these stages of impact. Therefore the optimisation of the descent stage of the response curve was not considered to be necessary and the optimisation procedure was stopped.

3. Maximum values

The third criteria is the comparions of the peak values. The peak values of force, deflection, compression and acceleration response are of particular interest, because some of them are used for injury criteria calculations. The peak values of the simulated responses can be compared directly to the corresponding experimental results. This was done in tabular form during the validation process, as shown in Table C2.1.

	Experiment 4.8 m/s	**FE-model 4.8 m/s**	**Experiment 9.8 m/s**	**FE-model 9.8 m/s**
Force in kN	5.45 ± 1.65	4.64 (√)	11.20 ± 1.48	10.23 (√)
Deflection in mm	49.0 ± 16.0	53.3 (√)	78.3 ± 22.7	88.8 (√)
Compression in %	13.5 ± 4.0	14.8 (√)	22.9 ± 6.0	24.6 (√)
Acceleration T8 in g	7.7 ± 3.1	7.5 (√)	-	9.30
Acceleration T12 in g	15.0 ± 12.6	14.0 (√)	31.6 ± 1.0	28.9
Acceleration S3 in g	34.4 ± 15.0	29.8 (√)	39.9 ± 26.8	71.3

Table C2.1 (original table 4.6.1) Pelvic impact response data

Table C2.1 shows that some simulation responses do not fall within the range of the experimental results as seen for the T12 and S3 acceleration. Although there might be potential for further improvements, some optimisation processes were stopped due to computational time limits. Furthermore it is assumed that more advanced visco-elastic material models including fracture mechanisms bear more potential for improvements than the optimisation of the parameters of the elastic-plastic material model.

The described systematic validation process was automised to a certain extend only. The relevant simulation results were written by an ABAQUS post routine into an abaqus print file, which in turn was imported automatically into MS-Excel® where the valdiation analyses was conducted as described before. A fully automised optimisation procedure included into ABAQUS would require optimisation functions that significantly exceed the cababilities of the existing optimisation algorithms.

3. Contact and Friction

Appendix C 3 contains all information about contact conditions within the FE-model of the human body. After a general description of the different contact surfaces, the original ABAQUS contact-files are presented that contain all contacts defined in the FE-model.

All contact interactions are defined without friction in combination with the "penalty method" to provide high numerical stability. The main reason for not defining friction in all different contact pairs is the fact that friction effects are negligable in comparison to the impact deformation. The small amount of energy dissipation due to friction can be considered by damper elements if necessary.

The different contact pairs of the FE-model are categorised in five groups describing the contact between:

- Bones within joints (hard – hard contact)
- Bones and soft tissue (hard – soft contact)
- Surfaces consisting of muscles / bones and soft tissue (hard/soft - soft contact)
- Muscles and muscles (soft – soft contact)
- Skin and impactor/wall (body surface – hard contact)

Contact within joints (hard – hard contact)

The first group describes the surface interaction of bones within a joint. An example of the hip joint is shown in Figure C 3.1.

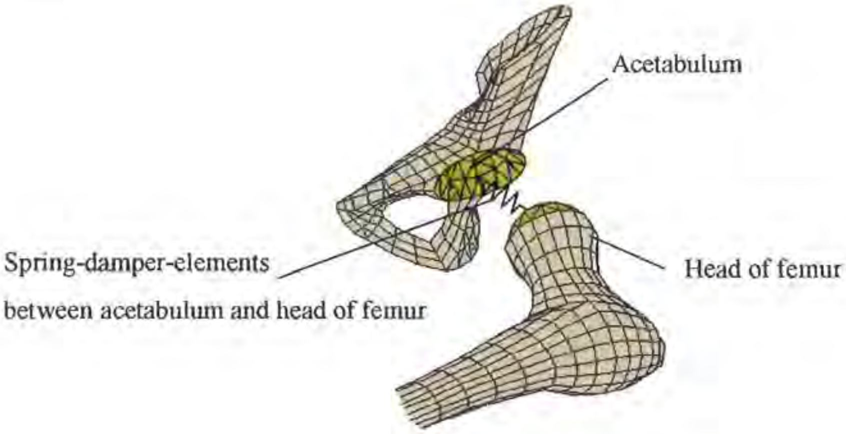

Figure C 3.1 (original Figure 3.7.2) Contact between two bony surfaces within a joint

The contact pair consists of the outer surface of the acetabulum and the corresponding surface of the head of the femur. To prevent a "noisy" contact between these two hard surfaces, spring-damper elements are placed between them. The relative movement is relatively small, so that friction has not been defined between these surfaces. Energy dissipation due to even small relative movement within the joint is considered by the damper element, so that the energy dissipation effect due to friction is not entirely neglected.

Contact between bones and soft tissue (hard – soft contact)

Examples of bony material that is in contact with soft tissue are shown in Figure C 3.2. Contact is defined between the visceral contents of the pelvis and the inner surfaces of the bony pelvis and the frontal surfaces of the lumbar vertebrae as illustrated in Figure C 3.2.

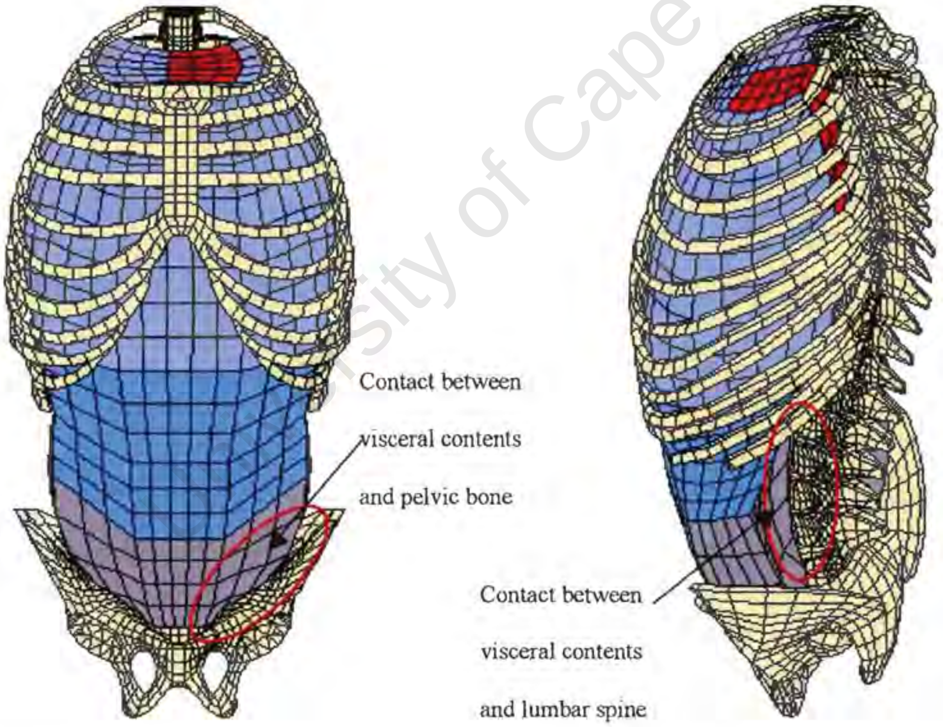

a) Front view *b) Oblique rear view*

Figure C 3.2 (original Figure 3.4.5) FE-model of the visceral contents

The energy dissipation caused by the relative movement between the visceral contents and the pelvis or the lumbar spine is assumed to be significantly smaller than the energy dissipation of the visceral contents due to plastic deformation. The range of friction coefficients of well lubricated soft tissue

Contact between skin and impactor or impacted wall

The entire skin surrounding the human body consists of a continous mesh without any multi point constraints. This continous surface is defined as the contact surface with the impactors and the impacted wall in the WSU and Heidelberg sled tests. No friction is defined between these contact surfaces. The friction between the human body and the supports underneath the lower limbs were small in the experiments, because a low friction Teflon sheet was placed between cadaver and the seat. However, the friction resulted in a reduced impact velocity prior to impact as described by Cavanaugh, et al. [Cav901, Cav90b, Cav93]. Therefore an initial velocity reduced by 0.2 m/s has been defined as recommended by Cavanaugh, et al. [Cav901, Cav90b, Cav93] and Huang, et al. [Hua94a].

Abaqus input file - Contact

```
**----------------- shoulder contact ----------------
**----------------- serratus ant ----------------
*SURFACE DEFINITION,NAME=shsscl, no thick
shsscl,spos
*SURFACE DEFINITION,NAME=shsscr, no thick
shsscr,spos
*SURFACE DEFINITION,NAME=shscpl, no thick
shscpl,sneg
*SURFACE DEFINITION,NAME=shscpr, no thick
shscpr,sneg
**----------------- subscapularis  ----------------
*SURFACE DEFINITION,NAME=shscal, no thick
shscal,spos
*SURFACE DEFINITION,NAME=shscar, no thick
shscar,spos
**----------------- infraspinatus ----------------
*SURFACE DEFINITION,NAME=shincl, no thick
shincl,spos
*SURFACE DEFINITION,NAME=shincr, no thick
shincr,spos
**----------------- scapula ----------------
*SURFACE DEFINITION,NAME=shccl, no thick
shccl,spos
*SURFACE DEFINITION,NAME=shccr, no thick
shccr,spos
*SURFACE DEFINITION,NAME=shscl, no thick
shscl,spos
*SURFACE DEFINITION,NAME=shscr, no thick
shscr,spos
**
**----------------- under arm contact ----------------
*SURFACE DEFINITION,NAME=aucl, no thick
aucl,spos
*SURFACE DEFINITION,NAME=aucr, no thick
aucr,spos
*SURFACE DEFINITION,NAME=aaucl, no thick
aaucl,spos
*SURFACE DEFINITION,NAME=aaucr, no thick
aaucr,spos
***SURFACE DEFINITION,NAME=aspl1
**aspl1,S5
***SURFACE DEFINITION,NAME=aspl2, no thick
**aspl2,sneg
***SURFACE DEFINITION,NAME=aspr1
**aspr1,S4
***SURFACE DEFINITION,NAME=aspr2, no thick
**aspr2,sneg
**
**----------------- wall ----------------
*SURFACE DEFINITION,NAME=WSH, no thick
WSH,spos
*SURFACE DEFINITION,NAME=WTH, no thick
WTH,spos
*SURFACE DEFINITION,NAME=WAB, no thick
WAB,spos
*SURFACE DEFINITION,NAME=WPE, no thick
WPE,spos
*SURFACE DEFINITION,NAME=WPE2, no thick
WPE2,spos
*SURFACE DEFINITION,NAME=WSE, no thick
WSE,spos
*SURFACE DEFINITION,NAME=Wkn, no thick
Wkn,spos
*SURFACE DEFINITION,NAME=WTH2, no thick
WTH2,spos
*SURFACE DEFINITION,NAME=WAB2, no thick
WAB2,spos
*SURFACE DEFINITION,NAME=Wfo, no thick
wfo,spos
**----------------- illiac wing ----------------
*SURFACE DEFINITION,NAME=pilwng, no thick
pilwng,spos
**----------------- femur ----------------
*SURFACE DEFINITION,NAME=pfhl, no thick
pfhl,spos
**----------------- shoulder ----------------
*SURFACE DEFINITION,NAME=shpcl, no thick
shpcl,spos
*SURFACE DEFINITION,NAME=shpcr, no thick
shpcr,spos
*SURFACE DEFINITION,NAME=shclvl1, no thick
shclvl1,spos
**----------------- abdominal surface ----------------
```

```
**asulp
**asurp
**rib surface rcontl
**----------------- arm surface ----------------
**asurfl
**atubl
**afosul
**afosul
**----------------- pel surface ----------------
**pcont2
**
**----------------- semispinalis ----------------
*SURFACE DEFINITION,NAME=bslb, no thick
bslb,spos
*SURFACE DEFINITION,NAME=bsrb, no thick
bsrb,spos
**
**----------------- splenius ----------------
*SURFACE DEFINITION,NAME=bspln, no thick
bspll,sneg
*SURFACE DEFINITION,NAME=bsprn, no thick
bsplr,sneg
*SURFACE DEFINITION,NAME=bsplp, no thick
bspll,spos
*SURFACE DEFINITION,NAME=bsprp, no thick
bsplr,spos
**
**----------------- trapezius ----------------
*SURFACE DEFINITION,NAME=btrapf1, no thick
btrapf1,spos
*SURFACE DEFINITION,NAME=btrapf2, no thick
btrapf2,spos
**----------------- lattismus ----------------
*SURFACE DEFINITION,NAME=shlatcl, no thick
shlatcl,spos
*SURFACE DEFINITION,NAME=shlatcr, no thick
shlatcr,spos
**----------------- abdominal surface ----------------
*SURFACE DEFINITION,NAME=asuln, no thick
abdsurl,sneg
*SURFACE DEFINITION,NAME=asurn, no thick
abdsurr,sneg
*SURFACE DEFINITION,NAME=asulp, no thick
abdsurl,spos
*SURFACE DEFINITION,NAME=asurp, no thick
abdsurr,spos
*SURFACE DEFINITION,NAME=abd3sl, no thick
abd3sl,spos
*SURFACE DEFINITION,NAME=abd3sr, no thick
abd3sr,spos
**
**-----------------erector spinae ----------------
*SURFACE DEFINITION,NAME=berectsl, no thick
berectsl,spos
*SURFACE DEFINITION,NAME=berectsr, no thick
berectsr,spos
**----------------- rhomb.  ----------------
*SURFACE DEFINITION,NAME=brhomln, no thick
brhoml,sneg
*SURFACE DEFINITION,NAME=brhomrn, no thick
brhomr,sneg
*SURFACE DEFINITION,NAME=brhomlp, no thick
brhoml,spos
*SURFACE DEFINITION,NAME=brhomrp, no thick
brhomr,spos
**
**----------------- armsurface ----------------
*SURFACE DEFINITION,NAME=asurfl, no thick
asurfl,spos
*SURFACE DEFINITION,NAME=asurfr, no thick
asurfr,spos
*SURFACE DEFINITION,NAME=afosul, no thick
afosul,spos
*SURFACE DEFINITION,NAME=afosur, no thick
afosur,spos
**----------------- legsurface ----------------
*SURFACE DEFINITION,NAME=pcont1a, no thick
pcont1a,spos
*SURFACE DEFINITION,NAME=pcont1b, no thick
pcont1b,spos
*SURFACE DEFINITION,NAME=pcont2, no thick
pcont2,spos
*SURFACE DEFINITION,NAME=pksul, no thick
pksul,spos
*SURFACE DEFINITION,NAME=plegl, no thick
plegl,spos
```

```
*SURFACE DEFINITION,NAME=plegr, no thick
plegr,spos
**
**
**----------------- head ----------------
*SURFACE DEFINITION,NAME=bhl, no thick
bhl,spos
*SURFACE DEFINITION,NAME=bhr, no thick
bhr,spos
**----------------- shoulder ----------------
*SURFACE DEFINITION,NAME=bnsurl, no thick
bnsurl,spos
*SURFACE DEFINITION,NAME=bnsurr, no thick
bnsurr,spos
**atubl
**atubr
**
**----------------- deltoid ----------------
*SURFACE DEFINITION,NAME=shdesl, no thick
shdesl,spos
*SURFACE DEFINITION,NAME=shdesr, no thick
shdesr,spos
**----------------- rib----------------
*SURFACE DEFINITION,NAME=rcontl, no thick
rcontl,spos
*SURFACE DEFINITION,NAME=rcontr, no thick
rcontr,spos
*SURFACE DEFINITION,NAME=rcintl, no thick
rcintl,sneg
*SURFACE DEFINITION,NAME=rcintr, no thick
rcintr,sneg
**----------------- serratus ----------------
*SURFACE DEFINITION,NAME=shsercl, no thick
shsercl,spos
*SURFACE DEFINITION,NAME=shsercr, no thick
shsercr,spos
**----------------- sternum inner ----------------
*SURFACE DEFINITION,NAME=stebc, no thick
stebc,spos
**----------------- pelvis inner ----------------
*SURFACE DEFINITION,NAME=pinsl, no thick
pinsl,spos
*SURFACE DEFINITION,NAME=pinsr, no thick
pinsr,spos
**----------------- abdominal surface inner ----------------
*SURFACE DEFINITION,NAME=abdinl, no thick
abdinl,spos
*SURFACE DEFINITION,NAME=abdinr, no thick
abdinr,spos
**----------------- visc. cont. ----------------
*SURFACE DEFINITION,NAME=viscls, no thick
viscls,spos
*SURFACE DEFINITION,NAME=visc2s, no thick
visc2s,spos
*SURFACE DEFINITION,NAME=visc3s, no thick
visc3s,spos
**
**
*CONTACT PAIR,PENALTY
bhl,bnsurl
bhr,bnsurr
atubl,shdesl
atubr,shdesr
rcontl,shsercl
rcontr,shsercr
stebc,viscls
pinsl,visc3s
pinsr,visc3s
rcintl,viscls
rcintr,viscls
rcintl,visc2s
rcintr,visc2s
abdinl,visc3s
abdinr,visc3s
abdinl,visc2s
abdinr,visc2s
**
**
*CONTACT PAIR,PENALTY
bslb,bspln
bsrb,bsprn
bsplp,btrapf1
bsprp,btrapf2
shlatcl,asuln
shlatcr,asurn
berectsl,brhomln
```

```
berectsr,brhomrn
brhomlp,btrapfl
brhomrp,btrapf2
asurfl,asulp
asurfr,asurp
afosul,asulp
afosur,asurp
pcontla,pcontlb
**
**
*CONTACT PAIR,PENALTY
shsscl,shscal
shsscr,shscar
shccl,shscpl
shccr,shscpr
shincl,asuln
shincr,asurn
shscl,asuln
shscr,asurn
aaucl,aucl
aaucr,aucr
rcontl,aaucl
rcontr,aaucr
rcontl,asuln
rcontr,asurn
rcontl,abd3sl
rcontr,abd3sr
**
*CONTACT PAIR,PENALTY
wsh,bhl
wsh,bnsurl
wsh,shclvll
wsh,shpcl
wsh,shscpl
wsh,atubl
wsh,asurfl
wsh,asulp
wsh,afosul
wsh,rcontl
**
wth,shclvll
wth,shpcl
wth,shscpl
wth,atubl
wth,asulp
wth,rcontl
wth,asurfl
wth,afosul
wth,afosur
wth2,asurfl
wth2,afosul
wth2,afosur
**
WAB,asulp
WAB,rcontl
WAB,asurfl
wab,afosul
wab,afosur
WAB2,asurfl
wab2,afosul
wab2,afosur
**
WPE,pfhl
WPE,pilwng
WPE,pcont2
**
WPE2,pcont2
**
Wkn,pcont2
Wkn,pksul
Wkn,plegl
plegl,plegr
afosur,afosul
wfo,plegl
wfo,plegr
**----------------- head ----------------
**
*SURFACE DEFINITION,NAME=bhbl,no thick
bhbl,spos
*SURFACE DEFINITION,NAME=bhbr,no thick
bhbr,spos
**----------------- sacrum ----------------
**
*SURFACE DEFINITION,NAME=psl,no thick
psl,spos
*SURFACE DEFINITION,NAME=psr,no thick
```

```
psr,spos
**----------------- cerv. spine ---------------
**
*SURFACE DEFINITION,NAME=bc1ld,no thick
bc1ld,spos
*SURFACE DEFINITION,NAME=bc1rd,no thick
bc1rd,spos
*SURFACE DEFINITION,NAME=bc1lu,no thick
bc1lu,spos
*SURFACE DEFINITION,NAME=bc1ru,no thick
bc1ru,spos
**
*SURFACE DEFINITION,NAME=bc2ld,no thick
bc2ld,spos
*SURFACE DEFINITION,NAME=bc2rd,no thick
bc2rd,spos
*SURFACE DEFINITION,NAME=bc2lu,no thick
bc2lu,spos
*SURFACE DEFINITION,NAME=bc2ru,no thick
bc2ru,spos
**
*SURFACE DEFINITION,NAME=bc3ld,no thick
bc3ld,spos
*SURFACE DEFINITION,NAME=bc3rd,no thick
bc3rd,spos
*SURFACE DEFINITION,NAME=bc3lu,no thick
bc3lu,spos
*SURFACE DEFINITION,NAME=bc3ru,no thick
bc3ru,spos
**
*SURFACE DEFINITION,NAME=bc4ld,no thick
bc4ld,spos
*SURFACE DEFINITION,NAME=bc4rd,no thick
bc4rd,spos
*SURFACE DEFINITION,NAME=bc4lu,no thick
bc4lu,spos
*SURFACE DEFINITION,NAME=bc4ru,no thick
bc4ru,spos
**
*SURFACE DEFINITION,NAME=bc5ld,no thick
bc5ld,spos
*SURFACE DEFINITION,NAME=bc5rd,no thick
bc5rd,spos
*SURFACE DEFINITION,NAME=bc5lu,no thick
bc5lu,spos
*SURFACE DEFINITION,NAME=bc5ru,no thick
bc5ru,spos
**
*SURFACE DEFINITION,NAME=bc6ld,no thick
bc6ld,spos
*SURFACE DEFINITION,NAME=bc6rd,no thick
bc6rd,spos
*SURFACE DEFINITION,NAME=bc6lu,no thick
bc6lu,spos
*SURFACE DEFINITION,NAME=bc6ru,no thick
bc6ru,spos
**
*SURFACE DEFINITION,NAME=bc7ld,no thick
bc7ld,spos
*SURFACE DEFINITION,NAME=bc7rd,no thick
bc7rd,spos
*SURFACE DEFINITION,NAME=bc7lu,no thick
bc7lu,spos
*SURFACE DEFINITION,NAME=bc7ru,no thick
bc7ru,spos
**
**----------------- thor. spine ---------------
**
*SURFACE DEFINITION,NAME=bt1ld,no thick
bt1ld,spos
*SURFACE DEFINITION,NAME=bt1rd,no thick
bt1rd,spos
*SURFACE DEFINITION,NAME=bt1lu,no thick
bt1lu,spos
*SURFACE DEFINITION,NAME=bt1ru,no thick
bt1ru,spos
**
*SURFACE DEFINITION,NAME=bt2ld,no thick
bt2ld,spos
*SURFACE DEFINITION,NAME=bt2rd,no thick
bt2rd,spos
*SURFACE DEFINITION,NAME=bt2lu,no thick
bt2lu,spos
*SURFACE DEFINITION,NAME=bt2ru,no thick
bt2ru,spos
**
```

```
*SURFACE DEFINITION,NAME=bt3ld,no thick
bt3ld,spos
*SURFACE DEFINITION,NAME=bt3rd,no thick
bt3rd,spos
*SURFACE DEFINITION,NAME=bt3lu,no thick
bt3lu,spos
*SURFACE DEFINITION,NAME=bt3ru,no thick
bt3ru,spos
**
*SURFACE DEFINITION,NAME=bt4ld,no thick
bt4ld,spos
*SURFACE DEFINITION,NAME=bt4rd,no thick
bt4rd,spos
*SURFACE DEFINITION,NAME=bt4lu,no thick
bt4lu,spos
*SURFACE DEFINITION,NAME=bt4ru,no thick
bt4ru,spos
**
*SURFACE DEFINITION,NAME=bt5ld,no thick
bt5ld,spos
*SURFACE DEFINITION,NAME=bt5rd,no thick
bt5rd,spos
*SURFACE DEFINITION,NAME=bt5lu,no thick
bt5lu,spos
*SURFACE DEFINITION,NAME=bt5ru,no thick
bt5ru,spos
**
*SURFACE DEFINITION,NAME=bt6ld,no thick
bt6ld,spos
*SURFACE DEFINITION,NAME=bt6rd,no thick
bt6rd,spos
*SURFACE DEFINITION,NAME=bt6lu,no thick
bt6lu,spos
*SURFACE DEFINITION,NAME=bt6ru,no thick
bt6ru,spos
**
*SURFACE DEFINITION,NAME=bt7ld,no thick
bt7ld,spos
*SURFACE DEFINITION,NAME=bt7rd,no thick
bt7rd,spos
*SURFACE DEFINITION,NAME=bt7lu,no thick
bt7lu,spos
*SURFACE DEFINITION,NAME=bt7ru,no thick
bt7ru,spos
**
*SURFACE DEFINITION,NAME=bt8ld,no thick
bt8ld,spos
*SURFACE DEFINITION,NAME=bt8rd,no thick
bt8rd,spos
*SURFACE DEFINITION,NAME=bt8lu,no thick
bt8lu,spos
*SURFACE DEFINITION,NAME=bt8ru,no thick
bt8ru,spos
**
*SURFACE DEFINITION,NAME=bt9ld,no thick
bt9ld,spos
*SURFACE DEFINITION,NAME=bt9rd,no thick
bt9rd,spos
*SURFACE DEFINITION,NAME=bt9lu,no thick
bt9lu,spos
*SURFACE DEFINITION,NAME=bt9ru,no thick
bt9ru,spos
**
*SURFACE DEFINITION,NAME=bt10ld,no thick
bt10ld,spos
*SURFACE DEFINITION,NAME=bt10rd,no thick
bt10rd,spos
*SURFACE DEFINITION,NAME=bt10lu,no thick
bt10lu,spos
*SURFACE DEFINITION,NAME=bt10ru,no thick
bt10ru,spos
**
*SURFACE DEFINITION,NAME=bt11ld,no thick
bt11ld,spos
*SURFACE DEFINITION,NAME=bt11rd,no thick
bt11rd,spos
*SURFACE DEFINITION,NAME=bt11lu,no thick
bt11lu,spos
*SURFACE DEFINITION,NAME=bt11ru,no thick
bt11ru,spos
**
*SURFACE DEFINITION,NAME=bt12ld,no thick
bt12ld,spos
*SURFACE DEFINITION,NAME=bt12rd,no thick
bt12rd,spos
*SURFACE DEFINITION,NAME=bt12lu,no thick
```

```
bt12lu,spos
*SURFACE DEFINITION,NAME=bt12ru,no thick
bt12ru,spos
**
**------------------ lumb. spine ----------------
**
*SURFACE DEFINITION,NAME=bl1ld,no thick
bl1ld,spos
*SURFACE DEFINITION,NAME=bl1rd,no thick
bl1rd,spos
*SURFACE DEFINITION,NAME=bl1lu,no thick
bl1lu,spos
*SURFACE DEFINITION,NAME=bl1ru,no thick
bl1ru,spos
**
*SURFACE DEFINITION,NAME=bl2ld,no thick
bl2ld,spos
*SURFACE DEFINITION,NAME=bl2rd,no thick
bl2rd,spos
*SURFACE DEFINITION,NAME=bl2lu,no thick
bl2lu,spos
*SURFACE DEFINITION,NAME=bl2ru,no thick
bl2ru,spos
**
*SURFACE DEFINITION,NAME=bl3ld,no thick
bl3ld,spos
*SURFACE DEFINITION,NAME=bl3rd,no thick
bl3rd,spos
*SURFACE DEFINITION,NAME=bl3lu,no thick
bl3lu,spos
*SURFACE DEFINITION,NAME=bl3ru,no thick
bl3ru,spos
**
*SURFACE DEFINITION,NAME=bl4ld,no thick
bl4ld,spos
*SURFACE DEFINITION,NAME=bl4rd,no thick
bl4rd,spos
*SURFACE DEFINITION,NAME=bl4lu,no thick
bl4lu,spos
*SURFACE DEFINITION,NAME=bl4ru,no thick
bl4ru,spos
**
*SURFACE DEFINITION,NAME=bl5ld,no thick
bl5ld,spos
*SURFACE DEFINITION,NAME=bl5rd,no thick
bl5rd,spos
*SURFACE DEFINITION,NAME=bl5lu,no thick
bl5lu,spos
*SURFACE DEFINITION,NAME=bl5ru,no thick
bl5ru,spos
**
*CONTACT PAIR,PENALTY
bhbl,bc1lu
bhbr,bc1ru
**
bc1ld,bc2lu
bc1rd,bc2ru
**
bc2ld,bc3lu
bc2rd,bc3ru
**
bc3ld,bc4lu
bc3rd,bc4ru
**
bc4ld,bc5lu
bc4rd,bc5ru
**
bc5ld,bc6lu
bc5rd,bc6ru
**
bc6ld,bc7lu
bc6rd,bc7ru
**
bc7ld,bt1lu
bc7rd,bt1ru
**
bt1ld,bt2lu
bt1rd,bt2ru
**
bt2ld,bt3lu
bt2rd,bt3ru
**
bt3ld,bt4lu
bt3rd,bt4ru
**
bt4ld,bt5lu
```

```
bt4rd,bt5ru
**
bt5ld,bt6lu
bt5rd,bt6ru
**
bt6ld,bt7lu
bt6rd,bt7ru
**
bt7ld,bt8lu
bt7rd,bt8ru
**
bt8ld,bt9lu
bt8rd,bt9ru
**
bt9ld,bt10lu
bt9rd,bt10ru
**
bt10ld,bt11lu
bt10rd,bt11ru
**
bt11ld,bt12lu
bt11rd,bt12ru
**
bt12ld,bl1lu
bt12rd,bl1ru
**
bl1ld,bl2lu
bl1rd,bl2ru
**
bl2ld,bl3lu
bl2rd,bl3ru
**
bl3ld,bl4lu
bl3rd,bl4ru
**
bl4ld,bl5lu
bl4rd,bl5ru
**
bl5ld,psl
bl5rd,psr
**
**----------------- pel. joint ----------------
**
*SURFACE DEFINITION,NAME=pfhal, no thick
pfhal,spos
*SURFACE DEFINITION,NAME=pfhar, no thick
pfhar,spos
*SURFACE DEFINITION,NAME=pacetl, no thick
pacetl,spos
*SURFACE DEFINITION,NAME=pacetr, no thick
pacetr,spos
**----------------- shoulder joint ----------------
**
*SURFACE DEFINITION,NAME=atubl, no thick
atubl,spos
*SURFACE DEFINITION,NAME=atubr, no thick
atubr,spos
*SURFACE DEFINITION,NAME=shgll, no thick
shgll,spos
*SURFACE DEFINITION,NAME=shglr, no thick
shglr,spos
**
**----------------- elbow joint ----------------
**
*SURFACE DEFINITION,NAME=aelbcll, no thick
aelbcll,spos
*SURFACE DEFINITION,NAME=aelbclr, no thick
aelbclr,spos
*SURFACE DEFINITION,NAME=aelbcul, no thick
aelbcul,spos
*SURFACE DEFINITION,NAME=aelbcur, no thick
aelbcur,spos
**
**----------------- knee joint ----------------
**
*SURFACE DEFINITION,NAME=pknlol, no thick
```

```
pknlol,spos
*SURFACE DEFINITION,NAME=pknlor, no thick
pknlor,spos
*SURFACE DEFINITION,NAME=pknupl, no thick
pknupl,spos
*SURFACE DEFINITION,NAME=pknupr, no thick
pknupr,spos
**
*CONTACT PAIR,PENALTY
pfhal,pacetl
pfhar,pacetr
atubl,shgll
atubr,shglr
aelbcll,aelbcul
aelbclr,aelbcur
pknlol,pknupl
pknlor,pknupr
```

Contents of CD:

FE-model -	FE-model animation file
Impactor_tests -	Impactor tests animation files
Sled_tests -	Sled test animation files